

University of Louisville

## ThinkIR: The University of Louisville's Institutional Repository

---

Electronic Theses and Dissertations

---

8-2021

### Rapid annealing of Perovskite solar cell thin film materials through intense pulse light.

Amir Hossein Ghahremani  
*University of Louisville*

Follow this and additional works at: <https://ir.library.louisville.edu/etd>



Part of the [Manufacturing Commons](#), [Polymer and Organic Materials Commons](#), [Semiconductor and Optical Materials Commons](#), and the [Structural Materials Commons](#)

---

#### Recommended Citation

Ghahremani, Amir Hossein, "Rapid annealing of Perovskite solar cell thin film materials through intense pulse light." (2021). *Electronic Theses and Dissertations*. Paper 3688.  
<https://doi.org/10.18297/etd/3688>

This Doctoral Dissertation is brought to you for free and open access by ThinkIR: The University of Louisville's Institutional Repository. It has been accepted for inclusion in Electronic Theses and Dissertations by an authorized administrator of ThinkIR: The University of Louisville's Institutional Repository. This title appears here courtesy of the author, who has retained all other copyrights. For more information, please contact [thinkir@louisville.edu](mailto:thinkir@louisville.edu).

RAPID ANNEALING OF PEROVSKITE SOLAR CELL THIN FILM MATERIALS  
THROUGH INTENSE PULSE LIGHT

By:

Amir Hossein Ghahremani

A Dissertation

Submitted to the Faculty of the

J.B Speed School of Engineering of the University of Louisville

in Fulfillment of the Requirements

for the Degree of

Doctor of Philosophy in

Mechanical Engineering

Department of Mechanical Engineering

University of Louisville,

Louisville, KY 40292

August 2021

©Copyright 2021 by Amir Hossein Ghahremani

All Rights Reserved



RAPID ANNEALING OF PEROVSKITE SOLAR CELL THIN FILM MATERIALS  
THROUGH INTENSE PULSE LIGHT

*By:*

Amir Hossein Ghahremani

A Dissertation Approved on

June 03, 2021

by the Following Dissertation Committee:

---

Director: Dr. Kunal Kate

---

Director: Dr. Thad Druffel

---

Dr. Bhatia Bikram

---

Dr. Dan O. Popa

## DEDICATION

I dedicate this dissertation to my family whose indefinite support has been the reason for my progressive accomplishments. I also devote this dissertation to my committee, friends, and colleagues whose guidance and assistance paved the way of success towards this dissertation.

## ACKNOWLEDGEMENTS

I would like to express my gratitude to Dr. Thad Druffel whose guidance and assistance has been the means of my success. Besides mentoring, he has been a great friend whose strive was my development motivation. I would also like to appreciate my committee members, Dr. Kate, Dr. Bikram, and Dr. Popa, whose constructive advice was the pathway towards my accomplishments. I am also thankful to Dr Jacek Jasinski for assistance in material characterization, as well as other faculty, staff, and technicians at the University of Louisville, particularly Mr. Joshua Rimmer and Mr. John Jones for the CNC machining of different designed machine parts as well as Mrs. Eunice Salazar, Mrs. Laurie Ann Huelsman, and Mrs. Johanna Boone whose continuous management ensured our non-stop research and development to achieve this dissertation. I would also like to acknowledge the Conn Center for Renewable Energy Research at the University of Louisville, KY, USA, and the National Science Foundation (NSF) Awards # 1828355 and # 2025075 for supporting this research.

## ABSTRACT

### RAPID ANNEALING OF PEROVSKITE SOLAR CELL THIN FILM MATERIALS THROUGH INTENSE PULSE LIGHT

Amir Hossein Ghahremani

June 03, 2021

Perovskite solar cells (PSCs) have garnered a great attention due to their rapid efficiency improvement using cheap and solution processable materials that can be adapted for scalable high-speed automated manufacturing. Thin film perovskite photovoltaics (PVs) are typically fabricated in an inert environment, such as nitrogen glovebox, through a set of deposition and annealing steps, each playing a significant role on the power conversion efficiency (PCE), reproducibility, and stability of devices. However, atmospheric processing of PSCs would achieve lucrative commercialization. Therefore, it is necessary to utilize materials and methods that enable successful fabrication of efficient PSCs in the ambient environment. The lab scale experiments have been dominated using deposition methods, such as spin-coating or thermal evaporation in vacuum, which are not adaptable for automation; hence, taking advantage of scalable deposition methods, such as inkjet printing, is necessary for automation. Besides deposition, post process annealing is a pivotal aspect which crystallizes the thin film materials and determines the performance and stability of PSCs. Therefore, it is necessary to further investigate this step and develop new methods and utilize potential materials



that are amenable for scalable, high-throughput, and cost-effective automated manufacturing of PSCs. Conventional methods have successfully resulted in efficient lab-scale PSCs using prolonged and high temperature annealing; however, industrialization requires rapid annealing methods that allow for scalable, high-speed, and cost-effective manufacturing of efficient PSCs in the ambient environment. Intense pulse light is a rapid annealing method (IPL) that allows for the lucrative, scalable, and high throughput atmospheric processing of PSCs; thus, it is necessary to study the photothermal impact on the morphology and phase evolution of the thin film materials and develop ambient processable precursors that yield efficient perovskite modules. IPL exerts intermittent millisecond(s) duration flashes carrying energetic photons to anneal the material, and the parameters of flash energy, duration, count, and interval time between flashes determine the annealing extent and affect the PV performance of PSCs. This dissertation investigates the impact of these parameters on the morphology, phase change, and conductivity of the potential PSC thin films using various material characterization techniques of scanning electron microscopy (SEM), transmission electron microscopy (TEM), X-ray diffraction (XRD), photoluminescence (PL), impedance spectroscopy (IS), X-ray photoelectron spectroscopy (XPS), UV-Vis, as well as voltammetry, by introducing a novel additive and annealing approaches which allow for rapid fabrication of PSCs, and is applicable for rapid, cost-effective, and scalable automated fabrication of PSCs.

## TABLE OF CONTENTS

DEDICATION .....	iii
ACKNOWLEDGEMENTS .....	iv
ABSTRACT.....	v
LIST OF TABLES .....	x
LIST OF FIGURES .....	xi
CHAPTER I: INTRODUCTION.....	1
1.1. Global Energy Overview.....	1
1.2. Conventional Solar Cell Challenges .....	2
1.3. Thin Film Solar Cells and Challenges.....	3
1.4. Proposed Work.....	4
1.5. Objectives.....	6
1.6. Organization of Contents .....	7
2. CHAPTER II: BACKGROUND.....	10
2.1. Solar Irradiation Properties .....	10
2.2. Theory of Solar Cells .....	10
2.3. Progress in Photovoltaics .....	12
2.4. Perovskite.....	13
2.5. Perovskite Solar Cell (PSC).....	14
2.6. PSC Working Principle .....	15
2.7. Perovskite Materials.....	18
2.8. Electron Transport Layer .....	22
2.9. Hole Transport Layer .....	25
2.10. Contact Electrodes .....	27
2.11. Deposition Methods.....	31
2.11.1. Spin Coating.....	33

2.11.2.	Spray Coating.....	35
2.11.3.	Slot-die Coating .....	37
2.11.4.	Gravure Coating.....	38
2.11.5.	Inkjet Printing .....	39
2.12.	Crystallization.....	43
2.12.1.	Nucleation.....	44
2.12.2.	Crystal Growth.....	47
2.13.	Annealing.....	47
2.14.	Photonic Annealing .....	52
2.15.	Intense Pulse Light (IPL).....	52
2.16.	Conclusion .....	58
3.	CHAPTER III: METHODS.....	60
3.1.	Materials.....	60
3.2.	Electron Transport Layer (ETL) Fabrication .....	60
3.3.	Perovskite Film Fabrication .....	61
3.4.	Hole Transport Layer (HTL) Fabrication.....	62
3.5.	Back-contact Electrode Fabrication .....	63
3.6.	PSC Fabrication.....	63
3.7.	Temperature Measurement.....	64
3.8.	Finite Element Analysis (FEA) Modeling .....	65
3.9.	Characterization .....	67
4.	CHAPTER IV: IPL ANNEALING OF SnO <sub>2</sub> .....	69
4.1.	Introduction .....	69
4.2.	Morphology Inspections of SnO <sub>2</sub> .....	75
4.3.	Chemical State Evolution of SnO <sub>2</sub> .....	76
4.4.	Spectrophotometry of SnO <sub>2</sub> Upon Annealing .....	79
4.5.	Morphology of CH <sub>2</sub> I <sub>2</sub> -Cs <sub>0.05</sub> (MA <sub>0.85</sub> FA <sub>0.15</sub> ) <sub>0.95</sub> PbI <sub>3</sub> Perovskite Films.....	80
4.6.	Spectrophotometry of CH <sub>2</sub> I <sub>2</sub> -Cs <sub>0.05</sub> (MA <sub>0.85</sub> FA <sub>0.15</sub> ) <sub>0.95</sub> PbI <sub>3</sub> Perovskite Films.....	83
4.7.	Crystallography of CH <sub>2</sub> I <sub>2</sub> -Cs <sub>0.05</sub> (MA <sub>0.85</sub> FA <sub>0.15</sub> ) <sub>0.95</sub> PbI <sub>3</sub> Perovskite Films.....	84
4.8.	Voltammetry of Rigid CH <sub>2</sub> I <sub>2</sub> -Cs <sub>0.05</sub> (MA <sub>0.85</sub> FA <sub>0.15</sub> ) <sub>0.95</sub> PbI <sub>3</sub> Solar Cells.....	85
4.9.	Voltammetry of Flexible CH <sub>2</sub> I <sub>2</sub> -Cs <sub>0.05</sub> (MA <sub>0.85</sub> FA <sub>0.15</sub> ) <sub>0.95</sub> PbI <sub>3</sub> Solar Cells.....	88

4.10.	Conclusion .....	89
5.	CHAPTER V: IPL ANNEALING OF PEROVSKITE .....	91
5.1.	Introduction .....	91
5.2.	Nucleation of $\text{CH}_2\text{I}_2\text{-CH}_3\text{NH}_3\text{PbI}_3$ Perovskite Films Upon Annealing.....	93
5.3.	Phase Evolution of $\text{CH}_2\text{I}_2\text{-CH}_3\text{NH}_3\text{PbI}_3$ Perovskite Films Upon Annealing .....	95
5.4.	Annealing Approaches .....	97
5.5.	Morphology of Uniform Flash Annealed Perovskite Films.....	98
5.6.	Morphology of Gradient Flash Annealed Perovskite Films.....	100
5.7.	Role of Flash Delay Time on Perovskite Morphology .....	102
5.8.	Crystallography of Uniform and Gradient Flash Annealed Perovskite Films .	104
5.9.	Spectrophotometry of IPL Annealed Perovskite Films.....	108
5.10.	Voltammetry of Uniform and Gradient Flash Annealed PSCs .....	109
5.11.	IPL Temperature Measurement and Simulation.....	111
5.12.	Arrhenius plots for Uniform and Gradient Annealing.....	115
5.13.	Conclusion .....	117
6.	CHAPTER VI: AUTOMATED FABRICATION OF PSC .....	119
6.1.	Introduction .....	119
6.2.	Inkjet Printhead Mechanism.....	121
6.3.	$\text{SnO}_2$ Inkjet Deposition.....	123
6.4.	Characterization of $\text{CH}_3\text{NH}_3\text{PbI}_3$ Perovskite .....	126
6.5.	Inkjet Printing of Carbon.....	128
6.6.	Morphology Evolution of IPL Annealed Carbon Films .....	132
6.7.	Phase Evolution of IPL annealed Carbon Films .....	134
6.8.	Voltammetry of Robotic Fabricated PSCs .....	135
6.9.	Conclusion.....	136
7.	CHAPTER VII: CONCLUSION.....	139
8.	CHAPTER VIII: RECOMMENDATIONS .....	142
	REFERENCES .....	144
	APPENDIX A.....	174
	APPENDIX B .....	180
	CURRICULUM VITAE.....	193

## LIST OF TABLES

<b>Table 2.1.</b> A Summary of PSCs utilizing inorganic ETL materials. ....	25
<b>Table 2.2.</b> A Summary of PSCs utilizing inorganic HTL materials. ....	27
<b>Table 2.3.</b> A Summary of back-contact electrode materials used in PSCs. ....	31
<b>Table 4.1.</b> Core level binding energies for Sn and O1S states at different IPL conditions. .....	79
<b>Table 4.2.</b> Overall performance of PSCs with SnO <sub>2</sub> annealed through different IPL conditions (5 samples for each condition). ....	87
<b>Table 5.1.</b> Average photovoltaic parameters for five PSCs annealed through UFA and GFA methods. ....	111
<b>Table 6.1.</b> Estimated printing times for different areas of SnO <sub>2</sub> and printing speeds....	126
<b>Table 6.2.</b> Resistance and conductivity of naturally dried carbon films printed at different line distances. ....	131
<b>Table 6.3.</b> Estimated deposition times for different areas of carbon and printing speeds. .....	132
<b>Table 6.4.</b> Average photovoltaic parameters for 5 conventional and carbon PSCs. ....	136

## LIST OF FIGURES

<b>Figure 2.1.</b> Solar irradiance spectrum before and after atmospheric absorption. ....	10
<b>Figure 2.2.</b> Schematic showing the A) direct bandgap, indicating direct excitation (green arrow) of electrons to conduct electricity due to similar crystal momentum in CBM and VBM; and B) indirect bandgap, showing the excitation of electrons to conduct electricity after phonon transition (red arrow) due to momentum mismatch between CBM and VBM. ....	11
<b>Figure 2.3.</b> Schematic indicating the working principle of solar cells where the photon striking the semiconductor (1), excites the electrons (•) from VBM to CBM and leaves holes (◦) (2), which travel to the external circuit to conduct electricity (3). ....	12
<b>Figure 2.4.</b> p-n junction structure in solar cells, where the solar irradiation generates electron (•) - hole (◦) pairs that diffuse to the n and p zones to conduct electricity. ....	12
<b>Figure 2.5.</b> Schematic showing A) perovskite unit structure; B) $\text{CaTiO}_3$ crystal structure. ....	14
<b>Figure 2.6.</b> Schematic showing the working principle of PSCs, where the solar irradiation creates electron (•) - hole (◦) pairs that diffuse to the ETL and HTL, respectively, where they travel to the external circuit to conduct electricity. ....	17
<b>Figure 2.7.</b> Equivalent circuit diagram determining the output current (I) and voltage (V) of solar cells based on series ( $R_s$ ), and shunt resistance ( $R_{sh}$ ) as well as photoproduced (IL), diode (ID), and shunt (RSH) current. ....	17

<b>Figure 2.8.</b> Various deposition methods showing A) Spin; B) Spray; C) Slot-die; D) Gravure coating; and E) Inkjet printing.....	33
<b>Figure 2.9.</b> LaMer curve showing the nucleation of perovskite during spin coating. ....	46
<b>Figure 2.10.</b> Images showing A) An IPL machine; and B) Xenon filled lamps.....	53
<b>Figure 3.1.</b> Schematic showing the robotic setup used to fabricate the PSC films.....	61
<b>Figure 3.2.</b> A) Schematic; and B) Wiring diagram of the experimental setup used for temperature measurement at the film surface. ....	65
<b>Figure 3.3.</b> Schematic showing the boundary conditions used for FEA.....	67
<b>Figure 3.4.</b> Maximum absorbance of the useful energetic photons by the perovskite film during IPL annealing using UFA and GFA. ....	67
<b>Figure 4.1.</b> Top surface SEM images of A) FTO; and B) SnO <sub>2</sub> film coated on FTO showing SnO <sub>2</sub> coverage.....	76
<b>Figure 4.2.</b> A) XPS survey of the SnO <sub>2</sub> ETL annealed through 5 pulses at 2.1 kJ IPL condition; XPS patterns of B) O1s; and C) Sn states of the SnO <sub>2</sub> ETL annealed at various IPL conditions. ....	79
<b>Figure 4.3.</b> A) Tauc plot; and B) PL spectra indicating charge transfer capability at SnO <sub>2</sub> /perovskite interface at different IPL conditions. ....	80
<b>Figure 4.4.</b> Top surface SEM image of the perovskite layer A) with; and B) without CH <sub>2</sub> I <sub>2</sub> additive deposited on optimally IPL annealed SnO <sub>2</sub> films. ....	82
<b>Figure 4.5.</b> Histograms indicating the A,B) grain sizes; and C,D) grain areas of perovskite films with and without diiodomethane additive.....	83
<b>Figure 4.6.</b> Absorbance spectra of FTO/SnO <sub>2</sub> /perovskite and FTO/SnO <sub>2</sub> after optimum IPL annealing. ....	84

<b>Figure 4.7.</b> XRD pattern of the FTO/SnO <sub>2</sub> /perovskite structure demonstrating FTO/SnO <sub>2</sub> (marked with *) and perovskite (marked with •) peaks after IPL annealing. ....	85
<b>Figure 4.8.</b> J-V curves of PSCs fabricated using four different IPL conditions on SnO <sub>2</sub> .86	
<b>Figure 4.9.</b> Impedance spectra of PSCs at four different IPL conditions on SnO <sub>2</sub> . ....	88
<b>Figure 4.10.</b> Illustration of the fabricated PSCs on A) Rigid glass-FTO; and B) PET-ITO flexible substrates. C) Reverse and forward J-V curves of the champion rigid and flexible PSCs. ....	89
<b>Figure 5.1.</b> A) LaMer curve; formation of B) perovskite dendrites without antisolvent treatment; and C) perovskite intermediate upon antisolvent treatment. ....	95
<b>Figure 5.2.</b> DSC-TGA curves for 1.4 M solutions of A) CH <sub>3</sub> NH <sub>3</sub> I; B) PbI <sub>2</sub> ; and C) mixed CH <sub>3</sub> NH <sub>3</sub> PbI <sub>3</sub> perovskite in DMF-DMSO-CH <sub>2</sub> I <sub>2</sub> . ....	97
<b>Figure 5.3.</b> Schematic showing the IPL parameters for A) UFA; and B) GFA. ....	98
<b>Figure 5.4.</b> Evolution and top surface SEM images of the perovskite film A,D) upon spin-coating; after B,E) three, and C,F) five flashes through UFA; and G) 10, H) 20, and I) 30 seconds of hotplate annealing. ....	100
<b>Figure 5.5.</b> Evolution and top surface SEM images of the perovskite film A,D) upon spin-coating; after B,E) primary, and C,F) secondary annealing steps of GFA; G,H) Grain size histograms for perovskite films annealed through UFA and GFA. ....	102
<b>Figure 5.6.</b> Images indicating the quality of obtained perovskite black phase for different intervals of A,D) 100 ms – 500 ms; B,E) 100 ms – 1000 ms; and C,F) 250 ms – 500 ms during GFA. ....	104
<b>Figure 5.7.</b> XRD patterns of IPL annealed perovskite films through A) UFA; and B) GFA; C) ratio of perovskite to FTO (110) planes. ....	106



<b>Figure 5.8.</b> XRD patterns of the perovskite films annealed through different flash delay times during GFA. ....	107
<b>Figure 5.9.</b> A) UV-vis spectra; and B) PL peak of the IPL annealed perovskite films. ....	109
<b>Figure 5.10.</b> J-V curves of champion PSCs annealed through UFA and GFA.....	110
<b>Figure 5.11.</b> Experimental and numerical results demonstrating the maximum temperature rise reaching to the perovskite film for A) UFA, and B) GFA. ....	113
<b>Figure 5.12.</b> Temperature results at the surface of perovskite film annealed through GFA with different flash delay times of A) 100 ms – 500 ms; B) 100 ms – 1000 ms; and C) 250 ms – 500 ms. ....	114
<b>Figure 5.13.</b> Logarithmic plot of grain size versus IPL duration for UFA and GFA. ...	115
<b>Figure 5.14.</b> Arrhenius plots for UFA and GFA. ....	116
<b>Figure 6.1.</b> Schematic of the inkjet printhead showing the needle in A) Closed; B) Open position as controlled by the applied voltage. C) Actuation behavior of the needle for one cycle. ....	122
<b>Figure 6.2.</b> Microscope images showing the quality of printed SnO <sub>2</sub> lines at different strokes of A) 45%; B) 50%; C) 55%; and D) 60% within a constant frequency of 40 Hz, as well as E) 25; and F) 100 Hz at the constant stroke of 55%. Scale bar = 1 mm.....	124
<b>Figure 6.3.</b> Microscope images showing the morphology of printed SnO <sub>2</sub> films at A) 350; B) 525; C) 700; and D) 875 $\mu$ m line distancing. Scale bar = 1 mm. ....	125
<b>Figure 6.4.</b> A) PL peaks of the perovskite film deposited on FTO-glass and SnO <sub>2</sub> coated FTO-glass; B) XRD pattern; C) UV-Vis spectra; and D) SEM image of the processed perovskite film (Scale bar = 1 $\mu$ m). ....	128

<b>Figure 6.5.</b> Microscope images showing the quality of printed carbon lines at different strokes of A) 60%; B) 65%; and C) 70% within a constant frequency of 25 Hz, as well as D) 10; E) 40; and E) 100 Hz at the constant stroke of 65%. Scale bar = 1 mm. ....	129
<b>Figure 6.6.</b> Microscope images and profilometer spectra showing the top surface image and morphology of printed carbon films at A,E) 350; B,F) 525; C,G) 700; and D) 875 $\mu\text{m}$ line distancing. Scale bar = 1 mm. ....	131
<b>Figure 6.7.</b> Top surface SEM images showing the morphology of carbon film after A) natural drying; direct IPL annealing of thick wet film at 400 J – 500 $\mu\text{s}$ condition B) without, and C) with drying in the printing chamber; IPL annealing of dried carbon films at D) 100 J – 100 $\mu\text{s}$ ; and E) 100 J – 500 $\mu\text{s}$ condition. Scale bar = 5 $\mu\text{m}$ . ....	133
<b>Figure 6.8.</b> XRD patterns of the carbon film before and after IPL annealing. ....	135
<b>Figure 6.9.</b> J-V curves of the conventional and carbon PSCs. ....	136

# CHAPTER I

## INTRODUCTION

### **1.1. Global Energy Overview**

Rapid industrialization and the need to supply enough energy to satisfy the growth has led to the increasing consumption of energy, particularly the high energy producing resources such as gas and coal. Despite having high energy efficiency, these fuels are not renewable and generate a large quantity of noxious products such as CO<sub>2</sub>, and NO<sub>x</sub>. The release of such greenhouse gases has increased the global temperature about 1°C [1]. The world energy outlook 2019 reported steady growth of oil demand in 2018 which would rise by about 1 million barrel per day annually until 2025 [2] with the highest demand by China and US, respectively [3]. Based on the stated policies scenario, the energy demand would rise by 1% annually until 2040; hence, taking advantage of renewable energy resources would play a vital role on offsetting the great demand for the non-renewable resources to manage the global warming, alleviate the serious human and environmental health consequences, and supply the need for the growing demand. Hydro, geo, wind, and solar are promising renewable resources; however, the more abundance of solar energy as well as rapid growth in photovoltaic (PV) technology and fabrication of more efficient and cheaper modules has made it a more promising support for thermal and electrical energy demands. In 2018, the solar PV generation indicated the largest growth among all

renewables, representing a 31% increase, and is expected to account for 60% growth of the 50% renewable power capacity expansion between 2019-2024 [4]. Despite these astonishing growths, the fabricated solar modules have yet less energy efficiency and, thus, require fabrication of efficient devices using cheap materials through cost-effective manufacturing processes to make the technology more lucrative, and accessible for various industrial and residential applications.

## **1.2. Conventional Solar Cell Challenges**

Conventional PV devices consist of wafer-based semiconductors, such as monocrystalline and polycrystalline silicon, which are still the most dominating PVs to date due to being efficient and having a nominal life span around 30 years [5]. Despite these advantages, the wafer PV modules are typically made in a clean room environment using complex and expensive time-consuming processes which result in expensive modules. Recently, processing developments have increased the PCE of silicon-based PVs to over 27%, and 47% for single and multi-junction structures, respectively [6]. In addition, the indirect bandgap of silicon requires wafers with at least 100  $\mu\text{m}$  thickness to sufficiently harvest irradiation, generate charge carriers, and result in efficient modules [7]. Furthermore, the silicon PVs require rigid transparent glass shields and frames to protect the modules against any damages which makes them bulky, less convenient for shipping and handling, and expensive. Therefore, it is necessary to develop more lucrative modules utilizing cheap, abundant, and more environmentally friendly materials through cost-effective, scalable, and high throughput automated manufacturing.

### **1.3. Thin Film Solar Cells and Challenges**

Thin film solar cells were introduced after conventional silicon solar cells; hence, they are next generation photovoltaics and have undergone rapid development due to their facile and cost-effective fabrication. These PVs are fabricated by depositing micron thick films of the semiconducting material on metallic, glass, or plastic substrates, and the deposition of different layers would accomplish thin film solar cell fabrication. GaAs [8], CIGS [9, 10], and CdTe [11] are the common thin films which have been successfully fabricated and used to produce efficient solar cells. Recently, comprehensive research and development has made these photovoltaics exceed 29% [12], 23% [13], and 22% [14] in efficiency, respectively. The direct bandgap of these semiconducting composites would allow for efficient devices using thinner films, thus, less material consumption which, in turn, would enable fabricating flexible and less bulky modules. This is because the direct bandgap would allow for more charge production due to direct transition of the excited electrons from VBM to CBM. However, despite these advantages, the toxicity of materials and the costly fabrication using high energy consuming complex processes have remained challenging. For instance, despite attaining efficient GaAs solar cells, the preparation requires complex, slow, high energy consuming, and expensive methods such as vertical gradient freeze, and Bridgman-Stockbarger [15]. In addition, the carcinogenic nature of GaAs would impose environmental and human health and safety issues. Similarly, CIGS films can be produced through evaporation techniques that make the fabricated modules less lucrative. CdTe solar cells have low fabrication processing cost; however, the need for rare earth elements, the toxicity of Cd, and the need for sputtering processes are the major concerns for these PVs.

Dye sensitized solar cells (DSSC) are another type of thin film solar cells which have, so far, exceeded 13% efficiency [16] since their introduction [17]; however, instability of the liquid electrolyte undergoing contraction and expansion at different ambient environment temperatures as well as the high cost of dyes are major challenges for commercialization of DSSC. Therefore, research and development for alternative efficient thin film photovoltaics that can be fabricated from more environmentally friendly materials through simple cost-effective automation processes is necessary to make the solar PV modules more lucrative and affordable. Recently, Perovskite solar cells (PSCs) have emerged as the potential next generation thin film PVs which can be fabricated from cheap and abundant materials that are solution processable. These staggering advantages have focused the research on these rapid growing PVs towards high throughput, cost effective, and scalable automated fabrication. However, the processing has yet remained challenging which should be investigated thoroughly to achieve cheap efficient PSCs.

#### **1.4. Proposed Work**

PSCs are the most recent type of thin film PVs which has undergone intensive research and development towards commercialization. Processing of these PVs is a significant parameter determining the overall cost and performance; hence, it is necessary to investigate methods and approaches that maximize the production speed and minimize the cost and energy payback time of the fabricated modules. The processing of these solar cells spans material deposition followed by post-process annealing. Despite rapid efficiency and stability improvement, crucial parameters have impeded fabrication of these PVs entirely through automation. For instance, some of the films require an inert nitrogen environment to develop the desired morphology and phase purity which would increase the production

cost and complexity; hence, it is necessary to develop precursors that would result in superior perovskite films when fabricated in an uncontrolled humid ambient environment. PSC thin films have been mainly deposited using spin coating in an average period of 30 seconds and have also been successfully developed instantly using scalable depositions that are compatible for high-speed automated manufacturing. However, the postprocess annealing has yet remained challenging as they have been carried out using conductive and convective methods up to an hour time frame at high temperatures, up to 500°C, which are not lucrative for commercialization nor applicable for scalable flexible plastic substrates. Therefore, it is necessary to take advantage of methods that allow for instant post-processing of various PSC thin films, making them fabricable through automation such as roll-to-roll and robotic systems. In this regard, intense pulse light (IPL) has been introduced as a favorable method to rapidly anneal different PSC thin films. However, the studies have briefly spanned the impact of one or two parameters of flash duration, applied flash energy and counts, as well as the interval time between flashes on the performance of PSCs; yet an expansive study determining the photothermal interaction with the morphology and phase change of the materials with respect to all the individual IPL parameters have not been conducted. Furthermore, the back-contact electrodes used in PSCs have been developed from pure elements of gold and silver through vacuum thermal evaporation by heating the elements around their melting point. However, despite obtaining high quality films, it is not adaptable for automation and is accompanied with high energy consumption. This dissertation exhaustively studies the photothermal interaction from IPL with different thin film materials used in the electron transport layer (ETL), perovskite absorber, as well as back contact layer of PSCs. The use of carbon as the back contact film eliminates the

need for expensive organic charge transport films as well as vacuum thermal evaporation to develop back-contact electrodes. The successful IPL annealing of all the thin films establishes the pioneering work, attaining the fastest route for PSC processing, and is directly applicable for high-throughput, cost-effective, and scalable automated fabrication of PSCs.

### **1.5. Objectives**

Based on the mentioned criteria in the previous section, this dissertation will discuss the following objectives which achieve the fabrication of PSCs through scalable automated manufacturing.

- 1) Applying IPL to rapidly anneal the SnO<sub>2</sub> electron transport layer (ETL) in PSCs. This study investigates the impact of IPL annealing parameters of applied energy and flash (pulse) counts on the crystallization of SnO<sub>2</sub> and PSCs performance.
- 2) Enabling rapid fabrication of perovskite films by introducing a gradient flashing approach through IPL on CH<sub>3</sub>NH<sub>3</sub>PbI<sub>3</sub> perovskite films, eliminating the need for any short-term or long-term conductive or convective annealing. This study investigates the impact of all the individual IPL parameters of applied energy per flash, flash duration, count, and interval time between flashes on the extent of morphology and phase evolution of CH<sub>3</sub>NH<sub>3</sub>PbI<sub>3</sub> perovskite films.
- 3) Developing PSC films using an inkjet printing system followed by IPL annealing through an integrated robotic setup. This study investigates replacing the expensive organic Spiro-MeOTAD hole transport layer and vacuum thermal evaporated gold (Au) back-contact with carbon.



## 1.6. Organization of Contents

Chapter 1 provides an overview of energy consumption and explains the significance of research and development for renewable energy resources, particularly solar. This chapter introduces the conventional and thin film solar cells and explains the associated challenges to each type. The requirements for thicker films in silicon solar cells as well as the associated high cost and high energy consumption to fabricate these necessitates development of thin film photovoltaics (PVs), such as perovskite solar cells (PSCs). However, challenges, such as prolonged high temperature annealing of the thin film materials, are a hurdle for upscaling of these PVs. This chapter introduces the proposed work and objectives to be studied throughout this dissertation to address the issue.

Chapter 2 introduces the theory of solar cells, describes the perovskite material and its structure in a solar cell, and introduces utilized materials enabling the development of solution derived perovskite solar cells (PSCs). Various deposition techniques of spin, slot-die, spray, and inkjet printing are introduced with documented achievements yielding high performance PSCs. The chapter introduces annealing as the most important post-deposition process for PSC fabrication, and various annealing methods from conduction and radiation are reviewed. Finally, this chapter introduces radiative annealing through intense pulse light (IPL), allowing for rapid cost-effective processing of PSCs thin films, and will be investigated exhaustively throughout this dissertation. The discussion of the IPL includes the modelling equations for establishing the thermal response of the perovskite films.

Chapter 3 explains the utilized materials, fabrication, and characterization of processed thin films in PSCs. This chapter also describes the temperature measurement setup to measure the photothermal impact from IPL on perovskite films and explains the finite

element analysis (FEA) simulation procedure to verify the measured temperatures using ANSYS.

Chapter 4 investigates the role of IPL on the annealing of SnO<sub>2</sub> ETL and perovskite films. Successful IPL annealing of SnO<sub>2</sub> paves a promising pathway towards eliminating the conventional expensive and energy consuming TiO<sub>2</sub> and takes a step towards faster fabrication of PSCs. In this work, CH<sub>2</sub>I<sub>2</sub> is introduced into a mixed triple cation perovskite precursor, allowing the fabrication of perovskite films in a humid ambient environment (>60%). The SnO<sub>2</sub> ETL is directly annealed through IPL; however, the mixed triple cation perovskite precursor is annealed through IPL after a short-term conductive pre-annealing. This study introduces a faster route of fabricating PSCs in the ambient environment; hence, putting a further step towards achieving rapid and cost-effective atmospheric fabrication of PSCs with compatibility for automated manufacturing.

Chapter 5 investigates the crystallization kinetics of CH<sub>3</sub>NH<sub>3</sub>PbI<sub>3</sub> perovskite films by directly annealing the perovskite films through IPL without intermediate short-term conductive annealing. In this work, a gradient flash annealing (GFA) approach is developed which anneals the entire PSC films in about 10 seconds. The maximum surface temperature rise at the perovskite film during IPL annealing is measured and a finite element analysis (FEA) modeling is developed to verify the measurements and aid determining the impact of IPL annealing parameters of flash count, duration, energy, and interval time between flashes on the crystallization kinetics of perovskite film. This study establishes the pioneering work where the rapid fabrication of PSCs entirely through IPL is introduced and is applicable for swift atmospheric processing of PSCs through automation.

Chapter 6 details how the charge transport films are processed using an integrated robotic setup utilizing an inkjet printhead and IPL for annealing. This chapter utilizes and processes the SnO<sub>2</sub> ETL as introduced in chapter four; however, carbon film serving as both the hole transport and metal back-contact films is utilized as the back-contact in PSCs. This study particularly spans deposition optimization of the charge transport films and investigates the phase purity, morphology, and conductivity of IPL annealed carbon films on the performance of PSCs which exemplifies automated fabrication of PSCs in an uncontrolled ambient environment using a non-roll-to-roll setup.

Chapter 7 is a conclusion and Chapter 8 details recommendations for further work aligned with this study.

## CHAPTER II

### BACKGROUND

#### 2.1. Solar Irradiation Properties

The PV technology spans the development of solar cells which constitute solar modules that produce electricity upon harvesting the sun light; hence, understanding the properties of sun light and the kinetics of photo absorption-power generation are the key parameters in fabricating functional and efficient PVs. The sun is a profound source of energy that emits light and heat, and the spectrum spans electromagnetic irradiation consisted of ultraviolet (UV), visible, and infrared (IR) light and is close to a black body [18] as shown in Fig. 2.1. Despite atmospheric absorption, the visible spectrum between 400-700 nm constitutes the largest irradiation with the maximum around 500 nm. Therefore, the fabricated solar cells should utilize materials that can harvest the irradiation at this range.

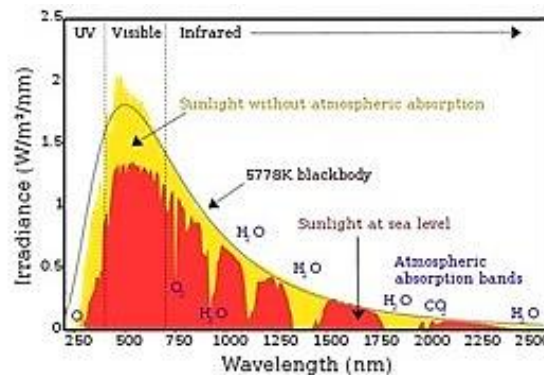


**Figure 2.1.** Solar irradiance spectrum before and after atmospheric absorption.

## 2.2. Theory of Solar Cells

As mentioned, PV cells are empowered by exposure to light. Therefore, the performance of all solar PV devices is depended on irradiation and the target material utilizing the irradiation. PV devices utilize a light harvesting semiconductor or a composite of semiconducting materials which harvest the light and generate charge carriers upon irradiation. The extent of charge carrier production is highly dependent on the photo absorptivity and bandgap energy of material which should fall below the irradiation energy. The bandgap properties of a semiconductor are, perhaps, the most significant parameters affecting the functionality of a solar cell. Semiconductors have generally two types of direct and indirect bandgaps. As shown in Fig. 2.2(A), direct bandgap semiconductors enable better conduction of electrons due to the similar crystal momentum of the electrons and holes in the conduction and valence bands, respectively, whereas the semiconductors with indirect bandgap (Fig. 2.2(B)) should undergo an intermediate state of crystal momentum change. Therefore, the semiconductor properties such as bandgap, valence band maximum (VBM) and conduction band minimum (CBM) energies determine the charge carrier flow and solar cell PV performance. The working principle of a solar cell is shown in Fig. 2.3 where the absorbed irradiation excites the electrons (1) and make them conductive by exciting them through the bandgap (2) with fixed valence and conduction energies. The excited electrons leave holes behind upon conduction, flow to the external circuit (3), generate power, and finally recombine with them upon returning to the cell; hence, irradiation and properties of the semiconducting materials determine the performance of PV cells. As shown in Fig. 2.4, practical solar cells are made as p-n junction devices consisted of two separate zones, each doped with materials that induce higher

mobility of negative (n) and positive (p) charges to attain higher performance solar cells upon irradiation. Solar cells can also be made of different semiconducting materials to form a multi-junction structure consisted of several p-n junctions, each harvesting different spectrum of light [19], thus resulting in better PV performance, and the parallel or series connection of multiple cells would produce a module with desired voltage and current. The sun irradiation reaching the earth's surface has a limited intensity and lasts for a couple of hours throughout the day; hence, it is necessary to develop semiconducting composites that enable maximum photo-absorption and power generation.

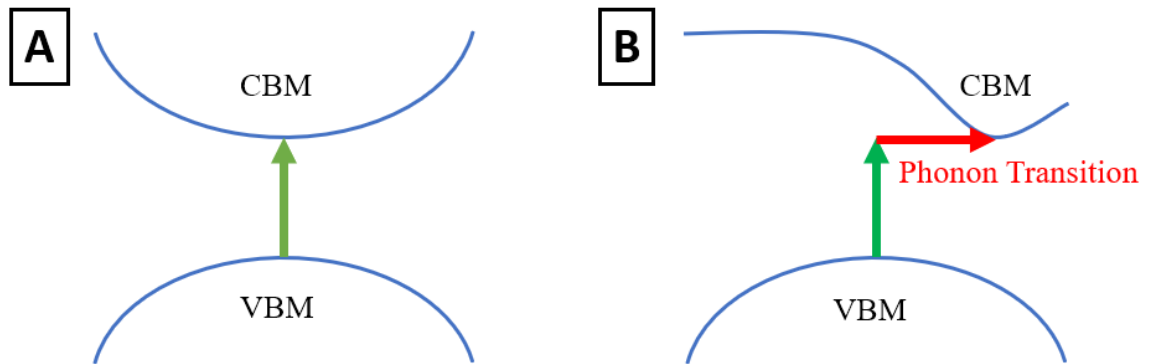


**Figure 2.2.** Schematic showing the A) direct bandgap, indicating direct excitation (green arrow) of electrons to conduct electricity due to similar crystal momentum in CBM and VBM; and B) indirect bandgap, showing the excitation of electrons to conduct electricity after phonon transition (red arrow) due to momentum mismatch between CBM and VBM.

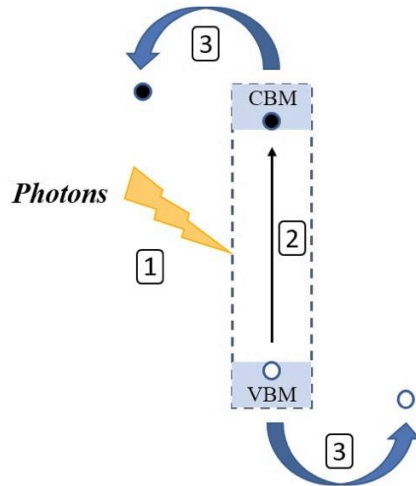


**Figure 2.3.** Schematic indicating the working principle of solar cells where the photon striking the semiconductor (1), excites the electrons (•) from VBM to CBM and leaves holes (◦) (2), which travel to the external circuit to conduct electricity (3).

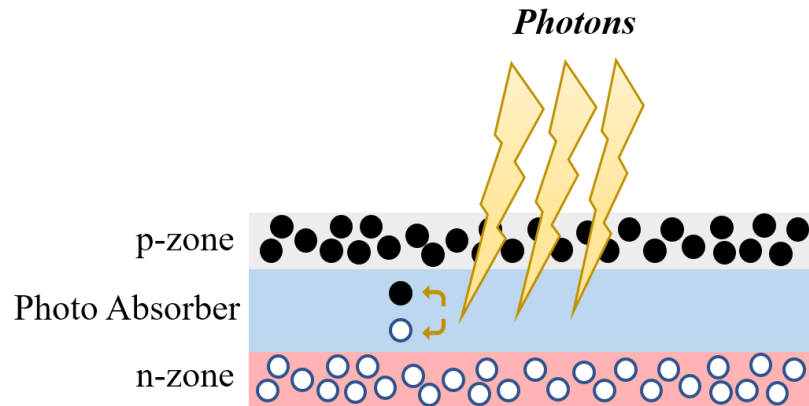


**Figure 2.4.** p-n junction structure in solar cells, where the solar irradiation generates electron (•) - hole (◦) pairs that diffuse to the n and p zones to conduct electricity.

### 2.3. Progress in Photovoltaics

The history of PV devices goes back to the 18<sup>th</sup> century when Alexander Edmond Becquerel observed the PV effect by exposing AgCl and AgBr electrodes placed in a conductive acidic solution to light [20, 21]. A few decades after the observation of PV

effect in Selenium [22], Charles Fritts fabricated the first solar cell with 1% efficiency using selenium on a thin layer of gold [23]. In 1904, Wilhelm Hallwachs fabricated semiconductor junction solar cells utilizing Cu and  $\text{Cu}_2\text{O}$  [24]. In 1932, Audobert and Stora discovered the PV effect in CdSe [25]. Bell Labs invented the first practical silicon solar cell with almost 6% efficiency in early 1954 [26], and further technical advances, such as surface passivation through thermal oxidation, enhanced the efficiency of solar cells [27]. In 1970, the first heterojunction GaAs solar cells were fabricated in USSR [28]. Two years later, Bonnet and Rabenhorst fabricated 6% efficient heterojunction CdTe-CdS solar cells which resulted in the introduction of the first CdTe solar cells [29]. The invention of photoelectrochemical dye sensitized solar cells (DSSC) utilizing organic dyes in 1988 [17] opened a new realm in fabricating cheaper solar cells compared to silicon PVs, and further development using copper complexes increased their efficiency to over 13% in 2018 [16]. Thereafter, extensive research has paved the pathway towards higher performance PVs, such as perovskite solar cells (PSCs), utilizing cheap and abundant materials which can be processed through scalable, high throughput, and cost-effective automated manufacturing and has been the focus of PV research over the past few years.

#### **2.4. Perovskite**

In 1839,  $\text{CaTiO}_3$  was found in the Ural Mountains of Russia [30]. This mineral has the  $\text{ABX}_3$  atomic formulation and is known as the perovskite structure as shown in Fig. 2.5, where B and A represent the  $\text{Ti}^{2+}$  and  $\text{Ca}^+$  cations with different ionic radius surrounded by an octahedral of 6-fold and cubo-octahedral of 12-fold oxygen atoms, respectively. Perovskites possess unique properties such as superconductivity [31], ferroelectricity [32], charge ordering, and colossal magnetoresistance [33]. These favorable characteristics have



enabled a broad application of perovskites, particularly for electronics such as light emitting diodes [34], transistors [35], scintillators [36], lasers [37], and PVs. Among these, successful application of perovskites to produce cheap and efficient PVs has resulted in the introduction of PSCs which have opened a new realm in next generation PVs and have been the focus of PVs research over the past few years.

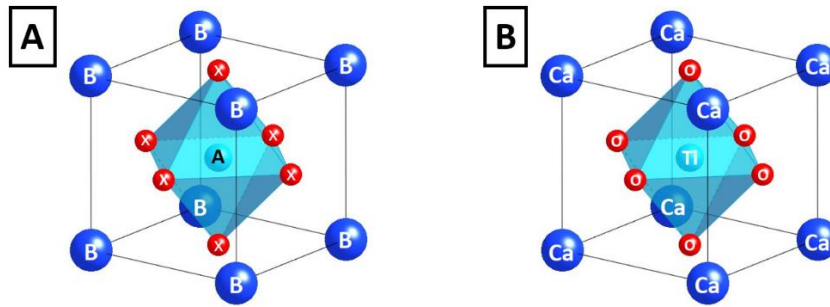


**Figure 2.5.** Schematic showing A) perovskite unit structure; B)  $\text{CaTiO}_3$  crystal structure.

## 2.5. Perovskite Solar Cell (PSC)

Perovskite solar cells (PSCs) are thin film PVs that utilize a light absorbing film capable of producing charge carriers upon illumination. The light harvesting film has the  $\text{ABX}_3$  perovskite structure, where, A is the inorganic compound, typically methylammonium ( $\text{MA}=\text{CH}_3\text{NH}_3^+$ ), formamidinium ( $\text{FA}=\text{CH}_3(\text{NH}_2)_2^+$ ) [38], as well as cesium ( $\text{Cs}^+$ ) [39, 40], and rubidium ( $\text{Rb}^+$ ) [41]; B is the divalent metal cation such as  $\text{Pb}^{2+}$ ,  $\text{Sn}^{2+}$  [42-44], and  $\text{Ge}^{2+}$  [45]; and X is  $\text{Cl}^-$  [46, 47],  $\text{Br}^-$  [48], and  $\text{I}^-$  [49] halides or mixture thereof, as well as non-halide compounds such as acetates (Ac) [50]. Therefore, perovskite films can be made from a variety of cheap and abundant organic and inorganic compounds which would allow bandgap tuning [51] and enable unique properties such as broad photo absorption range between ultraviolet (UV) to infrared (IR) [52], high charge mobility [53], long carrier diffusion length [54], exciton low binding energy [55], acute optical band edge

[56], and bipolar semi-conductivity [57]. In addition, unlike the common silicon PVs which require complex and expensive fabrication methods in a clean room environment, the mentioned potential materials are cheap, abundant, and solution processable and can be processed using simple and cost-effective fabrication processes. The use of cheap abundant materials would make the PSCs more lucrative and affordable, whereas solution processability would allow for the modules to be made through cost-effective automated manufacturing, such as roll to roll and robotic systems; hence, they enable minimization of the cost and energy payback time of PSCs. These exclusive properties have opened a broad realm for research and development towards making more efficient and stable PSCs, resulting in dramatic power conversion efficiency (PCE) improvement from 3.8% [58] to over 25% [6], rivaling the conventional silicon PVs. Despite these favorable advantages, PSCs yet undergo power decay as the result of material degradation by heat [59, 60], moisture [61, 62], and light soaking [63, 64], which requires special fabrication environments, such a nitrogen glovebox, and proper encapsulation of the fabricated modules to prolong the stability of PSCs [65, 66]. In addition, processes such as prolong high temperature annealing has yet remained challenging. Therefore, lucrative manufacturing requires further research and development towards rapid, cost-effective, and scalable atmospheric processing to achieve stable efficient PSCs.

## **2.6. PSC Working Principle**

As stated earlier, solar cells are made as p-n junction devices, where the semiconducting material, typically Si, is heavily doped with n-type and p-type materials to produce efficient modules. The next generation thin film PSCs have a simple structure which resembles to that of conventional p-n junction PVs. However, instead of doping, the

direct bandgap perovskite film (i), serving the role of indirect bandgap Si, is sandwiched between an n-type (n) electron transport layer (ETL) and a p-type (p) hole transport layer (HTL), and the location of charge transport layers can be swapped to form the inverted p-i-n or the regular n-i-p structures [67]. PSCs have the similar working principle to other PVs. As mentioned, the solar irradiation reaching the earth surface resembles to that of a black body at almost 5800K. These photons have a greater energy than the perovskite bandgap of about 1.6 eV which allows them to be sufficiently absorbed by this film. Based on the working principle of a conventional p-n junction solar cell, as shown in Fig. 2.6, the absorbed solar irradiation by the perovskite film excites the electrons, exciting them through the bandgap. The moving of electrons in this stage causes current generation through the drift of electrons, which pushes the electrons towards the ETL and the holes towards the HTL, as well as the charge carrier concentration induced diffusion which diffuses the electrons through the perovskite and charge transport films and shuttles them to the external circuit via contact electrodes. However, the charge carriers face series and shunt resistances which impede maximum charge transport throughout the cell and affect the PV parameters of PSCs such as the open circuit voltage ( $V_{OC}$ ), short circuit current ( $J_{SC}$ ), efficiency, and fill factor (FF). These parameters can be determined by the equivalent circuit of solar cells consisted of a solar cell placed parallel to a diode which reflects one direction charge transfer behavior of a solar cell, a series resistance ( $R_S$ ), and a shunt resistance ( $R_{SH}$ ) as shown in Fig. 2.7, all which affect the output current (I) and voltage (V) of solar cell as indicated in Eqn. 2.1 and 2.2, respectively.

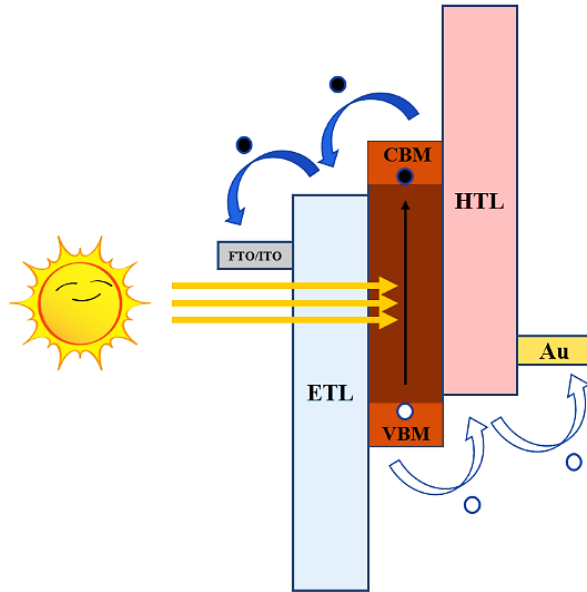


**Figure 2.6.** Schematic showing the working principle of PSCs, where the solar irradiation creates electron (•) - hole (◦) pairs that diffuse to the ETL and HTL, respectively, where they travel to the external circuit to conduct electricity.

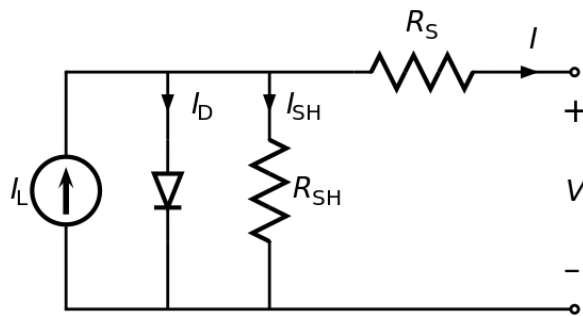


**Figure 2.7.** Equivalent circuit diagram determining the output current (I) and voltage (V) of solar cells based on series ( $R_s$ ), and shunt resistance ( $R_{sh}$ ) as well as photoproduced ( $I_L$ ), diode ( $I_D$ ), and shunt ( $R_{SH}$ ) current.

$$I = I_L - I_0 \left[ e^{\left(\frac{V'}{nV_T}\right)} - 1 \right] - \frac{V'}{R_{SH}} \quad (2.1)$$

In Eqn. 2.1,  $I_L$  is the photoproduced current by solar cell,  $I_0$  is the reverse saturation current,  $n=1$  is the ideality factor,  $V_{T \approx 25^\circ\text{C}} = 0.0259$  Volt is the thermal voltage, and  $V'$  is the voltage across both the diode and shunt resistor and can be expressed as:

$$V' = V + IR_S \quad (2.2)$$

Eqn. 2.1 indicates that the series and shunt resistances impact the generated current by PSCs and minimizing the series resistance and maximizing the shunt resistance maximize the generated current and voltage and, in turn, the PSC performance. These impedances are dependent on the chemistry of materials used for each layer as well as the processing of individual films. The former includes precursor development from potential materials that are cheap and solution processable, whereas the latter spans precursor deposition followed by post-process annealing. These parameters affect the morphology and crystallinity of individual films; hence, determine the performance and stability of PSCs. In this regard, it is important to understand the science behind engineering associated to the processing of PSCs. The deposition and post process annealing are discussed in the following sections of this chapter and novel approaches will be utilized and exhaustively studied in the other chapters of this dissertation.

## **2.7. Perovskite Materials**

The incorporation of organics into the perovskite structure was initially introduced in 1987 when Poglitsch and Weber replaced the cesium with MA in the cesium lead halide perovskites [68]. Later in 2009, metal cations of  $\text{PbBr}_2$  and  $\text{PbI}_2$  along with the ammonium halide salts of MABr and MAI were used to synthesize two different single cation perovskite chemistries of  $\text{MAPbBr}_3$  and  $\text{MAPbI}_3$  which resulted in the introduction of first

PSCs with 3.13% and 3.81% efficiency, respectively [58]. Later, extensive research unraveled higher performance PSCs utilizing materials such as Br<sup>-</sup> which improved the stability [69, 70] as well as Cl<sup>-</sup> which improved the charge carrier diffusion length, morphology, and crystallinity of the perovskite films and enhanced the PV performance of PSCs [71]. For instance, Jeon et. al [72] fabricated efficient MAPb(I<sub>1-x</sub>Br<sub>x</sub>)<sub>3</sub> solar cells surpassing 16% efficiency and reported enhanced atmospheric stability of the devices containing bromine. Colella et. al [73] investigated the role of Cl<sup>-</sup> by fabricating PSCs utilizing PbCl<sub>2</sub>, PbI<sub>2</sub>, MACl, and MAI, and their PSCs exhibited more than 16% efficiency using the chemistry obtained from PbCl<sub>2</sub> and MAI compounds compared to the more than 11% efficiency devices fabricated from PbI<sub>2</sub> and MACl compounds. They attributed the enhancement to the difference between ionic radii of the two perovskite chemistries. Yang et. al [74] investigated different quantities of MACl, in which, lower or higher concentrations of MACl affected the morphology, optoelectronic, and PV performance of MAPbI<sub>3</sub> solar cells. They reported an average PV performance of 16.77% for 30% of the additive and attributed the improvement to the enhanced crystallinity of perovskite films by the optimal quantity of additive. Besides the halogen section, other organic compounds have also been investigated in PSCs. For instance, FAPbI<sub>3</sub> and FAPbBr<sub>3</sub> [75, 76] perovskites have been introduced by replacing MA<sup>+</sup> with the FA<sup>+</sup>. Recently, FAPbI<sub>3</sub> based PSCs have exceeded 21% efficiency [77] which is credited to the development of more complex chemistries, achieving higher PV performance. For instance, Yang et. al [78] developed a double cation MA<sub>x</sub>FA<sub>(1-x)</sub>Pb(I<sub>y</sub>Br<sub>1-y</sub>)<sub>3</sub> chemistry containing different quantities of MA<sup>+</sup> (x=0-1) and FA<sup>+</sup> (y=0-0.2) cations. Their results indicated over 17% efficiency for MA<sub>0.7</sub>FA<sub>0.3</sub>Pb(I<sub>0.9</sub>Br<sub>0.1</sub>)<sub>3</sub> devices, where the substitution of 30% MA<sup>+</sup> ions with FA<sup>+</sup> ions

in MAPbI<sub>3</sub> improved the crystallinity, absorption, and carrier lifetime of the perovskite film, and other stoichiometries decreased the PV performance as the result of increased bandgap, affecting the charge extraction and transport. Recently, triple cation perovskites incorporating Cs<sup>+</sup> and Ru<sup>+</sup> cations into the perovskite chemistries containing MA<sup>+</sup>, and FA<sup>+</sup> have further resulted in more efficient and stable PSCs. For instance, Saliba et al. [79] fabricated PSCs from Cs<sub>x</sub>(MA<sub>0.17</sub>FA<sub>0.83</sub>)<sub>(100-x)</sub>Pb(I<sub>0.83</sub>Br<sub>0.17</sub>)<sub>3</sub> perovskite chemistry and indicated that the substitution of 5% MA<sup>+</sup> and FA<sup>+</sup> with Cs<sup>+</sup> cations increased the thermal and ambient environment stability of devices and increased the efficiency of PSCs from 16% to over 20%. In another study, Rb<sup>+</sup> has been investigated in PSCs. For instance, Zhang et. al [80] incorporated 5% Rb<sup>+</sup> in FAPbI<sub>3</sub> and FA<sub>x</sub>Rb<sub>(1-x)</sub>PbI<sub>3</sub> perovskite films. Their results indicated that unlike Cs, the Ru based films did not convert to perovskite black unless at elevated temperatures as high as 150°C. However, Rb<sub>0.05</sub>FA<sub>0.95</sub>PbI<sub>3</sub> perovskites with 5% Ru incorporation indicated 16.2% efficiency and kept over 90% of their initial efficiency after 4 weeks. Similarly, FA<sub>0.80</sub>MA<sub>0.15</sub>Cs<sub>0.05</sub>PbI<sub>2.55</sub>Br<sub>0.45</sub> and FA<sub>0.80</sub>MA<sub>0.15</sub>Rb<sub>0.05</sub>PbI<sub>2.55</sub>Br<sub>0.45</sub> chemistries incorporating 5% Cs<sup>+</sup> and Ru<sup>+</sup> exhibited 19.4% and 19.6% efficiency, respectively, whereas the (FAPbI<sub>3</sub>)<sub>0.85</sub>(MAPbBr<sub>3</sub>)<sub>0.15</sub> chemistry showed 17.1% efficiency which was attributed to better optical and electrical properties of the triple cation perovskite chemistries.

The mentioned studies introduced perovskite composite development to achieve PSCs with higher PV performance and enhanced moisture and thermal stability. However, the developed perovskite chemistries should be solution processable to allow for the industrialization of PSCs using scalable and high-speed automated manufacturing. Therefore, it is necessary to dissolve the perovskite chemistries into potential solvents that

yield thin films with superior morphology and optoelectronic properties. N,N-dimethylformamide (DMF), dimethyl sulfoxide (DMSO), and  $\gamma$ -butyrolactone (GBL), N-methyl-2-pyrrolidone (NMP), and dimethylacetamide (DMAC) are the common polar aprotic solvents used for the dissolution of lead and ammonium halides, and a mixture of these has shown to produce more efficient PSCs [81, 82]. For instance, the sole application of DMF has resulted in less PV performance as the result of poor morphology and optoelectronic performance caused by the rapid solvent evaporation, whereas a mixture of DMSO:DMF has resulted in high performance PSCs exceeding 19% which was attributed to the adduct of  $\text{PbI}_2$ -DMSO [83] and the formation of superior perovskite black morphology caused by the retarded crystallization as the result of increased boiling point of the mixed solvent [84]. Similarly, unlike GBL-DMSO mixture which produced better morphology and efficient PSCs [81], the sole use of GBL produced less efficient PSCs as the result of inadequate crystallization caused by the  $\text{PbI}_2$ -solvent coordination and solubility difference between the metal halides and ammonium salts [83, 85]. Therefore, solvent engineering plays a significant factor on the crystallization and performance of PSCs. The polar solvents, particularly DMF:DMSO mixture, have been widely used to fabricate efficient PSCs. However, DMF and NMP are carcinogenic; hence, are not favorable for upscaling purposes. PSC industrialization requires cheap and more environment friendly solvents that can produce efficient and stable cells in the shortest period. In this regard, substitution of a large portion of the common polar solvents with non-toxic solvents, such as acids and alcohols, have put a further step towards more environmentally friendly PSCs. For instance, PSCs with 13.5%, and 12% have been successfully fabricated using 60:20:20 V% GBL:ethanol:acetic acid and GBL:1-



propanol:acetic acid, respectively [86]. Ramadan et. al [87] reported efficient PSCs using acetonitrile and its mixture with methylamine and achieved over 18.5% efficiency compared to only 8% using DMF. In addition, Hendriks et. al [88] dissolved the  $\text{CH}_3\text{NH}_3\text{PbI}_3$  perovskite chemistry in 2-Methoxyethanol (2-ME) solvent and reported improved power conversion efficiency (PCE) of PSCs to 15.3% from 14.1% for DMF based devices.

Besides the significance of solute and solvent engineering, additives incorporated into the perovskite precursors have shown to considerably boost the perovskite crystallinity and morphology, resulting in higher PCE. For instance, Yang et al. [89] reported 30% and 58% performance improvement, exhibiting 12.2% and 14.8% average efficiency for PSCs utilizing 2.5 V% HI and HCl additives into the  $\text{CH}_3\text{NH}_3\text{PbI}_3$  perovskite chemistry. Wu et al. [90] investigated the role of NaAc and  $\text{NH}_4\text{Ac}$  additives on PSCs performance. Upon processing, the films without additive indicated a discontinuous morphology with pinhole defects. Unlike NaAc based PSCs which resulted in PCE of 13.78%, 10 wt% incorporation of  $\text{NH}_4\text{Ac}$  exhibited 17.02% efficiency which was attributed to the smoother morphology and enhanced crystallization. The use of Ac based additive eliminated the pinhole defects which was attributed to the possible formation of the intermediate methylamine acetate salt, providing higher nucleation density, thus, large quantity of small crystals as the result of lower decomposition temperature of the salt. Other similar works have also reported enhanced PSC performance as the result of morphology enhancement utilizing other potential additives such as MAAc and a molecular additive of thiosemicarbazone [91], and various alkyl halides [92, 93].

## **2.8. Electron Transport Layer**

Electron transport layer (ETL) has the similar functionality to n-doped zone in conventional solar cells. However, instead of inclusion into the light harvesting semiconductor, PSCs utilize a thin film consisted of a potential electron transporting material coated underneath (n-i-p structure) or above (p-i-n structure) the perovskite photo-absorber. Similar to perovskites, the ETL materials should be solution processable using perovskite friendly solvents that enable scalable deposition using potential automated methods and achieve long-term device stability, provide suitable band alignment with the perovskite layer to facilitate electron extraction, have high electron mobility to enable maximum charge extraction from the perovskite film, and have good structural stability for long-term durability of PSCs. ETLs have been successfully fabricated using both organic and inorganic complexes. Phenyl-C61-butyric acid methyl ester (PCBM) is the most potential organic material used for both regular and inverted PSCs [94, 95]. However, the high cost of the material and requiring an inert deposition environment, such as nitrogen glovebox, would make this material unfavorable for commercialization of PSCs. In this regard, metal oxides were successfully developed to fabricate efficient PSCs.  $\text{TiO}_2$  is the pioneering material and has been successfully used to fabricate efficient PSCs through two different structures of compact and mesoporous. PSCs fabricated using the former  $\text{TiO}_2$  ETL utilize a mixture of Titanium di-isopropoxide bis (acetylacetonate) and 1-butanol, whereas the latter can be obtained from a  $\text{TiO}_2$  paste diluted in ethanol and deposited on the compact  $\text{TiO}_2$  ETL to yield higher PCE as the result of more interfacial area, aiding better charge extraction at the  $\text{TiO}_2$ /perovskite interface [96]. Despite achieving efficient PSCs using  $\text{TiO}_2$ , it is not favorable for upscale manufacturing of PSCs due to the current-voltage hysteresis caused by the inefficient  $\text{TiO}_2$ /perovskite interface [97] as well as its

structural instability under UV illumination [98]. In addition, the mesoporous TiO<sub>2</sub> films require a specific coating method, particularly spin coating, to obtain the desired mesoporous structure and may not be obtained through scalable deposition methods. Furthermore, the material requires prolong and high temperature post-processing, such as 30 minutes to an hour period annealing in a furnace set to 500°C, which is not lucrative nor applicable for favorable plastic substrates for industrial scale manufacturing. Therefore, other metal oxides such as ZnO [99, 100], Al<sub>2</sub>O<sub>3</sub> [101, 102], WO<sub>3</sub> [103, 104], and CeO<sub>2</sub> [105, 106] have been successfully utilized to fabricate PSCs. However, the structural instability, lower electron mobility, and unsuitable band alignment of these compounds to the perovskite film has impeded producing efficient PSCs.

Recently, SnO<sub>2</sub> has been introduced as a potential replacement to TiO<sub>2</sub>, allowing for cost-effective and scalable manufacturing of PSCs. This metal oxide has a higher electron mobility and stability compared to TiO<sub>2</sub> [107] and possesses a wider bandgap of 3.7 eV compared to 3.2 eV for TiO<sub>2</sub>. In addition, the better VBM and CBM energy alignment with the perovskite film has improved charge extraction at the SnO<sub>2</sub>/perovskite interface [108] and enabled high efficiency PSCs exceeding 20% [109, 110]. Recently, doping with various elements such as Ta<sup>5+</sup> [111], Mo<sup>5+</sup> [112], Li<sup>+</sup> [113], Sb<sup>3+</sup> [114], as well as La<sup>3+</sup>, Sc<sup>3+</sup>, and Y<sup>3+</sup> [115] have shown to increase the conductivity of SnO<sub>2</sub> films by altering the Fermi energy position and providing better band energy alignment to the perovskite film. SnO<sub>2</sub> films can be fabricated from aqueous solutions containing the colloidal dispersion of the material [116, 117] as well as the dissolution of other Sn based compounds, such as SnCl<sub>2</sub>, in water or alcohols followed by short-term medium temperature annealing to obtain the desired SnO<sub>2</sub> phase [118, 119]; hence, the metal dopants can be added to the SnO<sub>2</sub>

precursor using soluble halogenated compounds of the elements. Therefore, it is necessary to further investigate SnO<sub>2</sub> towards successful commercialization using cost-effective and scalable processes that are amenable for high-throughput automated manufacturing. A brief performance summary of the utilized metal oxide ETL materials is provided in Table 2.1.

**Table 2.1.** A Summary of PSCs utilizing inorganic ETL materials.

Reference	ETL	V <sub>oc</sub> (V)	J <sub>sc</sub> (mA/cm <sup>2</sup> )	PCE (%)	FF (%)
[96]	TiO <sub>2</sub>	1.06	22.03	17.51	75.00
[99]	NH <sub>4</sub> Cl:ZnO	1.27	11.52	10.16	69.17
[100]	ZnO	1.09	22.86	18.31	73.52
[101]	Al <sub>2</sub> O <sub>3</sub>	0.92	21.56	12.79	64.00
[102]	Al <sub>2</sub> O <sub>3</sub>	1.03	20.92	13.07	62.00
[103]	TiO <sub>2</sub> :WO <sub>3</sub>	1.09	23.54	20.14	78.55
[104]	WO <sub>3</sub>	0.87	18.00	10.30	65.00
[105]	CeO <sub>2</sub>	1.036	21.44	13.77	61.92
[106]	CeO <sub>2</sub>	1.045	19.90	16.10	76.00
[109]	SnO <sub>2</sub>	1.125	23.26	20.39	77.92
[111]	Ta:SnO <sub>2</sub>	1.16	22.79	20.80	78.60
[112]	Mo:SnO <sub>2</sub>	0.972	15.20	10.52	71.10
[113]	Li:SnO <sub>2</sub>	0.76	22.18	10.01	59.00
[115]	La:SnO <sub>2</sub>	1.111	23.21	19.49	75.57
[115]	Sc:SnO <sub>2</sub>	1.116	23.36	20.03	76.80
[115]	Y:SnO <sub>2</sub>	1.117	23.61	20.63	78.16

## 2.9. Hole Transport Layer

Hole transport layer is another significant layer in PSCs with the same functionality to the P-doped region in conventional Si solar cells. Similar to ETL, the HTL can be fabricated using potential organic or inorganic complexes that enable high hole mobility and result in efficient PSCs through adequate band energy positioning to the perovskite film [120]. Successful commercialization of PSCs requires the HTL to be deposited from

solution-based precursors utilizing perovskite friendly solvents that allow for highly stable PSCs, and the ambient processing of these materials are favorable for upscaling to minimize the complexity and additional costs associated with providing an inert environment, such as nitrogen. However, unlike ETL, the HTL in PSCs have been dominated using expensive complex polymers such as Spiro-MeOTAD, PEDOT:PSS, PTAA, and P3HT, which require deposition in an inert nitrogen environment. Spiro-MeOTAD is the most common polymer used for PSC research and development which has produced the most efficient devices to date. However, this material requires other additives such as 4-tert butyl pyridine,  $\text{Li}^+$ , and  $\text{Co}^{3+}$  dopants to increase the hole conductivity. PEDOT:PSS has also resulted in efficient PSCs; however, its acidic nature would affect the stability of PSCs [121, 122]. Similar to other mentioned thin films in PSCs, commercialization requires successful application of abundant and cheap materials and processes that allow for efficient and stable PSCs. In this regard, CuO [123],  $\text{Cu}_2\text{O}$  [123, 124], CuI [125-127], CuSCN [128, 129], and NiO [130-133] have been introduced as potential alternatives to polymer materials. CuO has a narrow bandgap of 1.4 eV which provides less ideal band energy alignment with the perovskite layer and, in turn, less conductivity. CuI has produced relatively efficient solar cells; however, the material is solution processable using  $\text{NH}_4\text{OH}$  and propyl sulfide solvents that would degrade the perovskite film, hence affect the performance and stability of PSCs [134]. In addition, despite low temperature processability and obtaining efficient devices as the result of high hole mobility of CuSCN falling between  $0.01\text{-}0.1 \text{ cm}^2\cdot\text{V}^{-1}\cdot\text{s}^{-1}$  [135-137], its toxicity would make it unfavorable for commercialization of PSCs. NiO has a wide bandgap around 5.4 eV and is the preferred material due to its high hole mobility, suitable energy alignment to

the perovskite film, and allowing for higher stability PSCs than polymer hole transport materials. However, besides the toxicity of Ni, NiO is not solution processable and can be obtained from other compounds, such as aqueous derivatives of nitrate and acetate complexes of nickel followed by a prolong annealing, up to an hour, at temperatures as high as 500°C [138, 139]. Recently, the use of solution combustion and near IR (NIR) radiative annealing methods have decreased the annealing temperature to 150°C and the annealing time to 50 seconds, respectively, taking a step towards faster and more cost-effective fabrication of NiO films [130, 140, 141]. A performance summary of these non-polymer HTL materials is tabulated in Table 2.2.

**Table 2.2.** A Summary of PSCs utilizing inorganic HTL materials.

Reference	HTL	V <sub>oc</sub> (V)	J <sub>sc</sub> (mA/cm <sup>2</sup> )	PCE (%)	FF (%)
[123]	Cu <sub>2</sub> O	1.07	16.52	13.35	75.51
[123]	CuO	1.06	15.82	12.16	72.54
[124]	Cu <sub>2</sub> O	0.92	15.96	8.30	58.00
[126]	CuI	0.99	19.39	14.21	74.00
[127]	CuI	0.66	22.60	16.00	71.30
[128]	CuSCN	1.09	22.65	19.22	75.00
[129]	CuSCN	1.13	21.26	18.03	75.30
[130]	Cu:NiO	1.05	22.23	17.74	76.00
[131]	NiO	1.06	20.20	17.30	81.30
[132]	Y:NiO	1.00	23.82	16.31	68.00
[133]	Cs:NiO	1.083	21.62	17.44	74.40

## 2.10. Contact Electrodes

PSCs utilize two electrodes which collect and transfer the charge carriers from the ETL and HTL. PSCs are typically illuminated from the substrate side; hence, the substrate, charge carrier film, and the front contact electrode should be transparent to enable the light to reach the perovskite film without being absorbed by these layers. Fluorine doped tin oxide (FTO) and indium doped tin oxide (ITO) are transparent conductive metal oxides

used as the front contact electrodes in PSCs. A thin film of these materials can be deposited on rigid substrates such as glass, or flexible substrates such as PET and PEN. Upon illumination of an n-i-p structure PSC, the front contact electrode collects and transfers the electrons to the external circuit, whereas in the p-i-n structure, this electrode serves as the pathway for conducting the holes. The back-contact electrode has the similar functionality to the front contact electrode and is typically fabricated from silver (Ag), gold (Au), copper (Cu), or platinum (Pt) [142-144], and a thickness of 60-100 nm has been shown to sufficiently collect and transfer charge carriers. The better functionality of Au has made it the most dominating back-contact material for PSCs; however, besides requiring vacuum thermal evaporation or sputtering for deposition, the PV performance degradation associated to the migration of gold into the charge transport layer [145] and high cost of the material would make it unfavorable for industrialization. The incorporation of buffer layers, such as Cr [145],  $\text{VO}_x$  [146], carbon and  $\text{C}_{60}$  [147] at the interface of the contact electrodes and the charge transport films have shown to increase the stability and PV performance of PSCs as the result of conductivity enhancement. Copper is the cheapest material; however, it has shown lower performance compared to silver and gold with almost identical PV performance [144]. Recently, carbon back-contacts have been successfully used to make efficient PSCs with higher stability which can eliminate the use of HTL and metal back contacts [148]. Nevertheless, the superconductivity and cheaper cost of silver has made it the dominating back-contact electrode material for PV applications. The metal back-contact electrodes for lab scale fabricated PSCs have been dominated by vacuum thermal evaporation which is not compatible for automated manufacturing. In this process, pure pellets of the element melt in a high vacuum, deposit

on PSCs, and complete the fabrication process in a few minutes. In addition, the high melting point of the elements would increase the cost and energy payback time of the fabricated modules. Therefore, it is necessary to utilize other potential cheap materials that are processable using cost-effective scalable depositions and annealing in the ambient environment.

Carbon (C) films have recently been introduced as potential replacement to the expensive organic charge transport films and metallic electrodes in PSCs. Conventional HTLs utilize Spiro-MeOTAD which is expensive, has long-term structural instability, and requires inert nitrogen environment for fabrication. On the other hand, the inapplicability of high temperature vacuum deposition of metal back-contacts hinders high-throughput cost-effective automation, and their interaction with the halide phase migration from the perovskite film would impact device stability and deteriorate PSCs performance [149, 150], necessitating the use of alternative materials. Carbon films are hydrophobic, thus, repel moisture, impeding the formation of perovskite  $(\text{CH}_3\text{NH}_3)_4\text{PbI}_6 \cdot 2\text{H}_2\text{O}$  and  $\text{CH}_3\text{NH}_3\text{PbI}_3 \cdot \text{H}_2\text{O}$  hydrate phases which establish pathways for perovskite degradation [151, 152]. In addition, carbon composite films possess the VBM of -5 eV, closely aligned to that of Spiro-MeOTAD (-5.2 eV) and gold (-5.1 eV) [153, 154]. These films can be directly deposited on top of the perovskite absorber layer; hence, they can be potential charge transport and back contact substitutes, allowing for faster processing of PSCs and decreasing the cost of fabricated modules. Carbon films are typically obtained from a mixture of carbon black (CB), produced from the incomplete combustion of carbonous materials [155], as well as graphite, and other carbonous materials, such as carbon nanotubes, which have shown to improve the performance of PSCs [156-158]. These are



typically added to a solvent-binder mixture, and the quantity and ratio of these materials determine the viscosity and quality of the carbon films, affecting the electrical conductivity and adhesion to the perovskite surface, thus, PSC performance. For instance, Phillips et. al investigated the graphite to carbon black ratios between 0.5-3.2 and unraveled maximum electrical conductivity for the 29.4 wt.% ink with optimal ratio of 2.6 [159]. A study by Hatala et. al. also obtained the lowest resistance of carbon films for the 3:1 weight ratio of CB:graphite which was reduced to  $32.4 \Omega \cdot \text{sq}^{-1}$  by increasing the concentration between 15-35 wt%. They also reported enhanced conductivity in case of increasing the amount of ethyl cellulose (EC) binder which was reduced when polyvinylpyrrolidone (PVP) was used. In a similar attempt, Kartikay et. al [160] investigated the role of PVP, EC, and polymethyl methacrylate (PMMA) and different solvents of chlorobenzene, toluene, and terpineol on the performance of PSCs and obtained the maximum PCE of 10.74% for PMMA-chlorobenzene mixture and lowest PCE of 7.89% for PVP-terpineol devices which was attributed to the weak adhesion of carbon to perovskite as the result of incomplete removal of high boiling point terpineol during annealing. Recently, Chu et. al [161] investigated the impact of propylene glycol monomethyl ether acetate (PGMEA), propylene glycol monomethyl ether (PGME), diethylene glycol butyl ether acetate (EBAC), ethylene glycol monomethyl ether (EGME), isopropanol, terpineol, isophorone, cyclohexanone, cyclohexane, and hexane solvents on the stability and performance of PSCs and achieved the highest stability and performance for PGMEA based devices with 13.5% efficiency, whereas, PGME, EGME, isophorone, and cyclohexane severely degraded the perovskite film. In another study, Chu et. al [162] fabricated PSCs through two-step deposition of the carbon paste by initially screen printing the CB paste followed

by screen printing the CB/graphite paste with 1.5% carbon fiber in PGMEA-polyacrylic resin binder solution and annealing at 100°C. The segregation resulted in PSCs with better performance, surpassing 14% efficiency, as the result of better charge extraction at the perovskite/carbon interface. A brief performance summary of these studies is shown in Table. 2.3.

**Table 2.3.** A Summary of back-contact electrode materials used in PSCs.

Reference	Buffer/Electrode	Voc (V)	Jsc (mA/cm <sup>2</sup> )	PCE (%)	FF (%)
[142]	Cu	1.03	23.00	18.30	77.00
[143]	Cu	1.034	20.00	16.38	79.20
[144]	Cu	0.942	20.32	9.17	47.89
[144]	Ag	1.023	20.60	16.51	78.32
[144]	Au	1.0091	20.99	16.44	77.60
[144]	Pt	1.006	20.58	14.72	71.07
[144]	Ni	0.834	18.21	7.83	51.61
[144]	Cr	0.04	0.47	0.04	18.41
[145]	Cr/Au	1.105	23.30	17.70	69.00
[146]	VO <sub>x</sub> /Au	1.07	18.90	14.20	71.00
[147]	C <sub>60</sub> /Ag	0.97	22.47	14.00	64.00
[147]	Carbon/Ag	0.96	23.69	16.20	71.00
[160]	CB/Graphite	0.92	17.61	10.74	66.30
[161]	CB/Graphite	1.05	20.25	13.50	63.00
[162]	CB/Fiber/Graphite	1.01	19.90	14.10	69.00

## 2.11. Deposition Methods

As mentioned, compositional engineering of individual PSC thin films plays a significant factor on PV performance by influencing the photo absorption, as well as the bandgap, VBM, and CBM energy levels, determining the charge transport fluency in the thin films and at their interfaces. Material deposition is another significant parameter which affects the performance of PSCs by defining the morphology of individual thin films. The

morphology spans the quality and uniformity of deposited thin films, and high efficiency PSCs necessitate successful deposition of the precursors to achieve thin films with optimum thickness, high uniformity, and continuous morphology without any surface defects such as pinholes and cracks [163-165]. PSCs were shown to be susceptible for scalable automated manufacturing; hence, development of compatible deposition methods is a requisite to achieve this goal. The deposition of PSC thin films has been successfully conducted through vacuum and non-vacuum atmospheric environments, with the latter being the preferred method due to incompatibility of the former for rapid automated manufacturing. Vacuum deposition has enabled successful fabrication of PSCs. For instance, Liu et al. [166] utilized dual source thermal evaporation under vacuum by placing the organic MAI and inorganic  $\text{PbCl}_2$  in two separate sources and evaporated the substances simultaneously to fabricate  $\text{CH}_3\text{NH}_3\text{PbI}_{(3-x)}\text{Cl}_x$  perovskite films. Their results indicated an average PCE of 15.4% for the vapor deposited PSCs compared to solution-based devices with 8.6% efficiency which was attributed to the enhanced morphology and uniformity of films obtained from vapor deposition. In a similar attempt, Borchert et al. [167] reported 14.2% efficiency PSCs when fabricated through dual source evaporation under vacuum utilizing co-evaporation of FAI and  $\text{PbI}_2$  complexes to form highly uniform  $8\text{ cm} \times 8\text{ cm}$  large area perovskite thin films with superior morphology. Similarly, Ma et al. [168] reported 4.7% PSCs utilizing all inorganic  $\text{CsPbIBr}_2$  perovskite thin films fabricated through dual source evaporation of CsI and  $\text{PbBr}_2$ . In a similar attempt, Leyden et al. [169] fabricated PSCs, as high as 11.8% efficiency, through hybrid chemical vapor deposition by vapor deposition of MAI onto the thermally evaporated  $\text{PbCl}_2$  films produced under high vacuum. These results exemplified successful fabrication of large-scale PSCs;

however, they are not amenable for cost-effective high-speed automated manufacturing as the materials should undergo a prolonged and high temperature evaporation process in vacuum to develop the films. Therefore, it is necessary to take advantage of atmospheric compatible methods that enable cost-effective, high throughput, and scalable processing of efficient PSCs. Non-vacuum thin film development includes single and multi-step coating of the precursors using various potential methods of spin, blade, and gravure coating as well as inkjet printing. Fig. 2.8 shows the different potential deposition methods for depositing PSC films, and the following sections span some of the significant achievements pertinent to these methods.

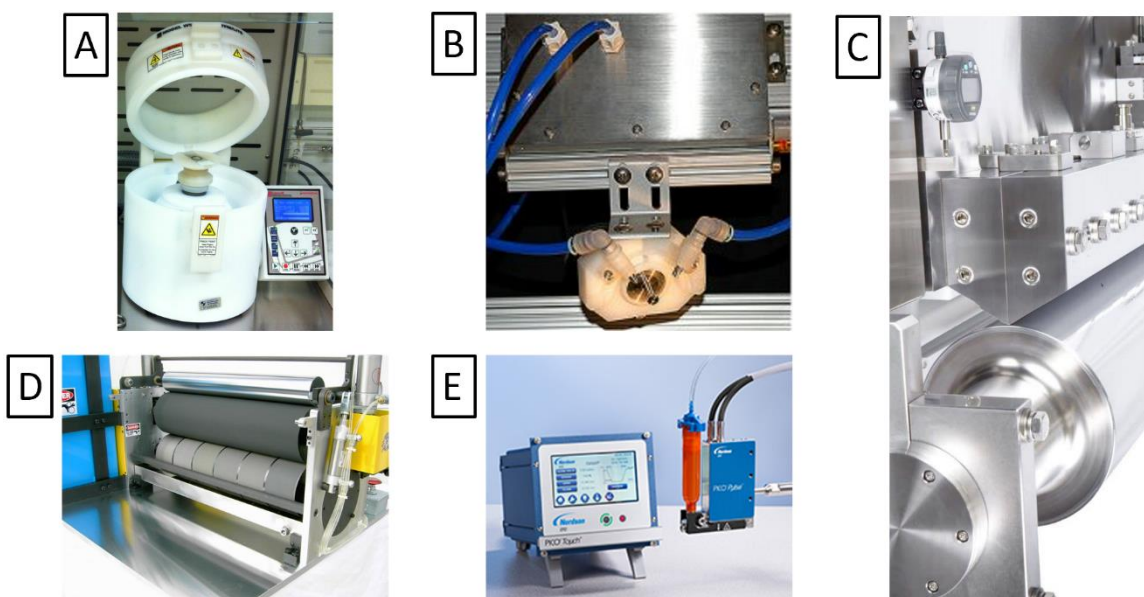


**Figure 2.8.** Various deposition methods showing A) Spin; B) Spray; C) Slot-die; D) Gravure coating; and E) Inkjet printing.

### 2.11.1. Spin Coating

Spin coating is the most dominating coating method used for lab-scale thin film development, and the highest performance PSCs have yet been produced using this method. In this technique, the spinning speed determines the morphology and thickness, and higher speeds produce thinner films [170]. The development of various techniques, such as sequential step coating, have produced higher performance PSCs as the result of obtaining better film morphology and material crystallinity, aiding better charge generation and transport, particularly for the perovskite film. For instance, Ko et al. [171] fabricated 15.76% PSCs by spin coating a solution of  $\text{PbI}_2$  in DMF followed by a short-term drying process and spin coating a solution of MAI in 2-propanol to form the perovskite film. Yuan et al. [172] introduced higher efficiency PSCs when the MAI solution was dropped on the wet perovskite film consisted of a mixture of  $\text{PbI}_2$  and  $\text{PbCl}_2$ . They fabricated 14.2% efficiency PSCs by drying the spin coated Pb-based films followed by spin coating the MAI solution on the top. However, when the drying process was removed, PSCs surpassing 17% efficiency was formed which was attributed to the penetration of MAI in the wet Pb-based films, resulting in enhanced morphology and crystallinity. Yang et al. [173] introduced 22.1% for small size and 19.7% efficiency for  $1 \text{ cm}^2$  PSCs using two-step spin coating by dissolving 95:5 molar ratio of  $\text{PbI}_2$ : $\text{PbBr}_2$  in 80:20 V/V DMF:DMSO and spin coating the solution on the substrates followed by spin coating a solution of FAI and MABr in isopropyl alcohol (IPA) to form the perovskite black phase. Besides these achievements, other techniques were also utilized to successfully fabricate PSCs. For instance, Liu et al. [174] reported PSCs exceeding 10% efficiency by immersing the spin-coated  $\text{PbI}_2$  films into a solution of MAI in 2-propanol for 40 seconds to form the perovskite film. In another attempt, MAI powder was spread on the spin-coated  $\text{PbI}_2$  films and was heated for 13 hours

to form the perovskite film, resulting in PSCs with 8.72% efficiency [175]. All these studies utilized spin coating to achieve efficient PSCs; however, this method has a high material waste and is unable to maintain the high uniformity for large area coatings. In addition, spin coating is not adaptable for automated manufacturing which demands investigating for scalable deposition methods that are amenable for low cost high-throughput automated manufacturing.

### **2.11.2. Spray Coating**

Spray coating is a scalable method that is adaptable for high-speed automated manufacturing. In this method, the atomized solution forms the desired thin film and the instrument parameters such as the flow rate, nozzle to substrate distance, and deposition speed can develop thin films with the desired morphology and thickness. For instance, Bi et al. [176] fabricated 13.54% efficiency PSCs using a 10 wt%  $\text{CH}_3\text{NH}_3\text{PbI}_3$  perovskite precursor in DMF through a spray gun placed 7 cm from the substrate at the horizontal angle of  $30^\circ$ . Recently, ultrasonic nozzles have enabled fabricating smoother and more uniform thin films and has been successfully used to fabricate various PSCs films, such as the  $\text{TiO}_2$  ETL [177], as well as different perovskite chemistries such as  $\text{CH}_3\text{NH}_3\text{PbI}_{(3-x)}\text{Cl}_x$  [178],  $\text{Cs}_x\text{FA}_{(3-x)}\text{PbI}_3$  [179], and  $\text{CsPbIBr}_2$  [180]. In these devices, the ultrafast oscillation of a piezoelectric transducer dispenses highly uniform micron size droplets that can form thin films with superior morphology and high uniformity, and an air or nitrogen stream is typically used to guide the atomized solution to the target. However, besides the mentioned parameters, the film quality is also dependent on the oscillation frequency [181]. To date, several studies have been conducted to testify the applicability of spray coating on PSCs fabrication. For instance, Das et al. [182] utilized a 120 kHz nozzle to deposit

$\text{CH}_3\text{NH}_3\text{PbI}_{(3-x)}\text{Cl}_x$  films and reported 13% PSCs. Chai et al. [70] fabricated PSCs exceeding 13% efficiency through a two-step ultrasonic spray deposition by spray coating the solutions of MAI and MAI+MABr on the spin coated  $\text{PbI}_2 + 0.15 \text{ MABr}$  and  $0.85\text{PbI}_2 + 0.15\text{PbBr}_2$  films, respectively, at the rate of  $150 \mu\text{l}/\text{min}$  using a 36 kHz ultrasonic nozzle placed 12 cm apart from the substrates. In another attempt, Huang et al. [183] utilized two-step spray coating by spray casting a solution of  $\text{PbI}_2$  in DMSO followed by spraying the MAI solution in IPA and achieved PSCs with over 16% efficiency. Tait et al. [184] reported efficient PSCs as high as 15.7% utilizing concurrent spray coating method which mixed two different perovskite precursors of  $\text{PbCl}_2/\text{MAI}$  and  $\text{PbAc}_2/\text{MAI}$  right before entering the nozzle. Recently, Yu et al. [185] spray coated FAI and FABr mixed solution on thermally evaporated CsI and  $\text{PbI}_2$  films to obtain  $\text{Cs}_x\text{FA}_{(1-x)}\text{PbI}_y\text{Br}_{(3-y)}$  perovskite films and obtained 18.21% and 14.71% efficiency for 0.16 and 25  $\text{cm}^2$  area PSCs. All these results indicated successful application of spray coating in PSCs fabrication. However, spray coating may require other post-processes, such as the use of masks to form the desired pattern, which can also make the process less lucrative due to material waste and complexity. In addition, the morphology and uniformity is sensitive to the mentioned spraying parameters and inadequate adjustments would negatively influence the quality of films, such as imposing Marangoni effect, or forming poor morphologies as the result of droplet drying before reaching the surface, leaving an unwetted thin film that can form a rough morphology with surface defects such as discontinuities [186]. In addition, the system and its maintenance are expensive which requires the application of other scalable deposition methods. Therefore, despite successful application to fabricate efficient PSCs, it is less favorable for commercialization of PSCs.

### 2.11.3. Slot-die Coating

Slot-dies are scalable coating devices that enable continuous deposition of highly uniform thin films with desired size and thickness and are amenable for high-speed automated manufacturing. A slot-die is consisted of a manifold which distributes the ink, typically using precision flow control syringe pumps, as well as shims that seal the manifold and bottom blocks and act as a conduit to transfer and spread the meniscus on the substrate. Therefore, the flow rate, substrate speed, distance of the shim tip to the substrate, and the thickness of shims determine the thickness of thin films, and the shim design enables continuous deposition of thin films with desired width. Slot-die coating provides a highly favorable processing window for automation through roll to roll [187, 188] as well as sheet to sheet manufacturing [189], and has provided a great interest among researchers towards commercialization of PSCs. Recently, efficient PSCs fabricated entirely through slot-die have been successfully introduced [188, 190] and the impact of different coating parameters on the performance of PSCs have been studied. For instance, Ciro et al. [191] slot-die coated the PEDOT:PSS,  $\text{MAPbI}_{(3-x)}\text{Cl}_x$ , and PCBM layers in a 65% humid ambient environment and reported PSCs with the average maximum efficiency of 2.39%. They attributed different performance results to the thickness variation, particularly the PCBM layer, by the change in the pumping rate of precursors. Except for the roughness of PCBM which remained constant, its thickness as well as the thickness and roughness of PEDOT:PSS and perovskite films increased as the flow rate was increased between 0.01-0.1 mL/min which indicates the significance of flow rate on the performance of PSCs. Whitaker et al. [192] investigated the impact of different perovskite precursor concentrations of 20, 23, 25, 30, and 40 wt% as well as the slot-die to substrate gaps of 40,



50, and 60  $\mu\text{m}$  on PSCs performance. The films made from 23 wt% indicated the maximum performance as the result of obtaining high quality films, whereas the lower concentrations made very thin films with poor morphology containing cracks and pinholes, and higher concentrations resulted in films with over 1  $\mu\text{m}$  thickness. Similarly, the higher gaps increased the thickness of films from  $457 \pm 7$  nm to  $563 \pm 5$  nm to  $647 \pm 5$  nm, resulting in 15.7%, 12.5%, and 9.4% efficiency, respectively. The lower cost and less complexity have made slot-dies the most favorable scalable deposition method for automated manufacturing of thin films in PSCs. Recently, Dou et. al [188] reported 19.6% efficiency large area PSCs with 22.5 cm width by slot-die coating the ETL, perovskite, and HTL through roll-to-roll, which indicates the plausibility of this deposition method for high-throughput fabrication of large area PSCs.

#### **2.11.4. Gravure Coating**

Gravure printing is a versatile coating method which was initially introduced in 1860 [193]. The system includes an engraved cylinder, an impression roller, a doctor-blade, and an ink reservoir or fountain. In gravure printing, the impression cylinder stamps the patterns from the engraved cylinder to the passing flexible substrates and the resolution of engraved patterns play a significant role on the printing quality. Over the past few years, several works have utilized gravure printing towards automated fabrication of PSCs [194, 195]. In addition, various deposition techniques have been utilized to achieve full roll-to-roll fabrication of PSCs through gravure printing. For instance, Kim et al. [196] studied high speed 18 m/min gravure coating of PSCs using one and two-step processing. For the single step processing, all the  $\text{SnO}_2$ ,  $\text{MAPbI}_3$ , Spiro-MeOTAD, and P3HT thin films were printed from their mixed precursors. In the two-step coating, the  $\text{PbI}_2$  precursor in 9:1 DMF:DMSO

was gravure printed and dip coated in a MAI:IPA bath to form the perovskite film. The PSCs fabricated from single and two-step printing using Spiro-MeOTAD as the HTL indicated 17.2% and 10.9% efficiency, respectively. Therefore, gravures enable high-speed and high-resolution printing of desired patterns and are amenable for scalable automated fabrication of PSCs. However, unlike slot-die coating, the high cost of the system, particularly the engraved cylinders, as well as the need for a large quantity of precursors for printing, and large printing volume to make the process profitable, has made gravure printing less favorable for research towards automated manufacturing of PSCs.

### **2.11.5. Inkjet Printing**

Inkjet printing has the history back in 18<sup>th</sup> century. It is the most common printing method which drives the ink droplets on the target substrate and is applicable for high-speed automated manufacturing. Continuous inkjet printing is the most primary form of inkjet printing where the ink is converted into droplets by being passed through a piezoelectric transducer using a high-pressure pump. Upon dispensing, the droplets pass through charging electrodes, enabling them to undergo deflection when passed through a deflector, and deposit on the passing substrate. The undeflected droplets are accumulated in a gutter. The high-pressure impingement allows for far nozzle to substrate distances, enabling printing on rough and sensitive to pressure surfaces. However, the high waste of material and reusing of the gutter ink, which might have been contaminated, are the major challenges for this mechanism [197, 198]. Later expansive technological achievements developed drop on demand (DOD) printing approaches, allowing for uniform and precise injection when required, thus, enabling printing of extremely small features with high resolution. Thermal DOD is the most common technology used in conventional inkjet

printers, where a heat pulse rapidly vaporizes the ink and forms a bubble in the ink which, in turn, produces and dispenses an ink drop; hence, a heat frequency would allow for continuous droplet dispensing. However, the ink drying which can clog the nozzle heads, the need for volatiles to facilitate vaporization, as well as the impact of heat on altering the viscosity and chemical properties of the ink are the major challenges which necessitates the application of other potential technologies, such as piezoelectric. In the piezoelectric DOD, rapid oscillation of a piezoelectric material enables uniform size and distribution of the droplets, thus, it does not impose the clogging challenges by the thermal approach and eliminates the need for volatiles in the precursor, allowing for the application of a broad range of inks. Various studies have utilized inkjet printing to fabricate efficient PSCs. Notably, inkjet printers have shown to produce more efficient PSCs compared to other coating methods which has been indebted to better morphology and uniformity of deposited thin films [199]. Therefore, optimum compositional engineering and processing parameters are necessary to form highly uniform films with superior morphology and achieve high performance PSCs [200, 201]. Li et al. [202] investigated different quantities of MAI additive in the MAPbI<sub>3</sub> perovskites and observed darkening of the perovskite films upon inkjet printing of the precursor which underwent a slower pace with higher MAI quantities. At the 60% MAI concentration, a continuous and uniform perovskite film was formed which resulted in over 12% efficiency, whereas the pristine precursor exhibited about 7% efficiency and was attributed to the poor morphology of the printed film. Besides composition, understanding the optimum precursor properties, such as solvent-substrate interaction, play a significant role on the morphology, thickness, and uniformity of thin films. For instance, Oh et al. [203] eliminated the detrimental coffee

stain effect of the inkjet-printed  $\text{Al}_2\text{O}_3$  films and formed a uniform morphology by incorporating DMF in the water based precursor. Similarly, Gao et al. [204] indicated that 60:40 vol% of high boiling point dodecane and low boiling point toluene solvent mixture could eliminate the coffee stain effect in  $\text{CsPbBr}_3$  perovskite films. In these experiments, the low boiling point solvent induced a capillary effect, thus accumulating the solutes at the edge of the droplets. The incorporation of higher boiling point solvent with lower surface tension induced Marangoni flow which contradicted the capillary flow and enabled uniform thin films upon evaporation.

The mentioned studies determined the significance of precursor engineering on the morphology of thin films. However, the uniformity and thickness of the thin films is another significant parameter affecting the performance of PSCs and is achieved by controlling the number of dispensing droplets, number of printing passes, and drop spacing defined as the center-to-center distance of two dispensed droplets. For instance, Huckaba et al. [205] obtained 55, 90, and 130 nm thick  $\text{TiO}_2$  thin films after a single printing pass with drop spacings of 20, 25, 30, and 35  $\mu\text{m}$ , and reported PSCs with 11.24%, 11.01%, 11.13%, and 11.84% efficiency, respectively. Later, they investigated the impact of the number of passes on PSC efficiency for the  $\text{TiO}_2$  films printed at 25, and 30  $\mu\text{m}$  spacing. It was found that the PCE of PSCs decreased from 13.91% to 11.07% and from 12.62% to 6.63% for the 25 and 30  $\mu\text{m}$  spacings when the number of passes was increased from 1 to 6, respectively. Similarly,  $\text{FA}_{0.15}\text{MA}_{0.85}\text{PbI}_{2.55}\text{Br}_{0.45}$  perovskite films printed between 25-45  $\mu\text{m}$  spacing range indicated higher photo absorption at shorter spacings which was attributed to the increased thickness of the perovskite film. However, the performance was decreased from over 12.15% to below 4.64%. In another work, Eggers et al. [206] used

the same strategy and fabricated the  $\text{Cs}_{0.1}\text{FA}_{0.75}\text{MA}_{0.15}\text{Pb}(\text{Br}_{0.15}\text{I}_{0.85})_3$  perovskite films with different thicknesses ranging between 400-4000 nm and reported a stabilized efficiency of 18%. Their results indicated enhanced charge carrier lifetime with increased thickness; however, the Cs:Pb ratio decreased at the surface for the films exceeding 1100 nm which, in turn, decreased the efficiency to about 4.5%. Mathies et al. [207] carried out inkjet printing of  $\text{Cs}_{0.1}(\text{FA}_{0.83}\text{MA}_{0.17})_{0.9}\text{Pb}(\text{Br}_{0.17}\text{I}_{0.83})_3$  triple cation perovskite films at different drop spacings of 25, 35, 45, and 60  $\mu\text{m}$  and obtained 780, 520, 380, and 175 nm thick films, respectively. The smaller drop spacings also increased the grain sizes and exhibited higher photo absorption. However, the 520 nm thick films exhibited the maximum PCE of 15.3%.

Previous studies utilized DOD printing techniques which developed superior perovskite films with high quality, resulting in efficient PSCs. Recent technological advances have enabled aerosol jet printing systems which have enabled 3D printing of high-resolution features such as electronic components. In these printing systems an atomizer creates an aerosol mist with micron size droplets and a sheath gas passes the mist through the nozzle and focuses the mist on the substrate. The sheath gas also eliminates clogging of the ink at the nozzle. Therefore, besides the printing speed, and the distance between adjacent printed lines, the sheath gas flow rate (SGFR), carrier gas flow rate (CGFR), as well as the nozzle diameter determine the thickness and morphology of the deposited films. Mahajan et al. [208] carried out a comprehensive study to determine the impact of these parameters on silver traces. Their results indicated that unlike increased and decreased line width and thickness with increased nozzle diameter size, they were found to decrease and increase by increasing the focus ratio, defined as the ratio of the SGFR to CGFR, respectively. However, the line width remained the same when CGFR

was increased. In addition, higher stage speeds decreased both the width and thickness of the silver lines. Tarabella et al. [209] conducted a comprehensive study to determine the impact of these parameters on the thickness and width of PEDOT:PSS thin film. Dalal et al. [210] investigated the impact of CGFR and SGFR on the quality and conductivity of printed silver traces. They observed that CGFR had a higher impact than SGFR and the conductivity of the traces were increased by increasing CGFR. Similar to DOD printing, aerosol inkjet printing systems enable scalable deposition of desired patterns, but through an extremely high resolution deposition within micron size scale which can develop patterns with superior morphology and uniformity; however, the high cost and complexity of the system compared to piezoelectric DOD technology, as well as the considerable lower deposition speed compared to spray, slot-die, and gravure printing systems would make it less favorable for industrial scale deposition of the larger area PSC thin films, such as the ETL, perovskite, and HTL. However, similar to DOD inkjet printing, they can be a potential candidate to deposit PSCs back-contact electrodes.

## **2.12. Crystallization**

As mentioned, conventional solar cells are consisted of wafers developed through prolong, delicate, and complex high energy consuming processes which yield expensive manufacturing. The crystallization process is at the heart of these processes which determines the PV performance of solar cells. The potential next generation PVs, such as PSCs, are consisted of stacked layers of charge carrier and photo-absorber films which should undergo crystallization upon deposition to achieve high performance devices. The crystallization process is consisted of two sub-processes of nucleation and growth which are influenced by the solid-liquid interactions. Therefore, understanding and developing

the kinetics of crystallization is the core of PV processing and play a significant role on the stability and PV performance of solar cells.

### **2.12.1. Nucleation**

Nucleation is the primary process where the material atoms and molecules are highly organized and form crystals which constitute the structure of thin films. The PV thin films should be constructed of a large array of crystals enabling facile diffusion and extraction of charge carriers throughout the films and at their interface. Therefore, the structure and properties of crystal lattice play a significant role on the PV parameters of PSCs. PSC thin films are solution processable which may require a nucleation process to form the desired array of crystals and can be provided depending on the coating method used for developing the thin films. For instance, spin-coating has been the most widely used method in PSC research and development. However, merely spin coating the perovskite film would exhibit a poor surface coverage due to the difference between low soluble  $\text{PbI}_2$  and high soluble MAI. This will result in poor PV performance due to short circuiting as the result of direct contact between the ETL and HTL as well as minimized recombination resistance. Therefore, a nucleating step is required to obtain the desired perovskite film. In this step, an antisolvent with a poor solubility and polarity to the perovskite solvents is dripped on the spinning perovskite precursor a few seconds before the end of the spinning process. The antisolvent nucleation during spin coating has been introduced with aid of the LaMer curve [211, 212] and contains three regions, each playing a significant factor on perovskite nucleation as shown in Fig. 2.9. In the first region, the antisolvent should be dropped right

before  $T_1$  where the solution concentration undergoes a critical state as the result of solvent evaporation during spinning. The antisolvent addition at this stage induces rapid stochastic intermolecular fluctuations of the atoms, resulting in the generation, distribution, and development of stable crystals across the surface during the remaining spinning process ( $T_3-T_1$ ). The antisolvent nucleation in this stage takes place through a primary nucleation where the first crystal is formed, as well as a secondary nucleation where the nucleation proliferates throughout the surface as the result of producing other crystals from the preexisting crystal [213]. In this regard, the adequate selection and on-time dropping of the antisolvent plays a significant factor on the morphology, structure, and performance of PSCs. Selection of the adequate antisolvent for the perovskite film plays a significant role on the morphology and structure of the films by defining the extent of supersaturation. Therefore, various antisolvents have been investigated on the nucleation of perovskite films and PSCs performance. For instance, Lee et al. [214] investigated toluene (TL), chloroform (CF), chlorobenzene (CB), dichlorobenzene (DCB), and IPA on the nucleation of 20 wt%  $\text{MAPbI}_3$  perovskite precursor in 1:1 DMSO:GBL solvent mixture. When TL was used, a metastable and stable intermediate perovskite phase was formed, which resulted in films with high photo absorption capability. However, the CF, CB, and DCB antisolvents, which have slightly higher dielectric and dipole moment constants, separated out the perovskite crystals and bypassed the supersaturation state, and the IPA changed the stoichiometry by dissolving and removing the MAI phase of the perovskite as the result of its much higher dielectric constant and slightly higher dipole moment. The average PCE of 8 PSCs indicated 0.33%, 7%, 9.11%, 10.88%, 11.12%, and 12.85% efficiency when fabricated without any antisolvents, IPA, CF, CB, DCB, and TL, respectively. In addition,



they investigated the volume of the dropped TL antisolvent and achieved maximum average PCE of 13.12% for 75  $\mu\text{L}$  of the antisolvent. In another work, Xiao et al. [215] investigated IPA, ethyl acetate (EA), TL, CB, and diethyl ether (DEE) on  $\text{Cs}_5(\text{FA}_{0.83}\text{MA}_{0.17})_{95}\text{Pb}(\text{I}_{0.83}\text{Br}_{0.17})_3$  precursor in 4:1 DMF:DMSO and achieved 12.62%, 12.82%, 13.18%, 14.05%, and 15.04% efficiency, respectively. They attributed the higher performance of DEE treated devices to the low dielectric constant, low polarity, and low boiling point of antisolvent, driving the perovskite into metastable mode than supersaturation. The mechanism of perovskite intermediate phase formation was exhaustively studied by Ahn et al. [83], where DEE treatment of  $\text{MAPbI}_3$  perovskite in DMF:DMSO formed a transparent film. The IR spectroscopy unraveled the stretching vibration of S=O to decrease from  $1045\text{ cm}^{-1}$  for DMSO to  $1020$ , and  $1015\text{ cm}^{-1}$  for  $\text{PbI}_2\cdot\text{DMSO}$ , and MAI.  $\text{PbI}_2\cdot\text{DMSO}$  complexes, respectively, which indicated more interaction as the result of more adducts by the Lewis acids of  $\text{MA}^+$  and  $\text{Pb}^{2+}$  ions with DMSO.

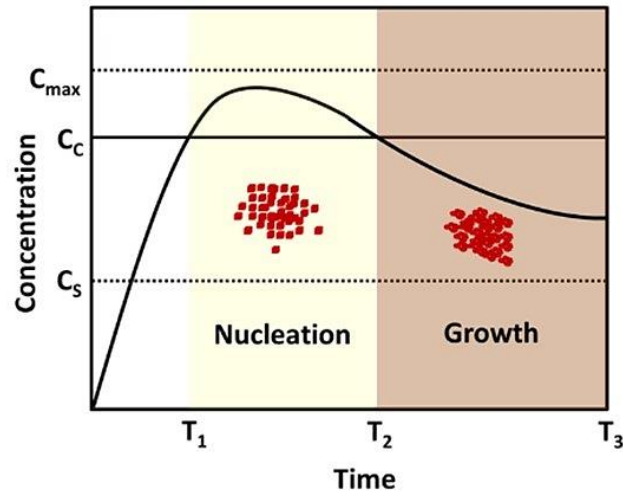


**Figure 2.9.** LaMer curve showing the nucleation of perovskite during spin coating.

### 2.12.2. Crystal Growth

Besides high organization, the crystals should have the optimal size and desired chemical properties to achieve maximum power generation. Therefore, a crystal growth process should be carried out right after nucleation to accomplish crystallization. This process enlarges the crystals, and is typically carried out using thermal treatment techniques, such as annealing, which will be fundamentally studied and developed in this dissertation.

### 2.13. Annealing

Annealing is the driving force of grain growth, affecting the physical and chemical properties of thin film materials. The annealing process increases the internal energy of crystals, making them grow through an exothermic process which progresses them towards the thermodynamic equilibrium state. Annealing increases the crystal sizes by enhancing the diffusion rate of atoms and can be explained using the Fick's law of diffusion [216] described in the following:

$$J = -D \frac{d\phi}{dx} \quad (2.1)$$

Where, J is the diffusion flux indicating the amount of substance in unit area per time, D is the diffusion constant, and the last term is the concentration change per unit volume at a specific location. The annealing dissociates the crystal atom bonds formed in the nucleation step, allowing them to redistribute. The redistribution performs the recrystallization and growth by diminishing the dislocations and crystal defects and can be explained using the Arrhenius equation [217] as stated in the following:

$$M = M_0 \cdot e^{\left(\frac{-E_a}{R.T}\right)} \quad (2.2)$$

$$M = \frac{\varnothing^{\frac{1}{n}} - \varnothing_0^{\frac{1}{n}}}{t} \quad (2.3)$$

Where, M is the thermal diffusivity (nm<sup>2</sup>/s) determining the grain boundary mobility, M<sub>0</sub> is the pre-exponential value, E<sub>a</sub> is the activation energy for grain boundary mobility (kJ/mol), R=8.314 J/(mol.K) is the gas constant,  $\varnothing$  and  $\varnothing_0$  are the average grain diameters after and before annealing, respectively, t is the annealing time, and n is the grain growth exponent. The synergy of above equations indicate that the annealing temperature determines the atomic diffusion rate, and recrystallization is temperature driven. Therefore, achieving the critical temperature is necessary to occur recrystallization, and the combination of annealing time and temperature determine the extent of recrystallization. Grain growth can be accompanied by recrystallization and is a stochastic and discontinuous process similar to nucleation. The grain growth and consumption can take place at the same time and the direction of the movement can abruptly change during annealing. The larger crystals are more energetic due to more piled-up dislocations and the grains would grow faster as they grow, thus, controlling the annealing time and temperature play a significant role on crystallization and recrystallization. The quantity and size of grains would decrease and increase upon annealing, respectively, which decrease the grain boundary mobility. Grain boundaries are defect states within the semiconducting thin films and are more energetic in larger crystals [218] which consume the smaller grains and diminish the grain boundary density. Grain boundaries are potential charge recombination centers which determine the density of extracted charge carriers and PV performance of PSCs. Therefore, optimum annealing is necessary to obtain maximum PV performance of PSCs by

minimizing the grain boundary density and improving the physical and chemical properties of the material. The spin coating process nucleates the perovskite precursor, forming a transparent intermediate phase containing numerous infinitesimal crystals which should be recrystallized to obtain the perovskite black phase with different crystal structure capable to produce charge carriers upon irradiation. Increasing the annealing temperature increases the grain sizes; however, optimum annealing temperature and time is necessary to avoid degrading the chemical and physical properties of the thin film material. Excess annealing would overgrow the crystals resulting in less grain boundary density; however, the chemical properties of the crystals change with annealing and can degrade the crystal lattice. As mentioned earlier, the crystallinity of the films affects the series and shunt resistances, thus, the PV parameters of PSCs. The generated defects by  $\text{Pb}^{2+}$  and  $\text{I}^-$  vacancies, interstitial  $\text{Pb}^{2+}$  and  $\text{I}^-$ , Pb-I substitution, grain boundary lattice mismatch, and surface dangling bonds are the major defects which increase the non-radiative charge recombination by increasing the series and decreasing the shunt resistances, thus, affecting the performance of PSCs [219, 220]. In this regard, besides the chemical composition of deposited films, the obtained phase and morphology upon annealing plays a significant factor on minimizing the series resistance, charge recombination, and performance of PSCs.

Various studies have so far studied the impact of annealing on the performance of PSCs. These studies utilized conductive, convective, and radiative annealing methods by investigating the impact of annealing time and temperature on the morphology and chemical properties of the PSCs thin films, particularly the perovskite photo-absorber layer. In conductive annealing, the developed thin films are subsequently put into contact

with a hotplate or placed in furnaces to perform annealing, whereas a hot stream of air passed on a heating element anneals the material through convective annealing [221-223]. Conductive annealing is the most dominating method used for annealing the PSC thin films. For instance, Mehdi et al. [224] investigated the impact of annealing temperature and time ranging between 80-110°C and 20-40 min on the performance of PSCs, respectively. The maximum PCE of 10.64% was obtained when the perovskite films were annealed at that 100°C which was attributed to maximized crystallinity of the perovskite films which, in turn, minimized and maximized the series and recombination resistances, respectively. However, further temperature increase reduced the efficiency to 9.43% as the result of perovskite film decomposition which increased the series and decreased the recombination resistances. Shargaieva et al. [225] investigated the impact of annealing temperature on the crystal size of the perovskite films annealed at high temperatures for a short period. The substrates heated to 200, 300, and 400°C exhibited surface temperatures of 125, 158, and 193°C after 15 seconds and remained constant afterwards. The two former temperatures indicated well-bound grains where the average sizes increased from 271 to 469 nm, respectively. However, 200°C temperature exhibited the maximum crystallinity of the perovskite film and the latter temperature indicated cracks which was conformed with the decomposition of the perovskite films at this level. After 5, 35, and 60 seconds, the surface temperature of the heated substrates at 200°C reached to 61, 170, and 176°C, respectively, and progressive annealing increased the grain sizes to over 1  $\mu\text{m}$ . Further similar results have also indicated the interdependency of annealing temperature and time and its impact on the phase purity, morphology, and performance of PSCs [226-228]. Therefore, it is necessary to develop more precise annealing methods that better control the

crystallization dynamics and yield PSCs with higher efficiency. In this regard, various methods have been utilized to enhance the performance of PSCs. For instance, Wang et al. [229] utilized two-step conductive method to anneal the CsPbIBr<sub>2</sub> perovskite films. The perovskite films were annealed through different annealing conditions of 50/280°C, 80/280°C, 100/280°C, 150/280°C, and 180/280°C for 10 minutes, where the values represent annealing temperatures used for the first and second annealing steps, respectively. Progressive primary annealing temperature increase up to 150°C enhanced the performance of PSCs from 5.84% to 8.31%, and further increase to 180°C decreased the performance to 6.86% which was attributed to the thermal degradation of perovskite film. Notably, compared to two-step method, the performance of PSCs annealed only at 280°C was 4.31% which was attributed to the better crystallinity and morphology of perovskite films annealed through the two-step method. In addition, the two-step favored the charge extraction at the perovskite and back-contact electrode interface which, in turn, enhanced the PV parameters of the PSCs. In another similar work, Kim et al. [230] annealed (FAPbI<sub>3</sub>)<sub>0.85</sub>(MAPbBr<sub>3</sub>)<sub>0.15</sub> perovskite films at 100°C, and 200°C, for 30, and 2 minutes, and at 300°C, and 400°C for 8, and 2 seconds, respectively. The highest temperature condition indicated a high-quality morphology with the largest perovskite crystal size of 1 μm which increased the PCE to 20.75%. This indicates that short-time high-temperature annealing is a favorable method which is applicable for rapid annealing of PSCs, making it compatible for high throughput manufacturing. Therefore, utilizing other scalable methods which can further shorten the annealing time would be a promising pathway towards industrialization of PSCs through rapid automated manufacturing.

## **2.14. Photonic Annealing**

Previous conductive and convective methods were able to anneal the films in a few minutes to an hour time frame using medium to high temperature hotplates and furnaces and achieved efficient devices surpassing 20% efficiency. However, prolonged annealing necessitates long ovens, batched ovens, or lowered web speeds which are not lucrative for high-speed automated manufacturing. In addition, roll-to-roll favorable flexible plastic substrates, such as PET, PEN, and PI would undergo severe deformation at temperatures greater than 120 °C. Therefore, it is necessary to take advantage of other methods, such as photonic annealing, and develop approaches that enable instant annealing of thin film composites. Photonic annealing is a radiative method; hence, unlike conventional methods, the extent of material annealing through photonic methods is dependent on the capability of the thin film material composite to harvest the irradiation. In these techniques, the irradiation spectrum plays a significant role on the annealing. Therefore, photonic annealing should be carried out based on the irradiation spectrum falling within the absorption range of the target composite. In this regard, various photonic methods such as intense pulse light (IPL) can be successfully utilized to anneal the PSC thin films.

## **2.15. Intense Pulse Light (IPL)**

Intense pulse light (IPL) is a radiative method which allows for rapid cost-effective annealing of large area thin film composites (Fig. 2.10). The main components of the system include a voltage control box, set of capacitors, and lamps filled with a noble gas, typically Xenon. The voltage control box stores the required electrical energy in the capacitors and allows for the energy to be released to the lamps when executed.

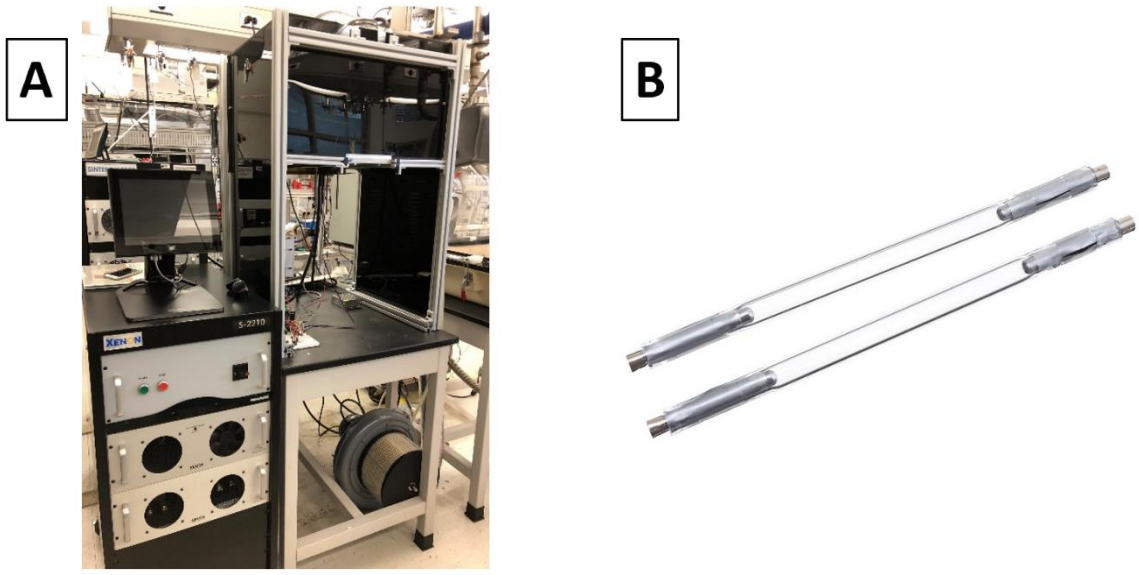


**Figure 2.10.** Images showing A) An IPL machine; and B) Xenon filled lamps.

This technology has the similar working principle to gas discharge lamps where the exertion of a high voltage to the lamp paralyzes the gas atoms near the anode into anion and cations which accelerate towards the anode and cathode, respectively. The cations collide with the neutral atoms during travelling where they transfer their electrons and subsequently accelerate towards the cathode, and the anions gained the electron go to a lower energy state while imparting energetic photons lasting for millisecond(s) which can be absorbed by the thin film material based on the Beer-Lambert equation as stated in the following equation:

$$\alpha = \frac{1}{d} \ln \left( \frac{P_0}{P} \right) \quad (2.4)$$

Where,  $\alpha$  is the absorbance coefficient,  $d$  is the film thickness,  $P_0$  is the applied, and  $P$  is the transmitted photon intensity. The annealing process is accompanied by rapid elevation of the intermolecular activity of material species as the result of photon absorption. Eqn.



2.4 indicates that darker or thicker films would harvest more photons at a fixed irradiation; hence, better absorption play a significant factor on the extent of annealing. The absorbed energetic photons carry out the annealing based on the one-dimensional steady state transient thermal equation as stated in the following:

$$\frac{\partial}{\partial z} \left( K \cdot \frac{\partial T}{\partial z} \right) + Q_{abs} = \rho \cdot C_p \cdot \frac{\partial T}{\partial t} \quad (2.5)$$

Where, K is the thermal conductivity,  $\rho$  is the density, and  $C_p$  is the specific heat transfer capacity of the material, respectively.  $Q_{abs}$  is the absorbed heat flux of the thin film material at a specific depth (z) and can be defined as stated in the following:

$$Q_{abs} = A \cdot \iint P_0(\lambda) e^{-\alpha z} d(\lambda) d(z) \quad (2.6)$$

Where, A is the irradiating source area. Eqn. 2.6 can be generalized into the following equation:

$$Q_{abs} = E_{light} \cdot C_d \cdot (Abs(\lambda) \cdot P_0(\lambda))_{max} \quad (2.7)$$

Eqn. 2.7 indicates that  $Q_{abs}$  can be computed from the product of the maximum interception of the thin film absorbance ( $Abs(\lambda)$ ) and gaussian fit of the Xenon flash lamp irradiation spectrum ( $P_0(\lambda)$ ), and distance coefficient ( $C_d$ ) expressing the light attenuation reaching to the substrate, as well as the photon flux released from the lamp ( $E_{light}$ ) which can be determined from the following equation:

$$E_{light} = \left( \frac{V \cdot I}{A} \right) \cdot \eta_{elec} \quad (2.8)$$

In which,  $V$  and  $I$  are the applied voltage and current to the lamp, respectively,  $\eta_{\text{elec}}$  is the electrical to photon conversion efficiency. Eqn. 2.5 indicates that, besides heat flux, the annealing is also time ( $t$ ) depended; hence, longer exposure can further anneal the material for a specific heat flux. In this regard, the compromised time and heat flux during IPL annealing would impact the maximum PSC performance and is determined by the flash duration, number of flashes, applied energy per flash, and interval time between flashes. Therefore, it is necessary to investigate the impact of all these parameters on the phase and structural evolution of PSC thin film materials to attain the maximum stability and PV performance. It is noteworthy that the use of IPL has superiority to lasers used in annealing of thin films [231-234] as it allows for large area annealing unlike the pinpoint processing area in lasers. In addition, unlike lasers that utilize a monochromatic light, materials annealed using IPL would take advantage of a broad spectrum between UV-IR. Various studies have, so far, utilized IPL to anneal polymer, metallic, and semiconducting thin films for electronics [235-237] and PVs [238-241]. Among these, successful application for PVs have instigated the researchers to investigate IPL towards achieving cost-effective and high throughput automated fabrication of large area perovskite PVs. These studies have been briefly conducted merely on the ETL and perovskite films. For instance, Lavery et. al fabricated  $\text{CH}_3\text{NH}_3\text{PbI}_3$  perovskite films through two steps of spin-coating the  $\text{PbI}_2$  film followed by immersing in an IPA solution of MAI to form the initial black phase and annealed them using a hotplate and IPL. The hotplate annealing was performed for 30 minutes at  $70^\circ\text{C}$ , and IPL annealing was conducted by applying a 2 ms duration flash carrying various energies between 1000-2000 with 250 J interval. Unlike hotplate annealed cells which resulted in an average efficiency of 8.21%, IPL annealed PSCs at 2000 J energy

exhibited 11.5% average efficiency which was attributed to the enlarged and well-developed grains as the result of better annealing by flash annealing [242]. Troughton et. al investigated the impact of different flash durations between 750-1500  $\mu\text{s}$  on perovskite film morphology and degradation, and indicated 1150  $\mu\text{s}$  to be sufficient to form the perovskite black phase free of  $\text{PbI}_2$  phase, and fabricated PSCs with 11.3% and 15.2% efficiency when annealed through photonic flash annealing and 90 min conventional hotplate, respectively [243]. Recently, Singh et. al [244] IPL annealed all inorganic  $\text{Cu}_2\text{ZnSnS}_4$  perovskite films by applying three different energies of 0.32, 1.11, and 2.23  $\text{J}/\text{cm}^2$ . At 2.23  $\text{J}/\text{cm}^2$ , the perovskite grains were enlarged and PSCs with 1.9% efficiency were obtained, and higher energies cracked the films which indicated material degradation. Besides the perovskite film, IPL has been successfully used to rapidly anneal the  $\text{TiO}_2$  and  $\text{SnO}_2$  ETL materials. For instance, Feleki et al. [245] investigated the impact of flash counts on the optoelectrical properties of mesoporous  $\text{TiO}_2$  ETL spin-coated on compact  $\text{TiO}_2$  films fabricated through evaporation. Their results indicated average PV efficiency of 15.3%, 15%, and 16.2% for three samples when annealed using 2 ms flashes, each with 12.3  $\text{J}/\text{cm}^2$  energy density. Das et al. [246] applied 25 flashes, with 7 ms duration and 500 ms delay time between flashes on  $\text{TiO}_2$  films, and each flash reflected the associated energy to that of the applied 200 V to the lamps. The IPL annealing of  $\text{TiO}_2$  films resulted in an average and maximum PCE of 12.6% and 15% for the photonic cured, as well as 13.3% and 15.1% for the PSCs utilizing  $\text{TiO}_2$  films annealed in furnace for 30 minutes at 500°C, respectively. Since the introduction of  $\text{SnO}_2$  as a potential replacement to  $\text{TiO}_2$  ETL, IPL has been investigated to anneal this potential metal oxide. For instance, Zhu et. al. [247] applied IPL on 0.1 M solution of  $\text{SnCl}_4$  films and derived pure  $\text{SnO}_2$  phase upon annealing.

They exposed the SnCl<sub>4</sub> films to various flash durations ranging between 5-40 ms and reported the maximum efficiency of 15.3% when the films were annealed through 20 ms light exposure at 46 J/cm<sup>2</sup> energy density.

In addition to the ETL and perovskite films, IPL has been used to anneal the potential materials used as the back-contact electrode in PVs, such as carbonous composites and silver. Chung et al. [248] IPL annealed the gravure coated 30 mm × 3 mm silver patterns on PET substrates after drying for 2-3 minutes. They investigated up to 10 flashes with various flash duration ranging between 1.5-6 ms, and the applied energy per flash and delay time between flashes were varied between 0.75-3.5 J/cm<sup>2</sup>, and 0-20 ms, respectively. The silver grain sizes increased with more flash counts and necking connections were formed upon flash annealing which became denser after more flashes and decreased the sheet resistance. Notably, the sheet resistance increased as the delay time between flashes was increased from 0 to 20 ms and decreased at shorter flash durations. At the optimal IPL condition of a single flash with 1.5 ms duration and 3 J/cm<sup>2</sup> energy density, sheet resistance as low as 0.95 Ω/□ was obtained which was lower compared to the sheet resistances of 2, 2.5, and 8.3 Ω/□ obtained from silver patterns thermally annealed for an hour between 80-150°C. Gokhale et al. [249] investigated the impact of different pulse counts of 1-20, different energy densities between 0.955-1.574 J/cm<sup>2</sup>, and the fixed duration of 1 ms on silver patterns printed on glass, PET, and PEN substrates. The patterns had a fixed length of 5 mm but different width of 1, 2, and 3 mm, and were made from two different commercially available silver inks of SW1012 (15-20 nm particle size) forming a 2500 nm thickness, and UTD AgIJ1 (10 nm particle size) forming a 330 nm thick layer. The minimum sheet resistances of 0.06 and 0.29 Ω/□ were obtained for the first and second ink,

respectively. Several other studies have also followed the same pathway to investigate the impact of printed silver traces made from different silver precursor chemistries on other substrates, such as polyimide (PI) and polyurethane (PU) [250-252]. These studies unraveled the conductivity change and the applicability of IPL to anneal another PSC thin film material and enhance the processing time of PSCs. Recently, Secor et al. [253] investigated the impact of 25 and 50 wt% ink concentrations and flash energy ranging between 5-10 J/cm<sup>2</sup> on the conductivity of graphene films inkjet printed on glass, PEN, PI, and PET substrates. Their results indicated the minimum sheet resistance happening for the films deposited on PI substrates, and the sheet resistance was progressively decreased at higher pulse energy and ink concentration. Therefore, IPL is a promising means to anneal other potential materials, such as carbon-based films, shown to serve the role of both charge transport and metal back-contact films. The impact of IPL on the conductivity of carbon films and performance of PSCs will be discussed in the last chapter of this dissertation.

## **2.16. Conclusion**

This chapter introduced PSCs and reviewed some of the staggering compositional engineering achievements that promoted the PSCs performance and stability. In addition, the deposition and annealing were shown to determine the stability and performance of PSCs. Unlike deposition, the annealing of PSCs was shown to take place for a long period through high temperature conductive annealing, and rapid cost-effective annealing methods, such as IPL, were shown to dramatically increase the processing pace. Various successful studies were presented where the ETL, perovskite films, and back contacts were annealed through IPL. It was shown that IPL is a promising candidate; however, novel

materials and annealing approaches should be utilized to achieve fully automated fabrication of PSCs.

## CHAPTER III

### METHODS

#### 3.1. Materials

Lead (II) Iodide (99.99%, trace metals basis) was purchased from TCI. di-iodomethane ( $\text{CH}_2\text{I}_2$ , 99%) and  $\text{SnO}_2$  solution (15% in  $\text{H}_2\text{O}$  colloidal dispersion) were purchased from Alfa Aesar. Methylammonium iodide (MAI) and Cobalt dopant FK209 were purchased from Greatcell solar. The 2,2',7,7'-Tetrakis[N,N-di(4-methoxyphenyl)amino]-9,9'-spirobifluorene (99.8%, Spiro-MeOTAD) was acquired from Lumtec. FTO glass slides ( $< 20 \Omega/\text{sq.}$ ,  $2 \text{ cm} \times 2 \text{ cm} \times 3 \text{ mm}$ ), and gold pellets (99.999%) were purchased Hartford glass, and Kurt J. Lesker, respectively. Graphite powder (spherical,  $< 20 \mu\text{m}$ ) and ITO coated PET sheets ( $60 \Omega/\text{sq.}$ ) were purchased from Sigma Aldrich. Carbon black (Vulcan-XC72R, 50 nm) was purchased from Cabot. All other materials were purchased from Sigma Aldrich without further purification.

#### 3.2. Electron Transport Layer (ETL) Fabrication

For spin coated  $\text{SnO}_2$  ETL, the  $\text{SnO}_2$  solution is made by diluting the  $\text{SnO}_2$  colloidal dispersion in DI water (1:4 V/V) to obtain a concentration of 3.75%. For inkjet printing, a 1% (1:15 V/V) diluted solution of  $\text{SnO}_2$  containing  $0.0005 \mu\text{L}$  Triton X-100 surfactant is used after 3 hours of mixing. The  $\text{SnO}_2$  solution is spin coated at 2000 rpm for 20 s

followed by IPL annealing (Sinteron S-2210, Xenon Corp.) as introduced and optimized in chapter 4.

For inkjet printing, the SnO<sub>2</sub> solution is fabricated using a robotic setup as shown in Fig. 3.1 by dispensing the solution using a Nordson Picopulse inkjet printing system equipped with 50 μm size nozzle in a serpentine pathway using a programmable stepper motor driven linear stage with 7 μm resolution per step. The SnO<sub>2</sub> films were formed at the optimal stroke and frequency of 50% and 40 Hz, respectively, and the line distancing was set 350 μm to optimally merge the lines and form a continuous wet film. The open and close times of the valve were set to 0.35 and 0.3 ms, respectively, and a constant 10 psi pressure was applied to the syringe reservoir to push the precursor to the nozzle during actuation. Upon inkjet printing, the SnO<sub>2</sub> ETL was transferred to the IPL station located 1000 mm apart by passing under a suction hood at the linear speed of 50 mm/s. Upon reaching to IPL station, the wet SnO<sub>2</sub> films were annealed using the optimized IPL annealing condition as described in chapter 4 to evaporate the water content and obtain a 40 nm thick crystallized film.

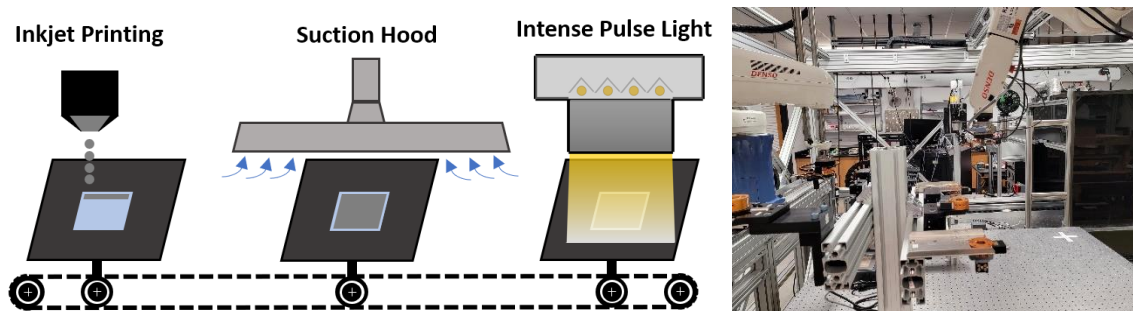


**Figure 3.1.** Schematic showing the robotic setup used to fabricate the PSC films.

### 3.3. Perovskite Film Fabrication



The  $\text{CH}_3\text{NH}_3\text{PbI}_3$  perovskite precursor was made similar to the previous work [254] by dissolving 0.6454 gr  $\text{PbI}_2$  and 0.2226 gr  $\text{CH}_3\text{NH}_3\text{I}$  in 1 mL DMF and 0.125 mL DMSO. The  $\text{Cs}_{0.05}(\text{MA}_{0.85}\text{FA}_{0.15})_{0.95}\text{PbI}_3$  triple cation perovskite ink was made by mixing 0.013 gr CsI, 0.6454 gr  $\text{PbI}_2$ , 0.0343 gr FAI, and 0.18 gr MAI in the similar solvent system. Upon complete dissolution and formation of the transparent yellow precursor, di-iodomethane was added to the solutions and stirred for two hours. Both precursors were fabricated in nitrogen glovebox. The perovskite precursors were spin coated on the ETL at 1000 rpm for 10 s followed by 3000 rpm for 30 s, where 100 and 200  $\mu\text{L}$  chlorobenzene was dripped on the substrate 12 seconds before the end of the spinning process to nucleate the single and triple cation precursors, respectively. During spinning, the spin coater chamber was purged with dry air to keep the humidity below 10%. Upon deposition, the perovskite films were immediately annealed in the humid ambient environment (>60%) to obtain a 450 nm thick film. For the perovskite films annealed with aid of a pre-annealing step, the wet adduct film was pre-heated on a hotplate set to 110°C for 30 seconds followed by optimized IPL annealing (Sinteron S-2210, Xenon Corp.) using 5 flashes, each with 400 J ( $1.72 \text{ J/cm}^2$ ) energy, 2 ms duration, and 1 second delay time between flashes as studied in another work [254]. For PSCs annealed directly through IPL, the slides were immediately transferred to the IPL machine to be annealed through a uniform and gradient approach as described and optimized in chapter 5. For flexible substrates with triple cation perovskite, the spin coated films were pre-heated at 75 °C for 10 s on the hotplate and were subsequently annealed through a single flash of IPL carrying 400 J ( $1.72 \text{ J/cm}^2$ ) energy, an optimal condition where perovskite film damage was observed at higher energy quantities.

### **3.4. Hole Transport Layer (HTL) Fabrication**

The Spiro-MeOTAD hole transport solution was made by mixing 72.3 mg of Spiro-MeOTAD, 28.8  $\mu\text{L}$  4-tert-butyl-pyridine, 17.5  $\mu\text{L}$  of a stock solution of 520 mg/ml lithium bis (trifluoromethylsulphonyl) imide in anhydrous acetonitrile, and 29  $\mu\text{L}$  of the cobalt dopant FK209 TFSI salt (300 mg/ml in anhydrous acetonitrile) in 1 mL anhydrous chlorobenzene. The Spiro-MeOTAD film is made by spin-coating 70  $\mu\text{L}$  of the prepared solution at 1700 rpm for 30 seconds to obtain 200 nm thickness.

### **3.5. Back-contact Electrode Fabrication**

For conventional PSCs, the gold metal back-contacts were made by thermally evaporating pure pellets of Au to obtain 60 nm thickness.

For inkjet printing, the carbon inks were made in the humid ambient environment (>60%) by adding 1:3 w/w ratio of carbon black to graphite (<20  $\mu\text{m}$ , spherical) into a 5 wt% solution of PMMA (15000 Mw) in chlorobenzene (CB) for a concentration of 10 wt%. For carbon PSCs, the custom developed carbon ink was directly deposited on the perovskite film through the similar setup showed in Fig. 3.1 using the Nordson Pico Pulse inkjet printing system equipped with 100  $\mu\text{m}$  diameter size nozzle. Similar to  $\text{SnO}_2$  deposition, the open and close times of the valve were set to 0.35 and 0.3 ms, respectively, and a constant 10 psi pressure was applied to the syringe reservoir to push the carbon ink to the nozzle during actuation. Upon deposition, the wet carbon films were transferred to the IPL station by passing under the suction hood at the speed of 25 mm/s to evaporate the solvent system. Upon reaching to IPL, the dry carbon films were annealed as described and optimized in chapter 6.

### **3.6. PSC Fabrication**

ITO-PET or FTO glass slides are first cleaned through 10 min individual sonication in a 1:10 V/V diluted solution of Hellmanex detergent in DI water, DI water, ethanol, and DI water, respectively. After blowing with nitrogen to remove the remainder water, plasma treatment is conducted to enhance the hydrophilicity of the slides. The TiO<sub>2</sub> and SnO<sub>2</sub> ETL is then coated on slides and annealed as described. Before annealing, the electrode locations covered with SnO<sub>2</sub> are wiped using cotton swabs dipped in DI water. Thereafter, the perovskite film is developed on the ETL and annealed as introduced. Right after perovskite annealing, the substrates are transferred to a nitrogen filled glovebox for Spiro-MeOTAD HTL coating, followed by back-contact electrode deposition to accomplish PSC fabrication, as described.

### **3.7. Temperature Measurement**

The estimated maximum temperature occurring at the perovskite film surface during IPL annealing was measured using a K-type thermocouple consisted of a Chromel and an Alumel wire (0.08 mm, Omega engineering) joint together through a hot junction and was kept tangent to the thin film surface to measure the photon temperature occurring at the perovskite film as shown in Fig. 3.2. The thermocouple was connected to a 300 MHz, 2.5 GSa/s high-speed oscilloscope (DS 8302, Owon smart) via a low noise amplifier (SR560, Stanford research systems) with a gain of 100X to measure the generated voltage during flashing. The obtained voltage was then converted to reflect the temperature rise during flash annealing.

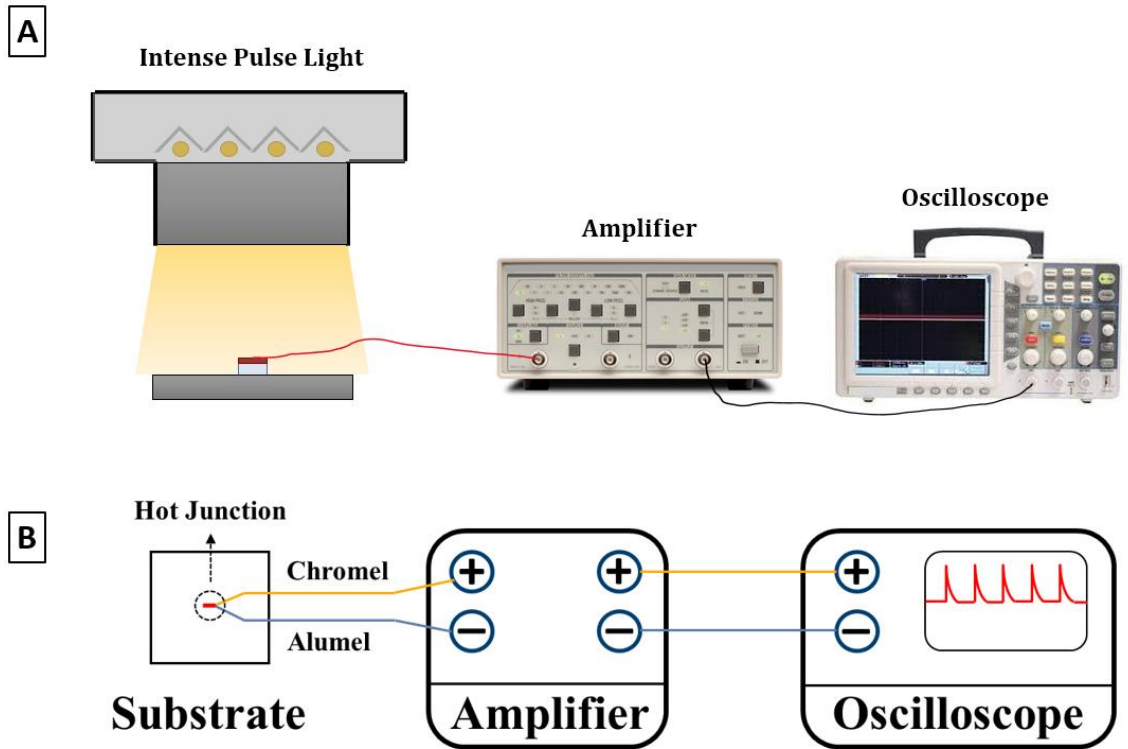


**Figure 3.2.** A) Schematic; and B) Wiring diagram of the experimental setup used for temperature measurement at the film surface.

### 3.8. Finite Element Analysis (FEA) Modeling

To verify the measured temperatures occurring at the surface of perovskite film, a transient thermal finite element analysis (FEA) simulation was conducted using ANSYS. The simulation was conducted by modeling the IPL annealing on perovskite films deposited on glass slides placed on the IPL Aluminum stage with 450 nm, 3 mm, and 6.35 mm thickness, respectively, and considering an ambient temperature as well as natural convection coefficient of  $T_{\infty} = 22^{\circ}\text{C}$  and  $h = 5 \text{ W/m}^2\cdot\text{K}$ , respectively. The model was considered insulated ( $Q=0 \text{ W}$ ) on the sides to carry out one dimensional heat transfer towards the depth direction of the thin film, and a contact resistance of  $R_c = 20\%$  between

glass and aluminum stage was used when placing the slides on the IPL stage for annealing. The application of the contact resistance is due to the rougher interface between substrate and IPL stage unlike the high adhesion of the processed perovskite on glass. The schematic showing the assigned boundary conditions is shown in Fig. 3.3. The designed model had the actual thicknesses, but a smaller surface with 2  $\mu\text{m}$  side length was chosen to speed up the calculations. The model was meshed uniformly using square elements, each with  $5 \times 10^{-7}$  m size. The slides were raised to be located at  $d=75$  mm from the lamp during IPL annealing. The thermal response equations governing the IPL annealing were discussed in chapter 2 which was shown to be dependent on the absorbed photons by the perovskite film as well as thermal conductivity, density, and specific heat transfer capacity of the perovskite film which was considered 1.1 W/m.K, 4.2864 g/cm<sup>3</sup>, and 190 J/mol.K, respectively, based on values reported in other studies [255-257]. Upon flashing, the useful energetic photons reach the perovskite film, where they can be absorbed based on the absorptivity of the layer. Considering almost an entire absorption of the incoming useful energetic photons by the thermocouple located on top of the perovskite film, as shown in Fig. 3.4, the yellow adduct perovskite absorbed nearly 63% of the useful photons and increased to 85% as the IPL annealing progressed which can be attributed to the darkening of perovskite film. The calculated useful power density absorbed by the thermocouple located on top of the perovskite film surface within a single flash of IPL released from four Xenon lamps powered by two capacitors during optimum annealing of perovskite films is tabulated in Table A-1 and Table A-2 of appendix A. In addition, the step-by-step procedures with screenshots showing the simulation processes in ANSYS is provided in Appendix B.

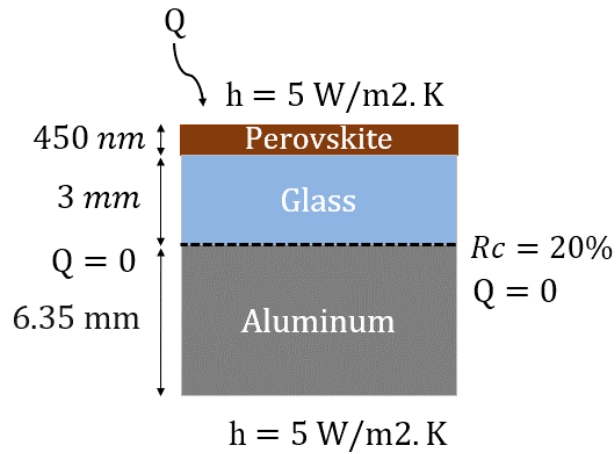


**Figure 3.3.** Schematic showing the boundary conditions used for FEA.

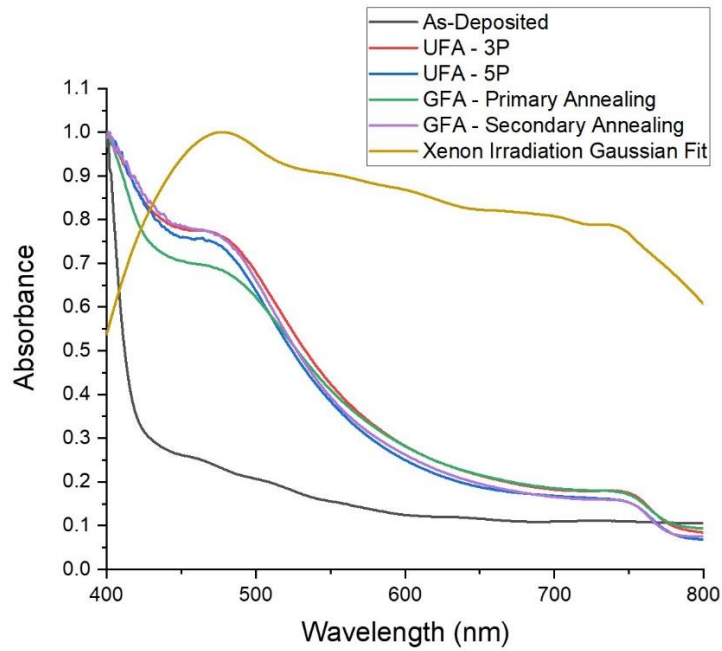


**Figure 3.4.** Maximum absorbance of the useful energetic photons by the perovskite film during IPL annealing using UFA and GFA.

### 3.9. Characterization

Surface morphology inspections are done through a FEI Nova NanoSEM 600 machine with an accelerating voltage of 10 kV and a working distance of 5 mm. XRD measurements are obtained at the  $2\theta$  range between  $10^\circ$ - $60^\circ$  using a Bruker AXS D8 X-ray Diffractometer equipped with a position sensitive detector (PCD) and an X-ray source of  $\text{CuK}\alpha$  ( $\lambda = 0.1548$  nm) with the scanning speed of 1 second/step and the step size of  $0.02^\circ$ . X-ray photoelectron spectroscopy (XPS) is carried out using VG scientific MultiLab 3000 at high vacuum pressure range of  $10^{-8}$  Torr using an  $\text{MgK}\alpha$  radiation X-ray source ( $h\nu > 1253.6$  eV) with respect to the carbon C1S peak position. The IS and voltammetry are conducted using an Autolab PGSTAT128-N potentiostat with the scanning rate of 0.1 V/Sec. Each cell is illuminated from the back side with an active area of  $0.24 \text{ cm}^2$  (Chapter 4) and  $0.45 \text{ cm}^2$  (Chapter 5 and 6) using an AM 1.5 simulated light from a Newport LCS-100 solar simulator. The transmission and absorption spectra are obtained using PerkinElmer Lambda 950 UV-Vis spectrometer between 250-800 nm wavelengths. PL analysis is carried out using a Renishaw inVia Raman microscope with a CCD detector and a 632 nm He-Ne laser source.

CHAPTER IV  
IPL ANNEALING OF SnO<sub>2</sub>

**4.1. Introduction**

Electron transport layer (ETL) plays a significant role in PSCs by facilitating the extraction of electrons from the perovskite photo-absorber film to the contact electrode. Therefore, the optimum chemistry and processing of ETL plays a significant role not only on the performance of PSCs, but on the overall cost and energy payback time of the fabricated modules. The utilized materials in ETL should enable superior morphology without pinhole surface defects to impede shunting as the result of the direct contact between the perovskite film and the contact electrode. In addition, they should yield high optical transmittance and possess an adequate refractive index to maximize photo absorption by the perovskite film, particularly in the n-i-p structure where the solar irradiation should pass through the substrate, transparent conductive oxide, as well as the ETL before being absorbed by the perovskite film. ETLs are typically deposited on rigid substrates, such as FTO coated glass, or ITO coated flexible substrates, such as polyethylene terephthalate (PET), in the n-i-p device structure, or on top of the perovskite film in the p-i-n structure. However, n-i-p structure is typically used to fabricate PSCs due to a more versatile chemistry engineering as the deposition of ETL on perovskite film requires perovskite friendly solvents to achieve efficient and stable PSCs upon deposition and processing. Besides these criteria, the band energy alignment is perhaps the most



important parameter affecting the selection of materials to be used in ETL. The CBM of the electron transport material (ETM) should be well aligned to the perovskite layer to facilitate charge extraction and avoid interfacial contact resistance, affecting the PV parameters of PSCs.

The Electron transport materials (ETMs) used in PSCs span organic and inorganic compounds. The organic ETLs utilize polymer materials containing fullerene derivatives [258-260], naphthalene di-imides (NDIs) [261], perylene di-imides (PDIs) [262-264], azaacene-based molecules [265, 266], and other n-type polymers. Among these, the use of fullerene based materials, particularly C<sub>60</sub> and C<sub>70</sub>, has developed phenyl-C<sub>61</sub>-butyric acid methyl ester (PCBM) as a potential organic ETM in PSCs due to its Lewis acid, acting as a good n-type material as well as its passivation capability by interacting with under-coordinated halide or Pb-I anti-site defect PbI<sup>3-</sup> [267, 268]. Since the pioneering work utilizing PCBM [269], the PCE of PSCs utilizing this organic compound has improved from 3.9% to over 20% [95, 270]. However, they lack thermal and long-term stability. In addition, the deposition requires inert environments, such as a nitrogen glovebox, to impede moisture penetration and degradation of the material, downgrading the functionality of PSCs. In addition, polymer-based materials are expensive, thus, not favorable for large-scale manufacturing. Therefore, it is necessary to develop and investigate for alternative materials that yield efficient PSCs with long-term stability through low-cost scalable manufacturing.

Recently, inorganic materials have garnered a great attention as potential candidates for ETL in PSCs. These materials include various metal oxide compounds such as TiO<sub>2</sub>, SnO<sub>2</sub>, ZnO [99], WO<sub>3</sub> [103, 271], In<sub>2</sub>O<sub>3</sub> [272, 273], Nb<sub>2</sub>O<sub>5</sub> [274, 275], CeO<sub>x</sub> [106], and

BaSnO<sub>3</sub> [276, 277]. Among these, TiO<sub>2</sub> is the most commonly used ETM due to its suitable bandgap and band alignment to the perovskite film [278], and PSCs with the state of the art efficiencies have been produced using TiO<sub>2</sub> [71]. However, several factors would impede achieving scalable low-cost manufacturing of PSCs using this compound. TiO<sub>2</sub> based PSCs require an additional mesoporous TiO<sub>2</sub> layer to be deposited on top of a compact TiO<sub>2</sub> layer to maximize charge extraction from the perovskite film due to low electron mobility, typically less than 1 cm<sup>2</sup>V<sup>-1</sup>s<sup>-1</sup> [278]. In addition, UV induced degradation of TiO<sub>2</sub> can affect the stability and performance of PSCs [279]. Furthermore, TiO<sub>2</sub> requires a high temperature and prolonged annealing, around 500°C up to an hour, to remove the organics and crystallize the material which is not favorable for low-cost scalable manufacturing and is not applicable for favorable plastic substrates that typically degrade at 120-150°C. ZnO is another favorable ETM used besides TiO<sub>2</sub>. This compound has the bulk electron mobility of up to 300 cm<sup>2</sup>V<sup>-1</sup>s<sup>-1</sup>, and over 0.06 cm<sup>2</sup>V<sup>-1</sup>s<sup>-1</sup> for the thin films [280]. However, despite low temperature processing advantage, the interfacial degradation caused by the hydroxyl groups has been reported to diminish PSCs stability [281] although passivation strategies have yielded efficient PSCs with more stability [282].

Recently SnO<sub>2</sub> has been introduced as the most potential ETM in PSCs due to its astonishing properties exceeding other ETMs. This compound has a tetragonal rutile structure with lattice parameters of  $\alpha = \beta = \gamma = 90^\circ$ ,  $a = b = 0.473$  nm, and  $c = 0.318$  nm [283], and has a direct bandgap ranging between 3.5-4.4 eV [284]. Unlike TiO<sub>2</sub>, SnO<sub>2</sub> has a high electron mobility and a deeper CBM which better aligns to the perovskite film, making it a more suitable ETM for PSCs [107]. In addition, SnO<sub>2</sub> has been shown to have high transmittance, exceeding 95% [285] with a refractive index of less than 2 [286]. SnO<sub>2</sub>

ETL have been fabricated using various methods such as chemical bath deposition (CBD) [287], atomic layer deposition (ALD) [108], electrochemical deposition [288], and sputtering [289]. However, they are not susceptible for a low-cost high-speed scalable manufacturing due to the high temperature and prolong processing time as well as requiring vacuum for deposition. In this case, SnO<sub>2</sub> ETL has been fabricated using solution processed precursors through annealing methods at lower temperatures between 150-180°C for 30 min. For instance, Fang et. al developed the SnO<sub>2</sub> ETL by spin coating a solution of SnCl<sub>2</sub>.2H<sub>2</sub>O in ethanol at room temperature followed by annealing at 180°C for an hour and reported 17.21% efficiency PSCs. In a similar attempt, Song et. al [290] fabricated 21.35% efficient PSCs using emulsion-based bottom-up self-assembly strategy by heating the spin-coated SnO<sub>2</sub> films for 30 min at 150°C. Similar annealing protocol has also been implemented on pristine and doped SnO<sub>2</sub> ETLs developed from colloidal based solutions [112, 291]. These advances unraveled the possibility of fabricating SnO<sub>2</sub> ETLs from precursors at lower temperatures; however, the processing time is yet challenging. In this case, various annealing methods have been conducted to develop efficient PSCs in a short span of time. Recently, rapid thermal annealing methods have been successfully shown to anneal SnO<sub>2</sub> films, resulting in efficient PSCs. For instance, Dou et. al. [188] successfully produced roll-to-roll printed PSCs, achieving 19.6% efficiency PSCs. However, the SnO<sub>2</sub> ETLs were annealed at 220°C through two ovens, each having one-meter length which is not favorable for rapid cost-effective manufacturing and the annealing temperature is not applicable for flexible plastic substrates. Zhu et. al. [247] reported rapid formation of SnO<sub>2</sub> ETL from a solution of SnCl<sub>4</sub> in ultra-pure water using IPL and reported 15.3% efficiency after 20 ms light exposure with the total energy of 46 J/cm<sup>2</sup>. Despite such improvements,

none of these investigations managed high throughput processing of both the ETL and perovskite films which would take a closer step towards rapid scalable fabrication of PSCs.

Besides the significance of ETL material and processing, the functionality of PSCs is highly dependent on the crystallinity and morphology of the perovskite absorber layer obtained by processing the film in an inert environment, particularly nitrogen glovebox. However, the use of special environments is not favorable for scalable manufacturing of PSCs. Recently, alkyl halide additives have been introduced into PSC thin films, particularly in the perovskite absorber chemistry. These compounds are cheap, and their incorporation enables developing precursors from more environmentally friendly solvents by offsetting the need for toxic polar solvents and achieving efficient PSCs. 1,8-Diiodooctane (DIO),  $C_8H_{16}I_2$ , is the pioneering alkyl halide that, once added to a perovskite chemistry, forms a momentary coordination with  $Pb^{2+}$  and occupies two I positions of the perovskite lattice and can be explained based on the hard and soft acid and base theory, where, I and  $Pb^{2+}$  with almost similar chemical hardness of 3.69 and 3.53 eV react with each other, respectively [292]. Tsai et. al [293] increased the efficiency of PSCs from 10.77% to 12.86% utilizing 1% DIO which was attributed to the optimum crystallization retardation by the additive, in which, the occupied iodine phases in perovskite lattice were replaced with the iodine phase of MAI and removed from the thin film during annealing. In another study, Chueh et. al [93] studied the role of different alkyl halides of 1,4-diiodobutane (DIB), 1,4-dibromobutane (DBrB), 1,4-dichlorobutane (DCIB), DIO, and 1,10-diiiododecane (DID) on the performance of PSCs and achieved 13.09%, 12.88%, 11.76%, 11.62%, and 10.01%, respectively, which was higher than pristine PSCs with 9.79% efficiency. Notably, the lower performance of DID devices was attributed to the low

solubility of the alkyl halide in the polar perovskite solvents. Xu et. al [294] indicated that the addition of low boiling point iodomethane ( $\text{CH}_3\text{I}$ ) alkyl halide into  $\text{CH}_3\text{NH}_3\text{PbI}_{3-x}\text{Cl}_x$  perovskite chemistry increased the number of excitons, diffusion length of generated charge carriers, and photoluminescent life time to over 4  $\mu\text{s}$  through improved film morphology and diminished trap states which, in turn, enhanced the PV performance from 13.07% to 15.06%. Recently, the incorporation of a novel alkyl halide, di-iodomethane ( $\text{CH}_2\text{I}_2$ ), enabled ambient environment processing of perovskite films for the first time [254]. The  $\text{CH}_2\text{I}_2$ - $\text{CH}_3\text{NH}_3\text{PbI}_3$  perovskite precursor resulted in a continuous morphology with larger grains, increasing the efficiency of PSCs to 16.5% upon IPL annealing. This staggering achievement was attributed to the crystallization retardation as the result of higher boiling point of  $\text{CH}_2\text{I}_2$ , decreasing the evaporation temperature of the perovskite precursor as well as the dissociation of the C-I bonds, supplying the annealing film with excess iodine, thus avoiding the formation of perovskite black phase with defected lattice as the result of iodine deficiency.

The mentioned studies exemplified how various alkyl halides could aid fabricating PSCs from cheap, more environmentally friendly materials, and achieve higher PV performance. However, all these studies annealed the developed films up to 30 minutes at 90-100°C which is not applicable for high throughput fabrication. In addition, the incorporation of these alkyl halides required the perovskite films to be deposited in the nitrogen glovebox to avoid being affected by the ambient humidity, resulting in low performance PSCs due to forming poor perovskite film morphologies with low crystallinity and optical absorption. Scalability of PSCs requires rapid ambient environment processing of PSCs through cost-effective automation to minimization the cost and energy payback

time of fabricated modules [295, 296]. This chapter investigates phase, morphology, crystallization, and spectrophotometry evolution of  $\text{CH}_3\text{NH}_3\text{PbI}_3$  perovskite films containing a novel alkyl halide, di-iodomethane ( $\text{CH}_2\text{I}_2$ ), which allows for ambient environment processing of perovskite films for the first time. In addition, it is shown that IPL annealing of  $\text{CH}_2\text{I}_2$ - $\text{CH}_3\text{NH}_3\text{PbI}_3$  perovskite precursor results in a considerably higher PSC efficiency than neat devices without the additive and is applicable for scalable high-throughput automated manufacturing, such as roll-to-roll.

This chapter investigates IPL annealing of amorphous  $\text{SnO}_2$  on glass-FTO and flexible PET-ITO substrates in a high humid ambient environment (>60%). The perovskite film is developed from a mixed triple cation precursor containing  $\text{CH}_2\text{I}_2$  alkyl-halide which indicates its compatibility with another perovskite chemistry. The study is conducted by initially finding the suitable flash (pulse) energy and counts for the optimum annealing of  $\text{SnO}_2$  ETL on rigid glass-FTO slides, studying  $\text{CH}_2\text{I}_2$  in the triple cation perovskite chemistry and, finally, applying the optimized conditions to make PSCs on both the rigid FTO coated glass and PET-ITO flexible substrates. The morphological inspections are carried out using SEM, the structural properties are investigated using XPS and XRD techniques, PL and IS are used to examine the interfacial charge transport capability, and voltammetry is used to measure the device performance. This study introduces a faster processing through shortening the annealing time of  $\text{SnO}_2$  films, which can be implemented for scalable fabrication of PSCs through low-cost automated manufacturing.

#### **4.2. Morphology Inspections of $\text{SnO}_2$**

In this work, planar n-i-p PSCs with ITO-PET and FTO-glass/ $\text{SnO}_2$ /Perovskite/Spiro-MeOTAD/Au structure are fabricated, where the  $\text{SnO}_2$  ETL is developed through a single

step spin coating followed by IPL annealing [297]. To determine the surface coverage and film quality of SnO<sub>2</sub>, SEM images of FTO and SnO<sub>2</sub> thin films on glass-FTO substrates were taken. The image of FTO, shown in Fig. 4.1(A), displays distinct grain boundaries under 200 nm magnification. In comparison, images of the SnO<sub>2</sub> film coated on glass-FTO (Fig. 4.1(B)) appear hazy and the distinct grain boundaries shown in Fig. 4.1(A) are less apparent. This indicates that glass-FTO surface is covered with SnO<sub>2</sub>, and the disappearance of grain boundaries determines successful uniform deposition of the SnO<sub>2</sub> film which should diminish shunting as the result of the direct contact between perovskite and FTO.

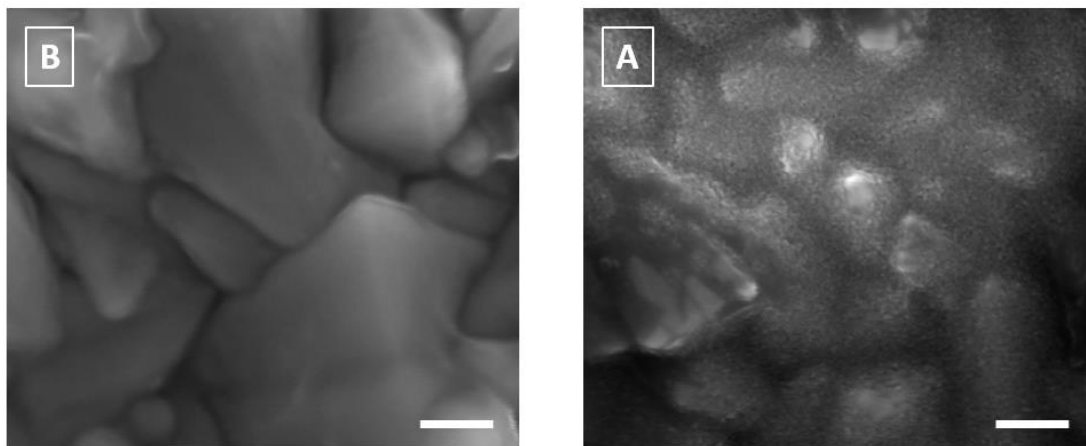


**Figure 4.1.** Top surface SEM images of A) FTO; and B) SnO<sub>2</sub> film coated on FTO showing SnO<sub>2</sub> coverage.

### 4.3. Chemical State Evolution of SnO<sub>2</sub>

To understand the feasibility of IPL annealing on SnO<sub>2</sub> ETL, FTO glass slides carrying the wet spin coated SnO<sub>2</sub> films were immediately transferred to the IPL machine and

different flash counts carrying various energy quantities were applied. During the IPL process, the water content evaporates from the wet film and the SnO<sub>2</sub> nanoparticles crystallize and become capable for charge carrier transportation. It is expected for the charge carrier transportation capability to be dependent on the degree of SnO<sub>2</sub> crystallinity which, in turn, is dependent on the heat flux per flash, as well as the duration and number of applied flashes. This study was carried out by merely varying the flash energy and count. The applied flash energies were 1.4 kJ (6 J/cm<sup>2</sup>) and 2.1 kJ (9 J/cm<sup>2</sup>), and five different pulse (flash) counts of 1, 3, 5, 10, and 15 were selected to anneal the SnO<sub>2</sub> films.

A previous study on the utilized SnO<sub>2</sub> material further exhibited the compositional fraction of the material elements, and TEM images verified the 1-3 nm size of the SnO<sub>2</sub> particles. In addition, the XRD peaks at 26.5°, 33.7°, and 51.6° corresponding to 110, 101 and 211 crystal planes of tetragonal SnO<sub>2</sub> structure with space group P42/mnm (JCPDS no. 41-1445) confirmed the formation of pure SnO<sub>2</sub> phase, respectively [116]. To further study SnO<sub>2</sub>, XPS was used to interpret the crystallization through chemical state change of the material at different IPL processing parameters. Fig. 4.2 (A) indicates the full XPS spectrum of SnO<sub>2</sub> films fabricated through the optimal annealing condition of 5 pulses at 2.1 kJ energy. It can be clearly observed that XPS indicated a neat pattern demonstrating intense peaks of tin and oxygen without any other chemical species and functional groups which can suggest the formation of uncontaminated samples containing high concentration of tin and oxygen elements. The two small peaks at 293 and 295.5 eV are attributed to K2P<sub>3/2</sub> and K2P<sub>1/2</sub> orbitals of potassium ions used as the stabilizer in making the commercial product of the SnO<sub>2</sub> colloidal dispersion solution [298]. It is assumed that the bonding nature of surface level Sn-O observed in XPS spectra will be indicative of the bulk



material given that the film is about 25-40 nm thick. The O1s peak can be deconstructed into two components indicative of O-Sn<sup>4+</sup> and O-Sn<sup>2+</sup>, as shown in Fig. 4.2(B) [299]. The O-Sn<sup>4+</sup> peak is higher in binding energy than the O-Sn<sup>2+</sup> peak; hence, the IPL processing condition that maximizes the O1s binding energy will maximize the surface concentration of SnO<sub>2</sub>. The O1s peak intensity for all the IPL annealing conditions remained similar which can be an indicator of unchanged oxygen concentration change. However, the binding energy of O1s peak was maximized when processed through 5 pulses at 2.1 kJ IPL condition, which can indicate enhanced Sn-O interaction and, thus, strengthened bonding that can better facilitate charge carrier transportation. Similar to O1s peak, the 3d<sub>5/2</sub> peak is a combination of the Sn<sup>4+</sup> and Sn<sup>2+</sup> oxidation states [299]. The Sn<sup>2+</sup> oxidation state arises from oxygen vacancies formed during the spin-coating process and is lower in binding energy than the Sn<sup>4+</sup> oxidation state [300]. The presence of Sn<sup>4+</sup> oxidation state indicates SnO<sub>2</sub> formation; therefore, the IPL processing condition that maximizes the binding energy of Sn 3d<sub>5/2</sub> peak is the optimal SnO<sub>2</sub> processing condition. Fig. 4.2(C) shows that the binding energy of Sn 3d<sub>5/2</sub> peak is maximized for SnO<sub>2</sub> thin films processed through 5 pulses at 2.1 kJ compared to other processing conditions, which, in addition to the obtained results from O1s peak, suggests that this condition would yield the optimal crystallization of the deposited SnO<sub>2</sub> films and is consistent with other reports [301]. The peak intensity for all IPL conditions were almost identical, suggesting that the relative change in tin concentration was negligible. Table 4.1 contains tin and oxygen core level binding energies from the XPS surveys for SnO<sub>2</sub> films annealed through different IPL conditions.

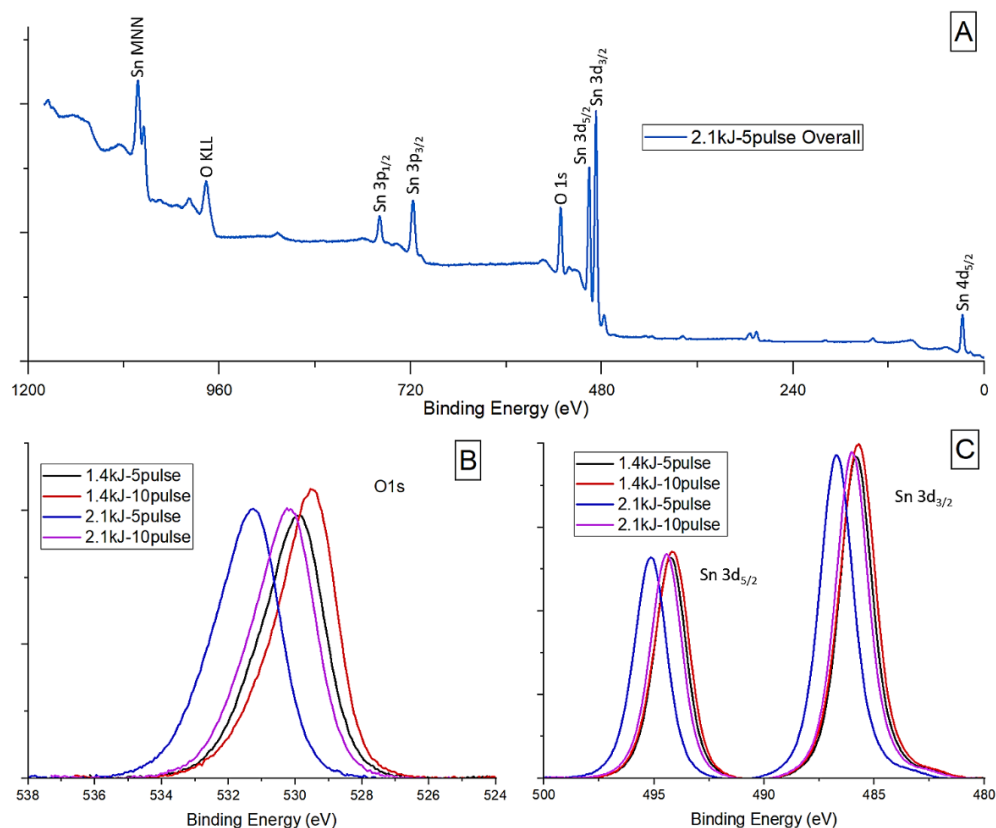


**Figure 4.2.** A) XPS survey of the SnO<sub>2</sub> ETL annealed through 5 pulses at 2.1 kJ IPL condition; XPS patterns of B) O1s; and C) Sn states of the SnO<sub>2</sub> ETL annealed at various IPL conditions.

**Table 4.1.** Core level binding energies for Sn and O1S states at different IPL conditions.

IPL condition	Sn3d <sub>5/2</sub> (eV)	Sn3d <sub>3/2</sub> (eV)	O1s (eV)
1.4 kJ_5 Pulse	494.25	485.85	529.85
1.4 kJ_10 Pulse	494.20	485.70	529.55
2.1 kJ_5 Pulse	495.15	486.70	531.25
2.1 kJ_10 Pulse	494.45	486.00	530.25

#### 4.4. Spectrophotometry of SnO<sub>2</sub> Upon Annealing

Fig. 4.3(A) shows the Tauc plot of SnO<sub>2</sub> used to measure the bandgap of material. As indicated, SnO<sub>2</sub> films annealed through 5 pulses at 1.4 kJ and 2.1 kJ IPL conditions had

the lowest and highest bandgap of 3.72 eV and 3.74 eV, respectively. Fig. 4.3(B) shows the PL spectra for SnO<sub>2</sub> thin films annealed through different IPL conditions. The peak intensity is minimized when SnO<sub>2</sub> films are fabricated through 5 pulses at 2.1 kJ IPL condition. A reduction in PL intensity indicates less charge recombination at the SnO<sub>2</sub>/perovskite interface [302]. Therefore, it can be suggested that the annealing of film through 5 pulses at 2.1 kJ condition would yield the maximum charge transport. In addition, it can be observed that the PL peaks were slightly shifted for the SnO<sub>2</sub> films annealed through different IPL conditions, indicating a blue shift at higher heat fluxes. This blueshift is in accordance with about 0.02 eV bandgap difference shown in Fig. 4.3(A) which can indicate diminished trap emissions and, thus, stronger exciton emissions at elevated flash heat fluxes and conforms with other reports [303, 304].

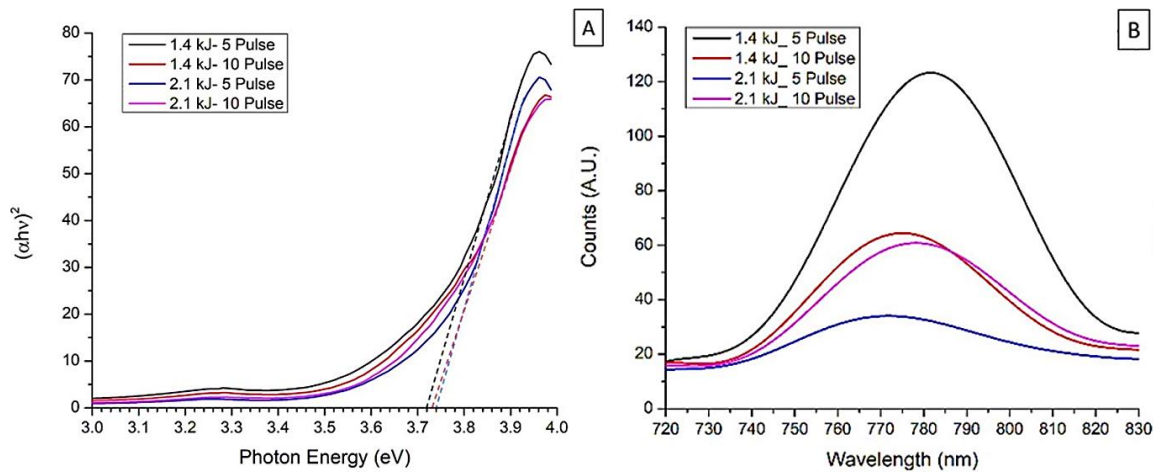


**Figure 4.3.** A) Tauc plot; and B) PL spectra indicating charge transfer capability at SnO<sub>2</sub>/perovskite interface at different IPL conditions.

#### 4.5. Morphology of CH<sub>2</sub>I<sub>2</sub>-Cs<sub>0.05</sub>(MA<sub>0.85</sub>FA<sub>0.15</sub>)<sub>0.95</sub>PbI<sub>3</sub> Perovskite Films

As studied earlier, the incorporation CH<sub>2</sub>I<sub>2</sub> into CH<sub>3</sub>NH<sub>3</sub>PbI<sub>3</sub> chemistry enabled atmospheric fabrication of efficient PSCs. Herein, CH<sub>2</sub>I<sub>2</sub> is added into

$\text{Cs}_{0.05}(\text{MA}_{0.85}\text{FA}_{0.15})_{0.95}\text{PbI}_3$  triple cation perovskite precursor to investigate the possibility of fabricating the perovskite film obtained from another chemistry in the high humid ambient environment (>60%). To discern whether  $\text{CH}_2\text{I}_2$  improved the perovskite film quality and surface coverage, top-down SEM images of the annealed perovskite film, with and without  $\text{CH}_2\text{I}_2$  after IPL annealing, is shown in Fig. 4.4. Fig. 4.4(A) suggests that a fine perovskite film without observable pinholes was formed when  $\text{CH}_2\text{I}_2$  was incorporated into the precursor solution. In comparison, Fig. 4.4(B) contains a top-down SEM image of the IPL annealed perovskite without additive. The image indicates the formation of smaller grain sizes with dendrite structures within the perovskite film, which can be attributed to rapid natural crystallization during spin coating prior to annealing. Formation of dendrite structures can reduce the quality of thin film, while smaller grain sizes can enhance charge recombination at the grain boundaries due to the formation of more grain boundary density within the film, thus, decreasing the photovoltaic performance. To find out the average grain sizes, ImageJ was used to obtain the size and area of individual grains in the perovskite films after IPL annealing. The results indicated average crystal size and area of 201 nm, and  $0.031 \mu\text{m}^2$  for the  $\text{CH}_2\text{I}_2$  containing perovskite films, and 138 nm, and  $0.015 \mu\text{m}^2$  for the films made from the solution without additive, delineating almost 1.45 times crystal growth for the devices made from the additive containing precursor. The histograms of grain size and area are shown in Fig. 4.5. The SEM images suggest that  $\text{CH}_2\text{I}_2$  additive improved surface coverage, grain growth, and quality of the triple cation perovskite film with a slight difference to that of  $\text{CH}_2\text{I}_2\text{-CH}_3\text{NH}_3\text{PbI}_3$  perovskite films [254], by implementing two significant roles. First, the addition of diiodomethane could potentially increase the solution boiling point and delay the unfavorable natural crystallization of the

as-spinning solution, thus, hindering the formation of dendrites and insufficient grain growth upon annealing. Second,  $\text{CH}_2\text{I}_2$  could improve the crystallinity of perovskite layer due to its role as an iodide source. When exposed to IPL, the C-I bond is broken, yielding equal parts of  $\text{CH}_2\text{I}^+$  and  $\text{I}^-$ . The  $\text{I}^-$  ions are then incorporated into the perovskite material by filling iodine vacancies. The released iodine from alkyl halide could replace the lost iodine through evaporation during the annealing processes, thus, avoiding the formation of defected perovskite black phase upon the completion of annealing. Therefore, it is expected that di-iodomethane addition would improve the device performance through enhanced charge carrier production and extraction to the transport films, thus decreasing and increasing the series and shunt resistances, respectively.

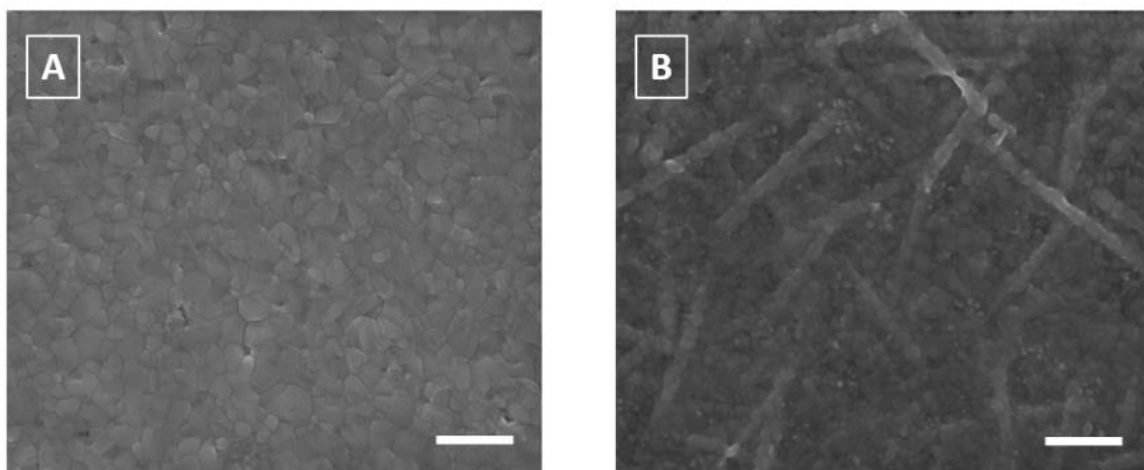


**Figure 4.4.** Top surface SEM image of the perovskite layer A) with; and B) without  $\text{CH}_2\text{I}_2$  additive deposited on optimally IPL annealed  $\text{SnO}_2$  films.

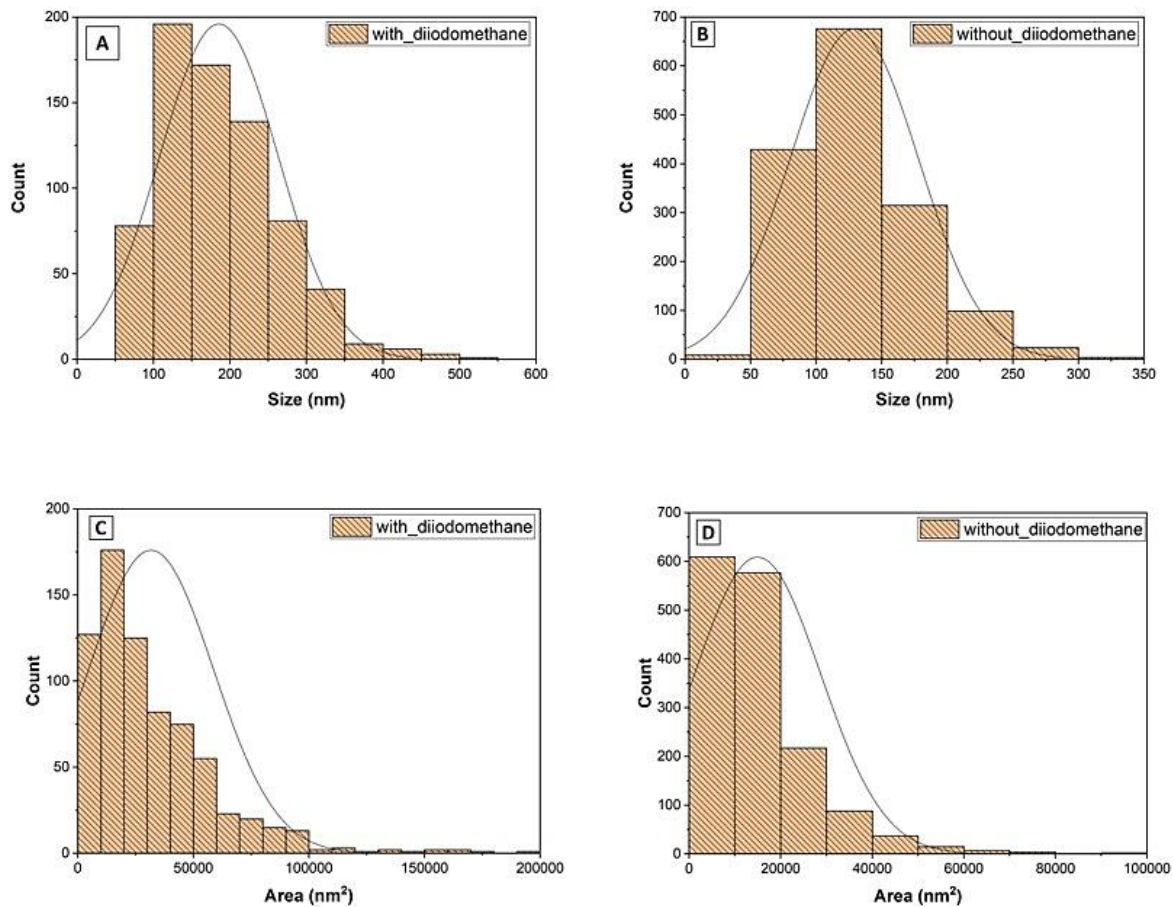


**Figure 4.5.** Histograms indicating the A,B) grain sizes; and C,D) grain areas of perovskite films with and without diiodomethane additive.

#### 4.6. Spectrophotometry of $\text{CH}_2\text{I}_2\text{-Cs}_{0.05}(\text{MA}_{0.85}\text{FA}_{0.15})_{0.95}\text{PbI}_3$ Perovskite Films

Fig. 4.6 shows the absorbance spectra for the FTO/SnO<sub>2</sub>/perovskite and FTO/SnO<sub>2</sub> structures after optimum IPL annealing. The FTO/SnO<sub>2</sub>/perovskite structure demonstrated high absorption between 400-800 nm wavelengths range, whereas, the FTO/SnO<sub>2</sub> structure indicated little to no absorption. This indicates that the solar irradiation reaches the perovskite absorber without being consumed by the ETL. The final device will be

constructed in a manner where light travels through glass, FTO, SnO<sub>2</sub>, then strikes perovskite where it can be absorbed to produce charge carriers.

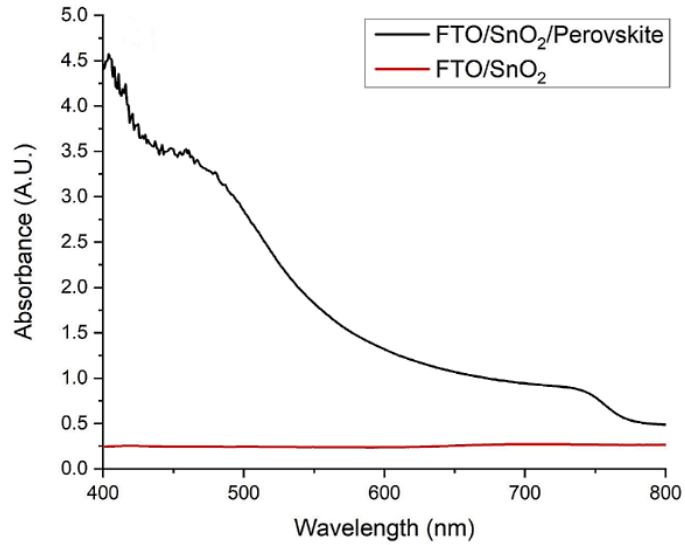


**Figure 4.6.** Absorbance spectra of FTO/SnO<sub>2</sub>/perovskite and FTO/SnO<sub>2</sub> after optimum IPL annealing.

#### 4.7. Crystallography of CH<sub>2</sub>I<sub>2</sub>-Cs<sub>0.05</sub>(MA<sub>0.85</sub>FA<sub>0.15</sub>)<sub>0.95</sub>PbI<sub>3</sub> Perovskite Films

XRD patterns shown in Fig. 4.7 reveal information about crystallinity of the perovskite layer after IPL annealing. The intense  $2\theta$  peaks around 26.5°, 33.75°, 37.5°, 51.2°, and 54.5° are indicative of FTO/SnO<sub>2</sub>, and the strong peaks around 14.06°, 20°, 24.4°, 28.4°, 31.8°, 34.9°, 40.5°, 43°, and 50.5° are associated to (110), (112), (202), (220), (310), (312), (224), (314), and (404) crystal planes indicating the formation of perovskite tetragonal black phase. The perovskite tetragonal black phase is the preferred conformation for PSCs. Fortunately, the patterns did not reveal the PbI<sub>2</sub> peak around 12.4° which indicates formation of a pure perovskite black phase, promoting higher PCE due to fewer series and higher recombination resistances within the perovskite absorber layer. Therefore, the applied IPL annealing condition of 5 pulses, each carrying 400 J (1.72 J/cm<sup>2</sup>)

in 2 ms duration and 1 second delay time in between, for the perovskite film could sufficiently crystallize the layer without causing post degradation of the film nor being insufficient to leave the perovskite yellow phase unconverted to black phase.

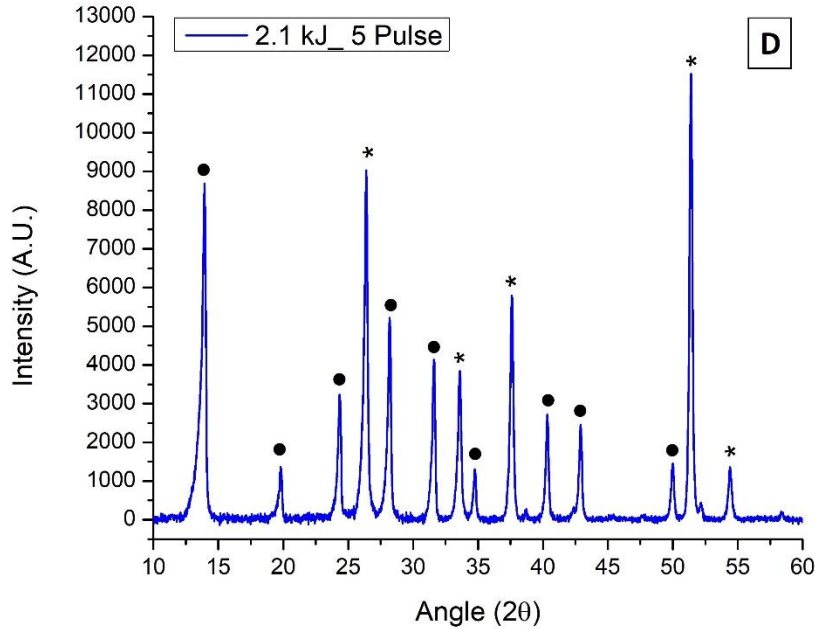


**Figure 4.7.** XRD pattern of the FTO/SnO<sub>2</sub>/perovskite structure demonstrating FTO/SnO<sub>2</sub> (marked with \*) and perovskite (marked with •) peaks after IPL annealing.

#### 4.8. Voltammetry of Rigid CH<sub>2</sub>I<sub>2</sub>-Cs<sub>0.05</sub>(MA<sub>0.85</sub>FA<sub>0.15</sub>)<sub>0.95</sub>PbI<sub>3</sub> Solar Cells

To verify the observed characterization results, voltammetry was used to measure the performance and study the functionality of PSCs. The overall performance summary of PSCs fabricated using four different IPL conditions on SnO<sub>2</sub> ETL is shown in Table 4.2, and the current J-V curves of champion cell for each IPL condition is shown in Fig. 4.8. The results indicate that exposing the SnO<sub>2</sub> thin films to higher pulse energy flux of 2.1 kJ can provide better device performance than the lower pulse energy of 1.4 kJ for all the



range of applied pulse counts which implies the significance of heat flux intensity on material crystallization. On the other hand, lower pulse counts for the higher pulse energy provides the maximum device performance, determining the 5 pulse at 2.1 kJ as the optimal IPL annealing condition which resulted in the highest device performance. As shown by the results, varying the IPL annealing conditions for SnO<sub>2</sub> ETL considerably affected the current flow for all fabricated cells while maintaining the voltage and fill factor. This observation can indicate the significance of IPL annealing conditions on the crystallization of SnO<sub>2</sub>, playing a vital role on facilitating charge extraction at the thin film interface and throughout the film. It was found after several experiments that pulse counts higher than 10 could not enhance the current flow, while pulse counts lower than five resulted in dead cells, demonstrating a resistor behavior. Therefore, thermal annealing is required to crystallize the material and there is an existing optimal annealing condition, where exceeding the limit would not result in an operative or economical fabrication of PSCs.

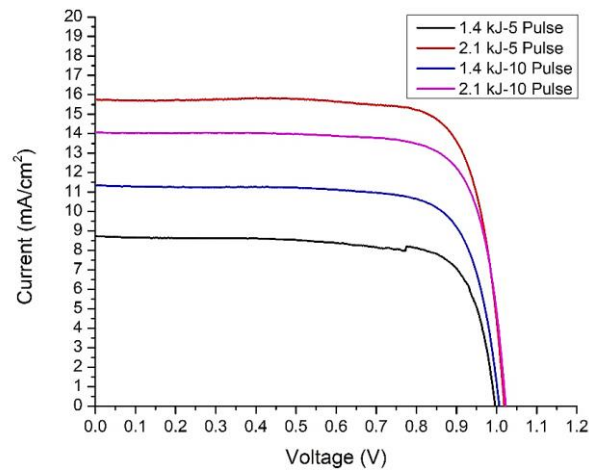


**Figure 4.8.** J-V curves of PSCs fabricated using four different IPL conditions on SnO<sub>2</sub>.

**Table 4.2.** Overall performance of PSCs with SnO<sub>2</sub> annealed through different IPL conditions (5 samples for each condition).

PSCs	CH <sub>2</sub> I <sub>2</sub>	V <sub>oc</sub> (V)	J <sub>sc</sub> (mA/cm <sup>2</sup> )	PCE (%)	FF (%)
1.4 kJ – 5 pulses	Yes	0.92 ± 0.045	11.80 ± 0.60	6.78 ± 0.39	67.40 ±3.71
1.4 kJ – 10 pulses	Yes	0.976 ±	12.67 ± 0.56	9.27 ± 0.49	74.98
2.1 kJ – 5 pulses	Yes	0.019	15.85 ± 0.54	11.98 ±	±0.49
2.1 kJ – 10 pulses	Yes	0.995 ±	14.22 ± 0.11	0.35	76.30
2.1 kJ – 5 pulses	No	0.014	14.95 ± 0.00	9.56 ± 0.98	±1.28
		0.989 ±		6.38 ± 0.74	67.78
		0.015			±6.18
		0.811 ±			53.80
		0.024			±2.16

To further investigate the functionality of PSCs, the interfacial and in-layer charge transportation capability of IPL processed PSCs is studied through impedance spectroscopy (IS) as shown in Fig. 4.9. Operating at open-circuit voltage under low light intensity has been shown to isolate the hole accumulation zone built up between perovskite absorber and ETL [305]. A reduction in overall impedance of the PSCs at open-circuit voltage indicates that charge carriers were more efficiently extracted from the perovskite absorber layer. The impedance was minimized for PSCs with the SnO<sub>2</sub> layer annealed through the 5 pulses at

2.1 kJ IPL condition. These results are consistent with the PL and voltammetry results showed in Fig. 4.3(B) and 4.8, respectively, suggesting that annealing through 5 pulses at 2.1 kJ would be the optimum IPL annealing condition for SnO<sub>2</sub>.

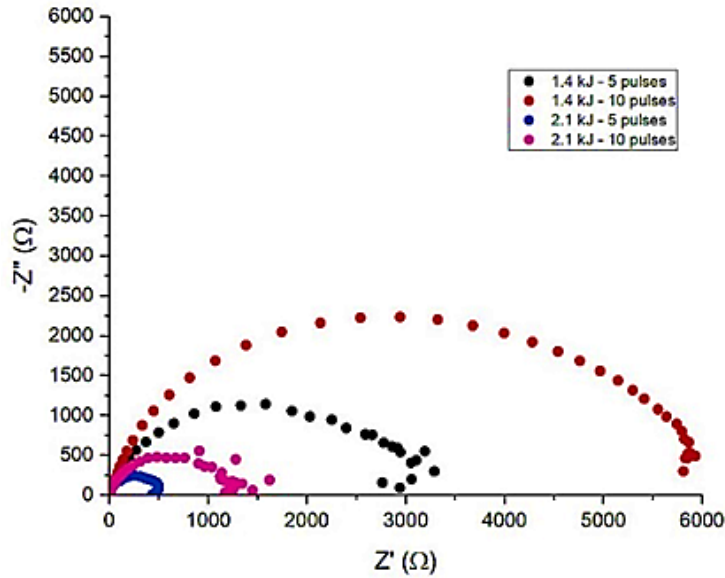


**Figure 4.9.** Impedance spectra of PSCs at four different IPL conditions on SnO<sub>2</sub>.

#### 4.9. Voltammetry of Flexible CH<sub>2</sub>I<sub>2</sub>-Cs<sub>0.05</sub>(MA<sub>0.85</sub>FA<sub>0.15</sub>)<sub>0.95</sub>PbI<sub>3</sub> Solar Cells

To further investigate the scalability and applicability of rapid thermal annealing through IPL on SnO<sub>2</sub>, PSCs were also fabricated on flexible PET-ITO substrates. Fig. 4.10 shows J-V curves indicating the forward and reverse scan of champion rigid and flexible substrates annealed through the optimum IPL annealing condition of 5 pulses at 2.1 kJ for SnO<sub>2</sub>. The J-V curves of rigid and flexible PSCs indicated the maximum reverse scan efficiency of 12.56% and 7.6%, open circuit voltage ( $V_{oc}$ ) of 1.02 and 0.993 volts, short-circuit current density ( $J_{sc}$ ) of 15.78 and 11.87 mA/cm<sup>2</sup>, and the fill factor of 78.3% and 64.75%, as well as the maximum forward scan efficiency of 11.33% and 6.16%,  $V_{oc}$  of 0.992 and 0.979 volts, short-circuit current density of 14.92 and 11.06 mA/cm<sup>2</sup>, and the fill

factor of 76.7% and 56.95%, demonstrating relatively low J-V hysteresis for both rigid and flexible PSCs. It can be observed from the experimental results that the flexible PSCs had a lower performance compared to rigid cells which can be attributed to the higher resistance of ITO coated sheets compared to FTO slides, handling of the flexible substrates during fabrication processes, as well as unsuitable nature of spin-coating method to form highly uniform films with superior quality, particularly for coating water based SnO<sub>2</sub> films on smooth ITO coated sheets compared to rough FTO substrates.

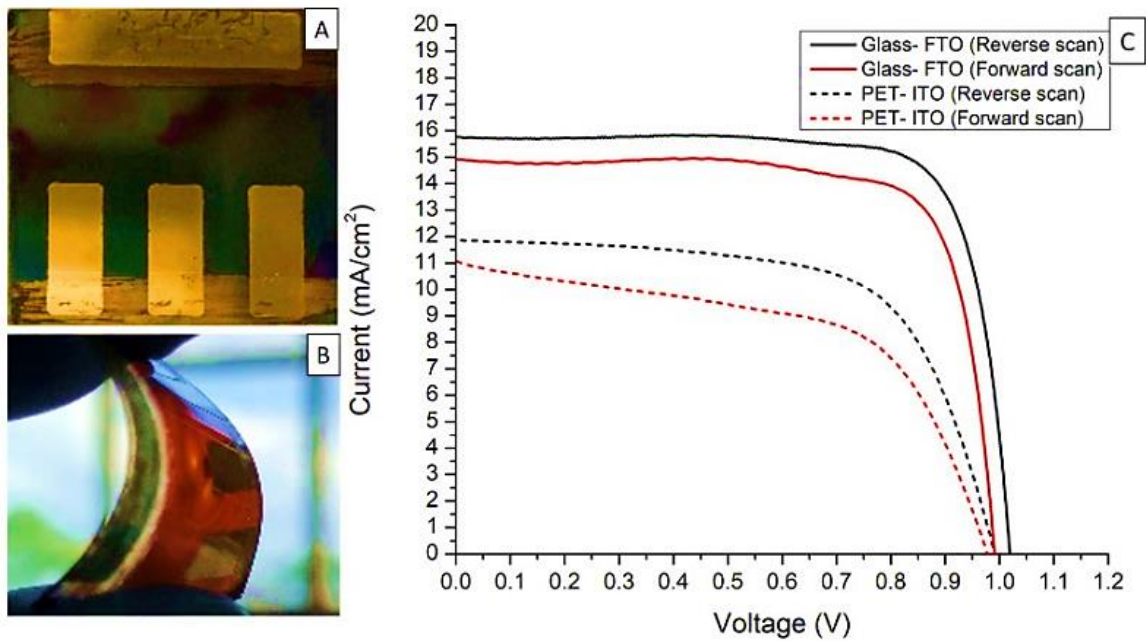


**Figure 4.10.** Illustration of the fabricated PSCs on A) Rigid glass-FTO; and B) PET-ITO flexible substrates. C) Reverse and forward J-V curves of the champion rigid and flexible PSCs.

#### 4.10. Conclusion

This chapter investigated IPL annealing of spin-coated SnO<sub>2</sub> films which was shown to be applicable on both rigid FTO-glass and flexible PET-ITO substrates, yet the

perovskite film was annealed through IPL after short-term conductive annealing. The addition of  $\text{CH}_2\text{I}_2$  resulted in perovskite films with superior morphology and larger grains upon annealing which was attributed to iodine release during annealing processes and crystallization retardation, eliminating dendrite structures by increasing the precursor boiling point. As the result, PSCs with efficiency and fill factor as high as 12.56% and 78.3% for rigid FTO-glass substrates, and 7.6% and 64.75% for flexible ITO-PET sheets were obtained, respectively, when the  $\text{SnO}_2$  ETL was optimally annealed through 5 flashes, each with 2 ms duration, carrying 2.1 kJ energy, and 1 second delay time in between. This study took a further step towards faster fabrication of PSCs through IPL annealing of the ETL layer which is amenable for high-throughput and cost-effective fabrication of PSCs through automation.

## CHAPTER V

### IPL ANNEALING OF PEROVSKITE

#### 5.1. Introduction

The carried-out study in the previous chapter allowed processing of PSCs in an uncontrolled high humid ambient environment (>60%), and the use of IPL indicated faster processing which is a step towards high- throughput fabrication of PSCs. However, like other conventional annealing processes, the perovskite film yet necessitated a short-term conductive annealing for 30 seconds to evaporate the solvents and initiate crystallization since the ultrashort duration was not providing sufficient time to convert the intermediate adduct into the pure perovskite black phase. Therefore, it is necessary to develop approaches that yield rapid formation of the perovskite black phase without short-term conductive pre-annealing upon IPL annealing. In this case, various studies have determined the plausibility of multistep conductive annealing methods on boosting the performance of PSCs. For instance, a pioneering work by Fan et. al [306] utilized a gradient approach by annealing the perovskite films at 80, 85, and 90°C for 20 minutes each, and compared the results to a constant annealing where the perovskite films were merely annealed at 90°C for 20 min. Their PSCs indicated improved PCE from 12.6% to 14% which was credited to better surface coverage and morphology of the perovskite films annealed through gradient annealing. Hao et. al [307] have recently shown to increase the efficiency of PSCs from 16.14% using a uniform annealing (UA) to 20.16%

using a gradient annealing (GA) approach. The UA interacted the as-deposited perovskite films with methylamine alcohol atmosphere for 2 seconds followed by annealing for 30 min at 100°C in a glovebox, whereas the gradient approach included a pre-annealing at 60°C before CA which induced a bottom-up growth of the perovskite film, regulating the growth direction of  $\text{CH}_3\text{NH}_3\text{PbI}_3$  perovskite films, thus, improved the performance as the result of diminished defect states and improved charge transport at  $\text{TiO}_2$ /perovskite interface. The application of GA by Xi et. al [308] also improved the performance of PSCs from 18.64% to 20.04% which was attributed to the better crystallinity of perovskite films. Xiao et. al [309] investigated the impact of temperature fall-off gradient on the quality of perovskite films and PV performance upon annealing. Their results indicated 31% performance improvement, reaching as high as 17.37% when the fall-off temperature gradient was minimized. This enhancement was attributed to the obtained superior morphology and increase of grain size to 1.2  $\mu\text{m}$ . In another work, Chen et. al [310] annealed the  $\text{CsPbI}_2\text{Br}$  perovskite films through a three-step gradated method consisted of 50°C for 1 min, 100°C for 1 min, and 160°C for 10 min annealing, and reported 16.07% efficiency PSCs. These studies introduced successful fabrication of efficient PSCs through gradient conductive annealing in a considerably shorter period than conventional methods; however, they are not amenable for rapid manufacturing, and the utilized higher than 120°C temperatures are not applicable for favorable plastic substrates. Therefore, it is necessary to develop gradated approaches using IPL that allows for the fabrication of PSCs in an extremely short period; hence, meeting the required speed for high-throughput manufacturing.

In this chapter, rapid fabrication of planar PSCs with glass/FTO/SnO<sub>2</sub>/perovskite/Spiro-MeOTAD/Au architecture is introduced by directly annealing the spin-coated CH<sub>3</sub>NH<sub>3</sub>PbI<sub>3</sub> perovskite films through IPL without short or long-term conductive annealing as was utilized in the previous chapter. The perovskite films are annealed entirely through IPL using a graded approach which forms good morphology with high crystallinity. The study is conducted by characterizing the perovskite films through SEM, PL, UV-Vis, XRD, and voltammetry. In addition, an experimental setup as well as a 2D ANSYS finite element analysis (FEA) is established to measure and model the maximum temperature at the surface of the perovskite thin film during IPL annealing, respectively. Finally, Arrhenius plots are introduced to help explaining the PSCs performance enhancement after GFA.

## **5.2. Nucleation of CH<sub>2</sub>I<sub>2</sub>-CH<sub>3</sub>NH<sub>3</sub>PbI<sub>3</sub> Perovskite Films Upon Annealing**

The as-prepared perovskite precursors are yellow, and an annealing process turns it into a dark brown phase. As mentioned, crystallization affects morphology and determines the performance of PSCs; hence, the applied annealing parameters should result in highly crystalline perovskite black phase with superb morphology to maximize charge carrier generation upon illumination. Perovskite photo-absorber crystallization includes nucleation of the as-deposited solution followed by grain growth that typically occurs during annealing. Nucleation kinetics of the perovskite film during spin coating explained with aid of the LaMer curve [211, 212] was introduced earlier in chapter 2 and is again shown in Fig. 5.1(A) to describe the nucleation of CH<sub>2</sub>I<sub>2</sub>-CH<sub>3</sub>NH<sub>3</sub>PbI<sub>3</sub> perovskite. Continuous spinning of the perovskite precursor precipitates the solute after exceeding the maximum supersaturation level, agglomerates the solute species, and forms a rough opaque film with dense dendrite structures as shown in Fig. 5.1(B). Post-process annealing of this



film would result in poor photovoltaic performance due to incomplete surface coverage and weak optical absorption. Therefore, a nucleation process through supersaturation of the precursor is necessary prior to annealing. In this process, chlorobenzene antisolvent with weak polarity and solubility to the perovskite polar solvents was dropped on the spinning perovskite precursor at the 10<sup>th</sup> second (T<sub>1</sub>) prior to the end of spinning process. Upon spin-coating (T<sub>3</sub>-T<sub>1</sub>), a transparent film was obtained and as shown in Fig. 5.1(C), numerous infinitesimal crystals arranging into smaller size dendrites were formed and covered the entire surface which could indicate the formation of CH<sub>3</sub>NH<sub>3</sub>I·PbI<sub>2</sub>·DMSO·DMF·CH<sub>2</sub>I<sub>2</sub> adduct, thus, successful formation of the perovskite yellow intermediate. This nucleation can be attributed to antisolvent dripping which resulted in rapid stochastic intermolecular fluctuations of the atoms to form nuclei and, in turn, crystals, as well as the nuclei shear off from the developing crystals to develop adjacent crystals and proliferate the nucleation throughout the surface [213], consuming and decreasing the size of dendrite clusters. Subsequent annealing of the developed intermediate phase (>T<sub>3</sub>) enables grain growth and formation of perovskite black phase to produce charge carriers upon illumination and will be exhaustively studied in this dissertation. Therefore, the synergy of solvent extraction and solute diffusion determines the nucleation which, in turn, determines the morphology, crystallization, and PSCs performance.

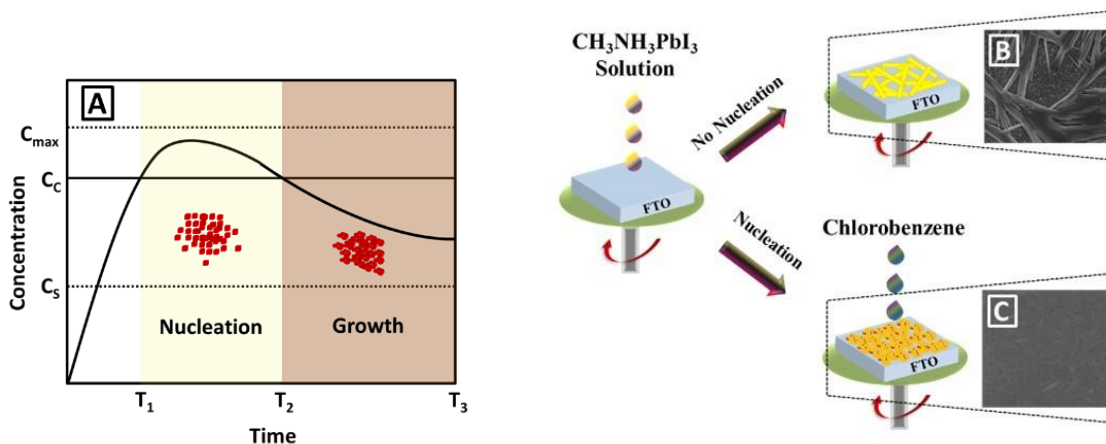


**Figure 5.1.** A) LaMer curve; formation of B) perovskite dendrites without antisolvent treatment; and C) perovskite intermediate upon antisolvent treatment.

### 5.3. Phase Evolution of $CH_2I_2$ - $CH_3NH_3PbI_3$ Perovskite Films Upon Annealing

As described, perovskite films are fabricated through a deposition process with aid of an antisolvent step to nucleate the precursor, and annealing is the driving force for phase change, crystallization, and morphology evolution to obtain the desired black phase, capable of producing charge carriers. Previous studies determined the maximum PV performance to occur for 1.4 M concentration of the perovskite precursors [311, 312]. Therefore, to better understand the impact of annealing on such evolutions, thermogravimetry and differential scanning calorimeter (TGA-DSC) analysis for 1.4 M concentration  $CH_3NH_3PbI_3$  perovskite precursor with  $CH_2I_2$  and its constituents in DMF-DMSO solvent mixture was conducted up to 800°C and is shown in Fig. 5.2. Fig. 5.2(A), shows the TGA-DSC curves for 1.4 M solution of  $CH_3NH_3I$  in the solvent mixture. The abrupt 80% weight loss in TGA graph as well as the intense DSC endothermic peak at 174°C is indicative of complete solvent evaporation. Right after this stage, the DSC curve indicated a strong exothermic peak with the maximum at 254°C, determining maximized

crystallization of  $\text{CH}_3\text{NH}_3\text{I}$ , while the TGA curve indicated a mild slope up to  $330^\circ\text{C}$  where 100% mass loss was observed. This indicates that the  $\text{CH}_3\text{NH}_3\text{I}$  phases could remain in the film up to  $254^\circ\text{C}$  then sublime from the perovskite film at higher temperatures and is consistent with other reports [313]. Similarly, as shown in Fig. 5.2(B), the DSC-TGA curve of the 1.4 M  $\text{PbI}_2$  solution indicated two endothermic peaks at  $157^\circ\text{C}$  and  $402^\circ\text{C}$ , indicating complete solvent evaporation and melting of  $\text{PbI}_2$ , respectively. The high melting point can indicate viability of  $\text{PbI}_2$  up to this temperature and further descend of the TGA graph for temperatures higher than  $430^\circ\text{C}$  demonstrated  $\text{PbI}_2$  decomposition and evaporation of the iodine phase as the result of Pb-I cleavage. Therefore, it can be inferred that the formation of crystal defects caused by  $\text{CH}_3\text{NH}_3\text{I}$  phase evaporation during annealing can be the potential factor for PSCs performance degradation and instability which needs to be considered during IPL annealing and is consistent with other reports [314, 315]. Compared to  $\text{CH}_3\text{NH}_3\text{I}$ , the DSC-TGA curves indicated a slightly lower volatiles evaporation temperature in case of  $\text{PbI}_2$  solution which can indicate stronger intermolecular forces between the solvent mixture and  $\text{CH}_3\text{NH}_3\text{I}$  and a potential retarding factor for perovskite crystallization and is consistent with other reports [302, 316]. Fig. 5.2(C) indicates DSC-TGA curves of the  $\text{CH}_2\text{I}_2$  assisted  $\text{CH}_3\text{NH}_3\text{PbI}_3$  precursor, indicating complete solvent evaporation at  $150^\circ\text{C}$ . The solvent component undergoes evaporation up to this temperature and the heat induced intermolecular activity stimulates crystal growth through diffusion and solvent evaporation, thus, transforms the perovskite yellow phase into black phase structure by amalgamating the  $\text{CH}_3\text{NH}_3\text{I}$  and  $\text{PbI}_2$  phases. The TGA curve indicated a weight loss of about 15% between  $150\text{-}250^\circ\text{C}$ , and the DSC curve indicated the formation of an exothermic peak at  $250^\circ\text{C}$  which is consistent with the data in Fig. 5.2(A) and can

indicate sublimation of the  $\text{CH}_3\text{NH}_3\text{I}$  phase, hence, beginning of the perovskite film degradation after  $150^\circ\text{C}$ . Unlike incomplete decomposition and remaining almost 10% of the mass in Fig. 5.2(B), the perovskite precursor DSC-TGA analysis demonstrated complete mass loss for temperatures higher than  $650^\circ\text{C}$  which can indicate complete elimination of the  $\text{CH}_3\text{NH}_3\text{PbI}_3$  perovskite constituents through evaporation. These results indicate that the annealing processes should be carried out in compliance with the perovskite material properties, and the optimal synergy of the applied heat flux and exposure time is pivotal for PSCs maximized stability and efficiency.

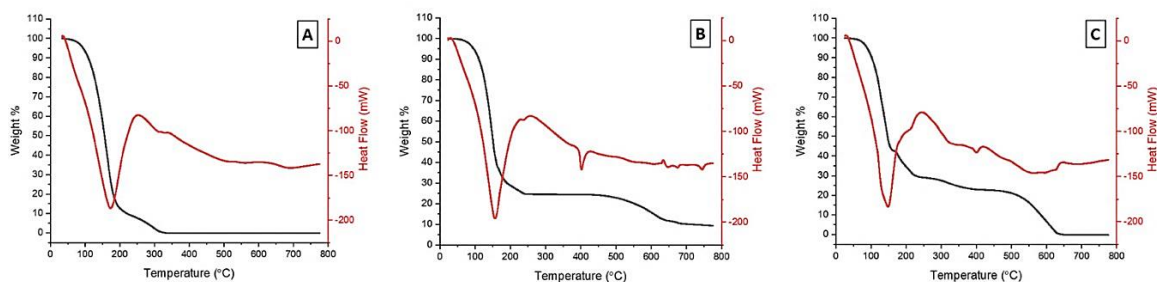


**Figure 5.2.** DSC-TGA curves for 1.4 M solutions of A)  $\text{CH}_3\text{NH}_3\text{I}$ ; B)  $\text{PbI}_2$ ; and C) mixed  $\text{CH}_3\text{NH}_3\text{PbI}_3$  perovskite in DMF-DMSO- $\text{CH}_2\text{I}_2$ .

#### 5.4. Annealing Approaches

To carry out the study, the supersaturated perovskite intermediate, formed by using toluene antisolvent during the spin-coating process, was rapidly annealed through uniform and gradient flashing approaches using IPL. The uniform flash annealing (UFA) was carried out by applying five similar flashes, each with the duration and delay time between flashes of  $t$  and  $D$ , respectively. The gradient flash annealing (GFA) was carried out through two sequential flashing steps consisted of a primary and a secondary annealing step, each consisted of five flashes with a fixed duration of  $t_1$  and  $t_2$ , and interval time

between flashes of  $D_1$  and  $D_2$ , respectively. The flash duration for a constant applied voltage determined the released energy; hence,  $t_1$  was set shorter for the primary annealing to apply lower energy in this step. The schematic indicating the IPL parameters of the two annealing approaches is shown in Fig. 5.3.

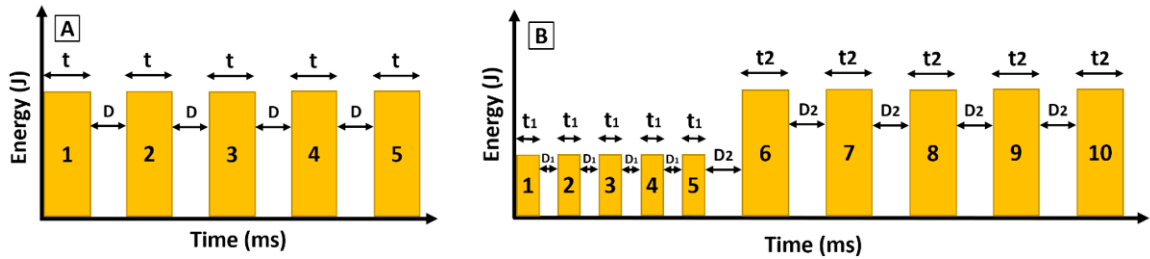


**Figure 5.3.** Schematic showing the IPL parameters for A) UFA; and B) GFA.

### 5.5. Morphology of Uniform Flash Annealed Perovskite Films

The fabrication was initiated by IPL annealing of the  $\text{SnO}_2$  ETL similar to the work introduced in previous chapter [297] followed by rapid annealing of the  $\text{CH}_3\text{NH}_3\text{PbI}_3$  perovskite intermediate through IPL. In the first stage, the perovskite films were annealed through UFA by applying only five flashes, each carrying 400 J energy ( $1.72 \text{ J/cm}^2$ ) and one second delay time between flashes, to anneal the perovskite films in almost 4 seconds as was utilized for IPL annealing of the perovskite film in the previous chapter. Fig. 5.4(A-C) shows the evolution of intermediate phase during IPL annealing. Upon spin-coating, the film was transparent and was associated with the intermediate phase (Fig. 5.4(A)). Fig. 5.4(B) shows the quality of perovskite film after applying three flashes indicating mixed yellow and black phases, and Fig. 5.4(C) shows the formation of darker films after five flashes. This evolution of the film mimics the transformation results using traditional hotplate annealing techniques [317]. Top surface SEM images corresponding to the as-

deposited, three, and five flashes demonstrate the morphology evolution of the perovskite films annealed through different flash counts (Fig. 5.4(D-F)). Fig. 5.4(D) shows the morphology of intermediate phase formed upon spin-coating. Upon annealing with three flashes, larger crystals with several observable defect states were formed which indicated that the applied photons were absorbed by the intermediate phase, converted to phonons, and aided grain growth through diffusion [318-322]. Further pulse count increase to five resulted in larger grains with very few defects on the surface, and pulse counts more than five damaged the film which can indicate material degradation due to excess annealing. For comparison, Fig. 5.4(G-I) shows the top surface SEM images indicating the morphology evolution of perovskite films when annealed through 30 seconds hotplate pre-annealing as was utilized in the previous chapter and introduced to remove the solvents and form the perovskite impure black phase prior to final IPL annealing [254, 297]. The images show diminishing dendrites upon further annealing and elimination of the dendrite structures upon 30 seconds. The comparison of short-term hotplate and uniform flash annealed perovskite films delineated similar morphology with a mixture of small and large grains, indicating that UFA is unable to achieve the desired morphology.

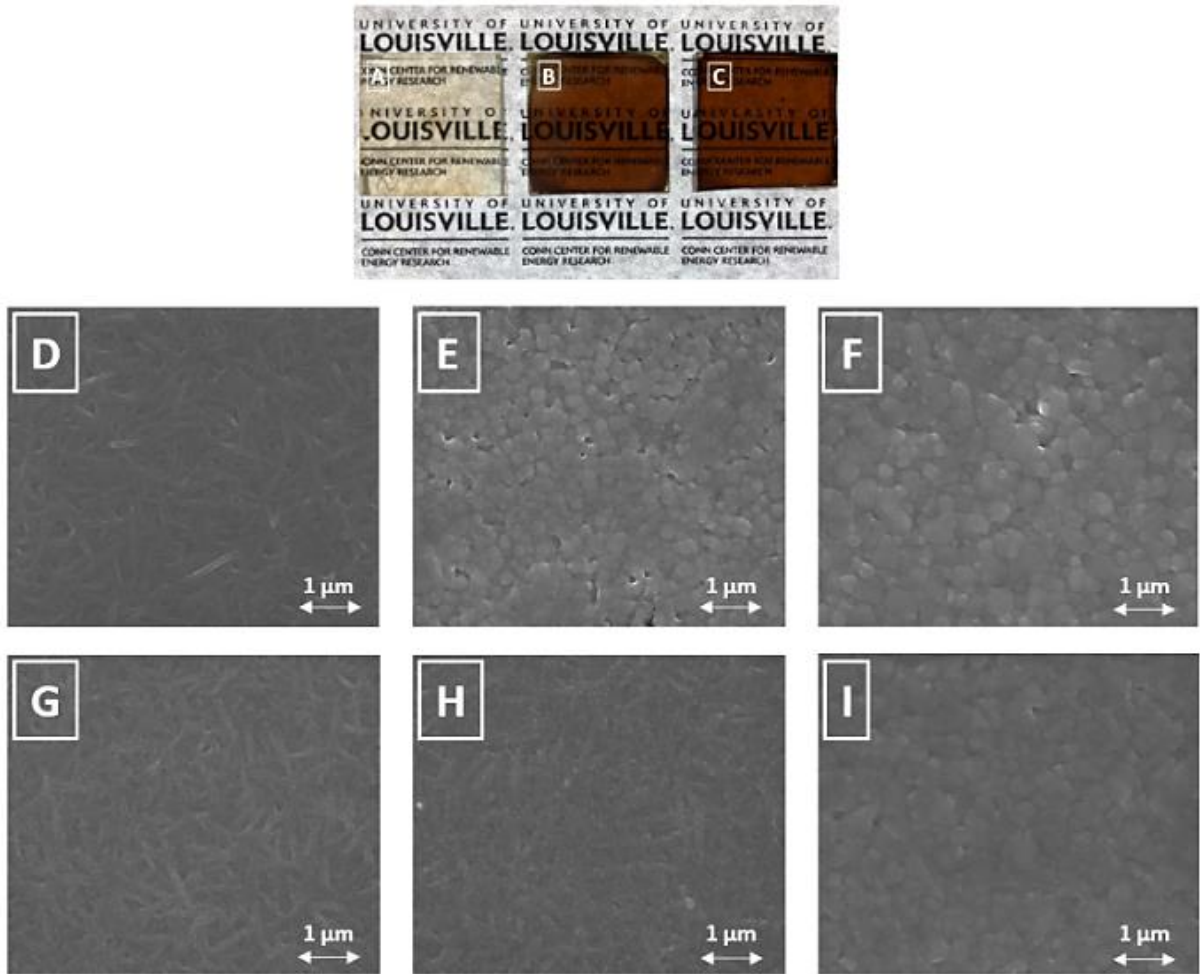


**Figure 5.4.** Evolution and top surface SEM images of the perovskite film (A,D) upon spin-coating; after B,E) three, and C,F) five flashes through UFA; and G) 10, H) 20, and I) 30 seconds of hotplate annealing.

### 5.6. Morphology of Gradient Flash Annealed Perovskite Films

The UFA method was able to anneal the films; however, they were observed to have a more optically matte finish which would indicate a rougher surface; hence, unoptimized annealing. To enable controlled annealing, the GFA approach, consisted of consecutive primary and secondary annealing steps, was utilized. In the former step, five flashes each carrying 200 J energy ( $0.86 \text{ J/cm}^2$ ) and 250 ms delay time between flashes was applied to

the as-deposited perovskite films, and five flashes each carrying 400 J energy ( $1.72 \text{ J/cm}^2$ ) and one second delay time between flashes, similar to UFA, was applied to the films in the latter step to accomplish the perovskite film annealing in about 6 seconds. Fig. 5.5(A-C) shows the evolution of perovskite film upon GFA, indicating darker films after each annealing stage. Compared to the indicated morphology in Fig. 5.4(B,E), the primary annealing step (Fig. 5.5(B)) formed a rough pale brown film which can be attributed to the incomplete formation of the perovskite black phase upon low heat flux exposure in this step. Upon completion of the secondary annealing stage, dark brown films with ultra-smooth quality were obtained which indicated the formation of favorable perovskite black phase. To investigate film morphology, top surface SEM images of the films were obtained and are shown in Fig. 5.5(D-F). Similar to UFA, as shown in Fig. 5.5(E), the primary annealing stage resulted in small grains with pinholes, indicating incomplete thin film annealing. In addition, the morphology indicated a monolithic ribbon with undetectable grains which can be attributed to the perovskite intermediate phase. As shown in Fig. 5.5(F), upon completion of the secondary annealing step, the entire intermediate phase was eliminated and continuous perovskite morphology with well-developed grains was formed. This indicates gradual consumption of the intermediate phase to develop grains during the primary and secondary annealing steps, thus, transforming the yellow intermediate to perovskite black phase with superior morphology and conforms with other reports [318]. It can be clearly observed from the top surface SEM images that the GFA resulted in well-bound grains with more uniformity which excels the obtained morphology showed in Fig. 5.4(F,I) with inconsistent grain growth and a mixture of small and large grains. As shown in Fig. 5.5(G,H) the ImageJ analysis indicated an average grain size of 196 and 251 nm for



the perovskite films processed through UFA and GFA, respectively, indicating 28% growth. Similarly, the average grain size of perovskite films annealed through 3 flashes of UFA and primary step of the GFA were found 158 and 150 nm, respectively.

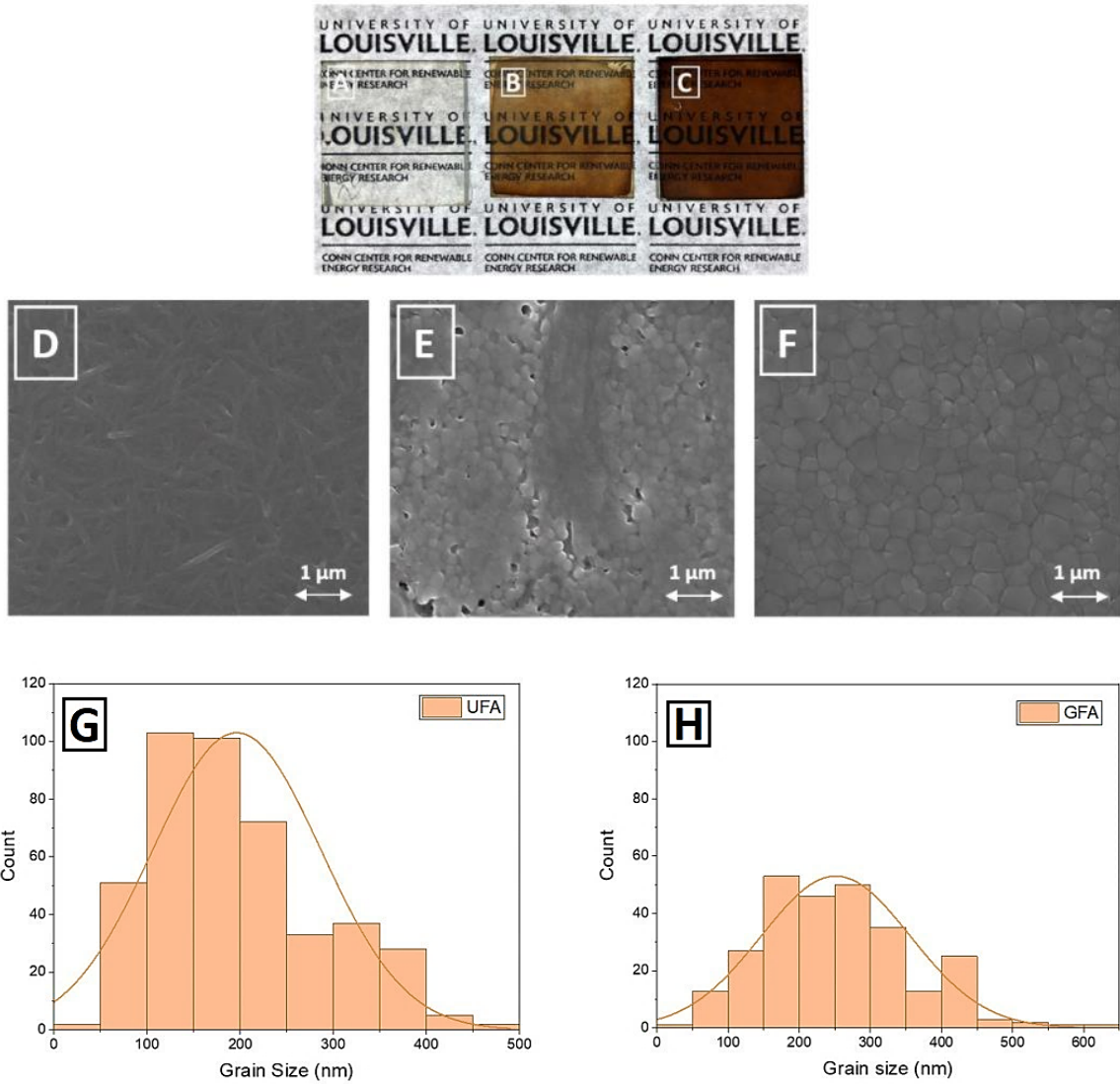


**Figure 5.5.** Evolution and top surface SEM images of the perovskite film A,D) upon spin-coating; after B,E) primary, and C,F) secondary annealing steps of GFA; G,H) Grain size histograms for perovskite films annealed through UFA and GFA.

### 5.7. Role of Flash Delay Time on Perovskite Morphology

To understand how the interval time between flashes influenced the perovskite black phase formation, three different IPL parameters with merely different interval time between flashes were applied. The three conditions had the similar total pulse counts of 10, as well as the 200 J ( $0.872 \text{ J/cm}^2$ ) and 400 J ( $1.74 \text{ J/cm}^2$ ) energy during GFA, but different interval times of 100 ms – 500 ms, 100 ms – 1000 ms, and 250 ms – 500ms, in which, the first and second values represent the interval time between flashes for the primary and secondary annealing steps, respectively. Fig. 5.6(A,D) and Fig. 5.6(B,E) show the evolution and SEM images of 100 ms – 500 ms and 100 ms – 1000 ms interval time conditions for GFA. It can be clearly observed that both interval times were unable to convert the adduct to perovskite black phase which, in addition to the results obtained from UFA, indicates that the ultrashort interval time of 100 ms was not providing enough time to evaporate the adduct solvent during annealing. Similarly, as shown in Fig. 5.6(C,F), shorter interval time of 500 ms for the secondary annealing stage revealed a mixture of black and yellow phases with several defect states and undeveloped grains for the 250 ms – 500 ms interval time condition which emphasizes the significance of delay time on solvent evaporation during IPL annealing. Therefore, in addition to heat flux, the rate of solvent evaporation between flashes plays a significant role on tuning the crystallization and forming pure perovskite black phase.

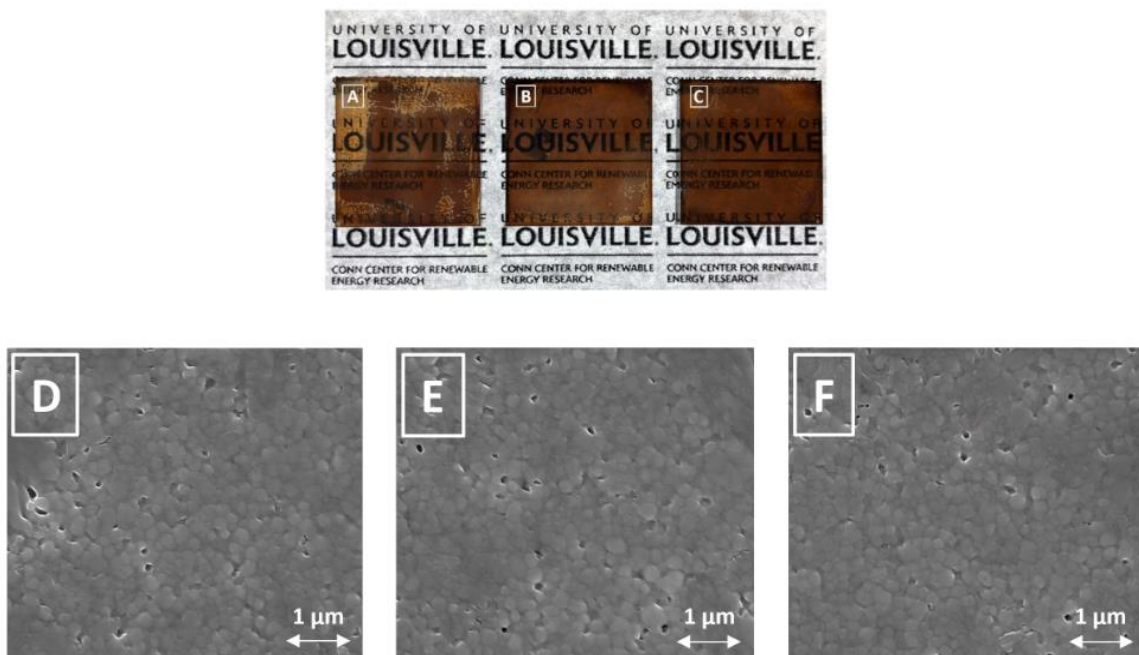


**Figure 5.6.** Images indicating the quality of obtained perovskite black phase for different intervals of A,D) 100 ms – 500 ms; B,E) 100 ms – 1000 ms; and C,F) 250 ms – 500 ms during GFA.

### 5.8. Crystallography of Uniform and Gradient Flash Annealed Perovskite Films

Fig. 5.7(A,B) shows XRD patterns of the FTO/SnO<sub>2</sub>/perovskite structure for each annealing stage where the intense  $2\theta$  peaks (marked with  $\blacksquare$ ) around 26.5°, 33.7°, 37.7°, 38.65°, 42.5°, 51.5°, and 54.5° are assigned to (110), (101), (200), (111), (210), (211), and (220) FTO/SnO<sub>2</sub> tetragonal rutile crystal planes (JCPDS 41–1445), and the peaks (marked with  $*$ ) around 14.1°, 20°, 23.5°, 24.45°, 28.4°, 31.86°, 34.94°, 40.7°, 43.15°, and 50.2° are attributed to (110), (112), (211), (202), (220), (310), (312), (224), (314), and (404) crystal planes, indicating perovskite tetragonal structure. The distinct low intensity  $2\theta$  peak (marked with  $\circ$ ) for the as-deposited perovskite films at 11.8° is assigned to 2H, and the peaks at 12.95° and 13.25° can be assigned to the 4H Ramsdell notations [323] indicating

hexagonal crystal system with  $P6_3/mmc$  space group of the perovskite intermediate phase [324]. As shown in Fig. 5.7(A), upon annealing through three flashes during UFA, the major perovskite peaks at  $14.1^\circ$  and  $28.4^\circ$  emerged, and the distinctive 2H and 4H polytypes were replaced with a  $\text{PbI}_2$  peak (marked with +) at  $12.4^\circ$  which indicated that the applied heat flux was excessive and, despite transforming the intermediate to the perovskite black phase, resulted in considerable intermediate phase evaporation, particularly the solvents and  $\text{CH}_3\text{NH}_3\text{I}$  phase. Further IPL exposure to five flashes increased the intensity of perovskite black peaks and eliminated the intermediate and  $\text{PbI}_2$  phases which can indicate fabrication of 3R(3C) pure black phase polytype. Interestingly, the evolution of perovskite phase during GFA presented a slightly different conversion process. As indicated in Fig. 5.7(B), the intermediate phase is remained after primary annealing stage and the intensity of the major perovskite black phase peaks is lower compared to the three pulses stage during UFA which is consistent with the evolution of perovskite films showed in Fig. 5.4(B) and Fig. 5.5(B), and can be attributed to the lower exposed IPL energy during this stage to retard the evaporation [318]. Upon completion of the GFA process, the developed films revealed 1.45 times enhanced intensity compared to the UFA which can be attributed to the retarded evaporation and, thus, possible intercalation of  $\text{CH}_3\text{NH}_3\text{I}$  phase to develop the perovskite black phase with better crystallinity. This is consistent with the obtained PL, UV-Vis, and SEM images with ununiform grain sizes and defect states for UFA and indicates how the primary annealing step played a significant role on crystallization. Similar to UFA, the resulted films did not reveal any  $\text{PbI}_2$  peaks after GFA which can indicate the formation of pure perovskite black 3R(3C) polytype. Both IPL annealing methods unraveled  $2\text{H} \rightarrow 6\text{H} \rightarrow 3\text{R}(3\text{C})$  conversion sequence and is consistent

with other reports [324]. For better clarification, the ratio of the major perovskite (110) plane to FTO (110) plane is shown in Fig. 5.7(C).

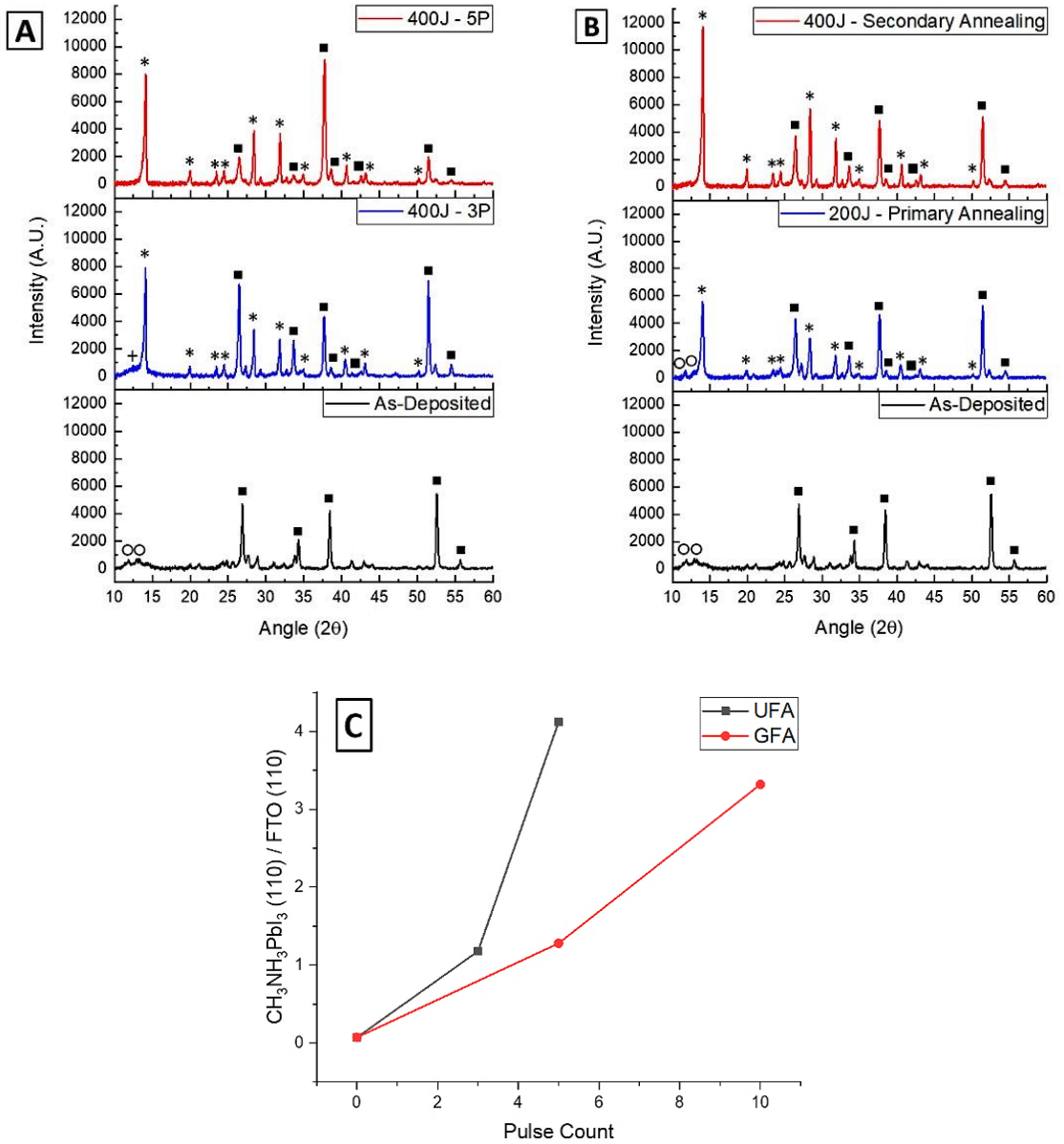


**Figure 5.7.** XRD patterns of IPL annealed perovskite films through A) UFA; and B) GFA; C) ratio of perovskite to FTO (110) planes.

To further investigate the crystallization kinetics of the perovskite films annealed with different delay time between flashes during GFA, XRD patterns delineating the phase purity of annealed films were obtained and the results are shown in Fig. 5.8. Unlike the formation of pure perovskite phase in Fig. 5.7, all XRD patterns indicated  $\text{PbI}_2$  and 2H intermediate phases upon annealing, indicating inadequate crystallization of the perovskite films when annealed through 100 ms – 500 ms, 100 ms – 1000 ms, and 250 ms – 500 ms conditions. These observations along with the morphology inspection results indicate that the 250 ms – 1000 ms delay time between flashes is the optimal condition to develop high quality perovskite films with pure black phase. Therefore, the spectrophotometry and voltammetry results will be investigated only for the UFA and the optimum GFA condition.

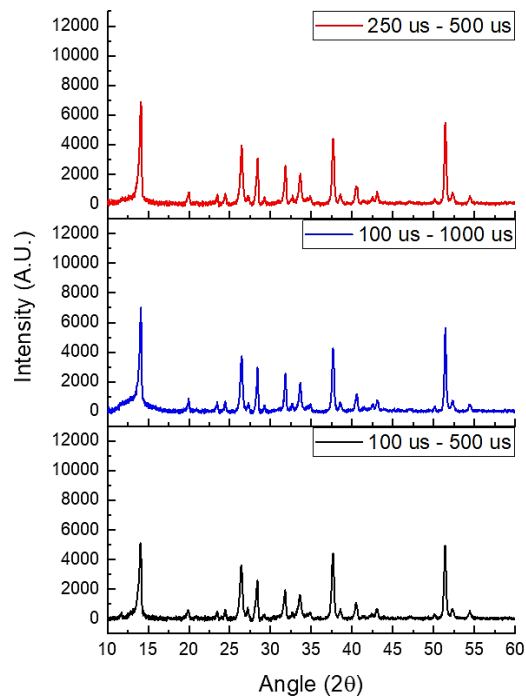


**Figure 5.8.** XRD patterns of the perovskite films annealed through different flash delay times during GFA.

## 5.9. Spectrophotometry of IPL Annealed Perovskite Films

UV-Vis absorption of the perovskite films can provide further information about the morphology and consistency of films over larger areas and the films ability to absorb the IPL energetic photons. As shown in Fig. 5.9(A), the as-deposited film indicated little absorbance within the visible and near IR range and a high absorption close to UV spectrum which can be attributed to the photon absorption by the  $\text{PbI}_2$  phase [325]. These films are a challenge to initiate the perovskite film formation as they do not absorb much of the IPL energetic photons. During the IPL process, the films progressively absorbed more of the visible energy which is consistent with the formation of darker films and elimination of pinholes and defects showed in Fig. 5.4 and 5.5. However, the GFA method showed higher absorption which can indicate the significance of primary annealing stage contributing to the enhanced phase and morphology of the perovskite film and is consistent with the XRD patterns showed in Fig. 5.7 and Fig. 5.8. To better determine the thin film quality, the PL peak of IPL annealed perovskite films was obtained. As shown in Fig. 6.7(B), the perovskite films annealed through GFA depicted the strongest peak, which can be attributed to enhanced charge carrier generation and diminished non-radiative recombination in the annealed film [326]. For all annealing stages, the PL peaks indicated a constant bandgap of 1.6 eV which is consistent with other reports [326, 327]. However, the primary annealing stage of GFA demonstrated a slight blueshift with the lowest peak intensity, indicating higher perovskite bandgap due to the existence of unconverted perovskite yellow adduct at this stage and is consistent with the and SEM, XRD, and UV-vis results showed previously as well as other reports [328]. These indicate that the primary annealing stage was acting as a foundation to initiate solvent evaporation and yield

adequate crystal growth throughout the entire annealing process by controlling the diffusion rate and, in turn, the crystallization pace, and is consistent with other reports [229, 310, 329].

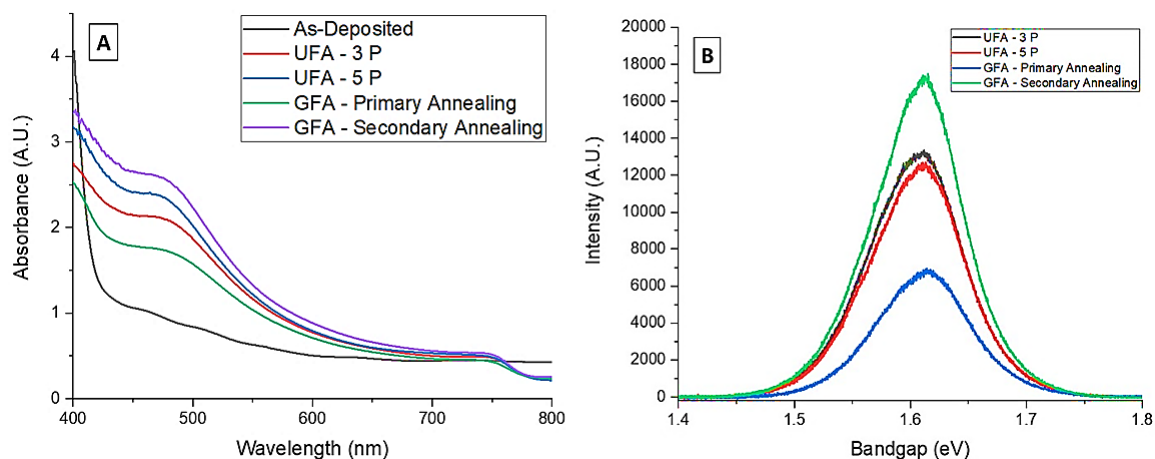


**Figure 5.9.** A) UV-vis spectra; and B) PL peak of the IPL annealed perovskite films.

### 5.10. Voltammetry of Uniform and Gradient Flash Annealed PSCs

The material characterization study indicated successful fabrication of perovskite films for UFA as well as the GFA method with 250 ms - 1000 ms interval time condition. To determine performance, the forward and reverse scan J-V curves indicating the photovoltaic parameters of fabricated PSCs were obtained. As shown in Fig. 5.10, the maximum PCE of fabricated solar cells were found for the reverse scans exhibiting the open circuit voltage ( $V_{OC}$ ), short circuit current ( $J_{SC}$ ), power conversion efficiency (PCE), and fill factor (FF) of 0.85V, 15.59 mA/cm<sup>2</sup>, 9.27%, and 69.92%, for the champion PSC fabricated through UFA, and were increased to 0.91V, 19.17 mA/cm<sup>2</sup>, 11.75%, and 68% when annealed through GFA, respectively, indicating 26.75% performance improvement when fabricated in a high humid ambient environment (>60%). The summary of the



photovoltaic parameters for five devices fabricated in each condition is shown in Table 5.1 which indicates average  $V_{OC}$ ,  $J_{SC}$ , PCE, and FF of 0.873 V, 14.58 mA/cm<sup>2</sup>, 8.67%, and 68.15% for UFA, and 0.8887 V, 19.11 mA/cm<sup>2</sup>, 11.23%, and 66.59% for GFA, respectively. Notably, the obtained  $V_{OC}$  is lower than the reported values in previous works which can be attributed to the type of Spiro-MeOTAD used in this study and conforms with other reports [330]. The statistical results show that the enhanced current density was the most impacting factor on device efficiency which can be attributed to the enhanced crystallinity and morphology of the perovskite films obtained through GFA method.

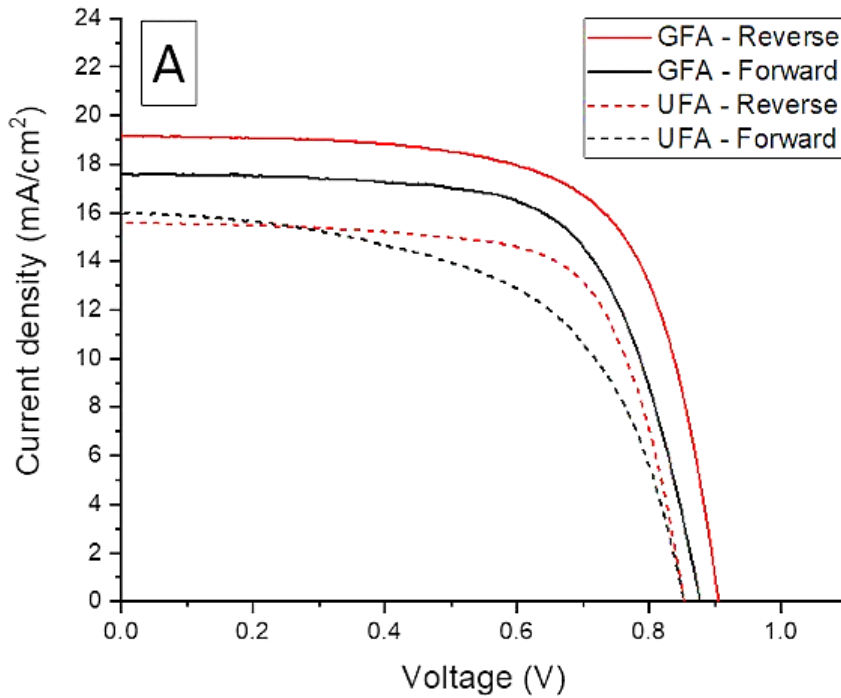


**Figure 5.10.** J-V curves of champion PSCs annealed through UFA and GFA.

**Table 5.1.** Average photovoltaic parameters for five PSCs annealed through UFA and GFA methods.

Annealing Method	Voc (V)	Jsc (mA/cm <sup>2</sup> )	PCE (%)	FF (%)
UFA	0.873 ± 0.016	14.58 ± 0.75	8.67 ± 0.35	68.15 ± 1.72
GFA	0.887 ± 0.017	19.11 ± 0.46	11.23 ± 0.60	66.59 ± 2.16

### 5.11. IPL Temperature Measurement and Simulation

To better understand the impact of IPL parameters on grain growth and morphology evolution, the flash peak temperature during IPL annealing was measured and the results were compared to a 2D FEA using ANSYS to estimate and validate the peak temperature rise at the perovskite films as described in chapter 3.

Fig. 5.11 shows the experimental and simulation results demonstrating the thermal response measured by the thermocouple located on top of the perovskite film during IPL annealing. As shown in Fig. 5.11(A), experimental and simulation results for UFA resulted in the peak temperatures between 760-820°C as the flashes progress, and the measured temperatures through experiment were within less than 5% of the simulation results. The delay time between flashes allowed for the film temperature to recover towards ambient with each subsequent flash increasing this resting temperature about 10-20°C. The reduction in temperature was primarily a result of the thermal diffusivity ( $k/\rho C_p$ ) and heat capacity ( $mC_p$ ) of the glass substrate to quickly transfer the heat from the perovskite film. Heat transfer to the surroundings through convection and radiation completed the rapid temperature decline following each flash. The broader temperature signal fall-off for the

experimental results is attributed to the high and low pass filtering of the amplifier as well as the mass of thermocouple. Similarly, simulation results indicated peak temperatures between 500-540°C for the primary annealing step, and 800-830°C for the secondary annealing step during GFA (Fig. 5.11(B)). In turn, the measured temperatures from experimental setup indicated the maximum temperatures between 480-590°C for the primary annealing, and between 740-840°C for the secondary annealing step, indicating less than 13.6% variation to the simulation results, and is consistent with other reports [237, 331]. The results indicated that the surface temperature reached to nearly 800°C which was over 5 times higher than the 150°C degradation temperature of the  $\text{CH}_3\text{NH}_3\text{PbI}_3$  black phase, and even exceeded the 650°C evaporation temperature of the entire perovskite phases unraveled through TGA/DSC. Therefore, the time dependent temperature determines the phase and morphology evolution of perovskite films during IPL annealing.

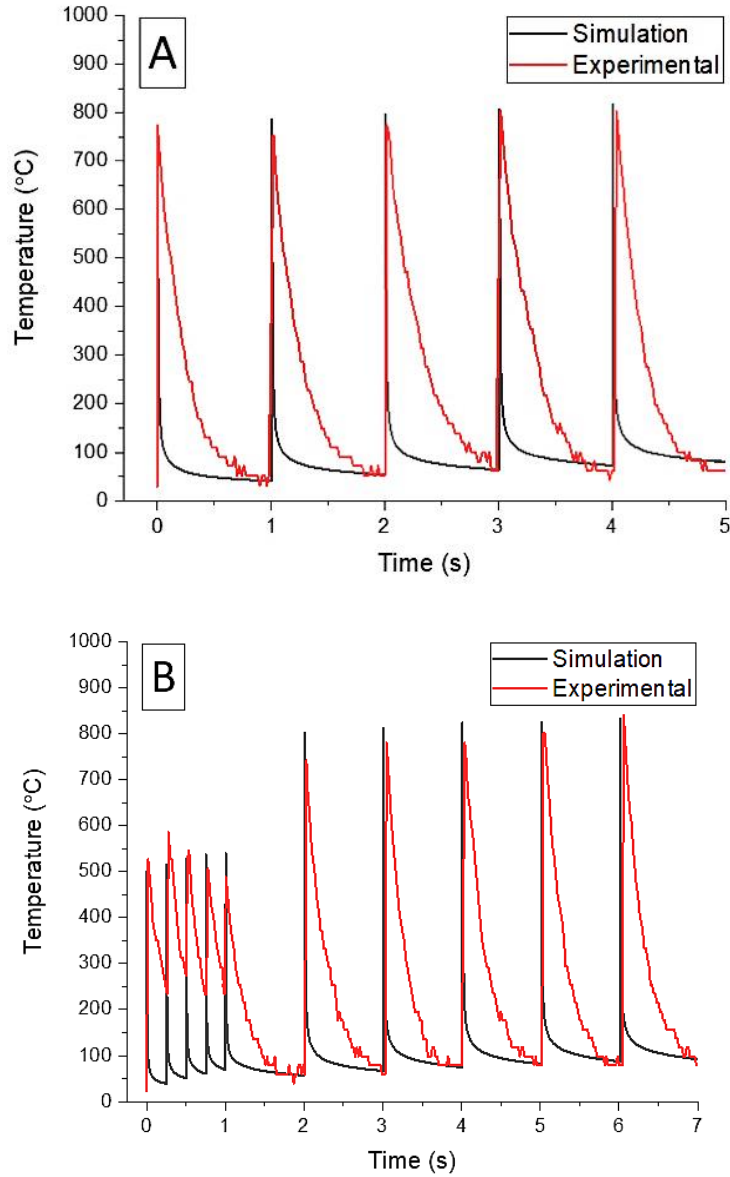


**Figure 5.11.** Experimental and numerical results demonstrating the maximum temperature rise reaching to the perovskite film for A) UFA, and B) GFA.

Fig. 5.12 shows the thermal response of thermocouple for the interval times of 100 ms, and 250 ms in the primary annealing step, as well as 500 ms and 1000 ms in the secondary annealing step of GFA. As shown in Fig. 5.12(A,C), the ultrashort interval of 100 ms indicated slightly higher temperatures than the 250 ms interval, reaching to almost 600°C,

which can indicate the predominating effect of the applied heat flux to natural convection during the delay time on elevating the surface temperature. Surprisingly, 500 ms interval for the secondary annealing step flashes indicated a lower peak temperature, reaching to about 650°C at the end of the annealing process and is consistent with the observed poor morphology and incomplete phase transformation in Fig. 5.6. This can be attributed to the hampered solvent evaporation as the result of insufficient delay time between flashes. Notably, the temperature survey of the secondary annealing stage showed in Fig. 5.12(B) is similar to Fig. 5.11(B); however, as was previous shown in Fig. 5.6, the 100 ms interval hindered achieving perovskite pure black phase with superior morphology which indicates the significance of solvent evaporation and phase transformation between flashes. Despite increasing the surface temperature, ultrashort delay times indicated poor morphology which is probably due to incomplete diffusion of species at these short time scales. Therefore, a compromise of heat flux and time is necessary to obtain superior morphology and pure perovskite black phase.

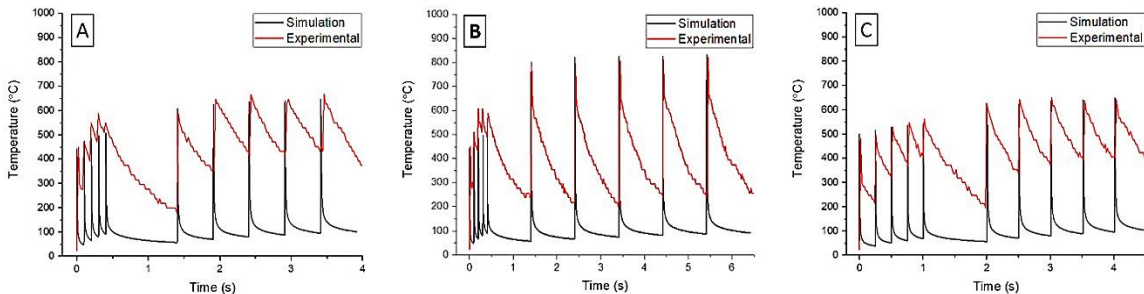


**Figure 5.12.** Temperature results at the surface of perovskite film annealed through GFA with different flash delay times of A) 100 ms – 500 ms; B) 100 ms – 1000 ms; and C) 250 ms – 500 ms.

## 5.12. Arrhenius plots for Uniform and Gradient Annealing

To realize how GFA could enhance the morphology and performance of PSCs, the estimated activation energy for grain boundary mobility was calculated using the Arrhenius equation which was shown to be dependent on temperature and thermal diffusivity in chapter 2. Fig. 5.13 shows the logarithmic plot of grain size ( $\phi$ ) versus flash duration ( $t$ ), where the slope indicates grain growth exponent ( $n$ ) and is used to estimate the thermal diffusivity. The plots indicated almost similar slopes, indicating  $n=0.5$  for both annealing approaches.

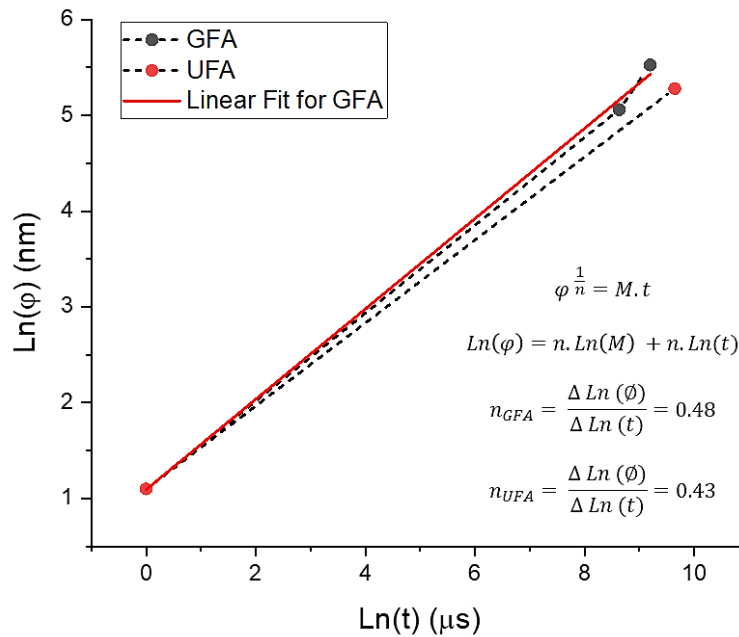


**Figure 5.13.** Logarithmic plot of grain size versus IPL duration for UFA and GFA.

Fig. 5.14 demonstrates the Arrhenius plots for UFA and GFA approaches, in which, the slope of graphs is determinative of the grain boundary mobility activation energy. The plots revealed nearby activation energies, indicating one-step increase of  $47 \text{ kJ} \cdot \text{mol}^{-1}$  during UFA and a two-step increase of  $55 \text{ kJ} \cdot \text{mol}^{-1}$  followed by a mild step of  $0.5 \text{ kJ} \cdot \text{mol}^{-1}$  for

the primary and secondary annealing steps during GFA, respectively. These results conform with the illustrated characterization results and can be attributed to the shrinkage of activation energy during GFA which implemented three significant roles to enhance the PSC performance. First, the lower applied temperature during primary annealing step of GFA mitigated the diffusion rate according to the Fick's law of diffusion [318] and, in turn, enabled controlled grain growth. Second, in addition to the diminished diffusion rate, the primary step during GFA retarded the crystallization pace as the result of providing longer overall annealing time of about 6 seconds during GFA approach compared to 4 seconds during UFA. Third, unlike UFA which rapidly induced high temperatures in a shorter time, the Arrhenius plot shrinkage during GFA regulated solvent evaporation, thus, enabled adequate solvent evaporation with respect to phase transformation during annealing which is consistent with phase transformation through XRD. The synergy of all these parameters indicates how the exerted photon flux and time through GFA could improve the perovskite morphology and impact PSC performance.

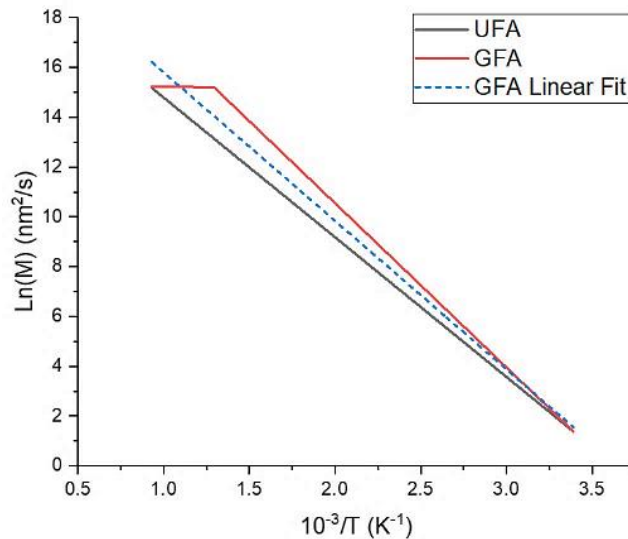


**Figure 5.14.** Arrhenius plots for UFA and GFA.

### 5.13. Conclusion

The rapid fabrication of  $\text{CH}_3\text{NH}_3\text{PbI}_3$  perovskite thin films entirely through IPL annealing was introduced by comparing the UFA with phased GFA approach consisted of primary and secondary annealing steps. The maximum device efficiency was enhanced from 9.27% to 11.75% when a primary annealing step with energy flux as low as 200 J/pulse ( $0.86 \text{ J/cm}^2$ ) was applied before the secondary annealing step with 400 J/pulse ( $1.72 \text{ J/cm}^2$ ). The simulation and experimental results indicated achieving high temperatures during IPL annealing, surpassing  $800^\circ\text{C}$ , which exceeded  $650^\circ\text{C}$ , where the perovskite was shown to entirely vanish through evaporation. However, the ultrashort exposure along with the application of a gradient approach could successfully develop pure perovskite black phase with superior morphology. The low-quality perovskite morphology obtained after UFA was found to be dependent on the exertion of an intense activation energy on the perovskite adduct which rapidly evaporated the intermediate phases before being consumed for perovskite black phase formation. In contrast, the higher performance of PSCs annealed through GFA was attributed to the regulated atomic diffusion rate to retard the crystallization pace as the result of activation energy shrinkage, exerting 55 and  $0.5 \text{ kJ.mol}^{-1}$  for the primary and secondary annealing steps during GFA, respectively. In addition to the photothermal effect, the interval time between flashes determined the phase transformation and morphology evolution during IPL annealing. Ultrashort interval of 100 ms increased the surface temperature but was unable to provide superior perovskite black phase upon annealing which signified the importance of solvent evaporation between flashes. Similarly, despite exceeding  $650^\circ\text{C}$ , the shorter interval time of 500 ms for the secondary annealing stage impeded the formation of pure perovskite black phase with



ultra-smooth morphology as the result of insufficient solvent evaporation during IPL annealing. The GFA condition with 250 ms – 1000 ms interval between flashes led to the optimal PSC performance as the result of obtaining better perovskite morphologies through retarded crystallization, regulated atomic diffusion rate, and sufficient evaporation between each flashing. The utilization of GFA technique reduced the perovskite film annealing time to about 10 seconds after deposition. This study demonstrated the rapid fabrication of PSCs through direct IPL annealing of both the SnO<sub>2</sub> ETL and perovskite absorber film which is applicable for low-cost, large-scale, and high-speed automated fabrication of PSCs.

## CHAPTER VI

### AUTOMATED FABRICATION OF PSC

#### 6.1. Introduction

Previous chapters increased the pace of PSC fabrication through IPL annealing of the SnO<sub>2</sub> and perovskite films which is amenable for high throughput scalable manufacturing of PSCs. However, all devices yet required the expensive Spiro-MeOTAD HTL requiring a nitrogen environment for deposition as well as a metal back-contact electrode requiring vacuum evaporation or sputtering deposition which are not adaptable for high-speed automation. As previously mentioned in chapter 2, carbon composite films consisted of graphite, carbon black (CB), have garnered a great attention for PSCs due to their good conductivity, low-cost, and suitable band energy alignment with the perovskite film; hence they can be a potential replacement to Spiro-MeOTAD HTL and metal back-contacts. These films are fabricated by depositing a carbon composite ink or paste followed by a post-deposition high-temperature annealing, and the perovskite solution is then incorporated into the annealed carbon film, or before the perovskite film, where the carbon films are deposited on the perovskite layer followed by a lower temperature annealing. In the pioneering works utilized the former approach to fabricate the carbon based PSCs, in which, the carbon films were deposited on top of a high temperature annealed TiO<sub>2</sub> and a passivating ZrO<sub>2</sub> film that impeded the direct contact between the TiO<sub>2</sub> ETL and carbon back-contact, and annealed at about 400°C for 30 min [332-335].

However, the prolong high temperature annealing is not amenable for rapid and low-cost fabrication of PSCs and is not applicable on plastic substrates. To address this issue, other studies introduced depositing carbon directly on the perovskite layer, with and without an interfacial HTL, followed by low temperature annealing in a few minutes to accomplish faster and more facile fabrication of PSCs [336, 337]. This method is applicable for scalable deposition of PSCs; however, as mentioned in chapter 2, the annealing process lasts for a couple minutes which is not favorable for high-throughput manufacturing. Therefore, it is necessary to utilize other annealing approaches, such as IPL, to allow for successful fabrication of carbon-based PSCs in a short period. This chapter introduces a non-roll-to-roll scalable platform to fabricate charge transport films of PSCs in a humid ambient environment (>60%) using an inkjet printhead and IPL annealing.

To realize automated fabrication of the PSCs with required control of the printing and IPL annealing processes, a testbed, a custom designed “NEXUS” system integrating robotics, motion control, and additive manufacturing tools is proposed. The NEXUS is a novel instrument under development for flexible multiscale manufacturing by implementing precision robotic assembly, additive manufacturing, and multiscale integration of miniature devices and systems. NEXUS system includes various subsystems such as a Pico Pulse inkjet printhead from Nordson and Xenon Corporation IPL system combined with custom 6 Degree of Freedom (DOF) robotic positioner allowing not only fast transport of the samples between the processing tools (IPL and Pico Pulse), but also precise motion control during printing. Several additive

manufacturing techniques, such as a dual-head fused deposition modeling (FDM) 3D printing [338] and additive manufacturing subsystems integrating aerosol jetting and dispenser auger valve [339], have so far been investigated for the NEXUS. Furthermore, a novel bonding process has been developed utilizing ultrasonic vibration technique to embed metal wire in a polymer [340, 341].

This chapter spans the fabrication of SnO<sub>2</sub> ETL as well as the carbon back contact electrodes on CH<sub>3</sub>NH<sub>3</sub>PbI<sub>3</sub> perovskite films using the NEXUS robotic setup. The study initially demonstrates the successful fabrication of SnO<sub>2</sub> ETL through inkjet deposition followed by optimized IPL annealing of the film as introduced in chapter 4 through fabricating conventional PSCs with Spiro-MeOTAD HTL and gold back-contacts. Finally, carbon PSCs are fabricated by inkjet depositing the custom developed carbon ink on the perovskite films as processed in chapter 5. This chapter demonstrates automated fabrication of PSCs utilizing carbon back-contacts that enable rapid successful atmospheric processing of PSCs through a non-roll-to-roll setup.

## **6.2. Inkjet Printhead Mechanism**

The printing is carried out using a Nordson pico-pulse system with piezoelectric mechanism actuating a needle valve that can dispense micron size droplets; hence, optimizing the actuation parameters is important to obtain the desired thin film uniformity and morphology. Fig. 6.1 shows the structure as well as functionality of the piezoelectric mechanism of the inkjet printhead. At the start of a cycle, the valve is closed by the needle as the result of applied voltage to the actuating mechanism (Fig. 6.1(A)). As the voltage is adjusted, the needle will retract a distance, where the stroke length is related to the applied voltage, allowing pressurized fluid to be expelled (Fig. 6.1(B)). The full cycle of the valve

is shown in Fig. 6.1(C), where the applied voltage, actuation speed (opening and closing time of the valve), and piezoelectric frequency (delay time between droplet dispensing) influence the film uniformity.

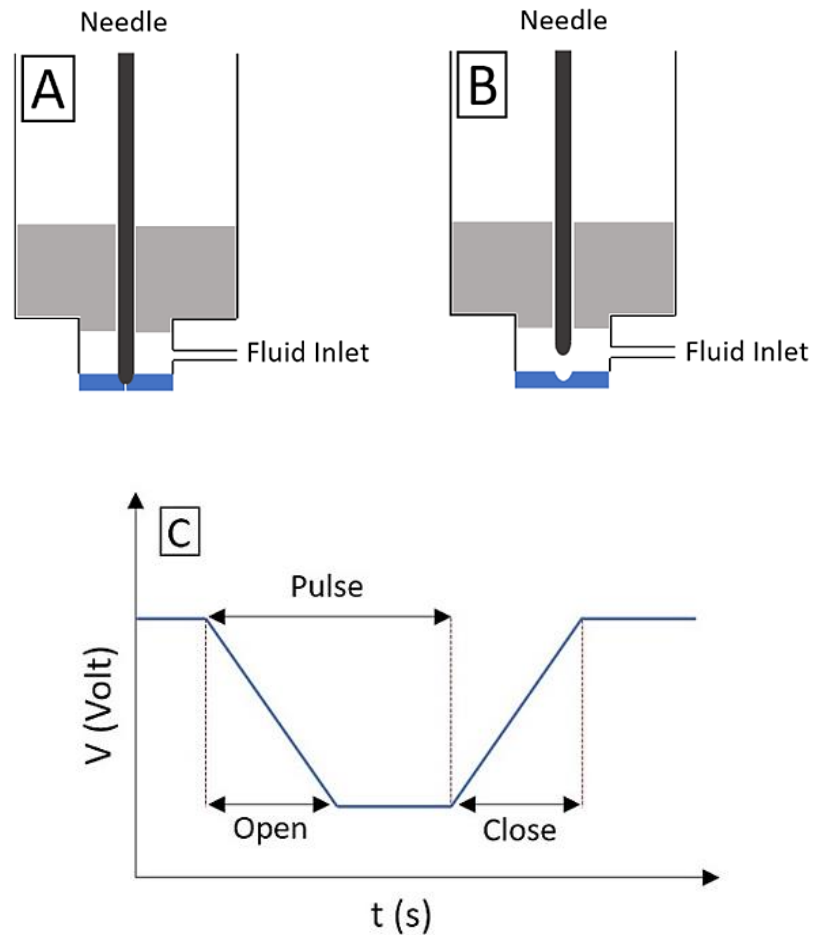


**Figure 6.1.** Schematic of the inkjet printhead showing the needle in A) Closed; B) Open position as controlled by the applied voltage. C) Actuation behavior of the needle for one cycle.

The piezoelectric inkjet system is capable of dispensing micron-size droplets in a specific period where the droplets coalesce to form bulk lines, which is driven by the precursor properties, such as viscosity, concentration, surface tension, as well as actuation

parameters to develop uniform films with good morphology. For both depositions, the stroke and frequency of the printhead as well as line distancing is studied to create continuous films with desired thickness.

### 6.3. SnO<sub>2</sub> Inkjet Deposition

Fig. 6.2 shows the top surface microscope images indicating the quality of printed SnO<sub>2</sub> lines at a constant dispensing frequency of 40 Hz but different stroke percentages, defined as the ratio of needle retraction from the full retraction range. As indicated, low stroke percentage of 45% (Fig. 6.2(A)) resulted in isolated droplets with an average diameter of 90 μm which can be attributed to the insufficient force to allow for uniform distribution of droplets on the substrate. Increasing the stroke to 50% resulted in continuous lines with an average width of 310 μm but with irregular edges (Fig. 6.2(B)). At 55% stroke (Fig. 6.2(C)), uniform lines with 350 μm width were deposited. The formation of continuous lines after 50% stroke can be attributed to the deposition robustness as the result of more forceful dispensing at a higher stroke, and the formation of wider lines with straight edges at the 55% stroke can be attributed to the coalescence of larger volume droplets adjusting the line quality. Notably, as shown in Fig. 6.2(D), increasing the stroke to 60% resulted in a nonuniform line with 400 μm width and numerous surrounding random droplets, indicating the printing of SnO<sub>2</sub> at an extreme stroke.

Dispensing frequency determines the number of dispensing droplets in a particular area during deposition, thus, playing a significant role on the printing quality. Fig. 6.2(E,F) shows the quality of printed SnO<sub>2</sub> at the optimal stroke of 55% but with different frequencies. As indicated, at 25 Hz (Fig. 6.2(E)) the print exhibited an irregular line with 453 μm width, whereas an inhomogeneous line with 872 μm width was formed at 100 Hz

(Fig. 6.2(F)), indicating over deposition of the material. These results suggest that the stroke and frequency of 55% and 40 Hz are the optimum parameters and are selected to print the SnO<sub>2</sub> films for PSC fabrication.

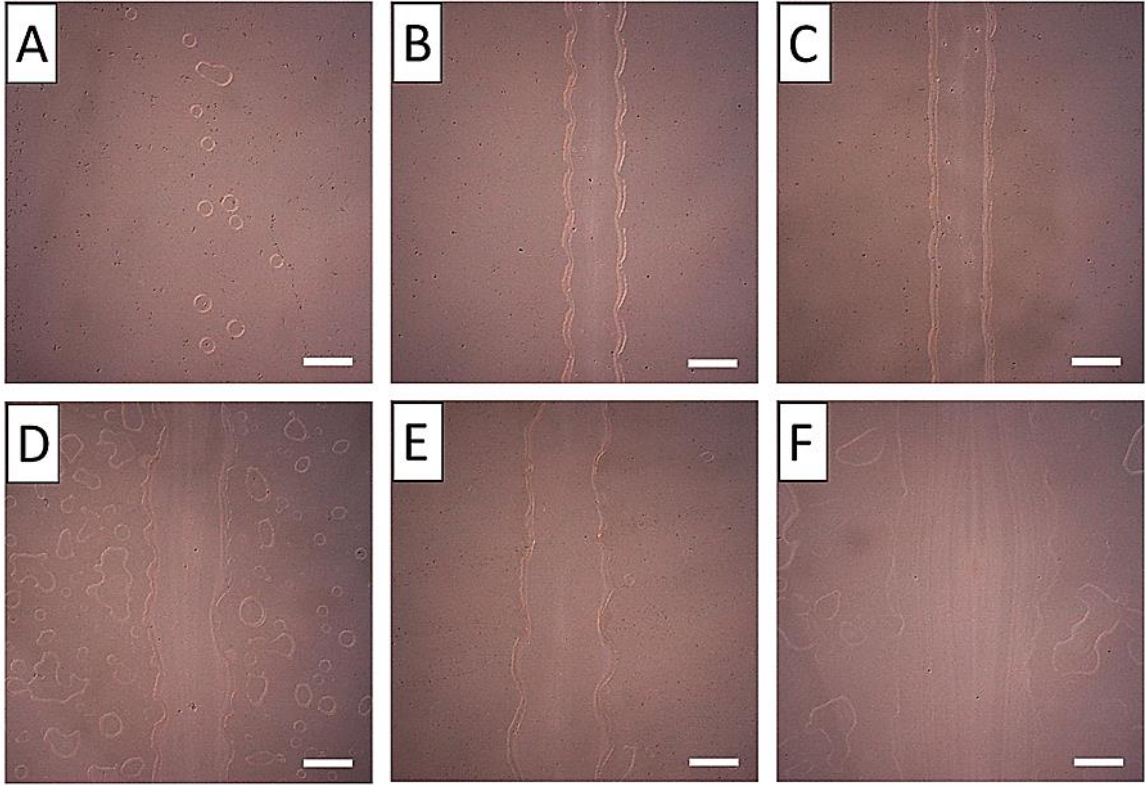


**Figure 6.2.** Microscope images showing the quality of printed SnO<sub>2</sub> lines at different strokes of A) 45%; B) 50%; C) 55%; and D) 60% within a constant frequency of 40 Hz, as well as E) 25; and F) 100 Hz at the constant stroke of 55%. Scale bar = 1 mm.

Besides optimization of the printhead parameters, line distance, determining the distance between two adjacent printed lines, plays a significant role on forming continuous films. To carry out the line distancing study, four different line distances of 350, 525, 700, and 875  $\mu\text{m}$  were selected to deposit the SnO<sub>2</sub> films. The line distances of 350  $\mu\text{m}$  (Fig. 6.3(A)) and 525  $\mu\text{m}$  (Fig. 6.3(B)) developed continuous films; However, they resulted in a

nonuniform morphology upon IPL annealing due to the Marangoni effect caused by the evaporation of thicker wet films at closer line distances. At 700  $\mu\text{m}$  (Fig. 6.3(C)), an average 40 nm thick continuous film with uniform morphology was obtained which can be attributed to the formation of  $\text{SnO}_2$  films from thinner wet films upon annealing. Notably, at 875  $\mu\text{m}$  (Fig. 6.3(D)) the lines did not merge to form uniform films; hence, the line distancing of 700  $\mu\text{m}$  was selected to fabricate  $\text{SnO}_2$  films for PSCs.

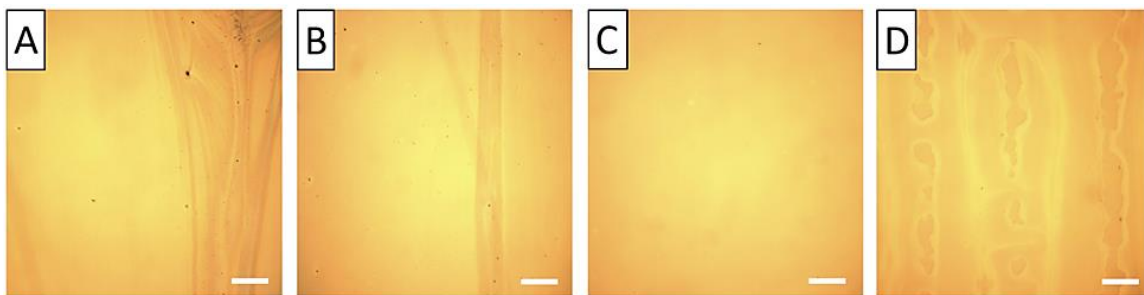


**Figure 6.3.** Microscope images showing the morphology of printed  $\text{SnO}_2$  films at A) 350; B) 525; C) 700; and D) 875  $\mu\text{m}$  line distancing. Scale bar = 1 mm.

The current study investigated the formation of a 2 cm side length squared area  $\text{SnO}_2$  film at a deposition speed of 5 mm/s. Table 6.1 shows the approximate deposition times of  $\text{SnO}_2$  films over larger areas and higher deposition speeds at the optimum line distancing of 700  $\mu\text{m}$  which can be used to estimate the processing time of the robotic setup on the scalability of  $\text{SnO}_2$  film.



**Table 6.1.** Estimated printing times for different areas of SnO<sub>2</sub> and printing speeds.

Area (cm <sup>2</sup> )	Deposition Speed (mm/s)	Deposition Time (min)
4	5	2
4	20	0.5
4	100	0.1
100	5	48
100	20	12
100	100	2.40
225	5	108
225	20	27
225	100	6

#### 6.4. Characterization of CH<sub>3</sub>NH<sub>3</sub>PbI<sub>3</sub> Perovskite

To examine the successful fabrication of SnO<sub>2</sub> films, PL peaks indicating the charge transfer capability at SnO<sub>2</sub>/perovskite interface is shown in Fig. 6.4(A), where the SnO<sub>2</sub> film is inkjet printed on FTO-glass substrates followed by direct IPL annealing. As previously reported, IPL releases intense flashes carrying energetic photons that once absorbed by the material, converts into phonons that aid crystallizing the material, enabling charge transport [297, 342, 343]. The intensity of the PL peak is considerably higher for the perovskite films deposited on FTO-glass than on IPL annealed SnO<sub>2</sub> films, revealing facilitated charge transfer at the perovskite/SnO<sub>2</sub> interface upon annealing. The PL peaks revealed no peak shift, indicating a constant bandgap of 1.6 eV for the CH<sub>3</sub>NH<sub>3</sub>PbI<sub>3</sub> perovskite film [344, 345]. XRD patterns showing the phase purity of the processed perovskite is shown in Fig. 6.4(B), where the film is processed as stated in chapter 5 [342]. The intense 2 $\theta$  peaks around 14.1°, 20°, 23.5°, 24.45°, 28.4°, 31.86°, 34.94°, 40.7°, 43.15°, and 50.2° indicate (110), (112), (211), (202), (220), (310), (312), (224), (314), and (404) crystal planes of perovskite tetragonal structure, and the peaks around 26.5°, 33.7°, 37.7°,

42.5°, 51.5°, and 54.5° are assigned to (110), (101), (200), (210), (211), and (220) FTO/SnO<sub>2</sub> tetragonal rutile crystal planes (JCPDS 41-1445). The XRD pattern revealed no PbI<sub>2</sub> peaks at 12.4° [346, 347], indicating fabrication of pure perovskite black phase and evaporation of the water content during IPL annealing of SnO<sub>2</sub>. In addition, the high UV-vis spectra showed in Fig. 6.4(C) reveals high photo absorption by the perovskite film within visible to near UV spectrum. Fig. 6.4(D) shows the top surface SEM image of the processed perovskite film, indicating a continuous morphology and bound grains which, in addition to the XRD and UV-Vis results, indicates successful fabrication of the pure CH<sub>3</sub>NH<sub>3</sub>PbI<sub>3</sub> perovskite phase.

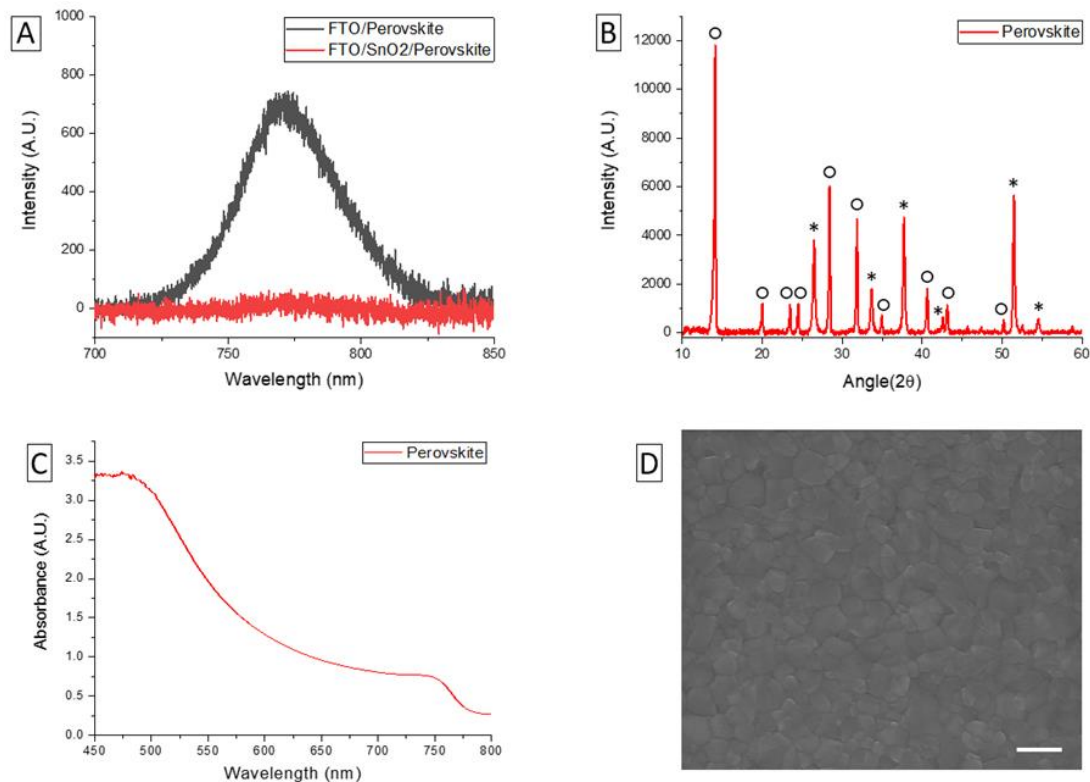


**Figure 6.4.** A) PL peaks of the perovskite film deposited on FTO-glass and SnO<sub>2</sub> coated FTO-glass; B) XRD pattern; C) UV-Vis spectra; and D) SEM image of the processed perovskite film (Scale bar = 1 μm).

### 6.5. Inkjet Printing of Carbon

To complete device fabrication, carbon films were deposited on top of the perovskite film by inkjet printing and annealed by IPL. Fig. 6.5 shows optical microscope images of printed carbon at 5X magnification, indicating the impact of three applied strokes at a constant frequency of 25 Hz on the quality of printed lines. As shown in Fig. 6.5(A), the 60% stroke resulted in nonuniform drop dispensing, whereas higher strokes of 65% (Fig. 6.5(B)), and 70% (Fig. 6.5(C)) developed continuous films with 570 and 1000 μm width, respectively. Notably, increasing the stroke increased the irregularity of the lines at the

edges. Fig. 6.5(C-D) shows the quality of printed carbon using different dispensing frequencies at the constant dispensing stroke of 65%. At the lowest applied frequency of 10 Hz (Fig. 6.5(D)), nearly perfect droplets with 631  $\mu\text{m}$  diameter were formed; however, the droplets did not merge. At 25 Hz, continuous lines with nonuniform edges were formed which was previously shown in Fig. 6.5(B). Increasing the frequency to 40 Hz resulted in straight edge continuous lines with 668  $\mu\text{m}$  width (Fig. 6.5(E)); however, at a high frequency of 100 Hz, the film width increased to 1144  $\mu\text{m}$  and irregular boundaries with random droplets were observed which can be attributed to the excess deposition of the material at extreme deposition frequency (Fig. 6.5(F)). These results indicted optimum deposition of both  $\text{SnO}_2$  and carbon films at 40 Hz; however, optimum carbon deposition required 10% higher stroke which can be attributed to the higher viscosity of the developed carbon ink compared to  $\text{SnO}_2$ .

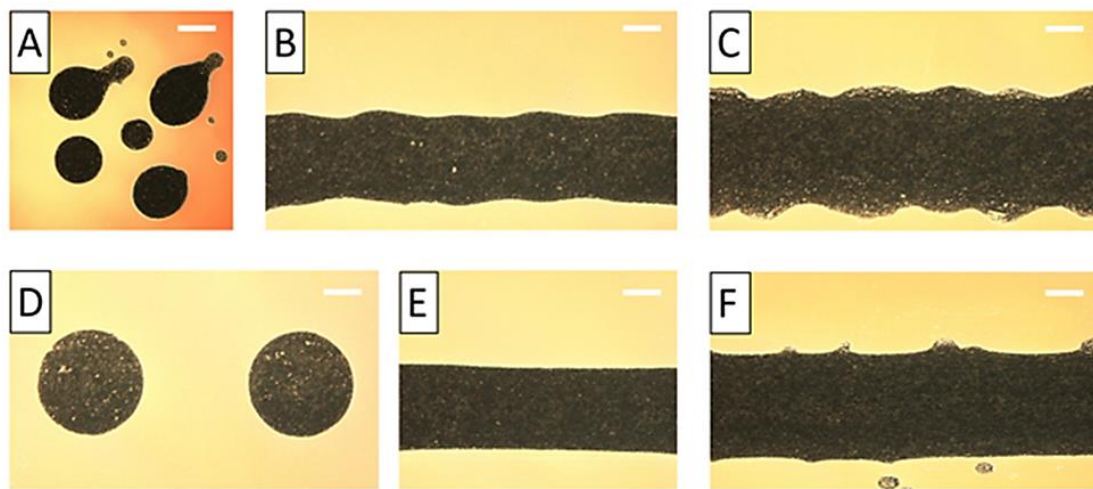


**Figure 6.5.** Microscope images showing the quality of printed carbon lines at different strokes of A) 60%; B) 65%; and C) 70% within a constant frequency of 25 Hz, as well as D) 10; E) 40; and E) 100 Hz at the constant stroke of 65%. Scale bar = 1 mm.

To develop films, the previously determined optimum dispensing parameters were utilized to print the carbon ink in a maze pathway; hence, the distance between printed lines play a significant role on the morphology and thickness of films. Fig. 6.6 shows the top surface microscope images at 5X magnification indicating the morphology of printed carbon films at line distances of 350, 525, 700, and 875  $\mu\text{m}$ . As shown in Fig. 6.6(A-C), the line distances of 350, 525, and 700  $\mu\text{m}$  indicated uniform morphologies; however, the film became discontinuous at the higher distance of 875  $\mu\text{m}$  (Fig. 6.6(D)). As indicated in Fig. 6.6(E-G), the films printed at the line distancing of 350, 525, and 700  $\mu\text{m}$ , resulted in films with 9.45, 7.20, and 5.50  $\mu\text{m}$  average thickness upon drying, indicating thicker films at shorter distances as the result of more material deposition. Notably, the morphology spectra of the scanned films revealed no irregularities which indicates merging of the lines and successful formation of carbon films. The conductivity of the naturally dried carbon films was measured using four-point probe and the results are summarized in Table 6.2. The thicker films formed at shorter line distances indicated higher conductivity; however, the conductivity was considerably increased for the 9.45  $\mu\text{m}$  thick films, indicating 279 and 43.9 S/m difference to the films printed at 525 and 700  $\mu\text{m}$ , respectively. These results are consistent with other reports indicating 9-10  $\mu\text{m}$  as the optimum thickness for carbon films in PSCs [153, 333].

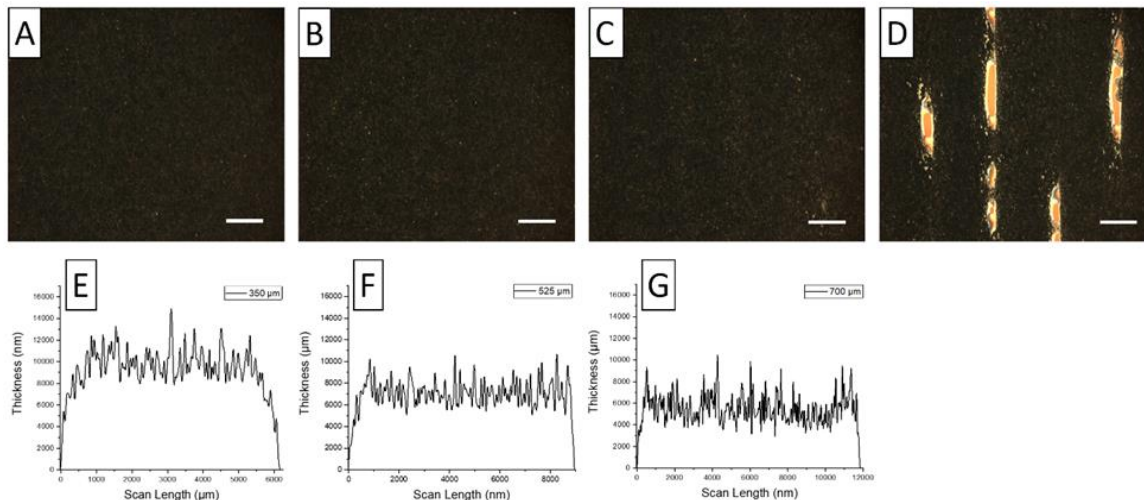


**Figure 6.6.** Microscope images and profilometer spectra showing the top surface image and morphology of printed carbon films at A,E) 350; B,F) 525; C,G) 700; and D) 875  $\mu\text{m}$  line distancing. Scale bar = 1 mm.

**Table 6.2.** Resistance and conductivity of naturally dried carbon films printed at different line distances.

Line distance ( $\mu\text{m}$ )	Thickness ( $\mu\text{m}$ )	Sheet Resistance ( $\Omega/\square$ )	Conductivity (S/m)
350	9.45	90.3	$1.17 \times 10^3$
525	7.2	154.5	$8.99 \times 10^2$
700	5.5	212.6	$8.5 \times 10^2$

In this study, 2 cm side length squared area carbon films were printed at the linear speed of 5 mm/s through a serpentine pathway. Table 6.3 shows the approximate deposition times of carbon films over various areas and deposition speeds at the optimum line distancing of 350  $\mu\text{m}$  which can be used to estimate the processing time of the robotic setup on the scalability of this layer.

**Table 6.3.** Estimated deposition times for different areas of carbon and printing speeds.

<b>Area (cm<sup>2</sup>)</b>	<b>Deposition Speed (mm/s)</b>	<b>Deposition Time (min)</b>
4	5	4
4	20	1
4	100	0.2
100	5	96
100	20	24
100	100	4.80
225	5	215
225	20	54
225	100	11

### **6.6. Morphology Evolution of IPL Annealed Carbon Films**

Top surface SEM images unravelling the morphology evolution of the carbon films were used to optimize IPL annealing of the carbon films. After printing, the carbon films were wet and natural drying took place up to 2 minutes; hence, IPL can greatly reduce the drying time. Direct IPL drying of thick wet carbon films at 400 J (1.72 J/cm<sup>2</sup>) – 500 ms IPL condition required up to 10 flashes to evaporate the solvent entirely from the carbon film. Unlike natural drying which resulted in uniform films (Fig. 6.7(A)), IPL annealing of the thick wet film exhibited damaged film morphology (Fig. 6.7(B)), with high porosity attributed to the rapid evaporation of Chlorobenzene solvent. Notably, application of lower energy flashes decreased the solvent evaporation rate and resulted in rough films, forming ununiform morphology with coffee stain effect on the surface which can be attributed to the properties and evaporation dynamics of the carbon ink during IPL drying. To address this issue, the deposited carbon films were kept in the printing chamber equipped with a suction hood to accelerate solvent evaporation, making the films dry before IPL processing. After drying, the films annealed at the same IPL condition resulted in a compact film with

pinholes (Fig. 6.7(C)). Therefore, the dried carbon films were annealed at two different annealing conditions with a constant flash energy of 100 J ( $0.43 \text{ J/cm}^2$ ) but different durations of 100 and 500  $\mu\text{s}$ . Fig. 6.7(D,E) shows the morphology of IPL annealed carbon films at 100 J – 100  $\mu\text{s}$  and 100 J – 500  $\mu\text{s}$ , respectively, indicating damaged films at longer flash exposure. The conductivity of the carbon films annealed at 100 J – 100  $\mu\text{s}$  was 1170 S/m, a similar conductivity to that of naturally dried, and the films annealed at 100 J – 500  $\mu\text{s}$  resulted in 817 S/m, indicating decreased conductivity at the longer flash exposure. Notably, no pores were found to form in the films annealed at 100 J – 100  $\mu\text{s}$ ; however, the observation of scattered white spots on the surface can indicate a slight damaging of the film at the 100 J – 500  $\mu\text{s}$  condition. This indicates the successful faster post-processing of carbon films.

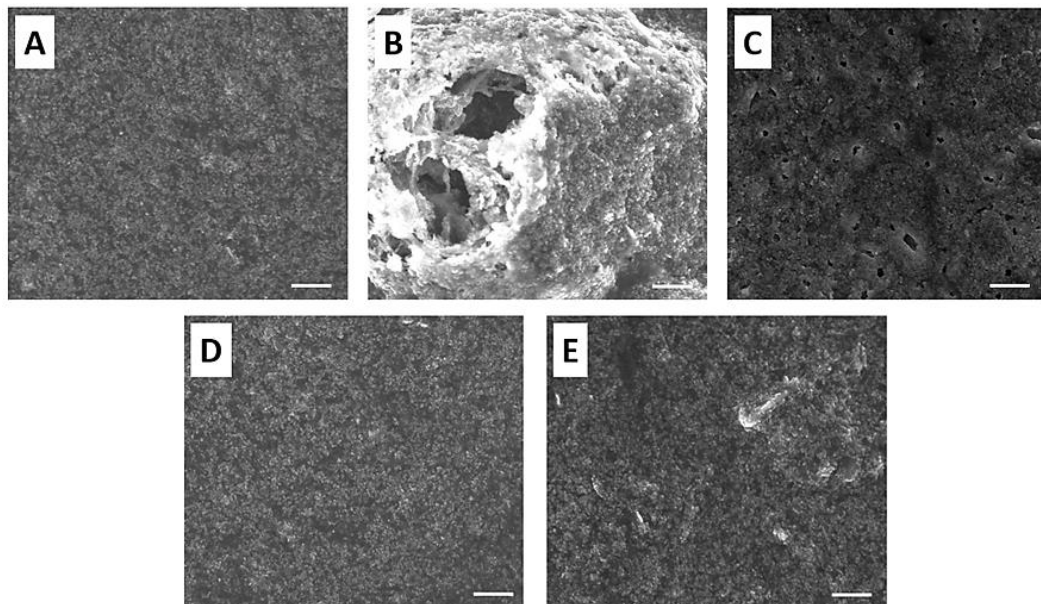


**Figure 6.7.** Top surface SEM images showing the morphology of carbon film after A) natural drying; direct IPL annealing of thick wet film at 400 J – 500  $\mu\text{s}$  condition B)



without, and C) with drying in the printing chamber; IPL annealing of dried carbon films at D) 100 J – 100  $\mu$ s; and E) 100 J – 500  $\mu$ s condition. Scale bar = 5  $\mu$ m.

### **6.7. Phase Evolution of IPL annealed Carbon Films**

Fig. 6.8 shows XRD patterns of the naturally dried as well as IPL processed carbon films, where the intense  $2\theta$  peaks around  $26.6^\circ$ , and  $54.6^\circ$  indicate (002) and (004) planes of carbon/graphite phase [348]. The as-deposited wet carbon showed a broad peak around  $18.5^\circ$  with considerably less intense peak of the major carbon/graphite at  $26.6^\circ$ , indicating the existence of solvent-binder in the wet carbon film. Upon natural drying and IPL annealing, the XRD patterns did not reveal any solvent-binder peaks; however, the carbon films annealed at 100 J – 100  $\mu$ s condition exhibited the highest intensity of the major carbon/graphite peak at  $26.6^\circ$  which indicates the positive role of IPL annealing on carbon than merely natural drying of the films. These results are consistent with the observed SEM images and can indicate the successful post-processing of carbon films after annealing at 100 J – 100  $\mu$ s condition and is utilized to process the carbon films in PSCs.

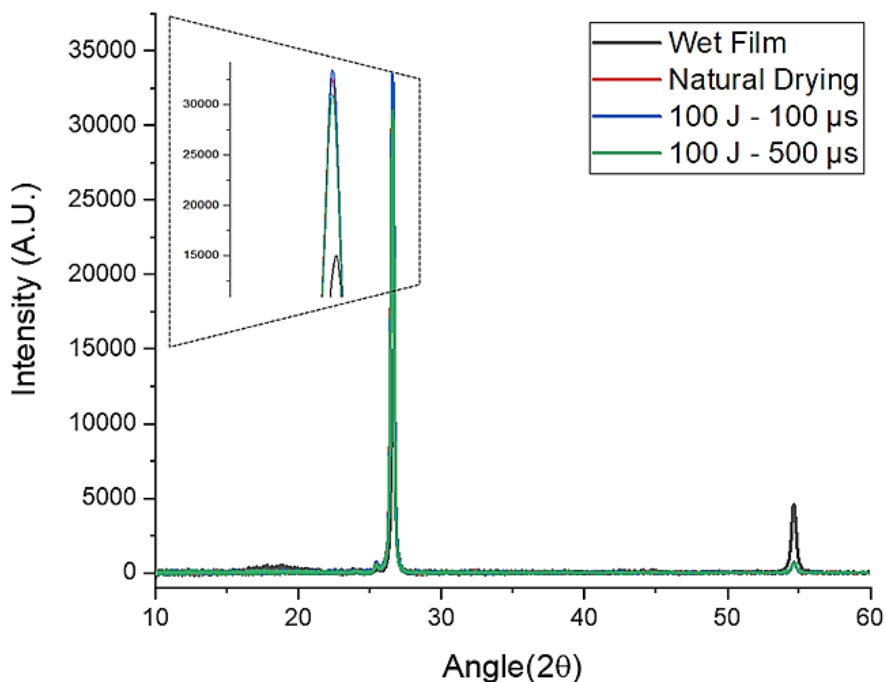


**Figure 6.8.** XRD patterns of the carbon film before and after IPL annealing.

### 6.8. Voltammetry of Robotic Fabricated PSCs

To determine device performance, J-V curves of the champion PSCs is shown in Fig. 6.9, and the average performance of 5 PSCs for each structure is shown in Table 6.4. The fabricated carbon PSCs had FTO-glass/SnO<sub>2</sub>/perovskite/carbon structure; however, PSCs with conventional FTO-glass/SnO<sub>2</sub>/perovskite/Spiro-MeOTAD/gold were initially fabricated to determine the successful fabrication of inkjet deposited SnO<sub>2</sub> films. The conventional structure devices indicated maximum open circuit voltage (V<sub>OC</sub>), short circuit current (J<sub>SC</sub>), power conversion efficiency (PCE), and fill factor (FF) of 0.983 V, 17.41 mA/cm<sup>2</sup>, 13.08%, and 76.49 %, respectively. The horizontal line of the conventional J-V curve PSCs shows high shunt resistance, indicating successful inkjet deposition and annealing of SnO<sub>2</sub> and is consistent with spectrophotometry results showed earlier. Champion PSCs utilizing the 9.45 μm thick carbon film resulted in the V<sub>OC</sub>, J<sub>SC</sub>, PCE, and

FF of 0.74V, 14.92 mA/cm<sup>2</sup>, 5.03%, and 45.4%. This lower performance of carbon PSCs can be attributed to the lower conductivity of the carbon films compared to gold, as well as lower shunt and higher series resistances observable from inclined horizontal and vertical lines of the carbon PSC J-V curves as the result of eliminating the Spiro-MeOTAD film. The fabricated devices retained their stability for up to two weeks when stored in the dark ambient; however, a complete study of stability is not conducted in this work.

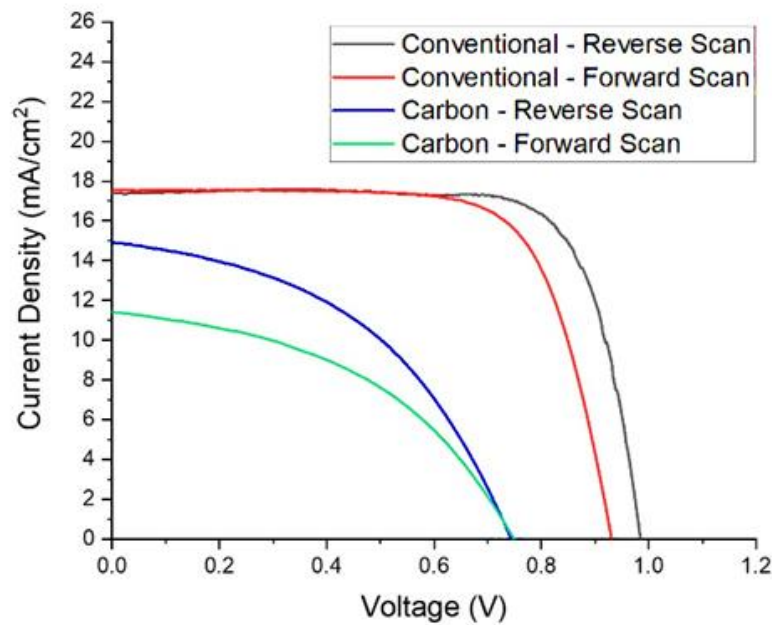


**Figure 6.9.** J-V curves of the conventional and carbon PSCs.

**Table 6.4.** Average photovoltaic parameters for 5 conventional and carbon PSCs.

Structure	V <sub>oc</sub> (V)	J <sub>sc</sub> (mA/cm <sup>2</sup> )	PCE (%)	FF (%)
Conventional	0.98 ± 0.022	17.24 ± 0.28	12.65 ± 0.39	75.15 ± 1.39
Carbon	0.77 ± 0.025	13.46 ± 1.67	4.53 ± 0.38	44 ± 1.31

## 6.9. Conclusion

This work introduced the inkjet printing of charge transport films in PSCs through an integrated robotic setup. It was shown that the optimal deposition parameters play a vital role on the morphology and performance of PSCs. The optimization demonstrated that a larger stroke is required for higher viscosity precursors. At a very low stroke, stochastic droplets with different sizes were impinged on the surface which was attributed to insufficient force forming reproducible droplets in a straight pathway. At higher stroke rates, the thickness and width of the printed lines were increased, forming more ununiform prints with irregular edges which was attributed to more intensified impinging of the larger volume droplets to the substrate. At an optimal dispensing frequency, straight lines with uniform boundaries were formed, yet increasing the frequency increased the line width as the result of more material deposition. Similarly, the line distancing, forming a film of the material, was found to play a significant role on the morphology, thickness, and conductivity of the film. IPL annealing of the wet SnO<sub>2</sub> films printed at shorter line distances indicated a nonuniform morphology as the result of Marangoni effect. Similarly, IPL annealing of the wet carbon films severely damaged the morphology and degraded the carbon film; however, naturally dried carbon films exhibited a uniform morphology. The faster drying of wet carbon films in the printing chamber equipped with a hood resulted in rapid solvent evaporation and maintained the film uniformity; however, XRD unraveled higher quality carbon films upon IPL annealing at 100 J – 100 μs condition. PSCs fabricated using the conventional method, where merely the SnO<sub>2</sub> film was deposited using inkjet printing, exhibited the maximum PCE of 13.08%, whereas the PSCs with inkjet printing of all the charge transport films exhibited maximum efficiency of 5.03% which was attributed to the lower conductivity of the carbon films and elimination of HTL. This

work exemplified the robotic fabrication of PSCs, where the charge transport films were rapidly and entirely fabricated through a non-roll-to-roll setup utilizing inkjet printing and IPL annealing in the ambient environment.

## CHAPTER VII

### CONCLUSION

The PSCs thin film materials are solution processable, hence can be rapidly deposited using scalable depositions. However, the post-process annealing of the film materials require medium to high temperatures for a long period, up to an hour, which is a hinderance for high throughput manufacturing in terms of processing speed as well as high energy and costs. In addition, some of the utilized films in PSCs, particularly the perovskite absorber layer, require an inert environment, such as nitrogen glovebox, for processing which is not favorable for upscale manufacturing. Chapter 1 explained the theory of solar cells, discussed the conventional solar cells and associated challenges, and introduced emerging thin film solar cells, particularly PSCs, and stated the challenge of rapid fabrication of PSCs through IPL in a high humid ambient environment (>60%). The second chapter investigated faster processing of PSCs through IPL annealing of an aqueous solution of SnO<sub>2</sub> by investigating the impact of flash energy and counts on the performance of PSCs. It was found that 5 flashes, each with 2 ms duration, 2000 J/pulse (8.89 J/cm<sup>2</sup>) could result in efficient PSCs as high as 12.56% efficiency, whereas lower applied energies of 1400 J/pulse (6.23 J/cm<sup>2</sup>) resulted in lower performance as the result of lower current extraction caused by less SnO<sub>2</sub> crystallization. Notably, lower and higher flash counts than five exhibited similar results. This work utilized CH<sub>2</sub>I<sub>2</sub> in the triple cation perovskite chemistry which enabled atmospheric processing of perovskite films by

producing superior morphology without dendrites, pushing a step towards ambient environment processing of PSCs, yet the HTL and back contacts utilized Spiro-MeOTAD, and gold deposited in the nitrogen environment and vacuum. The third chapter detailed the utilized materials and methods of fabricating PSCs and introduced a model to measure and simulate through ANSYS the rapid temperature rise occurring during IPL annealing. Chapter 4 introduced two annealing approaches of UFA and GFA which allowed for direct IPL annealing of deposited perovskite films in 4 and 6 seconds and resulted in 11.75% and 9.27%, respectively. To investigate this enhancement, the temperature during IPL annealing of perovskite was measured using a custom developed setup and were confirmed with FEA using ANSYS. In addition, Arrhenius equations were plotted to aid understanding the photothermal impact on morphology and phase purity of the perovskite film and attributed the enhancement to the retarded crystallization and diffusion of species as well as regulating the solvent evaporation. This study applied IPL to anneal both the SnO<sub>2</sub> and perovskite films deposited in the ambient environment which is applicable for high-throughput scalable fabrication of PSCs. Chapter six exemplified automated fabrication of SnO<sub>2</sub> ETL as well as carbon films replacing the Spiro-MeOTAD HTL and gold back-contact in PSCs using an integrated robotic setup consisted of a piezoelectric printhead and IPL. This chapter investigated the deposition optimization of both charge transport layers by investigation the role of frequency and stroke, as well as line distancing to provide the superior morphology. The IPL annealing of wet carbon films severely damaged the films, necessitating drying of films before IPL annealing. The exposure of high energy and durations of 400 J/pulse (1.7 J/cm<sup>2</sup>) and 500 μs yet damaged the dried carbon films, exhibiting pinholes and surface defects. However, at an optimum IPL

annealing condition of 100 J – 100  $\mu$ s, PSCs exceeding 5% efficiency were produced. This work establishes the pioneering work on utilizing IPL in an entirely automated fabrication line, allowing for scalable fabrication of PSC thin films through a non-roll-to-roll setup.



## CHAPTER VIII

### RECOMMENDATIONS

This dissertation established a pathway towards high-speed manufacturing of PSCs by promoting IPL towards successful annealing of the individual layers of SnO<sub>2</sub> ETL, perovskite, and carbon. The dissertation introduced a study by investigating the photothermal impact on the morphology, phase purity, and crystallization of the perovskite as the main pillar of PSCs. However, a similar approach is recommended to be carried out on SnO<sub>2</sub> ETL and carbon film to better anneal these layers, enabling for higher performance PSCs. In addition, in-depth interface study at the ETL/perovskite and perovskite/HTL is recommended to determine the bottom-up crystallization kinetics for better optimization towards higher performance PSCs. This dissertation utilized a two-step gradated approach to tune the temperature profile and fabricate higher quality perovskite films, however, multi-step approaches with three or more steps is recommended for investigation towards better crystallization of thin film materials. Furthermore, the current study investigated IPL for automation using robotic fabrication; however, it is recommended to investigate this annealing method on roll-to-roll fabrication of PSCs as a more favorable approach for PSC fabrication in terms of high-speed capability and lower manufacturing costs.

The utilized work investigated the use of CH<sub>2</sub>I<sub>2</sub> additive containing excess iodine which allowed for ambient processing of the perovskite films as the result of higher

boiling point and resulted in superior morphology due to releasing iodine during IPL annealing, avoiding iodide deficiency in perovskite films upon annealing. It is well known that the addition of chlorine and bromine in perovskite chemistries aids better crystallization as well as thermal and moisture stability, respectively. Therefore, the use of other alkyl halides containing two or more halides, such as chloro-iodomethane and chloro-bromo-iodomethane, is recommended to obtain better crystallization and moisture stability of ambient environment processed PSCs.

## REFERENCES

1. IPCC SR15 Summary for Policymakers 2018, p. W., p. 6.
2. IEA (2019), W. E. O., IEA, Paris.
3. <https://yearbook.enerdata.net/total-energy/world-consumption-statistics.html>.
4. IEA (2019), R., IEA, Paris <https://www.iea.org/reports/renewables-2019>.
5. Akinyele, D., Rayudu, R. & Nair, N. (2017) Life cycle impact assessment of photovoltaic power generation from crystalline silicon-based solar modules in Nigeria, *Renewable Energy*. 101, 537-549.
6. Green, M. A., Dunlop, E. D., Hohl-Ebinger, J., Yoshita, M., Kopidakis, N. & Hao, X. (2020) Solar cell efficiency tables (version 56), *Progress in Photovoltaics: Research and Applications*. 28, 629-638.
7. Wolden, C. A., Kurtin, J., Baxter, J. B., Repins, I., Shaheen, S. E., Torvik, J. T., Rockett, A. A., Fthenakis, V. M. & Aydil, E. S. (2011) Photovoltaic manufacturing: Present status, future prospects, and research needs, *Journal of Vacuum Science & Technology A: Vacuum, Surfaces, and Films*. 29(3), 030801.
8. Moon, S., Kim, K., Kim, Y., Heo, J. & Lee, J. (2016) Highly efficient single-junction GaAs thin-film solar cell on flexible substrate, *Scientific reports*. 6(1), 30107.
9. Zhao, Y., Yuan, S., Kou, D., Zhou, Z., Wang, X., Xiao, H., Deng, Y., Cui, C., Chang, Q. & Wu, S. (2020) High Efficiency CIGS Solar Cells by Bulk Defect Passivation through Ag Substituting Strategy, *ACS Applied Materials & Interfaces*. 12, 12717-12726.
10. Jackson, P., Hariskos, D., Wuerz, R., Wischmann, W. & Powalla, M. (2014) Compositional investigation of potassium doped Cu (In, Ga) Se<sub>2</sub> solar cells with efficiencies up to 20.8%, *physica status solidi (RRL)–Rapid Research Letters*. 8(3), 219-222.
11. Kephart, J., McCamy, J., Ma, Z., Ganjoo, A., Alamgir, F. & Sampath, W. (2016) Band alignment of front contact layers for high-efficiency CdTe solar cells, *Solar Energy Materials and Solar Cells*. 157, 266-275.
12. Ma, C. & Park, N.-G. (2020) A Realistic Methodology for 30% Efficient Perovskite Solar Cells, *Chem*. 6(6), 1254-1264.

13. Kumar, A., Goyal, A. K., Gupta, U., Gupta, N. & Chaujar, R. (2020) Increased efficiency of 23% for CIGS solar cell by using ITO as front contact, *Materials Today: Proceedings*. 28, 361-365.
14. Li, D.-B., Bista, S. S., Song, Z., Awni, R. A., Subedi, K. K., Shrestha, N., Pradhan, P., Chen, L., Bastola, E. & Grice, C. R. (2020) Maximize CdTe solar cell performance through copper activation engineering, *Nano Energy*, 73, 104835.
15. Moss, S. J. & Ledwith, A. (1989) Chemistry of the Semiconductor Industry, *Springer Science & Business Media*.
16. Cao, Y., Liu, Y., Zakeeruddin, S. M., Hagfeldt, A. & Grätzel, M. (2018) Direct contact of selective charge extraction layers enables high-efficiency molecular photovoltaics, *Joule*. 2(6), 1108-1117.
17. O'regan, B. & Grätzel, M. (1991) A low-cost, high-efficiency solar cell based on dye-sensitized colloidal TiO<sub>2</sub> films, *nature*. 353(6346), 737-740.
18. Appleton, E. V. (1945) Departure of long-wave solar radiation from black-body intensity, *Nature*. 156(3966), 534-535.
19. Lumb, M. P., Mack, S., Schmieder, K. J., González, M., Bennett, M. F., Scheiman, D., Meitl, M., Fisher, B., Burroughs, S. & Lee, K. T. (2017) GaSb-based solar cells for full solar spectrum energy harvesting, *Advanced energy materials*. 7(20), 1700345.
20. Becquerel's, E. (2005) electrochemical actinometer, *Archives des sciences*. 58, 149-158.
21. Fatet, J. (2006) Recreating Edmond Becquerel's electrochemical Actinometer: What can historical experiments replication teach us?. In *Colloquium Theory of Science and History of Science*.
22. Adams, W. G. & Day, R. (1877) V. The action of light on selenium, *Proceedings of the Royal Society of London*. 25(171-178), 113-117.
23. Fraas, L. M. (2014) History of solar cell development, *Low-Cost Solar Electric Power*. 1-12, Springer.
24. Choudhury, S. A., Fairouz, F., Rifat, R. A. & Chowdhury, M. H. (2019) Metal nanostructures for solar cells, *Nanomaterials for Solar Cell Applications*. 447-511, Elsevier.
25. Tobin, L. L., O'Reilly, T., Zerulla, D. & Sheridan, J. T. (2011) Characterising dye-sensitised solar cells, *Optik*. 122(14), 1225-1230.
26. Chapin, D. M., Fuller, C. & Pearson, G. (1954) A new silicon p-n junction photocell for converting solar radiation into electrical power, *Journal of applied physics*. 25(5), 676-677.
27. Lojek, B. (2007) *History of semiconductor engineering*, Springer.

28. Alferov, Z. I., Andreev, V., Kagan, M., Protasov, I. & Trofim, V. (1971) Solar-energy converters based on pn  $\text{Al}_x\text{Ga}_{1-x}\text{As-GaAs}$  heterojunctions, *Soviet Physics-Semiconductors(English Translation);(United States)*. 4(12).
29. Bonnet, D. & Rabenhorst, H. (1972). New results on the development of a thin-film p-CdTe-n-CdS heterojunction solar cell, *Photovoltaic Specialists Conference, 9 th, Silver Spring, MD*, 129-132.
30. Attfield, J. P., Lightfoot, P. & Morris, R. E. (2015) Perovskites, *Dalton Transactions*. 44(23), 10541-10542.
31. Maeno, Y., Hashimoto, H., Yoshida, K., Nishizaki, S., Fujita, T., Bednorz, J. & Lichtenberg, F. (1994) Superconductivity in a layered perovskite without copper, *Nature*. 372(6506), 532-534.
32. Fong, D. D., Stephenson, G. B., Streiffer, S. K., Eastman, J. A., Auciello, O., Fuoss, P. H. & Thompson, C. (2004) Ferroelectricity in ultrathin perovskite films, *Science*. 304(5677), 1650-1653.
33. Rao, C., Mahesh, R., Raychaudhuri, A. & Mahendiran, R. (1998) Giant magnetoresistance, charge ordering and other novel properties of perovskite manganates, *Journal of Physics and Chemistry of Solids*. 59(4), 487-501.
34. Shan, Q., Song, J., Zou, Y., Li, J., Xu, L., Xue, J., Dong, Y., Han, B., Chen, J. & Zeng, H. (2017) High performance metal halide perovskite light-emitting diode: from material design to device optimization, *Small*. 13(45), 1701770.
35. Liu, X., Yu, D., Song, X. & Zeng, H. (2018) Metal Halide Perovskites: Synthesis, Ion Migration, and Application in Field-Effect Transistors, *Small*. 14(36), 1801460.
36. Chen, Q., Wu, J., Ou, X., Huang, B., Almutlaq, J., Zhumeckenov, A. A., Guan, X., Han, S., Liang, L. & Yi, Z. (2018) All-inorganic perovskite nanocrystal scintillators, *Nature*. 561(7721), 88-93.
37. Zhu, H., Fu, Y., Meng, F., Wu, X., Gong, Z., Ding, Q., Gustafsson, M. V., Trinh, M. T., Jin, S. & Zhu, X. (2015) Lead halide perovskite nanowire lasers with low lasing thresholds and high quality factors, *Nature materials*. 14(6), 636-642.
38. Hanusch, F. C., Wiesenmayer, E., Mankel, E., Binek, A., Angloher, P., Fraunhofer, C., Giesbrecht, N., Feckl, J. M., Jaegermann, W. & Johrendt, D. (2014) Efficient planar heterojunction perovskite solar cells based on formamidinium lead bromide, *The journal of physical chemistry letters*. 5(16), 2791-2795.
39. Zhang, X., Ren, X., Liu, B., Munir, R., Zhu, X., Yang, D., Li, J., Liu, Y., Smilgies, D.-M. & Li, R. (2017) Stable high efficiency two-dimensional perovskite solar cells via cesium doping, *Energy & Environmental Science*. 10(10), 2095-2102.
40. Wang, K., Jin, Z., Liang, L., Bian, H., Bai, D., Wang, H., Zhang, J., Wang, Q. & Liu, S. (2018) All-inorganic cesium lead iodide perovskite solar cells with stabilized efficiency beyond 15%, *Nature communications*. 9(1), 1-8.

41. Park, Y. H., Jeong, I., Bae, S., Son, H. J., Lee, P., Lee, J., Lee, C. H. & Ko, M. J. (2017) Inorganic rubidium cation as an enhancer for photovoltaic performance and moisture stability of  $\text{HC}(\text{NH}_2)_2\text{PbI}_3$  perovskite solar cells, *Advanced Functional Materials*. 27(16), 1605988.
42. Meng, X., Wang, Y., Lin, J., Liu, X., He, X., Barbaud, J., Wu, T., Noda, T., Yang, X. & Han, L. (2020) Surface-controlled oriented growth of  $\text{FASnI}_3$  crystals for efficient lead-free perovskite solar cells, *Joule*. 4(4), 902-912.
43. Yu, B. B., Xu, L., Liao, M., Wu, Y., Liu, F., He, Z., Ding, J., Chen, W., Tu, B. & Lin, Y. (2019) Synergy Effect of Both 2, 2, 2-Trifluoroethylamine Hydrochloride and  $\text{SnF}_2$  for Highly Stable  $\text{FASnI}_{3-x}\text{Cl}_x$  Perovskite Solar Cells, *Solar RRL*. 3(3), 1800290.
44. Shao, S., Liu, J., Portale, G., Fang, H. H., Blake, G. R., ten Brink, G. H., Koster, L. J. A. & Loi, M. A. (2018) Highly reproducible Sn-based hybrid perovskite solar cells with 9% efficiency, *Advanced Energy Materials*. 8(4), 1702019.
45. Chen, M., Ju, M.-G., Garces, H. F., Carl, A. D., Ono, L. K., Hawash, Z., Zhang, Y., Shen, T., Qi, Y. & Grimm, R. L. (2019) Highly stable and efficient all-inorganic lead-free perovskite solar cells with native-oxide passivation, *Nature communications*. 10(1), 1-8.
46. Lee, B., Hwang, T., Lee, S., Shin, B. & Park, B. (2019) Microstructural evolution of hybrid perovskites promoted by chlorine and its impact on the performance of solar cell, *Scientific reports*. 9(1), 1-8.
47. Fan, L., Ding, Y., Luo, J., Shi, B., Yao, X., Wei, C., Zhang, D., Wang, G., Sheng, Y. & Chen, Y. (2017) Elucidating the role of chlorine in perovskite solar cells, *Journal of Materials Chemistry A*. 5(16), 7423-7432.
48. Tong, G., Chen, T., Li, H., Song, W., Chang, Y., Liu, J., Yu, L., Xu, J., Qi, Y. & Jiang, Y. (2019) High efficient hole extraction and stable all-bromide inorganic perovskite solar cells via derivative-phase gradient bandgap architecture, *Solar RRL*. 3(5), 1900030.
49. Park, B.-w., Kedem, N., Kulbak, M., Yang, W. S., Jeon, N. J., Seo, J., Kim, G., Kim, K. J., Shin, T. J. & Hodes, G. (2018) Understanding how excess lead iodide precursor improves halide perovskite solar cell performance, *Nature communications*. 9(1), 1-8.
50. Singh, T. & Miyasaka, T. (2016) High performance perovskite solar cell via multi-cycle low temperature processing of lead acetate precursor solutions, *Chemical Communications*. 52(26), 4784-4787.
51. Filip, M. R., Eperon, G. E., Snaith, H. J. & Giustino, F. (2014) Steric engineering of metal-halide perovskites with tunable optical band gaps, *Nature communications*. 5(1), 1-9.
52. Hao, F., Stoumpos, C. C., Cao, D. H., Chang, R. P. H. & Kanatzidis, M. G. (2014) Lead-free solid-state organic-inorganic halide perovskite solar cells, *Nature Photonics*. 8(6), 489-494.

53. Ponseca Jr, C. S., Savenije, T. J., Abdellah, M., Zheng, K., Yartsev, A., Pascher, T. r., Harlang, T., Chabera, P., Pullerits, T. & Stepanov, A. (2014) Organometal halide perovskite solar cell materials rationalized: ultrafast charge generation, high and microsecond-long balanced mobilities, and slow recombination, *Journal of the American Chemical Society*. 136(14), 5189-5192.
54. Dong, Q., Fang, Y., Shao, Y., Mulligan, P., Qiu, J., Cao, L. & Huang, J. (2015) Electron-hole diffusion lengths  $>175 \mu\text{m}$  in solution-grown  $\text{CH}_3\text{NH}_3\text{PbI}_3$  single crystals, *Science*. 347(6225), 967-970.
55. Yang, Z., Surrente, A., Galkowski, K., Bruyant, N., Maude, D. K., Haghighirad, A. A., Snaith, H. J., Plochocka, P. & Nicholas, R. J. (2017) Unraveling the Exciton Binding Energy and the Dielectric Constant in Single-Crystal Methylammonium Lead Triiodide Perovskite, *The journal of physical chemistry letters*. 8(8), 1851-1855.
56. De Wolf, S., Holovsky, J., Moon, S.-J., Loÿper, P., Niesen, B., Ledinsky, M., Haug, F.-J., Yum, J.-H. & Ballif, C. (2014) Organometallic halide perovskites: sharp optical absorption edge and its relation to photovoltaic performance, *The journal of physical chemistry letters*. 5(6), 1035-1039.
57. Xiao, Z., Yuan, Y., Wang, Q., Shao, Y., Bai, Y., Deng, Y., Dong, Q., Hu, M., Bi, C. & Huang, J. (2016) Thin-film semiconductor perspective of organometal trihalide perovskite materials for high-efficiency solar cells, *Materials Science and Engineering: R: Reports*. 101, 1-38.
58. Kojima, A., Teshima, K., Shirai, Y. & Miyasaka, T. (2009) Organometal halide perovskites as visible-light sensitizers for photovoltaic cells, *Journal of the American Chemical Society*. 131(17), 6050-6051.
59. Divitini, G., Cacovich, S., Matteocci, F., Cinà, L., Di Carlo, A. & Ducati, C. (2016) In situ observation of heat-induced degradation of perovskite solar cells, *Nature Energy*. 1(2), 1-6.
60. Juarez-Perez, E. J., Hawash, Z., Raga, S. R., Ono, L. K. & Qi, Y. (2016) Thermal degradation of  $\text{CH}_3\text{NH}_3\text{PbI}_3$  perovskite into  $\text{NH}_3$  and  $\text{CH}_3\text{I}$  gases observed by coupled thermogravimetry–mass spectrometry analysis, *Energy & environmental science*. 9(11), 3406-3410.
61. Wang, Q., Chen, B., Liu, Y., Deng, Y., Bai, Y., Dong, Q. & Huang, J. (2017) Scaling behavior of moisture-induced grain degradation in polycrystalline hybrid perovskite thin films, *Energy & Environmental Science*. 10(2), 516-522.
62. Salado, M., Contreras-Bernal, L., Caliò, L., Todinova, A., López-Santos, C., Ahmad, S., Borrás, A., Idígoras, J. & Anta, J. A. (2017) Impact of moisture on efficiency-determining electronic processes in perovskite solar cells, *Journal of Materials Chemistry A*. 5(22), 10917-10927.

63. Nie, W., Blancon, J.-C., Neukirch, A. J., Appavoo, K., Tsai, H., Chhowalla, M., Alam, M. A., Sfeir, M. Y., Katan, C. & Even, J. (2016) Light-activated photocurrent degradation and self-healing in perovskite solar cells, *Nature communications*. 7(1), 1-9.
64. Deng, X., Wen, X., Zheng, J., Young, T., Lau, C. F. J., Kim, J., Green, M., Huang, S. & Ho-Baillie, A. (2018) Dynamic study of the light soaking effect on perovskite solar cells by in-situ photoluminescence microscopy, *Nano Energy*. 46, 356-364.
65. Ma, S., Bai, Y., Wang, H., Zai, H., Wu, J., Li, L., Xiang, S., Liu, N., Liu, L. & Zhu, C. (2020) 1000 h Operational Lifetime Perovskite Solar Cells by Ambient Melting Encapsulation, *Advanced Energy Materials*. 10(9), 1902472.
66. Cheacharoen, R., Boyd, C. C., Burkhard, G. F., Leijtens, T., Raiford, J. A., Bush, K. A., Bent, S. F. & McGehee, M. D. (2018) Encapsulating perovskite solar cells to withstand damp heat and thermal cycling, *Sustainable Energy & Fuels*. 2(11), 2398-2406.
67. Druffel, T., Lavery, B., Ankireddy, K., Ghahremani, A. H., Martin, B. & Gupta, G. (2021) Methods for forming a perovskite solar cell, U.S. Patent No. 10,950,794, issued March 16, 2021.
68. Poglitsch, A. & Weber, D. (1987) Dynamic disorder in methylammoniumtrihalogenoplumbates (II) observed by millimeter-wave spectroscopy, *The Journal of chemical physics*. 87(11), 6373-6378.
69. Zhang, Y., Wu, C., Wang, D., Zhang, Z., Qi, X., Zhu, N., Liu, G., Li, X., Hu, H. & Chen, Z. (2019) High Efficiency (16.37%) of Cesium Bromide—Passivated All-Inorganic CsPbI<sub>2</sub>Br Perovskite Solar Cells, *Solar RRL*. 3(11), 1900254.
70. Chai, G., Luo, S., Zhou, H. & Daoud, W. A. (2017) CH<sub>3</sub>NH<sub>3</sub>PbI<sub>3-x</sub>Br<sub>x</sub> perovskite solar cells via spray assisted two-step deposition: Impact of bromide on stability and cell performance, *Materials & Design*. 125, 222-229.
71. Kim, M., Kim, G.-H., Lee, T. K., Choi, I. W., Choi, H. W., Jo, Y., Yoon, Y. J., Kim, J. W., Lee, J. & Huh, D. (2019) Methylammonium chloride induces intermediate phase stabilization for efficient perovskite solar cells, *Joule*. 3(9), 2179-2192.
72. Jeon, N. J., Noh, J. H., Kim, Y. C., Yang, W. S., Ryu, S. & Seok, S. I. (2014) Solvent engineering for high-performance inorganic–organic hybrid perovskite solar cells, *Nature materials*. 13(9), 897-903.
73. Colella, S., Mosconi, E., Fedeli, P., Listorti, A., Gazza, F., Orlandi, F., Ferro, P., Besagni, T., Rizzo, A. & Calestani, G. (2013) MAPbI<sub>3-x</sub>Cl<sub>x</sub> mixed halide perovskite for hybrid solar cells: the role of chloride as dopant on the transport and structural properties, *Chemistry of Materials*. 25(22), 4613-4618.
74. Yang, M., Li, Z., Reese, M. O., Reid, O. G., Kim, D. H., Siol, S., Klein, T. R., Yan, Y., Berry, J. J. & Van Hest, M. F. (2017) Perovskite ink with wide processing window for scalable high-efficiency solar cells, *Nature Energy*. 2(5), 1-9.



75. Jeon, N. J., Noh, J. H., Yang, W. S., Kim, Y. C., Ryu, S., Seo, J. & Seok, S. I. (2015) Compositional engineering of perovskite materials for high-performance solar cells, *Nature*. 517(7535), 476-480
76. Eperon, G. E., Stranks, S. D., Menelaou, C., Johnston, M. B., Herz, L. M. & Snaith, H. J. (2014) Formamidinium lead trihalide: a broadly tunable perovskite for efficient planar heterojunction solar cells, *Energy & Environmental Science*. 7(3), 982-988.
77. Zhang, Y., Seo, S., Lim, S. Y., Kim, Y., Kim, S.-G., Lee, D.-K., Lee, S.-H., Shin, H., Cheong, H. & Park, N.-G. (2019) Achieving Reproducible and High-Efficiency (> 21%) Perovskite Solar Cells with a Presynthesized FAPbI<sub>3</sub> Powder, *ACS Energy Letters*. 5(2), 360-366.
78. Yang, Z., Chueh, C.-C., Liang, P.-W., Crump, M., Lin, F., Zhu, Z. & Jen, A. K.-Y. (2016) Effects of formamidinium and bromide ion substitution in methylammonium lead triiodide toward high-performance perovskite solar cells, *Nano Energy*. 22, 328-337.
79. Saliba, M., Matsui, T., Seo, J.-Y., Domanski, K., Correa-Baena, J.-P., Nazeeruddin, M. K., Zakeeruddin, S. M., Tress, W., Abate, A. & Hagfeldt, A. (2016) Cesium-containing triple cation perovskite solar cells: improved stability, reproducibility and high efficiency, *Energy & Environmental Science*. 9(6), 1989-1997.
80. Zhang, M., Yun, J. S., Ma, Q., Zheng, J., Lau, C. F. J., Deng, X., Kim, J., Kim, D., Seidel, J. & Green, M. A. (2017) High-efficiency rubidium-incorporated perovskite solar cells by gas quenching, *ACS Energy Letters*. 2(2), 438-444.
81. Seo, Y.-H., Kim, E.-C., Cho, S.-P., Kim, S.-S. & Na, S.-I. (2017) High-performance planar perovskite solar cells: Influence of solvent upon performance, *Applied Materials Today*. 9, 598-604.
82. Lv, M., Dong, X., Fang, X., Lin, B., Zhang, S., Ding, J. & Yuan, N. (2015) A promising alternative solvent of perovskite to induce rapid crystallization for high-efficiency photovoltaic devices, *RSC Advances*. 5(26), 20521-20529.
83. Ahn, N., Son, D.-Y., Jang, I.-H., Kang, S. M., Choi, M. & Park, N.-G. (2015) Highly reproducible perovskite solar cells with average efficiency of 18.3% and best efficiency of 19.7% fabricated via Lewis base adduct of lead (II) iodide, *Journal of the American Chemical Society*. 137(27), 8696-8699.
84. Chen, J., Xiong, Y., Rong, Y., Mei, A., Sheng, Y., Jiang, P., Hu, Y., Li, X. & Han, H. (2016) Solvent effect on the hole-conductor-free fully printable perovskite solar cells, *Nano Energy*. 27, 130-137.
85. Cai, B., Zhang, W.-H. & Qiu, J. (2015) Solvent engineering of spin-coating solutions for planar-structured high-efficiency perovskite solar cells, *Chinese Journal of Catalysis*. 36(8), 1183-1190.
86. Gardner, K. L., Tait, J. G., Merckx, T., Qiu, W., Paetzold, U. W., Kootstra, L., Jaysankar, M., Gehlhaar, R., Cheyens, D. & Heremans, P. (2016) Nonhazardous solvent

systems for processing perovskite photovoltaics, *Advanced Energy Materials*. 6(14), 1600386.

87. Ramadan, A. J., Noel, N. K., Fearn, S., Young, N., Walker, M., Rochford, L. A. & Snaith, H. J. (2018) Unravelling the improved electronic and structural properties of methylammonium lead iodide deposited from acetonitrile, *Chemistry of Materials*. 30(21), 7737-7743.

88. Hendriks, K. H., van Franeker, J. J., Bruijnaers, B. J., Anta, J. A., Wienk, M. M. & Janssen, R. A. (2017) 2-Methoxyethanol as a new solvent for processing methylammonium lead halide perovskite solar cells, *Journal of Materials Chemistry A*. 5(5), 2346-2354.

89. Yang, L., Wang, J. & Leung, W. W.-F. (2015) Lead iodide thin film crystallization control for high-performance and stable solution-processed perovskite solar cells, *ACS applied materials & interfaces*. 7(27), 14614-14619.

90. Wu, Q., Zhou, P., Zhou, W., Wei, X., Chen, T. & Yang, S. (2016) Acetate Salts as Nonhalogen Additives To Improve Perovskite Film Morphology for High-Efficiency Solar Cells, *ACS applied materials & interfaces*. 8(24), 15333-15340

91. Wu, Y., Xie, F., Chen, H., Yang, X., Su, H., Cai, M., Zhou, Z., Noda, T. & Han, L. (2017) Thermally Stable MAPbI<sub>3</sub> Perovskite Solar Cells with Efficiency of 19.19% and Area over 1 cm<sup>2</sup> achieved by Additive Engineering, *Advanced Materials*. 29(28), 1701073.

92. Fu, G., Hou, L., Wang, Y., Liu, X., Wang, J., Li, H., Cui, Y., Liu, D., Li, X. & Yang, S. (2017) Efficiency enhancement in planar CH<sub>3</sub>NH<sub>3</sub>PbI<sub>3-x</sub>Cl<sub>x</sub> perovskite solar cells by processing with bidentate halogenated additives, *Solar Energy Materials and Solar Cells*. 165, 36-44.

93. Chueh, C.-C., Liao, C.-Y., Zuo, F., Williams, S. T., Liang, P.-W. & Jen, A. K.-Y. (2015) The roles of alkyl halide additives in enhancing perovskite solar cell performance, *Journal of Materials Chemistry A*. 3(17), 9058-9062.

94. Li, J., Wang, N., Bi, F., Chen, S., Zhao, C., Liu, L., Yao, Q., Huang, C., Xue, Y. & Liu, H. (2019) Inverted MAPbI<sub>3</sub> Perovskite Solar Cells with Graphdiyne Derivative-Incorporated Electron Transport Layers Exceeding 20% Efficiency, *Solar RRL*. 3(10), 1900241.

95. Yang, D., Zhang, X., Wang, K., Wu, C., Yang, R., Hou, Y., Jiang, Y., Liu, S. & Priya, S. (2019) Stable efficiency exceeding 20.6% for inverted perovskite solar cells through polymer-optimized PCBM electron-transport layers, *Nano Letters*. 19(5), 3313-3320.

96. Jeong, I., Park, Y. H., Bae, S., Park, M., Jeong, H., Lee, P. & Ko, M. J. (2017) Solution-processed ultrathin TiO<sub>2</sub> compact layer hybridized with mesoporous TiO<sub>2</sub> for high-performance perovskite solar cells, *ACS applied materials & interfaces*. 9(42), 36865-36874.

97. Xie, H., Yin, X., Liu, J., Guo, Y., Chen, P., Que, W., Wang, G. & Gao, B. (2019) Low temperature solution-derived TiO<sub>2</sub>-SnO<sub>2</sub> bilayered electron transport layer for high performance perovskite solar cells, *Applied Surface Science*. 464, 700-707.
98. Leijtens, T., Eperon, G. E., Pathak, S., Abate, A., Lee, M. M. & Snaith, H. J. (2013) Overcoming ultraviolet light instability of sensitized TiO<sub>2</sub> with meso-superstructured organometal tri-halide perovskite solar cells, *Nature communications*. 4(1), 1-8.
99. Wang, H., Cao, S., Yang, B., Li, H., Wang, M., Hu, X., Sun, K. & Zang, Z. (2020) NH<sub>4</sub>Cl-Modified ZnO for High-Performance CsPbI<sub>3</sub> Perovskite Solar Cells via Low-Temperature Process, *Solar RRL*. 4(1), 1900363.
100. Cao, J., Wu, B., Chen, R., Wu, Y., Hui, Y., Mao, B. W. & Zheng, N. (2018) Efficient, hysteresis-free, and stable perovskite solar cells with ZnO as electron-transport layer: effect of surface passivation, *Advanced Materials*. 30(11), 1705596.
101. Liang, Z., Bi, Z., Gao, K., Fu, Y., Guan, P., Feng, X., Chai, Z., Xu, G. & Xu, X. (2019) Interface modification via Al<sub>2</sub>O<sub>3</sub> with retarded charge recombinations for mesoscopic perovskite solar cells fabricated with spray deposition process in the air, *Applied Surface Science*. 463, 939-946.
102. Guarnera, S., Abate, A., Zhang, W., Foster, J. M., Richardson, G., Petrozza, A. & Snaith, H. J. (2015) Improving the long-term stability of perovskite solar cells with a porous Al<sub>2</sub>O<sub>3</sub> buffer layer, *The journal of physical chemistry letters*. 6(3), 432-437.
103. You, Y., Tian, W., Min, L., Cao, F., Deng, K. & Li, L. (2020) TiO<sub>2</sub>/WO<sub>3</sub> bilayer as electron transport layer for efficient planar perovskite solar cell with efficiency exceeding 20%, *Advanced Materials Interfaces*. 7(1), 1901406.
104. Ali, F., Pham, N. D., Fan, L., Tiong, V., Ostrikov, K., Bell, J. M., Wang, H. & Tesfamichael, T. (2019) Low Hysteresis Perovskite Solar Cells Using an Electron-Beam Evaporated WO<sub>3-x</sub> Thin Film as the Electron Transport Layer, *ACS Applied Energy Materials*. 2(8), 5456-5464.
105. Wang, X., Deng, L.-L., Wang, L.-Y., Dai, S.-M., Xing, Z., Zhan, X.-X., Lu, X.-Z., Xie, S.-Y., Huang, R.-B. & Zheng, L.-S. (2017) Cerium oxide standing out as an electron transport layer for efficient and stable perovskite solar cells processed at low temperature, *Journal of Materials Chemistry A*. 5(4), 1706-1712.
106. Hu, T., Xiao, S., Yang, H., Chen, L. & Chen, Y. (2018) Cerium oxide as an efficient electron extraction layer for p-i-n structured perovskite solar cells, *Chemical Communications*. 54(5), 471-474.
107. Jiang, Q., Zhang, X. & You, J. (2018) SnO<sub>2</sub>: a wonderful electron transport layer for perovskite solar cells, *Small*. 14(31), 1801154.
108. Jeong, S., Seo, S., Park, H. & Shin, H. (2019) Atomic layer deposition of a SnO<sub>2</sub> electron-transporting layer for planar perovskite solar cells with a power conversion efficiency of 18.3%, *Chemical Communications*. 55(17), 2433-2436.

109. Lee, H. B., Kumar, N., Ovhal, M. M., Kim, Y. J., Song, Y. M. & Kang, J. W. (2020) Dopant-Free, Amorphous–Crystalline Heterophase SnO<sub>2</sub> Electron Transport Bilayer Enables > 20% Efficiency in Triple-Cation Perovskite Solar Cells, *Advanced Functional Materials*. 30(24), 2001559.
110. Halvani Anaraki, E., Kermanpur, A., Mayer, M. T., Steier, L., Ahmed, T., Turren-Cruz, S.-H., Seo, J., Luo, J., Zakeeruddin, S. M. & Tress, W. R. (2018) Low-temperature Nb-doped SnO<sub>2</sub> electron-selective contact yields over 20% efficiency in planar perovskite solar cells, *ACS Energy Letters*. 3(4), 773-778.
111. Liu, Q., Zhang, X., Li, C., Lu, H., Weng, Z., Pan, Y., Chen, W., Hang, X.-C., Sun, Z. & Zhan, Y. (2019) Effect of tantalum doping on SnO<sub>2</sub> electron transport layer via low temperature process for perovskite solar cells, *Applied Physics Letters*. 115(14), 143903.
112. Bahadur, J., Ghahremani, A. H., Martin, B., Druffel, T., Sunkara, M. K. & Pal, K. (2019) Solution processed Mo doped SnO<sub>2</sub> as an effective ETL in the fabrication of low temperature planer perovskite solar cell under ambient conditions, *Organic Electronics*. 67, 159-167.
113. Qiang, Y., Xie, Y., Qi, Y., Wei, P., Shi, H., Geng, C. & Liu, H. (2020) Enhanced performance of carbon-based perovskite solar cells with a Li<sup>+</sup>-doped SnO<sub>2</sub> electron transport layer and Al<sub>2</sub>O<sub>3</sub> scaffold layer, *Solar Energy*. 201, 523-529.
114. Cao, Q., Li, Z., Han, J., Wang, S., Zhu, J., Tang, H., Li, X. & Li, X. (2019) Electron Transport Bilayer with Cascade Energy Alignment for Efficient Perovskite Solar Cells, *Solar RRL*. 3(12), 1900333.
115. Guo, Q., Wu, J., Yang, Y., Liu, X., Lan, Z., Lin, J., Huang, M., Wei, Y., Dong, J. & Jia, J. (2019) High-Performance and Hysteresis-Free Perovskite Solar Cells Based on Rare-Earth-Doped SnO<sub>2</sub> Mesoporous Scaffold, *Research*. 2019, 4049793.
116. Bahadur, J., Ghahremani, A. H., Martin, B., Pishgar, S., Druffel, T., Sunkara, M. K. & Pal, K. (2019) A study on the material characteristics of low temperature cured SnO<sub>2</sub> films for perovskite solar cells under high humidity, *Journal of Materials Science: Materials in Electronics*. 30(20), 18452-18461.
117. Yun, A. J., Kim, J., Hwang, T. & Park, B. (2019) Origins of Efficient Perovskite Solar Cells with Low-Temperature Processed SnO<sub>2</sub> Electron Transport Layer, *ACS Applied Energy Materials*. 2(5), 3554-3560.
118. Liu, J., Li, N., Dong, Q., Li, J., Qin, C. & Wang, L. (2019) Tailoring electrical property of the low-temperature processed SnO<sub>2</sub> for high-performance perovskite solar cells, *Science China Materials*. 62(2), 173-180.
119. Sun, Q., Li, H., Gong, X., Ban, H., Shen, Y. & Wang, M. (2020) Interconnected SnO<sub>2</sub> nanocrystals electron transport layer for highly efficient flexible perovskite solar cells, *Solar RRL*. 4(2), 1900229.

120. Bakr, Z. H., Wali, Q., Fakharuddin, A., Schmidt-Mende, L., Brown, T. M. & Jose, R. (2017) Advances in hole transport materials engineering for stable and efficient perovskite solar cells, *Nano Energy*. 34, 271-305.
121. Cameron, J. & Skabara, P. J. (2020) The damaging effects of the acidity in PEDOT:PSS on semiconductor device performance and solutions based on non-acidic alternatives, *Materials Horizons*. 7(7), 1759-1772.
122. You, J., Meng, L., Song, T.-B., Guo, T.-F., Yang, Y. M., Chang, W.-H., Hong, Z., Chen, H., Zhou, H. & Chen, Q. (2016) Improved air stability of perovskite solar cells via solution-processed metal oxide transport layers, *Nature nanotechnology*. 11(1), 75-81.
123. Zuo, C. & Ding, L. (2015) Solution-processed Cu<sub>2</sub>O and CuO as hole transport materials for efficient perovskite solar cells, *Small*. 11(41), 5528-5532.
124. Chatterjee, S. & Pal, A. J. (2016) Introducing Cu<sub>2</sub>O thin films as a hole-transport layer in efficient planar perovskite solar cell structures, *The Journal of Physical Chemistry C*. 120(3), 1428-1437.
125. Gharibzadeh, S., Nejand, B. A., Moshaii, A., Mohammadian, N., Alizadeh, A. H., Mohammadpour, R., Ahmadi, V. & Alizadeh, A. (2016) Two-step physical deposition of a compact CuI Hole-Transport layer and the formation of an interfacial species in perovskite solar cells, *ChemSusChem*. 9(15), 1929-1937.
126. Khadka, D. B., Shirai, Y., Yanagida, M. & Miyano, K. (2020) Ammoniated aqueous precursor ink processed copper iodide as hole transport layer for inverted planar perovskite solar cells, *Solar Energy Materials and Solar Cells*. 210, 110486.
127. Sun, W., Ye, S., Rao, H., Li, Y., Liu, Z., Xiao, L., Chen, Z., Bian, Z. & Huang, C. (2016) Room-temperature and solution-processed copper iodide as the hole transport layer for inverted planar perovskite solar cells, *Nanoscale*. 8(35), 15954-15960.
128. Arora, N., Dar, M. I., Hinderhofer, A., Pellet, N., Schreiber, F., Zakeeruddin, S. M. & Grätzel, M. (2017) Perovskite solar cells with CuSCN hole extraction layers yield stabilized efficiencies greater than 20%, *Science*. 358(6364), 768-771.
129. Madhavan, V. E., Zimmermann, I., Baloch, A. A., Manekkathodi, A., Belaidi, A., Tabet, N. & Nazeeruddin, M. K. (2019) CuSCN as Hole Transport Material with 3D/2D Perovskite Solar Cells, *ACS Applied Energy Materials*. 3(1), 114-121.
130. Jung, J. W., Chueh, C. C. & Jen, A. K. Y. (2015) A Low-Temperature, Solution-Processable, Cu-Doped Nickel Oxide Hole-Transporting Layer via the Combustion Method for High-Performance Thin-Film Perovskite Solar Cells, *Advanced Materials*. 27(47), 7874-7880.
131. Park, J. H., Seo, J., Park, S., Shin, S. S., Kim, Y. C., Jeon, N. J., Shin, H.-W., Ahn, T. K., Noh, J. H. & Yoon, S. C. (2015) Efficient CH<sub>3</sub>NH<sub>3</sub>PbI<sub>3</sub> Perovskite Solar Cells Employing Nanostructured p-Type NiO Electrode Formed by a Pulsed Laser Deposition, *Advanced Materials*. 27(27), 4013-4019.

132. Hu, Z., Chen, D., Yang, P., Yang, L., Qin, L., Huang, Y. & Zhao, X. (2018) Sol-gel-processed yttrium-doped NiO as hole transport layer in inverted perovskite solar cells for enhanced performance, *Applied Surface Science*. 441, 258-264.
133. Chen, W., Liu, F. Z., Feng, X. Y., Djurišić, A. B., Chan, W. K. & He, Z. B. (2017) Cesium doped NiOx as an efficient hole extraction layer for inverted planar perovskite solar cells, *Advanced Energy Materials*. 7(19), 1700722.
134. Gil, B., Yun, A. J., Lee, Y., Kim, J., Lee, B. & Park, B. (2019) Recent progress in inorganic hole transport materials for efficient and stable perovskite solar cells, *Electronic Materials Letters*, 15(5), 505-524.
135. Pattanasattayavong, P., Yaacobi-Gross, N., Zhao, K., Ndjawa, G. O. N., Li, J., Yan, F., O'Regan, B. C., Amassian, A. & Anthopoulos, T. D. (2013) Hole-transporting transistors and circuits based on the transparent inorganic semiconductor copper (I) thiocyanate (CuSCN) processed from solution at room temperature, *Adv Mater*. 25(10), 1504-1509.
136. Pattanasattayavong, P., Ndjawa, G. O. N., Zhao, K., Chou, K. W., Yaacobi-Gross, N., O'Regan, B. C., Amassian, A. & Anthopoulos, T. D. (2013) Electric field-induced hole transport in copper (I) thiocyanate (CuSCN) thin-films processed from solution at room temperature, *Chemical Communications*. 49(39), 4154-4156.
137. O'Regan, B., Schwartz, D. T., Zakeeruddin, S. M. & Grätzel, M. (2000) Electrodeposited Nanocomposite n-p Heterojunctions for Solid-State Dye-Sensitized Photovoltaics, *Advanced Materials*. 12(17), 1263-1267.
138. Liu, S., Liu, R., Chen, Y., Ho, S., Kim, J. H. & So, F. (2014) Nickel oxide hole injection/transport layers for efficient solution-processed organic light-emitting diodes, *Chemistry of Materials*. 26(15), 4528-4534.
139. Liu, Z., Zhang, M., Xu, X., Cai, F., Yuan, H., Bu, L., Li, W., Zhu, A., Zhao, Z. & Wang, M. (2015) NiO nanosheets as efficient top hole transporters for carbon counter electrode based perovskite solar cells, *Journal of Materials Chemistry A*. 3(47), 24121-24127.
140. Liu, Z., Chang, J., Lin, Z., Zhou, L., Yang, Z., Chen, D., Zhang, C., Liu, S. & Hao, Y. (2018) High-Performance Planar Perovskite Solar Cells Using Low Temperature, Solution-Combustion-Based Nickel Oxide Hole Transporting Layer with Efficiency Exceeding 20%, *Advanced Energy Materials*. 8(19), 1703432.
141. Lee, P.-H., Li, B.-T., Lee, C.-F., Huang, Z.-H., Huang, Y.-C. & Su, W.-F. (2020) High-efficiency perovskite solar cell using cobalt doped nickel oxide hole transport layer fabricated by NIR process, *Solar Energy Materials and Solar Cells*. 208, 110352.
142. Deng, Y., Dong, Q., Bi, C., Yuan, Y. & Huang, J. (2016) Air-stable, efficient mixed-cation perovskite solar cells with Cu electrode by scalable fabrication of active layer, *Advanced Energy Materials*. 6(11), 1600372.

143. Li, P., Wu, Z., Hu, H., Zhang, Y., Xiao, T., Lu, X., Ren, Z., Li, G., Wu, Z. & Hao, J. (2020) Efficient Flexible Perovskite Solar Cells Using Low-cost Cu Top and Bottom Electrodes, *ACS Applied Materials & Interfaces*. 12(23), 26050-26059.
144. Behrouznejad, F., Shahbazi, S., Taghavinia, N., Wu, H.-P. & Diao, E. W.-G. (2016) A study on utilizing different metals as the back contact of  $\text{CH}_3\text{NH}_3\text{PbI}_3$  perovskite solar cells, *Journal of Materials Chemistry A*. 4(35), 13488-13498.
145. Domanski, K., Correa-Baena, J.-P., Mine, N., Nazeeruddin, M. K., Abate, A., Saliba, M., Tress, W., Hagfeldt, A. & Grätzel, M. (2016) Not all that glitters is gold: metal-migration-induced degradation in perovskite solar cells, *ACS nano*. 10(6), 6306-6314.
146. Raiford, J. A., Belisle, R. A., Bush, K. A., Prasanna, R., Palmstrom, A. F., McGehee, M. D. & Bent, S. F. (2019) Atomic layer deposition of vanadium oxide to reduce parasitic absorption and improve stability in n-i-p perovskite solar cells for tandems, *Sustainable Energy & Fuels*. 3(6), 1517-1525.
147. Al Mamun, A., Ava, T. T., Zhang, K., Baumgart, H. & Namkoong, G. (2017) New PCBM/carbon based electron transport layer for perovskite solar cells, *Physical Chemistry Chemical Physics*. 19(27), 17960-17966.
148. Singh, R., Jun, H. & Arof, A. (2018) Activated carbon as back contact for HTM-free mixed cation perovskite solar cell, *Phase Transitions*. 91(12), 1268-1276.
149. Li, X., Ding, H.-h., Li, G.-h., Wang, Y., Fang, Z.-m., Yang, S.-f., Ju, H.-x. & Zhu, J.-f. (2019) In situ investigations of interfacial degradation and ion migration at  $\text{CH}_3\text{NH}_3\text{PbI}_3$  perovskite/Ag interface, *Chinese Journal of Chemical Physics*. 32(3), 299-305.
150. Yuan, Y. & Huang, J. (2016) Ion migration in organometal trihalide perovskite and its impact on photovoltaic efficiency and stability, *Accounts of chemical research*. 49(2), 286-293.
151. Christians, J. A., Miranda Herrera, P. A. & Kamat, P. V. (2015) Transformation of the excited state and photovoltaic efficiency of  $\text{CH}_3\text{NH}_3\text{PbI}_3$  perovskite upon controlled exposure to humidified air, *Journal of the American Chemical Society*. 137(4), 1530-1538.
152. Wang, S., Liu, H., Bala, H., Zong, B., Huang, L., Guo, Z.-a., Fu, W., Zhang, B., Sun, G. & Cao, J. (2020) A highly stable hole-conductor-free  $\text{Cs}_x\text{MA}_{1-x}\text{PbI}_3$  perovskite solar cell based on carbon counter electrode, *Electrochimica Acta*. 335, 135686.
153. Li, H., Cao, K., Cui, J., Liu, S., Qiao, X., Shen, Y. & Wang, M. (2016) 14.7% efficient mesoscopic perovskite solar cells using single walled carbon nanotubes/carbon composite counter electrodes, *Nanoscale*. 8(12), 6379-6385.
154. Pitchaiya, S., Eswaramoorthy, N., Natarajan, M., Santhanam, A., Asokan, V., Ramakrishnan, V. M., Rangasamy, B., Sundaram, S., Ravirajan, P. & Velauthapillai, D. (2020) perovskite Solar cells: A porous Graphitic carbon based Hole transporter/counter electrode Material extracted from an invasive plant Species Eichhornia Crassipes, *Scientific Reports*. 10(1), 1-16.

155. Cai, Y., Liang, L. & Gao, P. (2018) Promise of commercialization: Carbon materials for low-cost perovskite solar cells, *Chinese Physics B*. 27(1), 018805.
156. Mohammed, M. K. (2020) High-performance hole conductor-free perovskite solar cell using a carbon nanotube counter electrode, *RSC Advances*. 10(59), 35831-35839.
157. Ma, C., Clark, S., Liu, Z., Liang, L., Firdaus, Y., Tao, R., Han, A., Liu, X., Li, L.-J. & Anthopoulos, T. D. (2020) Solution-Processed Mixed-Dimensional Hybrid Perovskite/Carbon Nanotube Electronics, *ACS nano*. 14(4), 3969-3979.
158. Jeon, I., Yoon, J., Kim, U., Lee, C., Xiang, R., Shawky, A., Xi, J., Byeon, J., Lee, H. M. & Choi, M. (2019) High-performance solution-processed double-walled carbon nanotube transparent electrode for perovskite solar cells, *Advanced Energy Materials*. 9(27), 1901204.
159. Phillips, C., Al-Ahmadi, A., Potts, S.-J., Claypole, T. & Deganello, D. (2017) The effect of graphite and carbon black ratios on conductive ink performance, *Journal of Materials Science*. 52(16), 9520-9530.
160. Kartikay, P., Yella, A. & Mallick, S. (2020) Binder-solvent effects on low temperature-processed carbon-based, hole-transport layer free perovskite solar cells, *Materials Chemistry and Physics*. 256, 123594.
161. Chu, Q.-Q., Ding, B., Qiu, Q., Liu, Y., Li, C.-X., Li, C.-J., Yang, G.-J. & Fang, B. (2018) Cost effective perovskite solar cells with a high efficiency and open-circuit voltage based on a perovskite-friendly carbon electrode, *Journal of Materials Chemistry A*. 6(18), 8271-8279.
162. Chu, Q.-Q., Sun, Z., Ding, B., Moon, K.-s., Yang, G.-J. & Wong, C.-P. (2020) Greatly enhanced power conversion efficiency of hole-transport-layer-free perovskite solar cell via coherent interfaces of perovskite and carbon layers, *Nano Energy*. 77, 105110.
163. Li, B., Tian, J., Guo, L., Fei, C., Shen, T., Qu, X. & Cao, G. (2016) Dynamic growth of pinhole-free conformal  $\text{CH}_3\text{NH}_3\text{PbI}_3$  film for perovskite solar cells, *ACS Applied Materials & Interfaces*. 8(7), 4684-4690.
164. Qiu, W., Merckx, T., Jaysankar, M., De La Huerta, C. M., Rakocevic, L., Zhang, W., Paetzold, U., Gehlhaar, R., Froyen, L. & Poortmans, J. (2016) Pinhole-free perovskite films for efficient solar modules, *Energy & Environmental Science*. 9(2), 484-489.
165. Ye, F., Chen, H., Xie, F., Tang, W., Yin, M., He, J., Bi, E., Wang, Y., Yang, X. & Han, L. (2016) Soft-cover deposition of scaling-up uniform perovskite thin films for high cost-performance solar cells, *Energy & Environmental Science*. 9(7), 2295-2301.
166. Liu, M., Johnston, M. B. & Snaith, H. J. (2013) Efficient planar heterojunction perovskite solar cells by vapour deposition, *Nature*. 501(7467), 395-398.
167. Borchert, J., Milot, R. L., Patel, J. B., Davies, C. L., Wright, A. D., Martínez Maestro, L., Snaith, H. J., Herz, L. M. & Johnston, M. B. (2017) Large-area, highly uniform



evaporated formamidinium lead triiodide thin films for solar cells, *ACS Energy Letters*. 2(12), 2799-2804.

168. Ma, Q., Huang, S., Wen, X., Green, M. A. & Ho-Baillie, A. W. (2016) Hole transport layer free inorganic CsPbIBr<sub>2</sub> perovskite solar cell by dual source thermal evaporation, *Advanced energy materials*. 6(7), 1502202.

169. Leyden, M. R., Ono, L. K., Raga, S. R., Kato, Y., Wang, S. & Qi, Y. (2014) High performance perovskite solar cells by hybrid chemical vapor deposition, *Journal of Materials Chemistry A*. 2(44), 18742-18745.

170. Suárez, I., Juárez-Pérez, E. J., Bisquert, J., Mora-Seró, I. & Martínez-Pastor, J. P. (2015) Polymer/perovskite amplifying waveguides for active hybrid silicon photonics, *Advanced Materials*. 27(40), 6157-6162.

171. Ko, H.-S., Lee, J.-W. & Park, N.-G. (2015) 15.76% efficiency perovskite solar cells prepared under high relative humidity: importance of PbI<sub>2</sub> morphology in two-step deposition of CH<sub>3</sub>NH<sub>3</sub>PbI<sub>3</sub>, *Journal of Materials Chemistry A*. 3(16), 8808-8815.

172. Yuan, S., Qiu, Z., Gao, C., Zhang, H., Jiang, Y., Li, C., Yu, J. & Cao, B. (2016) High-quality perovskite films grown with a fast solvent-assisted molecule inserting strategy for highly efficient and stable solar cells, *ACS applied materials & interfaces*. 8(34), 22238-22245.

173. Yang, W. S., Park, B.-W., Jung, E. H., Jeon, N. J., Kim, Y. C., Lee, D. U., Shin, S. S., Seo, J., Kim, E. K. & Noh, J. H. (2017) Iodide management in formamidinium-lead-halide-based perovskite layers for efficient solar cells, *Science*. 356(6345), 1376-1379.

174. Liu, D. & Kelly, T. L. (2014) Perovskite solar cells with a planar heterojunction structure prepared using room-temperature solution processing techniques, *Nature photonics*. 8(2), 133-138.

175. Gujar, T. P. & Thelakkat, M. (2016) Highly Reproducible and Efficient Perovskite Solar Cells with Extraordinary Stability from Robust CH<sub>3</sub>NH<sub>3</sub>PbI<sub>3</sub>: Towards Large-Area Devices, *Energy Technology*. 4(3), 449-457.

176. Bi, Z., Liang, Z., Xu, X., Chai, Z., Jin, H., Xu, D., Li, J., Li, M. & Xu, G. (2017) Fast preparation of uniform large grain size perovskite thin film in air condition via spray deposition method for high efficient planar solar cells, *Solar Energy Materials and Solar Cells*. 162, 13-20.

177. Zhou, P., Li, W., Li, T., Bu, T., Liu, X., Li, J., He, J., Chen, R., Li, K. & Zhao, J. (2017) Ultrasonic Spray-coating of large-scale TiO<sub>2</sub> compact layer for efficient flexible perovskite solar cells, *Micromachines*. 8(2), 55.

178. Heo, J. H., Lee, M. H., Jang, M. H. & Im, S. H. (2016) Highly efficient CH<sub>3</sub>NH<sub>3</sub> PbI<sub>1-x</sub>Cl<sub>x</sub> mixed halide perovskite solar cells prepared by re-dissolution and crystal grain growth via spray coating, *Journal of Materials Chemistry A*. 4(45), 17636-17642.

179. Xia, X., Wu, W., Li, H., Zheng, B., Xue, Y., Xu, J., Zhang, D., Gao, C. & Liu, X. (2016) Spray reaction prepared  $\text{FA}_{1-x}\text{Cs}_x\text{PbI}_3$  solid solution as a light harvester for perovskite solar cells with improved humidity stability, *RSC Advances*. 6(18), 14792-14798.
180. Lau, C. F. J., Deng, X., Ma, Q., Zheng, J., Yun, J. S., Green, M. A., Huang, S. & Ho-Baillie, A. W. Y. (2016)  $\text{CsPbIBr}_2$  perovskite solar cell by spray-assisted deposition, *ACS Energy Letters*. 1(3), 573-577.
181. Hong, S. C., Lee, G., Ha, K., Yoon, J., Ahn, N., Cho, W., Park, M. & Choi, M. (2017) Precise morphology control and continuous fabrication of perovskite solar cells using droplet-controllable electrospray coating system, *ACS applied materials & interfaces*. 9(9), 7879-7884.
182. Das, S., Yang, B., Gu, G., Joshi, P. C., Ivanov, I. N., Rouleau, C. M., Aytug, T., Geohegan, D. B. & Xiao, K. (2015) High-performance flexible perovskite solar cells by using a combination of ultrasonic spray-coating and low thermal budget photonic curing, *ACS Photonics*. 2(6), 680-686.
183. Huang, H., Shi, J., Zhu, L., Li, D., Luo, Y. & Meng, Q. (2016) Two-step ultrasonic spray deposition of  $\text{CH}_3\text{NH}_3\text{PbI}_3$  for efficient and large-area perovskite solar cell, *Nano Energy*. 27, 352-358.
184. Tait, J., Manghooli, S., Qiu, W., Rakocevic, L., Kootstra, L., Jaysankar, M., De La Huerta, C. M., Paetzold, U. W., Gehlhaar, R. & Cheyns, D. (2016) Rapid composition screening for perovskite photovoltaics via concurrently pumped ultrasonic spray coating, *Journal of Materials Chemistry A*. 4(10), 3792-3797.
185. Yu, X., Yan, X., Xiao, J., Ku, Z., Zhong, J., Li, W., Huang, F., Peng, Y. & Cheng, Y.-B. (2020) Interface modification effect on the performance of  $\text{Cs}_x\text{FA}_{1-x}\text{PbI}_y\text{Br}_{3-y}$  perovskite solar cells fabricated by evaporation/spray-coating method, *The Journal of Chemical Physics*. 153(1), 014706.
186. Remeika, M., Raga, S. R., Zhang, S. & Qi, Y. (2017) Transferrable optimization of spray-coated  $\text{PbI}_2$  films for perovskite solar cell fabrication, *Journal of Materials Chemistry A*. 5(12), 5709-5718.
187. Burkitt, D., Patidar, R., Greenwood, P., Hooper, K., McGettrick, J., Dimitrov, S., Colombo, M., Stoichkov, V., Richards, D. & Beynon, D. (2020) Roll-to-roll slot-die coated P-I-N perovskite solar cells using acetonitrile based single step perovskite solvent system, *Sustainable Energy & Fuels*. 4(7), 3340-3351.
188. Dou, B., Whitaker, J. B., Bruening, K., Moore, D. T., Wheeler, L. M., Ryter, J., Breslin, N. J., Berry, J. J., Garner, S. M. & Barnes, F. S. (2018) Roll-to-Roll Printing of Perovskite Solar Cells, *ACS Energy Letters*. 3(10), 2558-2565.
189. Di Giacomo, F., Shanmugam, S., Fledderus, H., Bruijnaers, B. J., Verhees, W. J., Dorenkamper, M. S., Veenstra, S. C., Qiu, W., Gehlhaar, R. & Merckx, T. (2018) Up-

scalable sheet-to-sheet production of high efficiency perovskite module and solar cells on 6-in. substrate using slot die coating, *Solar Energy Materials and Solar Cells*. 181, 53-59.

190. Galagan, Y., Di Giacomo, F., Gorter, H., Kirchner, G., de Vries, I., Andriessen, R. & Groen, P. (2018) Roll-to-Roll Slot Die Coated Perovskite for Efficient Flexible Solar Cells, *Advanced Energy Materials*. 8(32), 1801935.

191. Ciro, J., Mejía-Escobar, M. A. & Jaramillo, F. (2017) Slot-die processing of flexible perovskite solar cells in ambient conditions, *Solar Energy*. 150, 570-576.

192. Whitaker, J. B., Kim, D. H., Larson, B. W., Zhang, F., Berry, J. J., van Hest, M. F. & Zhu, K. (2018) Scalable slot-die coating of high performance perovskite solar cells, *Sustainable Energy & Fuels*. 2(11), 2442-2449.

193. Lilien, O. M. (1972) *History of industrial gravure printing up to 1920*.

194. Hu, Q., Wu, H., Sun, J., Yan, D., Gao, Y. & Yang, J. (2016) Large-area perovskite nanowire arrays fabricated by large-scale roll-to-roll micro-gravure printing and doctor blading, *Nanoscale*. 8(9), 5350-5357.

195. Zhang, C., Luo, Q., Wu, H., Li, H., Lai, J., Ji, G., Yan, L., Wang, X., Zhang, D. & Lin, J. (2017) Roll-to-roll micro-gravure printed large-area zinc oxide thin film as the electron transport layer for solution-processed polymer solar cells, *Organic Electronics*. 45, 190-197.

196. Kim, Y. Y., Yang, T. Y., Suhonen, R., Välimäki, M., Maaninen, T., Kemppainen, A., Jeon, N. J. & Seo, J. (2019) Gravure-Printed Flexible Perovskite Solar Cells: Toward Roll-to-Roll Manufacturing, *Advanced Science*. 6(7), 1802094.

197. Sweet, R. G. (1971) Fluid droplet recorder, U.S. Patent No. 3,596,275, issued July 27, 1971.

198. Derby, B. (2010) Inkjet printing of functional and structural materials: fluid property requirements, feature stability, and resolution, *Annual Review of Materials Research*. 40, 395-414.

199. Li, P., Liang, C., Bao, B., Li, Y., Hu, X., Wang, Y., Zhang, Y., Li, F., Shao, G. & Song, Y. (2018) Inkjet manipulated homogeneous large size perovskite grains for efficient and large-area perovskite solar cells, *Nano Energy*. 46, 203-211.

200. Gheno, A., Huang, Y., Bouclé, J., Ratier, B., Rolland, A., Even, J. & Vedraïne, S. (2018) Toward Highly Efficient Inkjet-Printed Perovskite Solar Cells Fully Processed Under Ambient Conditions and at Low Temperature, *Solar RRL*. 2(11), 1800191.

201. Jung, S., Sou, A., Banger, K., Ko, D. H., Chow, P. C., McNeill, C. R. & Siringhaus, H. (2014) All-inkjet-printed, all-air-processed solar cells, *Advanced Energy Materials*. 4(14), 1400432.

202. Li, S.-G., Jiang, K.-J., Su, M.-J., Cui, X.-P., Huang, J.-H., Zhang, Q.-Q., Zhou, X.-Q., Yang, L.-M. & Song, Y.-L. (2015) Inkjet printing of CH<sub>3</sub>NH<sub>3</sub>PbI<sub>3</sub> on a mesoscopic

TiO<sub>2</sub> film for highly efficient perovskite solar cells, *Journal of Materials Chemistry A*. 3(17), 9092-9097.

203. Oh, Y., Kim, J., Yoon, Y. J., Kim, H., Yoon, H. G., Lee, S.-N. & Kim, J. (2011) Inkjet printing of Al<sub>2</sub>O<sub>3</sub> dots, lines, and films: From uniform dots to uniform films, *Current Applied Physics*. 11(3), S359-S363.

204. Gao, A., Yan, J., Wang, Z., Liu, P., Wu, D., Tang, X., Fang, F., Ding, S., Li, X. & Sun, J. (2020) Printable CsPbBr<sub>3</sub> perovskite quantum dot ink for coffee ring-free fluorescent microarrays using inkjet printing, *Nanoscale*. 12(4), 2569-2577.

205. Huckaba, A. J., Lee, Y., Xia, R., Paek, S., Bassetto, V. C., Oveisi, E., Lesch, A., Kinge, S., Dyson, P. J. & Girault, H. (2019) Inkjet-Printed Mesoporous TiO<sub>2</sub> and Perovskite Layers for High Efficiency Perovskite Solar Cells, *Energy Technology*. 7(2), 317-324.

206. Eggers, H., Schackmar, F., Abzieher, T., Sun, Q., Lemmer, U., Vaynzof, Y., Richards, B. S., Hernandez-Sosa, G. & Paetzold, U. W. (2020) Inkjet-Printed Micrometer-Thick Perovskite Solar Cells with Large Columnar Grains, *Advanced Energy Materials*. 10(6), 1903184.

207. Mathies, F., Eggers, H., Richards, B. S., Hernandez-Sosa, G., Lemmer, U. & Paetzold, U. W. (2018) Inkjet-printed triple cation perovskite solar cells, *ACS Applied Energy Materials*. 1(5), 1834-1839.

208. Mahajan, A., Frisbie, C. D. & Francis, L. F. (2013) Optimization of aerosol jet printing for high-resolution, high-aspect ratio silver lines, *ACS applied materials & interfaces*. 5(11), 4856-4864.

209. Tarabella, G., Vurro, D., Lai, S., D'Angelo, P., Ascari, L. & Iannotta, S. (2020) Aerosol jet printing of PEDOT: PSS for large area flexible electronics, *Flexible and Printed Electronics*. 5(1), 014005.

210. Dalal, N., Gu, Y., Chen, G., Hines, D. R., Dasgupta, A. & Das, S. (2020) Effect of Gas Flow Rates on Quality of Aerosol Jet Printed Traces With Nanoparticle Conducting Ink, *Journal of Electronic Packaging*. 142(1).

211. Lee, J. W., Lee, D. K., Jeong, D. N. & Park, N. G. (2019) Control of Crystal Growth toward Scalable Fabrication of Perovskite Solar Cells, *Advanced Functional Materials*. 29(47), 1807047.

212. Hu, H., Ren, Z., Fong, P. W., Qin, M., Liu, D., Lei, D., Lu, X. & Li, G. (2019) Room-Temperature Meniscus Coating of > 20% Perovskite Solar Cells: A Film Formation Mechanism Investigation, *Advanced Functional Materials*. 29(25), 1900092.

213. Yousuf, M. & Frawley, P. J. (2019) Secondary Nucleation from Nuclei Breeding and its Quantitative Link with Fluid Shear Stress in Mixing: A Potential Approach for Precise Scale-up in Industrial Crystallization, *Organic Process Research & Development*. 23(5), 926-934.

214. Lee, K.-M., Lin, C.-J., Liou, B.-Y., Yu, S.-M., Hsu, C.-C., Suryanarayanan, V. & Wu, M.-C. (2017) Selection of anti-solvent and optimization of dropping volume for the preparation of large area sub-module perovskite solar cells, *Solar Energy Materials and Solar Cells*. 172, 368-375.
215. Xiao, M., Zhao, L., Geng, M., Li, Y., Dong, B., Xu, Z., Wan, L., Li, W. & Wang, S. (2018) Selection of an anti-solvent for efficient and stable cesium-containing triple cation planar perovskite solar cells, *Nanoscale*. 10(25), 12141-12148.
216. Stokes, R. J. & Evans, D. F. (1996) *Fundamentals of interfacial engineering*, John Wiley & Sons.
217. Laidler, K. J. (1984) The development of the Arrhenius equation, *Journal of Chemical Education*. 61(6), 494.
218. Uberuaga, B. P., Vernon, L. J., Martinez, E. & Voter, A. F. (2015) The relationship between grain boundary structure, defect mobility, and grain boundary sink efficiency, *Scientific reports*. 5(1), 1-9.
219. Li, C., Guerrero, A., Huettner, S. & Bisquert, J. (2018) Unravelling the role of vacancies in lead halide perovskite through electrical switching of photoluminescence, *Nature communications*. 9(1), 1-8.
220. Stranks, S. D., Nayak, P. K., Zhang, W., Stergiopoulos, T. & Snaith, H. J. (2015) Formation of thin films of organic–inorganic perovskites for high-efficiency solar cells, *Angewandte Chemie International Edition*. 54(11), 3240-3248.
221. Su, J., Cai, H., Ye, X., Zhou, X., Yang, J., Wang, D., Ni, J., Li, J. & Zhang, J. (2019) Efficient Perovskite Solar Cells Prepared by Hot Air Blowing to Ultrasonic Spraying in Ambient Air, *ACS applied materials & interfaces*. 11(11), 10689-10696.
222. Mali, S. S., Patil, J. V. & Hong, C. K. (2019) Hot-Air-Assisted Fully Air-Processed Barium Incorporated CsPbI<sub>2</sub>Br Perovskite Thin Films for Highly Efficient and Stable All-Inorganic Perovskite Solar Cells, *Nano Letters*. 19(9), 6213-6220.
223. Liu, Y., Shin, I., Hwang, I.-W., Lee, J., Kim, S., Lee, D. Y., Lee, S.-H., Jang, J.-W., Jung, Y. K. & Jeong, J. H. (2017) Effective hot-air annealing for improving the performance of perovskite solar cells, *Solar Energy*. 146, 359-367.
224. Mehdi, H., Mhamdi, A. & Bouazizi, A. (2020) Effect of annealing treatment on the properties of inverted solar cells based on mixed halide perovskite, *Physica E: Low-dimensional Systems and Nanostructures*. 119, 114000.
225. Shargaieva, O., Lang, F., Rappich, J. r., Dittrich, T., Klaus, M., Meixner, M., Genzel, C. & Nickel, N. H. (2017) Influence of the grain size on the properties of CH<sub>3</sub>NH<sub>3</sub>PbI<sub>3</sub> thin films, *ACS applied materials & interfaces*. 9(44), 38428-38435.
226. Jaysankar, M., Qiu, W., Bastos, J., Tait, J., Debucquoy, M., Paetzold, U. W., Cheyns, D. & Poortmans, J. (2016) Crystallisation dynamics in wide-bandgap perovskite films, *Journal of Materials Chemistry A*. 4(27), 10524-10531.

227. Ren, X., Yang, Y., Yang, D., Zhang, X., Cui, D., Liu, Y., Wei, Q., Fan, H. & Liu, S. (2016) Reaction temperature modulating crystal grain size and optoelectronic properties of perovskite film for solar cell application, *Nanoscale*. 8(6), 3816-3822.
228. Dualeh, A., Tétreault, N., Moehl, T., Gao, P., Nazeeruddin, M. K. & Grätzel, M. (2014) Effect of annealing temperature on film morphology of organic–inorganic hybrid perovskite solid-state solar cells, *Advanced Functional Materials*. 24(21), 3250-3258.
229. Wang, C., Zhang, J., Duan, J., Gong, L., Wu, J., Jiang, L., Zhou, C., Xie, H., Gao, Y. & He, H. (2020) All-inorganic, hole-transporting-layer-free, carbon-based CsPbIBr<sub>2</sub> planar perovskite solar cells by a two-step temperature-control annealing process, *Materials Science in Semiconductor Processing*. 108, 104870.
230. Kim, M., Kim, G.-H., Oh, K. S., Jo, Y., Yoon, H., Kim, K.-H., Lee, H., Kim, J. Y. & Kim, D. S. (2017) High-temperature–short-time annealing process for high-performance large-area perovskite solar cells, *ACS nano*. 11(6), 6057-6064.
231. You, P., Li, G., Tang, G., Cao, J. & Yan, F. (2020) Ultrafast laser-annealing of perovskite films for efficient perovskite solar cells, *Energy & Environmental Science*. 13(4), 1187-1196.
232. Park, J. H., Seo, J., Park, S., Shin, S. S., Kim, Y. C., Jeon, N. J., Shin, H. W., Ahn, T. K., Noh, J. H. & Yoon, S. C. (2015) Efficient CH<sub>3</sub>NH<sub>3</sub>PbI<sub>3</sub> perovskite solar cells employing nanostructured p-type NiO electrode formed by a pulsed laser deposition, *Advanced Materials*. 27(27), 4013-4019.
233. Jeon, T., Jin, H. M., Lee, S. H., Lee, J. M., Park, H. I., Kim, M. K., Lee, K. J., Shin, B. & Kim, S. O. (2016) Laser crystallization of organic–inorganic hybrid perovskite solar cells, *ACS nano*. 10(8), 7907-7914.
234. Li, F., Zhu, W., Bao, C., Yu, T., Wang, Y., Zhou, X. & Zou, Z. (2016) Laser-assisted crystallization of CH<sub>3</sub>NH<sub>3</sub>PbI<sub>3</sub> films for efficient perovskite solar cells with a high open-circuit voltage, *Chemical Communications*. 52(31), 5394-5397.
235. Kim, H.-S., Dhage, S. R., Shim, D.-E. & Hahn, H. T. (2009) Intense pulsed light sintering of copper nanoink for printed electronics, *Applied Physics A*. 97(4), 791-798.
236. Lim, H. S., Kim, S. J., Jang, H. W. & Lim, J. A. (2017) Intense pulsed light for split-second structural development of nanomaterials, *Journal of Materials Chemistry C*. 5(29), 7142-7160.
237. Ohkura, Y., Weisse, J. M., Cai, L. & Zheng, X. (2013) Flash ignition of freestanding porous silicon films: effects of film thickness and porosity, *Nano Letters*. 13(11), 5528-5533.
238. Singh, M., Rana, S. & Agarwal, S. (2020) Light induced morphological reforms in thin film of advanced nano-materials for energy generation: A review, *Optics & Laser Technology*. 129, 106284.

239. Ghahremani, A. H., Martin, B., Ankireddy, K. & Druffel, T. (2019) Rapid processing of perovskite solar cells through pulsed photonic annealing: a review, *Journal of Coatings Technology and Research*. 16(6), 1637-1642.
240. Dharmadasa, R., Lavery, B., Dharmadasa, I. & Druffel, T. (2014) Intense pulsed light treatment of cadmium telluride nanoparticle-based thin films, *ACS applied materials & interfaces*. 6(7), 5034-5040.
241. Dhage, S. R., Kim, H.-S. & Hahn, H. T. (2011) Cu (In, Ga) Se<sub>2</sub> thin film preparation from a Cu (In, Ga) metallic alloy and Se nanoparticles by an intense pulsed light technique, *Journal of electronic materials*. 40(2), 122-126.
242. Lavery, B. W., Kumari, S., Konermann, H., Draper, G. L., Spurgeon, J. & Druffel, T. (2016) Intense pulsed light sintering of CH<sub>3</sub>NH<sub>3</sub>PbI<sub>3</sub> solar cells, *ACS applied materials & interfaces*. 8(13), 8419-8426.
243. Troughton, J., Carnie, M. J., Davies, M. L., Charbonneau, C. c., Jewell, E. H., Worsley, D. A. & Watson, T. M. (2016) Photonic flash-annealing of lead halide perovskite solar cells in 1 ms, *Journal of Materials Chemistry A*. 4(9), 3471-3476.
244. Singh, M. & Suganuma, K. (2019) Light energy induced sintering of Cu<sub>2</sub>ZnSnS<sub>4</sub> nanocrystal-based film for solar cell, *Nano-Structures & Nano-Objects*. 19, 100369.
245. Feleki, B., Bex, G., Andriessen, R., Galagan, Y. & Di Giacomo, F. (2017) Rapid and low temperature processing of mesoporous TiO<sub>2</sub> for perovskite solar cells on flexible and rigid substrates, *Materials Today Communications*. 13, 232-240.
246. Das, S., Gu, G., Joshi, P. C., Yang, B., Aytug, T., Rouleau, C. M., Geohegan, D. B. & Xiao, K. (2016) Low thermal budget, photonic-cured compact TiO<sub>2</sub> layers for high-efficiency perovskite solar cells, *Journal of Materials Chemistry A*. 4(24), 9685-9690.
247. Zhu, M., Liu, W., Ke, W., Clark, S., Secor, E. B., Song, T.-B., Kanatzidis, M. G., Li, X. & Hersam, M. C. (2017) Millisecond-pulsed photonic-annealed tin oxide electron transport layers for efficient perovskite solar cells, *Journal of Materials Chemistry A*. 5(46), 24110-24115.
248. Chung, W.-H., Hwang, H.-J., Lee, S.-H. & Kim, H.-S. (2012) In situ monitoring of a flash light sintering process using silver nano-ink for producing flexible electronics, *Nanotechnology*. 24(3), 035202.
249. Gokhale, P., Mitra, D., Sowade, E., Mitra, K. Y., Gomes, H. L., Ramon, E., Al-Hamry, A., Kanoun, O. & Baumann, R. R. (2017) Controlling the crack formation in inkjet-printed silver nanoparticle thin-films for high resolution patterning using intense pulsed light treatment, *Nanotechnology*. 28(49), 495301.
250. Kang, J., Ryu, J., Kim, H.-S. & Hahn, H. (2011) Sintering of inkjet-printed silver nanoparticles at room temperature using intense pulsed light, *Journal of electronic materials*. 40(11), 2268.

251. Weise, D., Mitra, K. Y., Ueberfuhr, P. & Baumann, R. R. (2015). Effect of the light spectrum of various substrates for inkjet printed conductive structures sintered with intense pulsed light, *AIP Conference Proceedings* (Vol. 1646, No. 1, pp. 101-105). American Institute of Physics.
252. Nam, H. J., Kang, S. Y., Park, J. Y. & Choa, S.-H. (2019) Intense pulse light sintering of an Ag microparticle-based, highly stretchable, and conductive electrode, *Microelectronic Engineering*. 215, 111012.
253. Secor, E. B., Ahn, B. Y., Gao, T. Z., Lewis, J. A. & Hersam, M. C. (2015) Rapid and versatile photonic annealing of graphene inks for flexible printed electronics, *Advanced Materials*. 27(42), 6683-6688.
254. Ankireddy, K., Ghahremani, A. H., Martin, B., Gupta, G. & Druffel, T. (2018) Rapid thermal annealing of  $\text{CH}_3\text{NH}_3\text{PbI}_3$  perovskite thin films by intense pulsed light with aid of diiodomethane additive, *Journal of Materials Chemistry A*. 6(20), 9378-9383.
255. Baikie, T., Fang, Y., Kadro, J. M., Schreyer, M., Wei, F., Mhaisalkar, S. G., Graetzel, M. & White, T. J. (2013) Synthesis and crystal chemistry of the hybrid perovskite  $(\text{CH}_3\text{NH}_3)\text{PbI}_3$  for solid-state sensitised solar cell applications, *Journal of Materials Chemistry A*. 1(18), 5628-5641.
256. Heiderhoff, R., Haeger, T., Pourdavoud, N., Hu, T., Al-Khafaji, M., Mayer, A., Chen, Y., Scheer, H.-C. & Riedl, T. (2017) Thermal conductivity of methylammonium lead halide perovskite single crystals and thin films: A comparative study, *The Journal of Physical Chemistry C*. 121(51), 28306-28311.
257. Tyson, T., Gao, W., Chen, Y.-S., Ghose, S. & Yan, Y. (2017) Large thermal motion in halide perovskites, *Scientific Reports*. 7(1), 1-10.
258. Kumari, M. A., Swetha, T. & Singh, S. P. (2018) Fullerene derivatives: A review on perovskite solar cells, *Materials Express*. 8(5), 389-406.
259. Jia, L., Chen, M. & Yang, S. (2020) Functionalization of fullerene materials toward applications in perovskite solar cells, *Materials Chemistry Frontiers*. 4(8), 2256-2282.
260. Deng, L. L., Xie, S. Y. & Gao, F. (2018) Fullerene-Based Materials for Photovoltaic Applications: Toward Efficient, Hysteresis-Free, and Stable Perovskite Solar Cells, *Advanced Electronic Materials*. 4(10), 1700435.
261. Heo, J. H., Lee, S.-C., Jung, S.-K., Kwon, O.-P. & Im, S. H. (2017) Efficient and thermally stable inverted perovskite solar cells by introduction of non-fullerene electron transporting materials, *Journal of Materials Chemistry A*. 5(39), 20615-20622.
262. Nielsen, C. B., Holliday, S., Chen, H.-Y., Cryer, S. J. & McCulloch, I. (2015) Non-fullerene electron acceptors for use in organic solar cells, *Accounts of chemical research*. 48(11), 2803-2812.
263. Liu, Y., Mu, C., Jiang, K., Zhao, J., Li, Y., Zhang, L., Li, Z., Lai, J. Y. L., Hu, H. & Ma, T. (2015) A Tetraphenylethylene Core-Based 3D Structure Small Molecular Acceptor



Enabling Efficient Non-Fullerene Organic Solar Cells, *Advanced Materials*. 27(6), 1015-1020.

264. Liu, S. Y., Wu, C. H., Li, C. Z., Liu, S. Q., Wei, K. H., Chen, H. Z. & Jen, A. K. Y. (2015) A tetraperylene diimides based 3D nonfullerene acceptor for efficient organic photovoltaics, *Advanced Science*. 2(4), 1500014.

265. Wang, Z., Gu, P., Liu, G., Yao, H., Wu, Y., Li, Y., Rakesh, G., Zhu, J., Fu, H. & Zhang, Q. (2017) A large pyrene-fused N-heteroacene: fifteen aromatic six-membered rings annulated in one row, *Chemical Communications*. 53(55), 7772-7775.

266. Gu, P.-Y., Wang, Z. & Zhang, Q. (2016) Azaacenes as active elements for sensing and bio applications, *Journal of Materials Chemistry B*. 4(44), 7060-7074.

267. Wang, S., Wang, A., Deng, X., Xie, L., Xiao, A., Li, C., Xiang, Y., Li, T. S., Ding, L. & Hao, F. (2020) Lewis Acid/Base Approach for Efficacious Defect Passivation in Perovskite Solar Cells, *Journal of Materials Chemistry A*. 8(25), 12201-12225.

268. Xu, J., Buin, A., Ip, A. H., Li, W., Voznyy, O., Comin, R., Yuan, M., Jeon, S., Ning, Z. & McDowell, J. J. (2015) Perovskite–fullerene hybrid materials suppress hysteresis in planar diodes, *Nature communications*. 6(1), 1-8.

269. Jeng, J. Y., Chiang, Y. F., Lee, M. H., Peng, S. R., Guo, T. F., Chen, P. & Wen, T. C. (2013) CH<sub>3</sub>NH<sub>3</sub>PbI<sub>3</sub> perovskite/fullerene planar-heterojunction hybrid solar cells, *Advanced Materials*. 25(27), 3727-3732.

270. Li, D., Kong, W., Zhang, H., Wang, D., Li, W., Liu, C., Chen, H., Song, W., Gao, F. & Amini, A. (2020) Bifunctional Ultrathin PCBM Enables Passivated Trap States and Cascaded Energy Level toward Efficient Inverted Perovskite Solar Cells, *ACS Applied Materials & Interfaces*. 12(17), 20103-20109.

271. Tsarev, S. & Troshin, P. A. (2020) Surface modification of ZnO electron transport layer with thermally evaporated WO<sub>3</sub> for stable perovskite solar cells, *Synthetic Metals*. 269, 116547.

272. Zhang, X., Li, J., Bi, Z., He, K., Xu, X., Xiao, X., Zhu, Y., Zhan, Y., Zhong, L. & Xu, G. (2020) Stable and efficient air-processed perovskite solar cells employing low-temperature processed compact In<sub>2</sub>O<sub>3</sub> thin films as electron transport materials, *Journal of Alloys and Compounds*, 836, 155460.

273. Dong, J., Jia, J., Cao, B., Lin, J., Fan, L., Lan, Z. & Wu, J. (2019) Enhanced performance of TiO<sub>2</sub>-based planar perovskite solar cells by In<sub>2</sub>O<sub>3</sub> interfacial modification layer, *Organic Electronics*. 75, 105426.

274. Zhao, F., Guo, Y., Wang, X., Tao, J., Jiang, J., Hu, Z. & Chu, J. (2019) Enhanced performance of carbon-based planar CsPbBr<sub>3</sub> perovskite solar cells with room-temperature sputtered Nb<sub>2</sub>O<sub>5</sub> electron transport layer, *Solar Energy*. 191, 263-271.

275. Ye, X., Ling, H., Zhang, R., Wen, Z., Hu, S., Akasaka, T., Xia, J. & Lu, X. (2020) Low-temperature solution-combustion-processed Zn-Doped Nb<sub>2</sub>O<sub>5</sub> as an electron

transport layer for efficient and stable perovskite solar cells, *Journal of Power Sources*. 448, 227419.

276. Zhu, L., Ye, J., Zhang, X., Zheng, H., Liu, G., Pan, X. & Dai, S. (2017) Performance enhancement of perovskite solar cells using a La-doped BaSnO<sub>3</sub> electron transport layer, *Journal of Materials Chemistry A*. 5(7), 3675-3682.

277. Sun, C., Guan, L., Guo, Y., Fang, B., Yang, J., Duan, H., Chen, Y., Li, H. & Liu, H. (2017) Ternary oxide BaSnO<sub>3</sub> nanoparticles as an efficient electron-transporting layer for planar perovskite solar cells, *Journal of Alloys and Compounds*. 722, 196-206.

278. Lian, J., Lu, B., Niu, F., Zeng, P. & Zhan, X. (2018) Electron-Transport Materials in Perovskite Solar Cells, *Small Methods*. 2(10), 1800082.

279. Roose, B., Johansen, C. M., Dupraz, K., Jaouen, T., Aebi, P., Steiner, U. & Abate, A. (2018) A Ga-doped SnO<sub>2</sub> mesoporous contact for UV stable highly efficient perovskite solar cells, *Journal of Materials Chemistry A*. 6(4), 1850-1857.

280. Zheng, D., Wang, G., Huang, W., Wang, B., Ke, W., Logsdon, J. L., Wang, H., Wang, Z., Zhu, W. & Yu, J. (2019) Combustion Synthesized Zinc Oxide Electron-Transport Layers for Efficient and Stable Perovskite Solar Cells, *Advanced Functional Materials*. 29(16), 1900265.

281. Yang, J., Siempelkamp, B. D., Mosconi, E., De Angelis, F. & Kelly, T. L. (2015) Origin of the thermal instability in CH<sub>3</sub>NH<sub>3</sub>PbI<sub>3</sub> thin films deposited on ZnO, *Chemistry of Materials*. 27(12), 4229-4236.

282. Han, J., Kwon, H., Kim, E., Kim, D.-W., Son, H. J. & Kim, D. H. (2020) Interfacial engineering of a ZnO electron transporting layer using self-assembled monolayers for high performance and stable perovskite solar cells, *Journal of Materials Chemistry A*. 8(4), 2105-2113.

283. Viana, E., González, J., Ribeiro, G. & De Oliveira, A. (2013) Photoluminescence and high-temperature persistent photoconductivity experiments in SnO<sub>2</sub> nanobelts, *The Journal of Physical Chemistry C*. 117(15), 7844-7849.

284. Shi, L. & Lin, H. (2011) Preparation of band gap tunable SnO<sub>2</sub> nanotubes and their ethanol sensing properties, *Langmuir*. 27, 3977-3981.

285. Xiong, L., Qin, M., Chen, C., Wen, J., Yang, G., Guo, Y., Ma, J., Zhang, Q., Qin, P. & Li, S. (2018) Fully high-temperature-processed SnO<sub>2</sub> as blocking layer and scaffold for efficient, stable, and hysteresis-free mesoporous perovskite solar cells, *Advanced Functional Materials*. 28(10), 1706276.

286. Khan, A. F., Mehmood, M., Aslam, M. & Ashraf, M. (2010) Characteristics of electron beam evaporated nanocrystalline SnO<sub>2</sub> thin films annealed in air, *Applied Surface Science*. 256(7), 2252-2258.

287. Jun, Y., Ko, Y., Kim, Y., Lee, C., Kim, T., Kim, S., Yun, Y. J., Gwon, H.-j. & Lee, N.-H. (2020) Self-aggregation Controlled Rapid Chemical Bath Deposition of SnO<sub>2</sub> Layers

and Stable Dark Depolarization Process for Highly Efficient Planar Perovskite Solar Cells, *ChemSusChem*. 13(16), 4051-4063.

288. Ko, Y., Kim, Y. R., Jang, H., Lee, C., Kang, M. G. & Jun, Y. (2017) Electrodeposition of SnO<sub>2</sub> on FTO and its application in planar heterojunction perovskite solar cells as an electron transport layer, *Nanoscale research letters*. 12(1), 1-7.

289. Bai, G., Wu, Z., Li, J., Bu, T., Li, W., Li, W., Huang, F., Zhang, Q., Cheng, Y.-B. & Zhong, J. (2019) High performance perovskite sub-module with sputtered SnO<sub>2</sub> electron transport layer, *Solar Energy*. 183, 306-314.

290. Song, J., Li, G., Wang, D., Sun, W., Wu, J. & Lan, Z. (2020) High-Efficiency Low-Temperature-Processed Mesoscopic Perovskite Solar Cells from SnO<sub>2</sub> Nanorod Self-Assembled Microspheres, *Solar RRL*. 4(4), 1900558.

291. Jiang, Q., Zhang, L., Wang, H., Yang, X., Meng, J., Liu, H., Yin, Z., Wu, J., Zhang, X. & You, J. (2017) Enhanced electron extraction using SnO<sub>2</sub> for high-efficiency planar-structure HC(NH<sub>2</sub>)<sub>2</sub>PbI<sub>3</sub>-based perovskite solar cells, *Nature Energy*. 2(1), 16177.

292. Pearson, R. G. (1988) Absolute electronegativity and hardness: application to inorganic chemistry, *Inorganic Chemistry*. 27(4), 734-740.

293. Tsai, C.-H., Lin, C.-M. & Kuei, C.-H. (2018) Improving the performance of perovskite solar cells by adding 1, 8-diiodooctane in the CH<sub>3</sub>NH<sub>3</sub>PbI<sub>3</sub> perovskite layer, *Solar Energy*. 176, 178-185.

294. Xu, W., McLeod, J. A., Yang, Y., Wang, Y., Wu, Z., Bai, S., Yuan, Z., Song, T., Wang, Y. & Si, J. (2016) Iodomethane-mediated organometal halide perovskite with record photoluminescence lifetime, *ACS Applied Materials & Interfaces*. 8(35), 23181-23189.

295. Li, Z., Zhao, Y., Wang, X., Sun, Y., Zhao, Z., Li, Y., Zhou, H. & Chen, Q. (2018) Cost analysis of perovskite tandem photovoltaics, *Joule*. 2(8), 1559-1572.

296. Bruening, K., Dou, B., Simonaitis, J., Lin, Y.-Y., van Hest, M. F. & Tassone, C. J. (2018) Scalable Fabrication of Perovskite Solar Cells to Meet Climate Targets, *Joule*. 2(11), 2464-2476.

297. Ghahremani, A. H., Martin, B., Gupta, A., Bahadur, J., Ankireddy, K. & Druffel, T. (2020) Rapid fabrication of perovskite solar cells through intense pulse light annealing of SnO<sub>2</sub> and triple cation perovskite thin films, *Materials & Design*. 185, 108237.

298. Bu, T., Li, J., Zheng, F., Chen, W., Wen, X., Ku, Z., Peng, Y., Zhong, J., Cheng, Y.-B. & Huang, F. (2018) Universal passivation strategy to slot-die printed SnO<sub>2</sub> for hysteresis-free efficient flexible perovskite solar module, *Nature communications*. 9(1), 1-10.

299. Kwoka, M., Ottaviano, L., Passacantando, M., Santucci, S., Czempik, G. & Szuber, J. (2005) XPS study of the surface chemistry of L-CVD SnO<sub>2</sub> thin films after oxidation, *Thin Solid Films*. 490(1), 36-42.

300. Noh, M. F. M., Arzaee, N. A., Safaei, J., Mohamed, N. A., Kim, H. P., Jang, J. & Teridi, M. A. M. (2019) Eliminating oxygen vacancies in SnO<sub>2</sub> films via aerosol-assisted chemical vapour deposition for perovskite solar cells and photoelectrochemical cells, *Journal of Alloys and Compounds*. 773, 997-1008.
301. Wen, L., Sahu, B. B. & Han, J. G. (2018) Development and utility of a new 3-D magnetron source for high rate deposition of highly conductive ITO thin films near room temperature, *Physical Chemistry Chemical Physics*. 20(7), 4818-4830.
302. Zhang, W., Saliba, M., Moore, D. T., Pathak, S. K., Hörantner, M. T., Stergiopoulos, T., Stranks, S. D., Eperon, G. E., Alexander-Webber, J. A. & Abate, A. (2015) Ultrasoft organic-inorganic perovskite thin-film formation and crystallization for efficient planar heterojunction solar cells, *Nature Communications*. 6(1), 6142.
303. Shi, J., Zhang, H., Li, Y., Jasieniak, J. J., Li, Y., Wu, H., Luo, Y., Li, D. & Meng, Q. (2018) Identification of high-temperature exciton states and their phase-dependent trapping behaviour in lead halide perovskites, *Energy & Environmental Science*. 11(6), 1460-1469.
304. Priante, D., Dursun, I., Alias, M., Shi, D., Melnikov, V., Ng, T. K., Mohammed, O. F., Bakr, O. & Ooi, B. S. (2015) The recombination mechanisms leading to amplified spontaneous emission at the true-green wavelength in CH<sub>3</sub>NH<sub>3</sub>PbBr<sub>3</sub> perovskites, *Applied Physics Letters*. 106(8), 081902.
305. Zarazua, I., Han, G., Boix, P. P., Mhaisalkar, S., Fabregat-Santiago, F., Mora-Seró, I., Bisquert, J. & Garcia-Belmonte, G. (2016) Surface recombination and collection efficiency in perovskite solar cells from impedance analysis, *The journal of physical chemistry letters*. 7(24), 5105-5113.
306. Fan, B., Peng, D., Lin, S., Wang, N., Zhao, Y. & Sun, Y. (2015) Enhanced efficiency of planar-heterojunction perovskite solar cells through a thermal gradient annealing process, *RSC Advances*. 5(71), 58041-58045.
307. Hao, L., Li, Z., Wang, L., Liu, R., Shao, Z., Zhou, Z., Guo, X., Cui, G., Liu, S. F. & Pang, S. (2020) A temperature gradient-induced directional growth of a perovskite film, *Journal of Materials Chemistry A*. 8(33), 17019-17024.
308. Xi, J., Yuan, J., Yan, X., Binks, D. & Tian, J. (2020) Gradient annealing of halide perovskite films for improved performance of solar cells, *ACS Applied Energy Materials*. 3(9), 8130-8134.
309. Xiao, Y. Y., Meng, Y., Gao, H., Chen, Y., Meng, Q., Bai, Y., Wang, H., Zhang, Y., Yan, H. & Han, C. B. (2020) Flexible perovskite solar cells fabricated by a gradient heat treatment process, *Sustainable Energy & Fuels*. 4(2), 824-831.
310. Chen, W., Chen, H., Xu, G., Xue, R., Wang, S., Li, Y. & Li, Y. (2019) Precise control of crystal growth for highly efficient CsPbI<sub>2</sub>Br perovskite solar cells, *Joule*. 3(1), 191-204.

311. Salado, M., Kokal, R. K., Calio, L., Kazim, S., Deepa, M. & Ahmad, S. (2017) Identifying the charge generation dynamics in Cs<sup>+</sup>-based triple cation mixed perovskite solar cells, *Physical Chemistry Chemical Physics*. 19(34), 22905-22914.
312. Akin, S. The effect of absorber layer thickness on the performance of perovskite solar cells, *ENTECH*. 19, 81.
313. Dualeh, A., Gao, P., Seok, S. I., Nazeeruddin, M. K. & Grätzel, M. (2014) Thermal behavior of methylammonium lead-trihalide perovskite photovoltaic light harvesters, *Chemistry of Materials*. 26(21), 6160-6164.
314. Lee, Y. H., Luo, J., Humphry-Baker, R., Gao, P., Grätzel, M. & Nazeeruddin, M. K. (2015) Unraveling the reasons for efficiency loss in perovskite solar cells, *Advanced Functional Materials*. 25(25), 3925-3933.
315. Kim, J., Lee, S.-H., Lee, J. H. & Hong, K.-H. (2014) The role of intrinsic defects in methylammonium lead iodide perovskite, *The journal of physical chemistry letters*. 5(8), 1312-1317.
316. Liu, Y., Yang, Z., Cui, D., Ren, X., Sun, J., Liu, X., Zhang, J., Wei, Q., Fan, H. & Yu, F. (2015) Two-inch-sized perovskite CH<sub>3</sub>NH<sub>3</sub>PbX<sub>3</sub> (X= Cl, Br, I) crystals: growth and characterization, *Advanced Materials*. 27(35), 5176-5183.
317. Wang, Y. C., Chang, J., Zhu, L., Li, X., Song, C. & Fang, J. (2018) Electron-Transport-Layer-Assisted Crystallization of Perovskite Films for High-Efficiency Planar Heterojunction Solar Cells, *Advanced Functional Materials*. 28(9), 1706317.
318. Cao, X., Zhi, L., Li, Y., Fang, F., Cui, X., Ci, L., Ding, K. & Wei, J. (2018) Fabrication of perovskite films with large columnar grains via solvent-mediated ostwald ripening for efficient inverted perovskite solar cells, *ACS Applied Energy Materials*. 1(2), 868-875.
319. Pham, N. D., Tiong, V. T., Yao, D., Martens, W., Guerrero, A., Bisquert, J. & Wang, H. (2017) Guanidinium thiocyanate selective Ostwald ripening induced large grain for high performance perovskite solar cells, *Nano Energy*. 41, 476-487.
320. Yang, M., Zhang, T., Schulz, P., Li, Z., Li, G., Kim, D. H., Guo, N., Berry, J. J., Zhu, K. & Zhao, Y. (2016) Facile fabrication of large-grain CH<sub>3</sub>NH<sub>3</sub>PbI<sub>3-x</sub>Br<sub>x</sub> films for high-efficiency solar cells via CH<sub>3</sub>NH<sub>3</sub>Br-selective Ostwald ripening, *Nature Communications*. 7(1), 12305.
321. Yang, Y., Wu, J., Wang, X., Guo, Q., Liu, X., Sun, W., Wei, Y., Huang, Y., Lan, Z. & Huang, M. (2019) Suppressing Vacancy Defects and Grain Boundaries via Ostwald Ripening for High-Performance and Stable Perovskite Solar Cells, *Advanced Materials*. 32(7), 1904347.
322. Li, S., Hu, L., Zhang, C., Wu, Y., Liu, Y., Sun, Q., Cui, Y., Hao, Y. & Wu, Y. (2020) In-situ growth of 2D/3D mixture perovskite interface layer by seed-mediated and solvent-assisted Ostwald ripening for stable and efficient photovoltaics, *Journal of Materials Chemistry C*. 8(7), 2425-2435.

323. Ramsdell, L. S. (1947) Studies on silicon carbide, *American Mineralogist: Journal of Earth and Planetary Materials*. 32(1-2), 64-82.
324. Gratia, P., Zimmermann, I., Schouwink, P., Yum, J.-H., Audinot, J.-N., Sivula, K., Wirtz, T. & Nazeeruddin, M. K. (2017) The many faces of mixed ion perovskites: unraveling and understanding the crystallization process, *ACS Energy Letters*. 2(12), 2686-2693.
325. Eze, V. O., Lei, B. & Mori, T. (2016) Air-assisted flow and two-step spin-coating for highly efficient  $\text{CH}_3\text{NH}_3\text{PbI}_3$  perovskite solar cells, *Japanese Journal of Applied Physics*. 55(2S), 02BF08.
326. Wang, J., Zhang, J., Zhou, Y., Liu, H., Xue, Q., Li, X., Chueh, C.-C., Yip, H.-L., Zhu, Z. & Jen, A. K. (2020) Highly efficient all-inorganic perovskite solar cells with suppressed non-radiative recombination by a Lewis base, *Nature communications*. 11(1), 1-9.
327. Tan, H., Che, F., Wei, M., Zhao, Y., Saidaminov, M. I., Todorović, P., Broberg, D., Walters, G., Tan, F. & Zhuang, T. (2018) Dipolar cations confer defect tolerance in wide-bandgap metal halide perovskites, *Nature Communications*. 9(1), 1-10.
328. Kour, P., Chenna Reddy, M., Naphade, R. & Ogale, S. (2018) Quaternary alkylammonium salt incorporated 2D/3D mixed halide perovskite with highly enhanced photoluminescence and arrested iodide/bromide phase segregation, *APL Materials*. 6(8), 086107.
329. Xiao, Y. Y., Meng, Y., Gao, H., Chen, Y., Meng, Q., Bai, Y., Wang, H., Zhang, Y., Yan, H. & Han, C. B. (2020) Flexible perovskite solar cells fabricated by a gradient heat treatment process, *Sustainable Energy Fuels*. 4(2), 824-831.
330. Huang, L., Hu, Z., Xu, J., Zhang, K., Zhang, J. & Zhu, Y. (2015) Multi-step slow annealing perovskite films for high performance planar perovskite solar cells, *Solar Energy Materials and Solar Cells*. 141, 377-382.
331. Dharmadasa, R., Dharmadasa, I. & Druffel, T. (2014) Intense pulsed light sintering of electrodeposited CdS thin films, *Advanced Engineering Materials*. 16(11), 1351-1361.
332. Ku, Z., Rong, Y., Xu, M., Liu, T. & Han, H. (2013) Full printable processed mesoscopic  $\text{CH}_3\text{NH}_3\text{PbI}_3/\text{TiO}_2$  heterojunction solar cells with carbon counter electrode, *Scientific reports*. 3(1), 3132.
333. Zhang, L., Liu, T., Liu, L., Hu, M., Yang, Y., Mei, A. & Han, H. (2015) The effect of carbon counter electrodes on fully printable mesoscopic perovskite solar cells, *Journal of Materials Chemistry A*. 3(17), 9165-9170.
334. Raminafshar, C., Dracopoulos, V., Mohammadi, M. R. & Lianos, P. (2018) Carbon based perovskite solar cells constructed by screen-printed components, *Electrochimica Acta*. 276, 261-267.
335. Mishra, A., Ahmad, Z., Zimmermann, I., Martineau, D., Shakoor, R., Touati, F., Riaz, K., Al-Muhtaseb, S. A. & Nazeeruddin, M. K. (2019) Effect of annealing temperature on

the performance of printable carbon electrodes for perovskite solar cells, *Organic Electronics*. 65, 375-380.

336. Zhou, H., Shi, Y., Dong, Q., Zhang, H., Xing, Y., Wang, K., Du, Y. & Ma, T. (2014) Hole-conductor-free, metal-electrode-free  $\text{TiO}_2/\text{CH}_3\text{NH}_3\text{PbI}_3$  heterojunction solar cells based on a low-temperature carbon electrode, *The journal of physical chemistry letters*. 5(18), 3241-3246.

337. Wei, Z., Chen, H., Yan, K. & Yang, S. (2014) Inkjet printing and instant chemical transformation of a  $\text{CH}_3\text{NH}_3\text{PbI}_3$ /nanocarbon electrode and interface for planar perovskite solar cells, *Angewandte Chemie International Edition*. 53(48), 13239-13243.

338. McGrady, G. & Walsh, K. (2020). Dual Extrusion FDM Printer for Flexible and Rigid Polymers, *International Manufacturing Science and Engineering Conference* (Vol. 84256, p. V001T01A009). American Society of Mechanical Engineers.

339. McGrady, G. & Walsh, K. (2018) Embedding Sensing Capabilities in FDM-Printed Objects.

340. Tofangchi, A., Han, P., Izquierdo, J., Iyengar, A. & Hsu, K. (2019) Effect of ultrasonic vibration on interlayer adhesion in fused filament fabrication 3D printed ABS, *Polymers*. 11(2), 315.

341. Deshpande, A. & Hsu, K. (2018) Acoustoplastic metal direct-write: Towards solid aluminum 3D printing in ambient conditions, *Additive Manufacturing*. 19, 73-80.

342. Ghahremani, A. H., Pishgar, S., Bahadur, J. & Druffel, T. (2020) Intense Pulse Light Annealing of Perovskite Photovoltaics Using Gradient Flashes, *ACS Applied Energy Materials*. 3(12), 11641-11654.

343. Druffel, T., Dharmadasa, R., Lavery, B. W. & Ankireddy, K. (2018) Intense pulsed light processing for photovoltaic manufacturing, *Solar Energy Materials and Solar Cells*. 174, 359-369.

344. Bhattarai, S. & Das, T. (2021) Optimization of the perovskite solar cell design to achieve a highly improved efficiency, *Optical Materials*. 111, 110661.

345. Ahangharnejhad, R. H., Friedl, J. D., Phillips, A. B. & Heben, M. J. (2021) Understanding VOC and performance deficit in wide bandgap perovskite photovoltaic devices, *Solar Energy Materials and Solar Cells*. 225, 111015.

346. Meng, Q., Chen, Y., Xiao, Y. Y., Sun, J., Zhang, X., Han, C. B., Gao, H., Zhang, Y. & Yan, H. (2020) Effect of temperature on the performance of perovskite solar cells, *Journal of Materials Science: Materials in Electronics*, 1-9.

347. Li, G., Zou, X., Cheng, J., Bai, X., Chen, D., Yao, Y., Chang, C., Yu, X., Zhou, Z. & Wang, J. (2020) Effect of  $\text{PbI}_2$  passivation to grain boundary of perovskite film with cation and anion co-mixing on performance of photovoltaic devices, *Materials Letters*. 273, 127979.

348. Ain, Q. T., Haq, S. H., Alshammari, A., Al-Mutlaq, M. A. & Anjum, M. N. (2019) The systemic effect of PEG-nGO-induced oxidative stress in vivo in a rodent model, *Beilstein journal of nanotechnology*. 10(1), 901-911.



## APPENDIX A

**Table A-1:** Radiative heat flux from a single flash carrying 200 J (0.86 J/cm<sup>2</sup>) energy absorbed by thermocouple located on top of the perovskite film surface for the optimal condition of primary annealing step during GFA.

<b>Flash Duration (μs)</b>	<b>Current (Amps)</b>	<b>Voltage (Volts)</b>	<b>Power (W)</b>	<b>Useful Power density absorbed by thermocouple released from two capacitors (W/m<sup>2</sup>)</b>
0	0	1737	0	0
16	16	1737	27792	1136770
32	48	1737	83376	3410311
48	128	1736	222208	9088927
64	240	1735	416400	17031921
80	304	1732	526528	21536464
96	336	1730	581280	23775973
112	352	1727	607904	24864969
128	352	1724	606848	24821776
144	352	1721	605792	24778582
160	352	1719	605088	24749787
176	352	1716	604032	24706594
192	352	1713	602976	24663400
208	352	1710	601920	24620207
224	352	1707	600864	24577013
240	336	1705	572880	23432390
256	336	1702	571872	23391160
272	336	1699	570864	23349930
288	336	1696	569856	23308700
304	336	1694	569184	23281213
320	336	1691	568176	23239983
336	336	1688	567168	23198753
352	336	1686	566496	23171266
368	336	1683	565488	23130036
384	336	1680	564480	23088806
400	336	1678	563808	23061320

416	336	1675	562800	23020090
432	336	1672	561792	22978860
448	336	1670	561120	22951373
464	336	1667	560112	22910143
480	336	1664	559104	22868913
496	336	1662	558432	22841426
512	320	1659	530880	21714473
528	320	1656	529920	21675206
544	320	1654	529280	21649028
560	320	1651	528320	21609762
576	320	1649	527680	21583584
592	320	1646	526720	21544317
608	320	1644	526080	21518139
624	320	1641	525120	21478873
640	320	1638	524160	21439606
656	320	1636	523520	21413428
672	320	1633	522560	21374161
688	320	1631	521920	21347984
704	320	1628	520960	21308717
720	320	1626	520320	21282539
736	320	1623	519360	21243273
752	320	1621	518720	21217095
768	320	1618	517760	21177828
784	304	1615	490960	20081633
800	304	1613	490352	20056764
816	304	1611	489744	20031896
832	304	1608	488832	19994592
848	304	1606	488224	19969723
864	304	1603	487312	19932420
880	304	1601	486704	19907551
896	304	1598	485792	19870248
912	304	1596	485184	19845379
928	304	1594	484576	19820510
944	304	1591	483664	19783207
960	304	1589	483056	19758338
976	304	1586	482144	19721034
992	304	1584	481536	19696165
1008	304	1581	480624	19658862
1024	304	1579	480016	19633993
1040	304	1577	479408	19609124
1056	304	1574	478496	19571821
1072	288	1572	452736	18518165

1088	304	1569	476976	19509649
1104	288	1567	451296	18459265
1120	288	1565	450720	18435705
1136	288	1562	449856	18400365
1152	288	1560	449280	18376805
1168	288	1558	448704	18353245
1184	112	1556	174272	7128211
1200	16	1556	24896	1018316
1216	0	1556	0	0

**Table A-2:** Radiative heat flux from a single flash carrying 400 J (1.72 J/cm<sup>2</sup>) energy absorbed by thermocouple located on top of the perovskite film surface for the optimal condition of UFA as well as the secondary annealing step during GFA.

<b>Flash Duration (μs)</b>	<b>Current (Amps)</b>	<b>Voltage (Volts)</b>	<b>Power (W)</b>	<b>Useful Power density absorbed by thermocouple released from two capacitors (W/m<sup>2</sup>)</b>
0	0	1737	0	0
16	16	1737	27792	1136770
32	112	1736	194432	7952811
48	352	1735	610720	24980151
64	560	1731	969360	39649528
80	560	1726	966560	39535000
96	592	1722	1019424	41697285
112	576	1717	988992	40452531
128	544	1713	931872	38116164
144	544	1708	929152	38004908
160	528	1704	899712	36800730
176	528	1700	897600	36714344
192	512	1696	868352	35518019
208	512	1692	866304	35434250
224	512	1687	863744	35329539
240	512	1683	861696	35245770
256	496	1679	832784	34063188
272	496	1675	830800	33982037
288	496	1671	828816	33900886
304	496	1667	826832	33819735
320	480	1664	798720	32669876
336	480	1660	796800	32591342

352	480	1656	794880	32512809
368	480	1652	792960	32434276
384	480	1648	791040	32355742
400	480	1644	789120	32277209
416	480	1640	787200	32198676
432	480	1637	785760	32139776
448	480	1633	783840	32061242
464	480	1629	781920	31982709
480	480	1625	780000	31904176
496	480	1621	778080	31825642
512	480	1617	776160	31747109
528	480	1614	774720	31688209
544	480	1610	772800	31609675
560	464	1606	745184	30480104
576	464	1602	743328	30404188
592	464	1599	741936	30347252
608	464	1595	740080	30271336
624	464	1591	738224	30195421
640	464	1587	736368	30119505
656	464	1584	734976	30062568
672	464	1580	733120	29986653
688	464	1576	731264	29910737
704	464	1573	729872	29853801
720	464	1569	728016	29777885
736	448	1565	701120	28677764
752	448	1562	699776	28622790
768	448	1558	697984	28549492
784	448	1554	696192	28476195
800	448	1551	694848	28421221
816	448	1547	693056	28347923
832	448	1544	691712	28292950
848	448	1540	689920	28219652
864	448	1537	688576	28164679
880	448	1533	686784	28091381
896	448	1529	684992	28018083
912	432	1526	659232	26964427
928	432	1522	657504	26893747
944	432	1519	656208	26840737
960	432	1515	654480	26770057
976	432	1512	653184	26717047
992	432	1509	651888	26664037
1008	432	1505	650160	26593357

1024	432	1502	648864	26540347
1040	432	1498	647136	26469667
1056	432	1495	645840	26416657
1072	432	1491	644112	26345977
1088	432	1488	642816	26292967
1104	432	1484	641088	26222287
1120	416	1481	616096	25200045
1136	416	1478	614848	25148998
1152	416	1474	613184	25080936
1168	416	1471	611936	25029889
1184	416	1468	610688	24978842
1200	416	1464	609024	24910780
1216	416	1461	607776	24859734
1232	416	1458	606528	24808687
1248	416	1454	604864	24740625
1264	416	1451	603616	24689578
1280	416	1448	602368	24638531
1296	416	1444	600704	24570469
1312	400	1441	576400	23576368
1328	400	1438	575200	23527284
1344	400	1435	574000	23478201
1360	400	1432	572800	23429118
1376	400	1428	571200	23363673
1392	400	1425	570000	23314590
1408	400	1422	568800	23265506
1424	400	1419	567600	23216423
1440	400	1416	566400	23167340
1456	400	1412	564800	23101895
1472	400	1409	563600	23052812
1488	400	1406	562400	23003729
1504	400	1403	561200	22954645
1520	384	1400	537600	21989339
1536	384	1397	536448	21942219
1552	384	1393	534912	21879393
1568	384	1390	533760	21832273
1584	384	1387	532608	21785153
1600	384	1384	531456	21738033
1616	384	1381	530304	21690913
1632	384	1378	529152	21643793
1648	384	1375	528000	21596673
1664	384	1372	526848	21549553
1680	384	1369	525696	21502433

1696	384	1366	524544	21455313
1712	368	1363	501584	20516185
1728	368	1360	500480	20471028
1744	368	1357	499376	20425871
1760	368	1354	498272	20380715
1776	368	1351	497168	20335558
1792	368	1348	496064	20290401
1808	368	1345	494960	20245245
1824	368	1342	493856	20200088
1840	368	1339	492752	20154931
1856	368	1336	491648	20109774
1872	368	1333	490544	20064618
1888	368	1330	489440	20019461
1904	368	1327	488336	19974304
1920	352	1325	466400	19077061
1936	352	1322	465344	19033868
1952	352	1319	464288	18990674
1968	352	1316	463232	18947481
1984	352	1313	462176	18904287
2000	352	1311	461472	18875492
2016	352	1308	460416	18832299
2032	96	1306	125376	5128228
2048	16	1305	20880	854050.2
2064	0	1305	0	0

## APPENDIX B

Step-by-step procedures with screenshots of the FEA for temperature estimation of the perovskite film surface through ANSYS are included in Fig. B(1-12) in the following. These figures show the consecutive steps attributed to the input of material properties for the Aluminum stage of IPL, glass substrate, and perovskite layer deposited on top of glass, followed by the design and meshing of geometry, designation of boundary conditions, and finally, temperature profile results.

### 1) Material Properties

Open the ANSYS software and choose the *transient thermal* from the left panel, then select the *engineering data* (Fig. B-1). Delete any prior saved materials in the column A of *contents of engineering data* by selecting *delete* upon right clicking on the material name. In the engineering data wizard (Fig. B-2) right click in the bottom empty row of column A of *contents of engineering data* and select *engineering data sources*. This wizard (Fig. B-3) contains the properties of numerous materials such as Aluminum and glass but does not include the properties of the perovskite. Therefore, it is necessary to manually input the perovskite properties. To add glass and Aluminum, simply select the *thermal materials* in the *engineering data sources* and add the material by right clicking on the material in the *contents of thermal materials* and selecting *add to engineering data*. Finally, to add the perovskite properties, type *perovskite* in the last row of the column A of *contents of engineering data* and enter its density and thermal properties.

Upon adding all materials, the engineering data wizard should include all materials of Aluminum, glass, and perovskite (Fig. B-4).

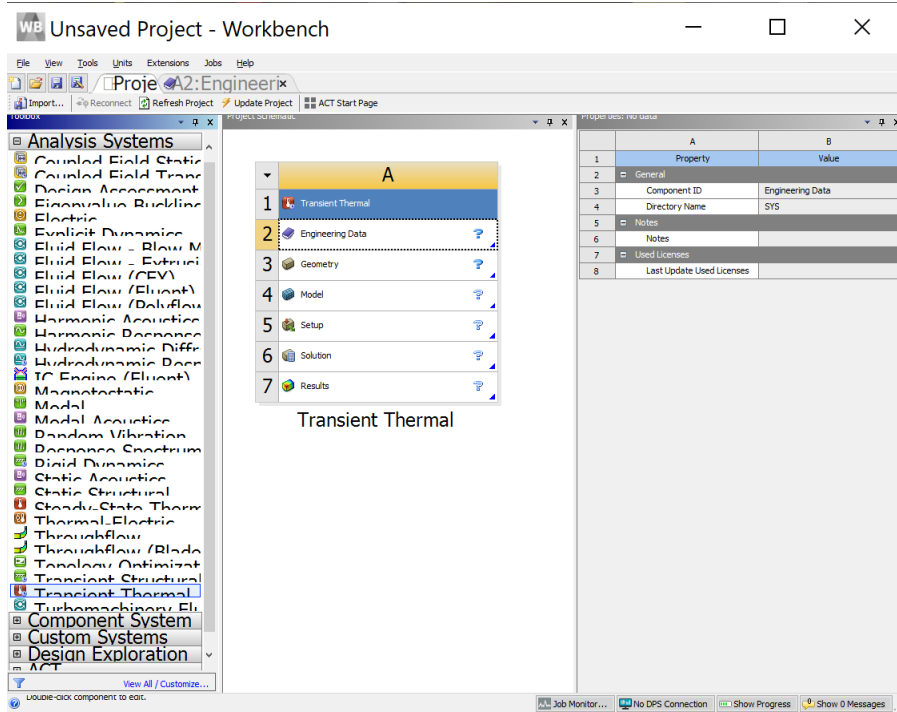


**Fig. B-1:** ANSYS startup showing the processing tree for transient thermal simulation.

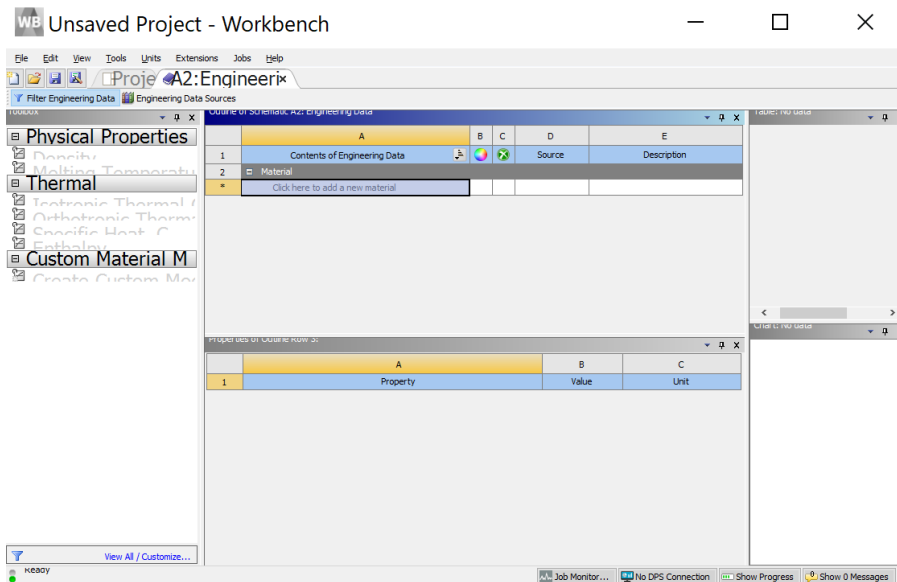


**Fig. B-2:** Engineering data wizard.



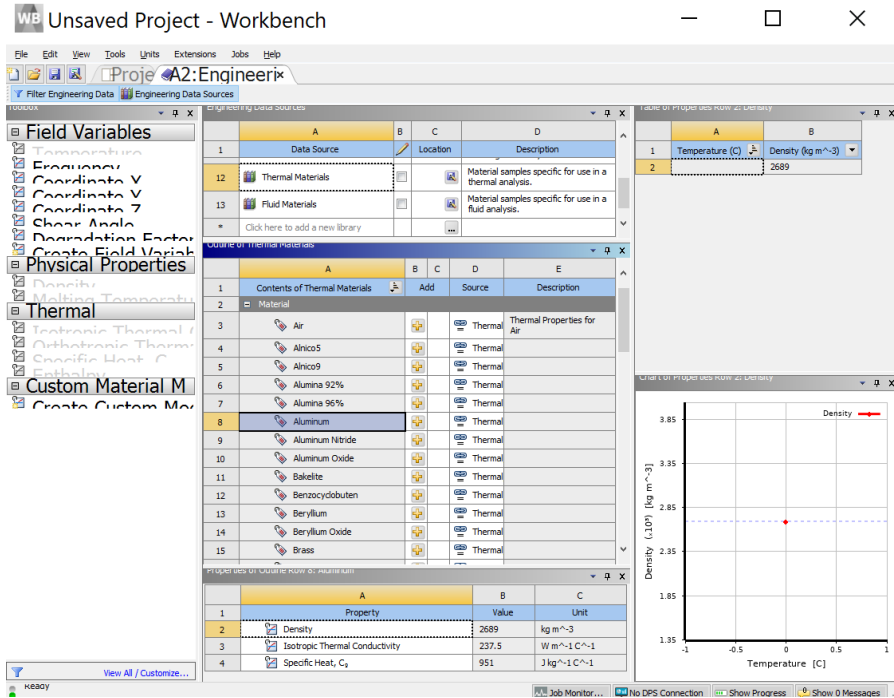


**Fig. B-3:** Engineering data sources wizard.

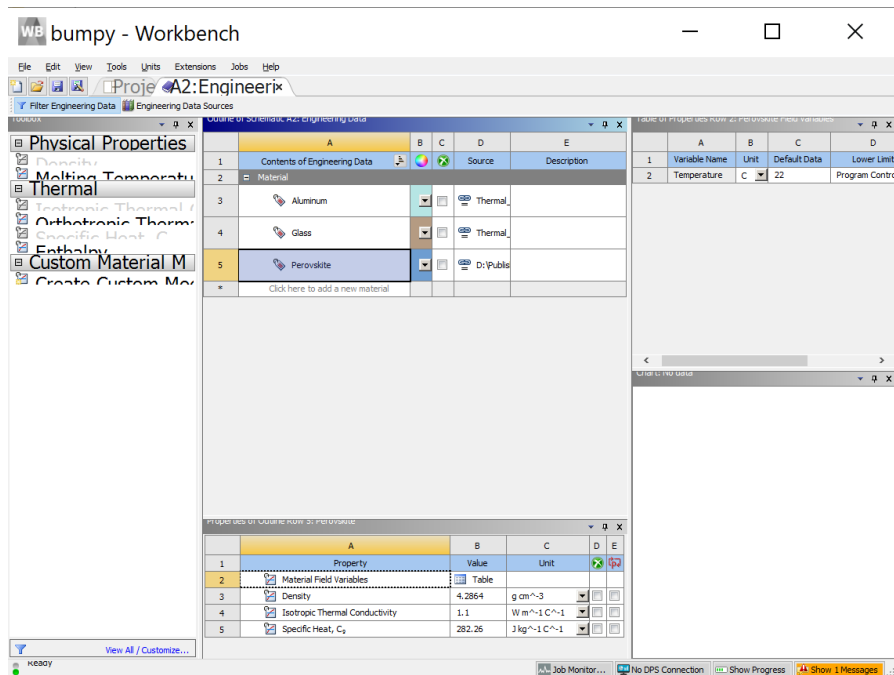


**Fig. B-4:** Engineering data wizard indicating the successful addition of Aluminum, glass, and perovskite materials used in the simulation.

## 2) Geometry Design

To create the design, select *geometry* in the ANSYS simulation design tree and choose the *analysis type* to *2D* in the right panel then select *New DesignModeler Geometry* by right clicking on the *geometry* tab (Fig. B-5). In the DesignModeler window select the *micrometer* scale from the *Units* tab, then right click on the *XY plane* and select *Look at*. At this stage, create the model based on the sketch shown in Fig. B-6 by drawing a rectangle through the *draw* tab inside the *sketching* tab at the bottom left corner of the screen and subsequently adjust the width and length to 2 and 6350  $\mu\text{m}$  from the *dimensions* tab inside the *sketching tab* to create the Aluminum stage model. Repeat the same process to create two more rectangles on top of each other to create the glass and perovskite models with the same width but two different lengths of 3000 and 0.45  $\mu\text{m}$ , respectively. Upon drawing the sketches, choose *sketch 1* (Aluminum stage) and select *Surfaces From Sketches* from the *Concept* tab and click *Apply* in the *Base Objects* tab and finally click *Generate* to create the geometry. Repeat the same process for *sketch 2* (glass) and *sketch 3* (perovskite). Notably, instead of *Add Material* for the first and third sketch, select *Add Frozen* in the *operations* tab for the *sketch 2* (glass) otherwise the simulation will assume the design consisted of three different layers as a single piece of a uniform sketch. The created stacked model is shown in Fig B-7, where the Aluminum, glass and perovskite layers are zoomed and indicated in Figures B-8, B-9, and B-10, respectively.

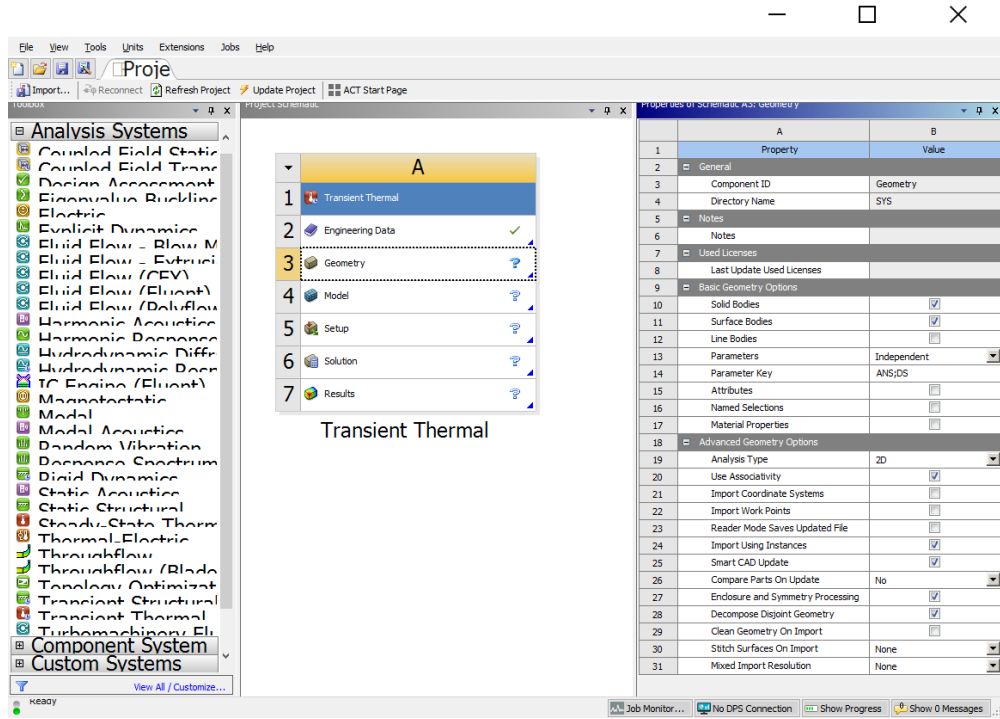


**Fig. B-5:** Selection of the geometry tab to create the design geometry.

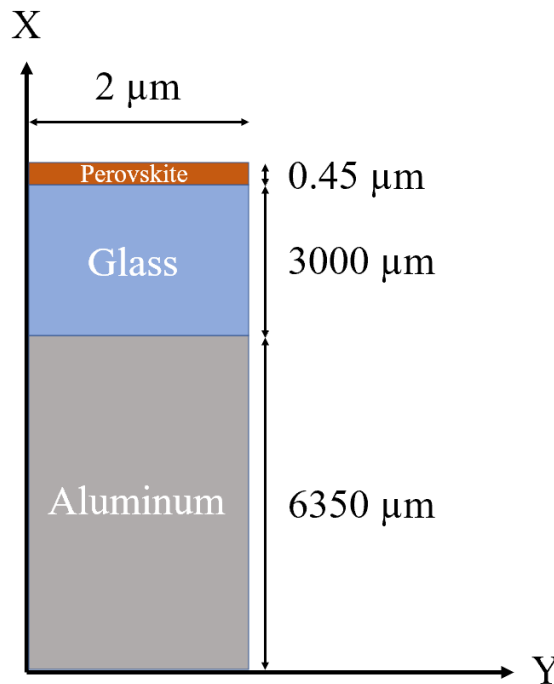


**Fig. B-6:** Geometry design showing the stacked layers of Aluminum, glass, and perovskite with dimensions.

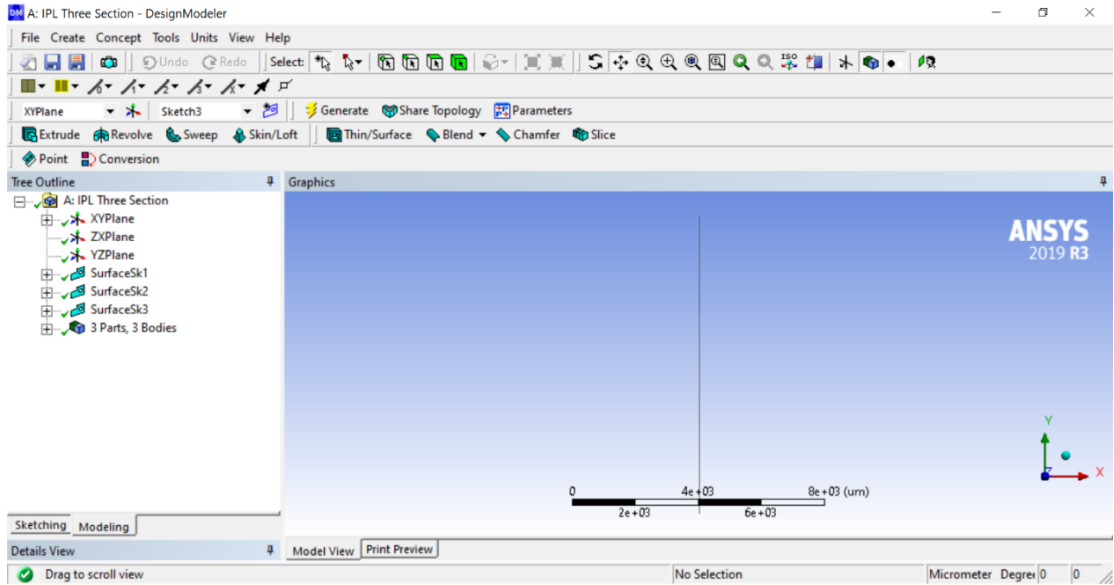


**Fig. B-7:** Stacked design model of Aluminum, glass, and perovskite.

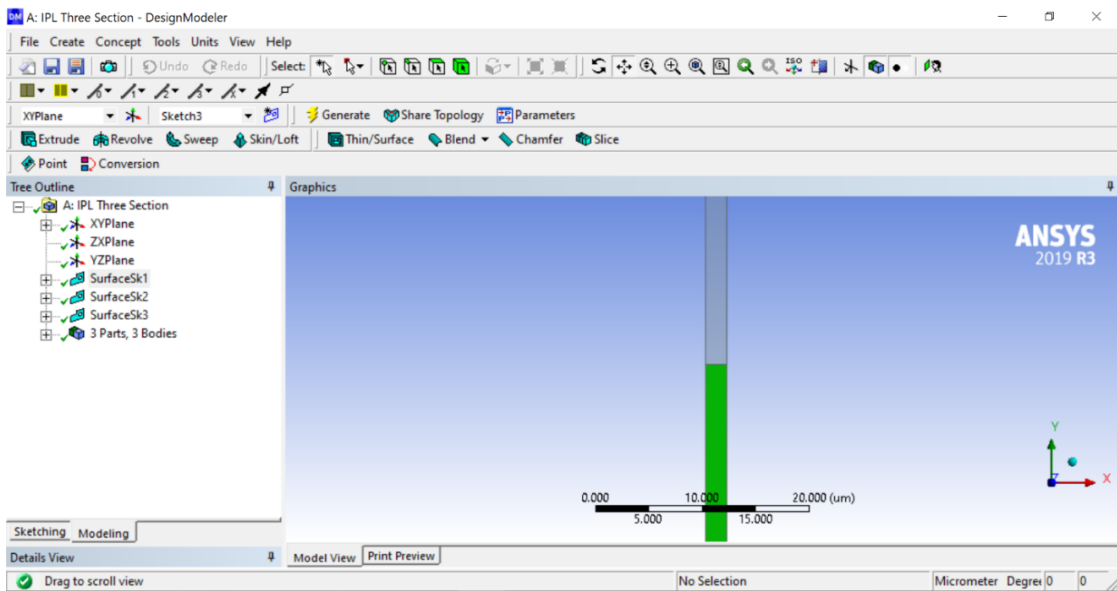


**Fig. B-8:** Schematic showing the Aluminum underneath glass.

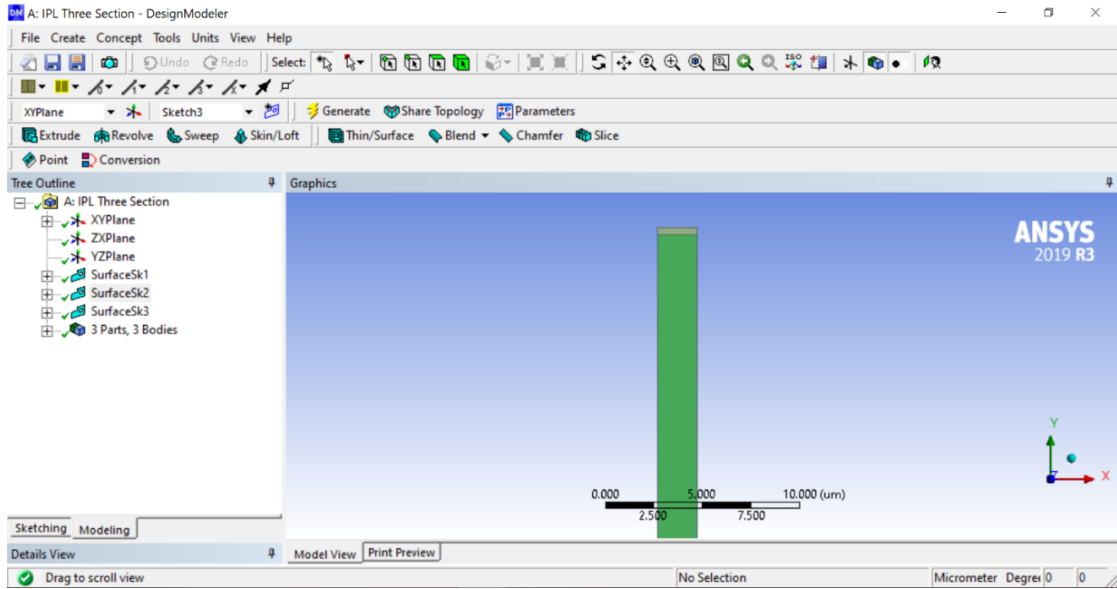


**Fig. B-9:** Schematic showing the designed glass underneath the perovskite film.

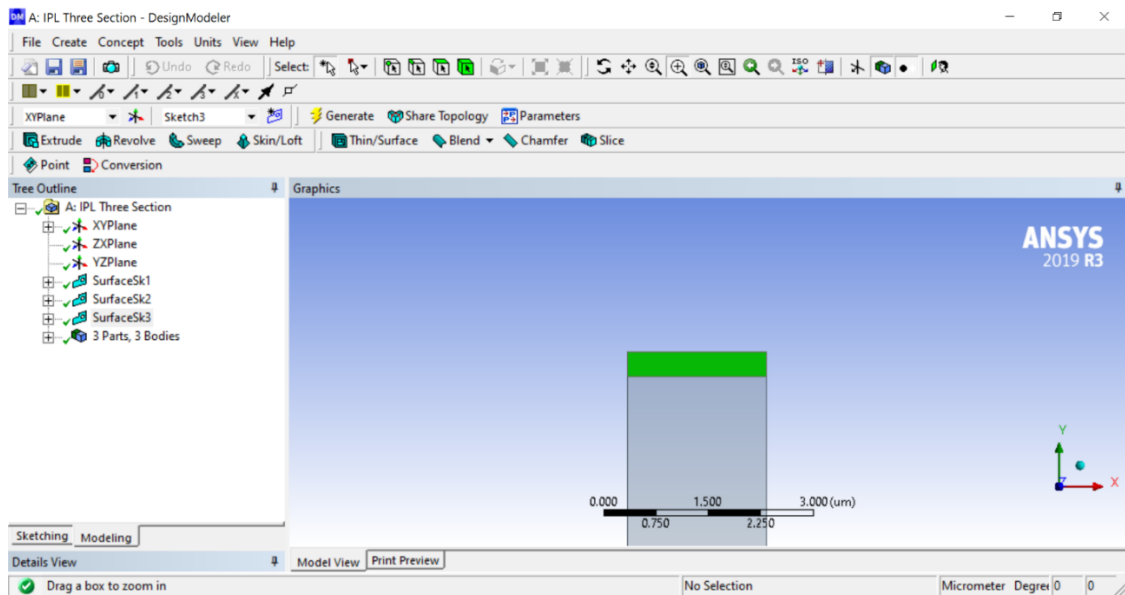


**Fig. B-10:** Schematic showing the designed perovskite film on glass.

### 3) Geometry Meshing

Select *Model* in the ANSYS simulation tree (Fig. B-11) to enter the wizard used for meshing, applying the boundary simulations, and solving. Upon opening of the wizard, the created geometry in the previous section is automatically showed up. Before, meshing the geometry ensure the geometry, materials, coordinate systems, and connections tabs are all checked in the *Outline* panel, and the list of the selected materials is entirely showed in the materials tab (Fig. B-12). In the geometry tab, select *Surface Body*, where the associated sketch to the selected body lights in the model. Select *Assignment* in the *Details* panel and choose the material used for that layer. Repeat this step until are layers are assigned to Aluminum, glass, and perovskite. As indicated in Fig. B-13, select *Mesh* in the *outline tab* and adjust the meshing size and quality as indicated in the *Details* tab, and finally select *Generate Mesh* by right clicking on the *Mesh* tab to create the Mesh.

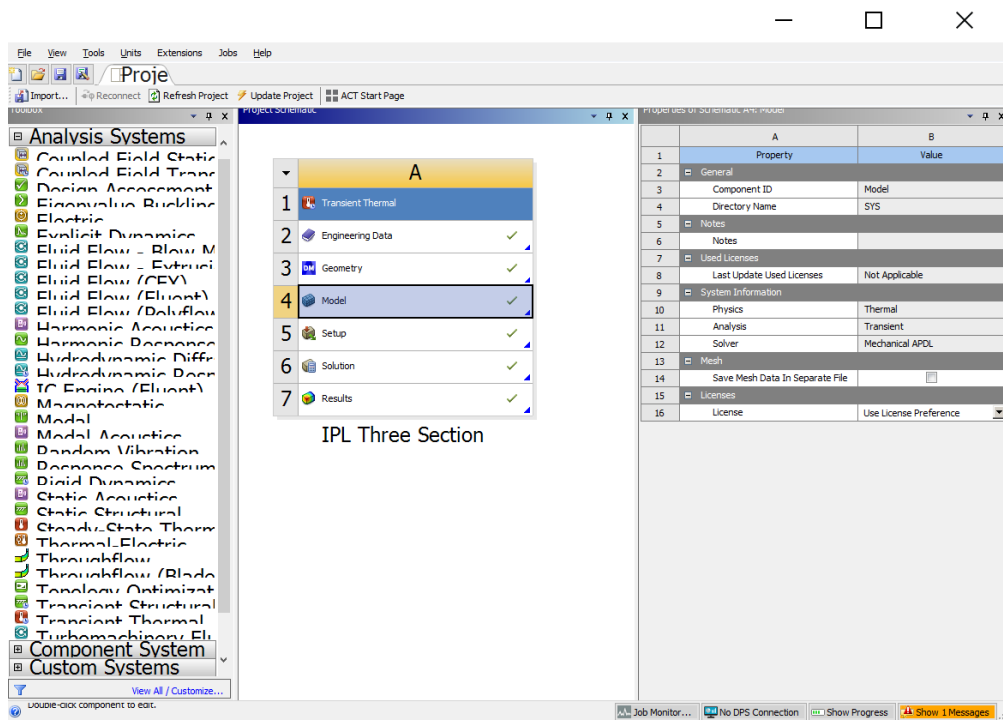


**Fig. B-11:** Selection of the model tab.

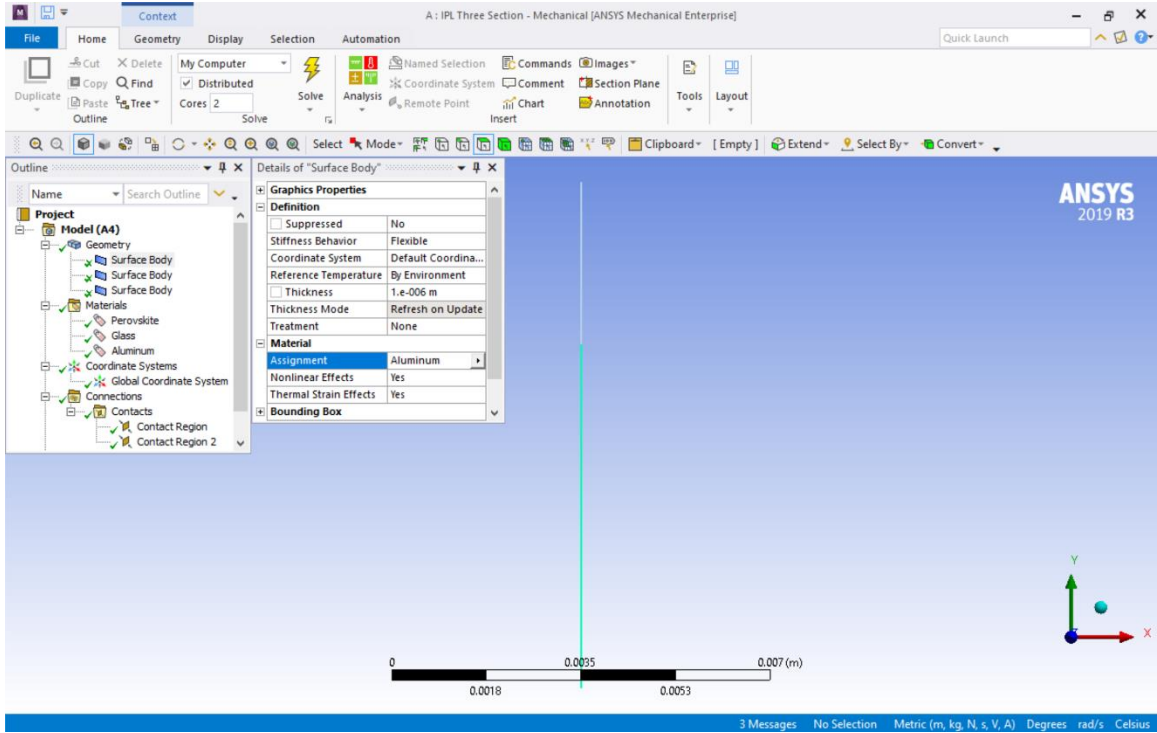


Fig. B-12: Schematic showing the assignment of materials to the designed geometry.

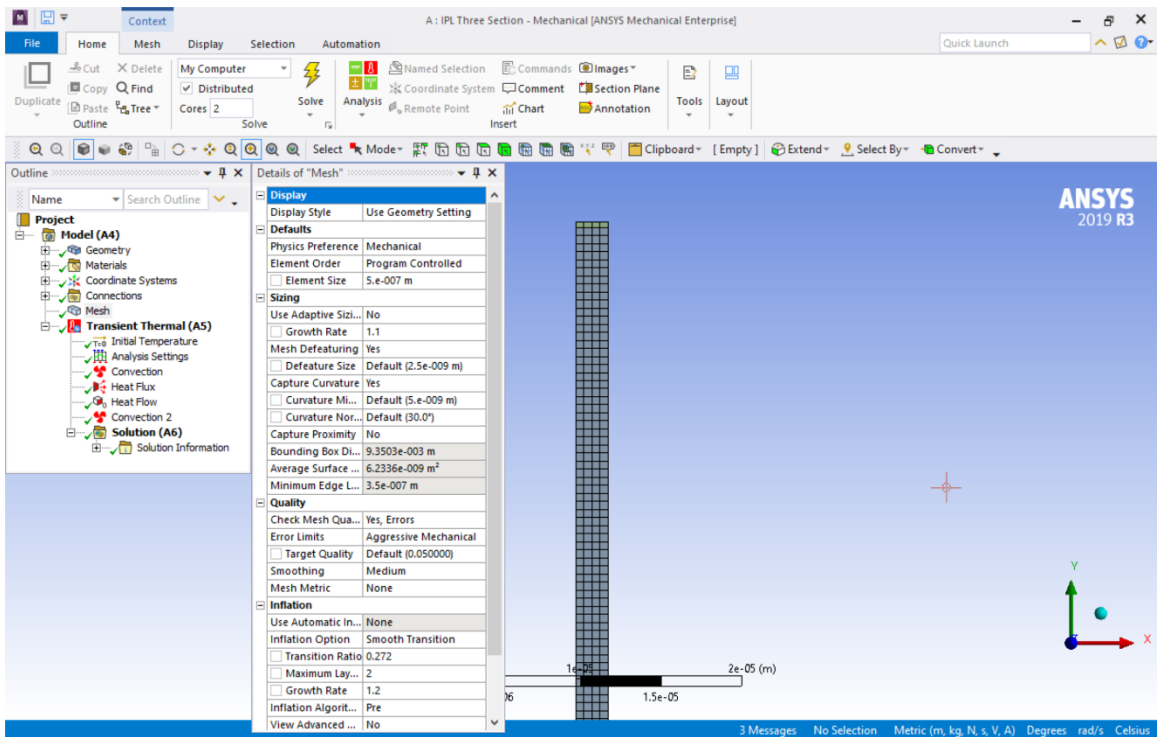
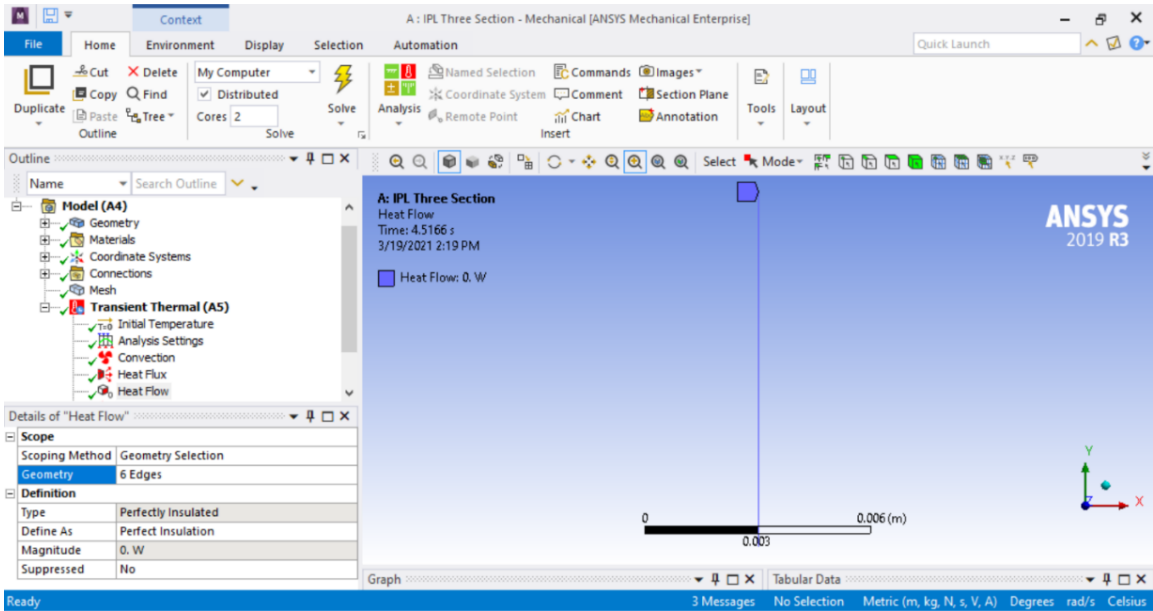


Fig. B-13: Schematic showing the meshing parameters.

#### 4) Boundary Conditions

To assign the boundary conditions to the meshed geometry, right click on the *Transient Thermal* tab in the *Outline* panel and select the desired condition from the *Insert* menu. As introduced in Fig. 3.3 in chapter 3, the right and left sides of the model are insulated; hence, *Perfectly Insulated* condition was selected from the *Insert* menu. To select the boundaries, all right and left sides of all the three layers were selected by clicking on them individually while pressing the *Ctrl* key on Keyboard and clicking on *Apply* upon selection of all boundaries (Fig. B-14). This procedure is repeated to apply a natural convection condition underneath and on top of the Aluminum and perovskite layers, respectively, by selecting *Convection* from the *Insert* menu, selecting the top of the perovskite film (Fig. B-15) and bottom of the Aluminum (Fig. B-16), and entering 5 W/m<sup>2</sup>.K and 22°C as the natural convection coefficient and ambient temperature, respectively, in the *Details* panel. To model the IPL heat flux (Fig. B-17), add a *Heat Flux* boundary condition from the *Insert* menu and upload the calculated tabulated data of the IPL photon energy in Appendix A. Notably, set the initial temperature to 22°C in the *Initial Temperature* tab within the *Transient Thermal* Tab, and adjust the *initial, minimum, and maximum time step* in the *Analysis Settings* tab in the *Transient Thermal* tab within a suitable range for simulation. These times should be adjusted based on the flash duration and delay time between flashes during IPL annealing.





**Fig. B-14:** Schematic showing insulated boundary conditions applied to the left and right sides of the entire design stack to merely simulate heat transfer towards the depth of the model from perovskite top surface.

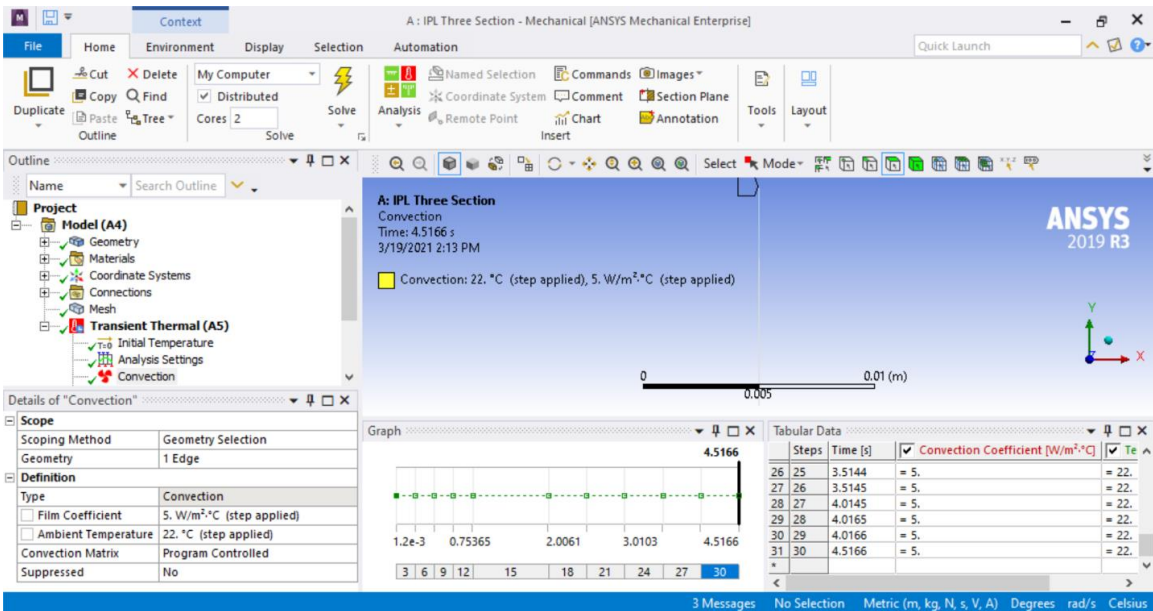


**Fig. B-15:** Schematic showing the natural convection condition applied on top of the perovskite film and bottom of Aluminum stage.

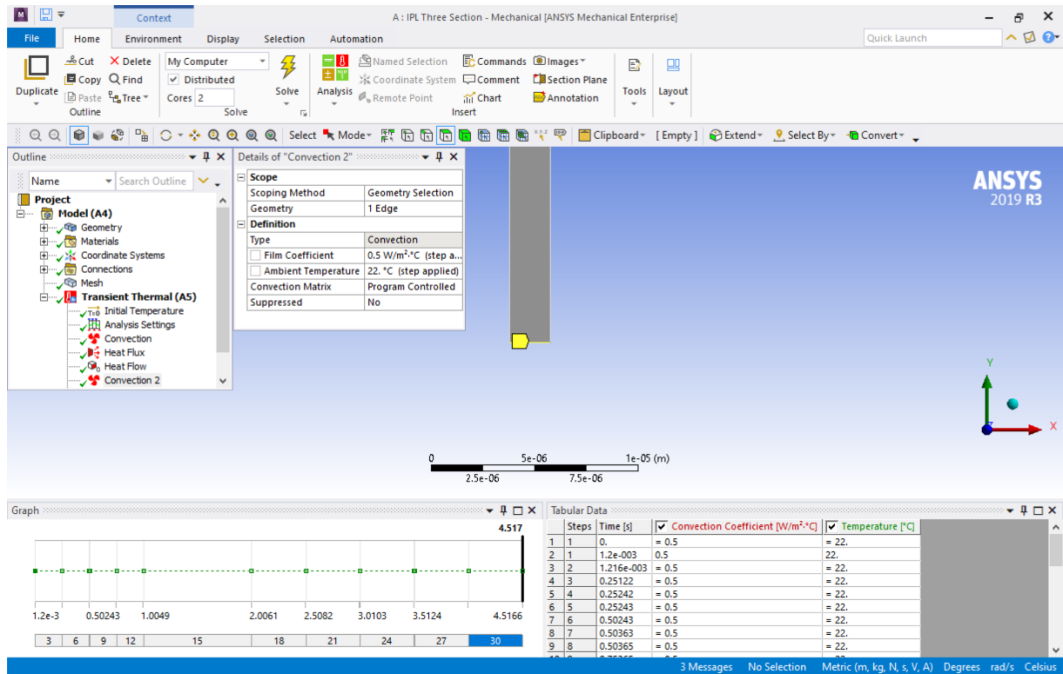


**Fig. B-16:** Schematic showing the natural convection condition applied at the bottom of Aluminum stage.

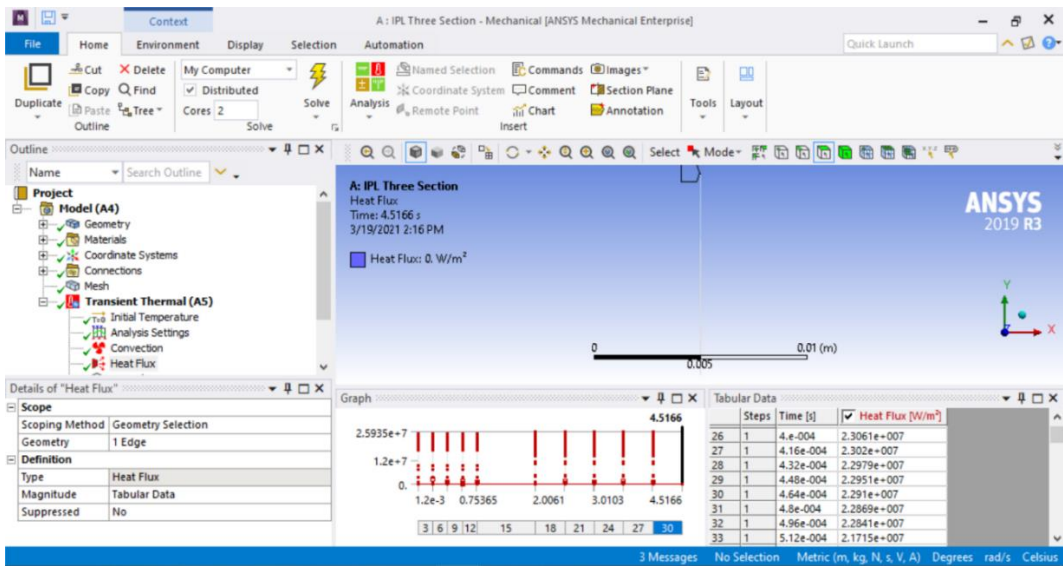


**Fig. B-17:** Schematic showing the radiative heat flux boundary condition on top of the perovskite film during IPL annealing where the data was entered manually from a spreadsheet based on calculations tabulated in Appendix A.

## 5) Solution

To carry out the solution, click on *Solve* and select *Temperature – Global Maximum* from the *Solution* tab of the *Outline* panel upon completion to see the temperature profile. To save the temperatures, choose *Export* by right clicking in the temperature column of the *Tabular Data* table as indicated in Fig. B-18. The ANSYS simulation files is provided [here](#).

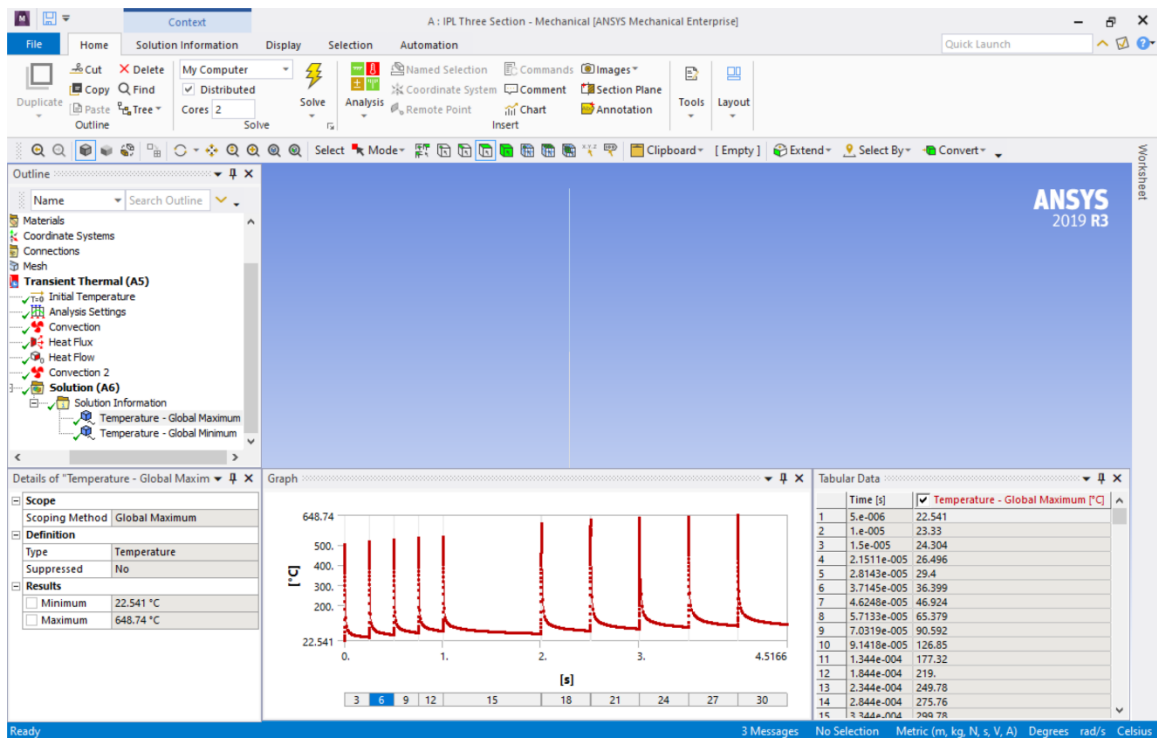


**Fig. B-18:** Schematic showing the temperature profile results.

## CURRICULUM VITAE

Amir Hossein Ghahremani

Solar manufacturing Lab. at University of Louisville

216 Eastern Parkway, Louisville, KY, 40208

### **Education**

2016 – 2021.....PhD, Mechanical Engineering, University of Louisville

2014 – 2016.....M.S, Mechanical Engineering, Azad University

2009 – 2013.....B.S, Mechanical Engineering, Azad University

### **Patent**

- 1) Druffel, Thad, Brandon Lavery, Krishnamraju Ankireddy, Amir Hossein Ghahremani, Blake Martin, and Gautam Gupta. "Methods for forming a perovskite solar cell." U.S. Patent 10,950,794 issued March 16, 2021.
- 2) Druffel, Thad, Brandon Lavery, Krishnamraju Ankireddy, Amir Hossein Ghahremani, Blake Martin, and Gautam Gupta. "Methods for forming a perovskite solar cell." U.S. Patent 10,714,688 issued July 22, 2020.

## Journal Publications

- 1) Ghahremani, Amir H., Ratnayake Dilan, Sherehiy Andriy, Dan O. Popa, and Thad Druffel. "Automated fabrication of perovskite photovoltaics using inkjet printing and intense pulse light annealing." (Submitted)
- 2) Ghahremani, Amir H., Sahar Pishgar, Jitendra Bahadur, and Thad Druffel. "Intense Pulse Light Annealing of Perovskite Photovoltaics Using Gradient Flashes." *ACS Applied Energy Materials* (2020).
- 3) Ghahremani, Amir H., Blake Martin, Alexander Gupta, Jitendra Bahadur, Krishnamraju Ankireddy, and Thad Druffel. "Rapid fabrication of perovskite solar cells through intense pulse light annealing of SnO<sub>2</sub> and triple cation perovskite thin films." *Materials & Design* 185 (2020): 108237.
- 4) Ghahremani, Amir H., Blake Martin, Krishnamraju Ankireddy, and Thad Druffel. "Rapid processing of perovskite solar cells through pulsed photonic annealing: a review." *Journal of Coatings Technology and Research* 16, no. 6 (2019): 1637-1642.
- 5) Bahadur, Jitendra, Amir H. Ghahremani, Blake Martin, Sahar Pishgar, Thad Druffel, Mahendra K. Sunkara, and Kaushik Pal. "A study on the material characteristics of low temperature cured SnO<sub>2</sub> films for perovskite solar cells under high humidity." *Journal of Materials Science: Materials in Electronics* 30, no. 20 (2019): 18452-18461.
- 6) Bahadur, Jitendra, Amir H. Ghahremani, Sunil Gupta, Thad Druffel, Mahendra K. Sunkara, and Kaushik Pal. "Enhanced moisture stability of MAPbI<sub>3</sub> perovskite solar cells through Barium doping." *Solar Energy* 190 (2019): 396-404.
- 7) Bahadur, Jitendra, Amir H. Ghahremani, Blake Martin, Thad Druffel, Mahendra K. Sunkara, and Kaushik Pal. "Solution processed Mo doped SnO<sub>2</sub> as an effective ETL in

- the fabrication of low temperature planer perovskite solar cell under ambient conditions." *Organic Electronics* 67 (2019): 159-167.
- 8) Ankireddy, Krishnamraju, Amir H. Ghahremani, Blake Martin, Gautam Gupta, and Thad Druffel. "Rapid thermal annealing of CH<sub>3</sub>NH<sub>3</sub>PbI<sub>3</sub> perovskite thin films by intense pulsed light with aid of diiodomethane additive." *Journal of Materials Chemistry A* 6, no. 20 (2018): 9378-9383.

### **Conference Publications**

- 1) Ghahremani, Amir H., and Thad Druffel. "Intense Pulse Light Annealing for Perovskite Photovoltaics." In *International Manufacturing Science and Engineering Conference*, vol. 84263, p. V002T06A040. American Society of Mechanical Engineers, 2020.
- 2) Ghahremani, Amir Hossein, and Thad Druffel. "Rapid Fabrication of Thin Films for Perovskite Solar Cells." *ECS Transactions* 92, no. 9 (2019): 1.
- 3) Ghahremani, Amir H., and Thad Druffel. "Realizing Perovskite Solar Cells on Roll Roll-to-Roll Compatible Processes." In *2019 IEEE 46th Photovoltaic Specialists Conference (PVSC)*, vol. 2, pp. 1-5. IEEE, 2019.
- 4) Armstrong, Peter, Amir Ghahremani, Thad Druffel, Robert Buchanan, and Craig Grapperhaus. "Hole Transporting Layers in Solar Cells: Stabilizing NiO Perovskite Inks with Organic Capping Agents." In *ECS Meeting Abstracts*, no. 39, p. 1776. IOP Publishing, 2019.
- 5) Martin, Blake, Amir Hossein Ghahremani, and Thad Druffel. "Scalable Hole Transport Materials for Roll-to-Roll Perovskite Photovoltaic Modules." In *ECS Meeting Abstracts*, no. 39, p. 1775. IOP Publishing, 2019.

## **Skills**

- Non-vacuum thin film development using spin, slot-die, and spray coating as well as inkjet printing.
- Vacuum thin film development through thermal evaporation, sputtering, and CVD.
- Material characterization using SEM, XRD, XPS, PL, Raman, UV-vis, ellipsometry, profilometry, as well as conductivity measurement of thin films using four-point probe.
- Solar cell performance testing through voltammetry, IPCE, and IS.
- FEA simulation using ANSYS.
- Design and CNC machining of machine parts using SolidWorks and CAM.
- Design, automation, and control of mechanisms using Arduino, PLC, and LabVIEW.

## **Awards**

- University of Louisville Fellowship.
- U.S National Science Foundation Award # 1828355.

## **Software**

- ANSYS
- SolidWorks
- LabVIEW
- ImageJ
- Ki CAD
- Arduino
- Origin

- Microsoft Office